Curtin University

The Lesueur, SW Hub: Improving seismic response and attributes. Final Report

ANLEC R&D Project 7-0115-0241

S. Glubokovskikh, B. Gurevich, R. Pevzner, S. Shevchenko, K. Tertyshnikov, and S. Ziramov

ACKNOWLEDGEMENTS

The authors wish to acknowledge financial assistance provided through Australian National Low Emissions Coal Research and Development (ANLEC R&D). ANLEC R&D is supported by Australian Coal Association Low Emissions Technology Limited and the Australian Government through the Clean Energy Initiative. In addition the authors thank SW Hub Project management and ODIN Geosciences ltd for numerous interactions and support.

CONTENTS

Acknowledgements 2

Contents 3

List of Figures 5

List of Tables 10

Executive summary 11

1. Introduction 14

2. Advanced VSP Processing 18

2.1. The Harvey 2 well 19

2.2. The Harvey 3 well 29

2.3. The Harvey 4 well 40

2.4. Estimation of attenuation 51

2.4.1. The Harvey 2 well 53

2.4.2. The Harvey 3 well 59

2.4.3. The Harvey 4 well 62

2.5. Conclusions 67

3. Seismic Data Processing and Imaging 68

3.1. Composite line 68

3.1.1. Signal to Noise Ratio (SNR) improvement 75

3.1.2. Velocity analysis 77

3.1.3. Pre-stack time imaging 78

3.1.4. Pre-stack depth imaging 82

3.1.5. Conclusions 86

3.2. Reprocessing of Harvey 3D – Generation 2 volume 87

3.2.1. Pre-stack time imaging 88

3.2.2. Velocity model building using PSDM on Generation 2 Harvey data 93

3.2.3. Conclusions 96

4. Stochastic AVO Seismic Inversion along the Composite Line 98
4.1. Workflow and data conditioning. 98
4.2. Data QC and Well to Seismic Tie. 101
4.3. Rock physics model and inversion analysis. 104
4.4. Conclusions 117
5. Stochastic Seismic Inversion of the Large 3D Survey 118
5.1. Inversion algorithm 119
5.1.1. A priori seismic model 120
5.1.2. Uncertainty of the seismic data 121
5.1.3. Final parameters of the inversion algorithm 125
5.2. Interpretation of the inversion results 126
5.2.1. Lithological classification 127
5.2.2. Porosity prediction 134
5.2.3. Comparison with the well data 136
5.3. Conclusions 138
6. Overall Conclusions 140
References 142
Appendix A – Check shot data 145
The Harvey 2 well 145
The Harvey 3 well 147
The Harvey 4 well 149
Appendix B – Acronyms and Notation 151
Appendix C – The Lesueur, SW Hub: Advanced well log analysis, constraints for the stress field and geomechanical modelling of CO2 injection - Milestone 6 Report 152

LIST OF FIGURES

Figure 1 Diagram of the workflow for seismic interpretation to constrain reservoir models. 14

Figure 2 Number of shots per receiver level in the Harvey 2 well. 20

Figure 3 The Harvey 2 well correlated ZVSP data (X, Y – horizontal components, Z – vertical). 21

Figure 4 The Harvey 2 well direct wave polarisation analysis used to orient horizontal components. 22

Figure 5 The Harvey 2 well ZVSP data after 3C orientation. Red arrows indicate reflection from the fault plane. 23

Figure 6 The Harvey 2 well ZVSP data, Z component, deconvolution and amplitude correction applied. 23

Figure 7 The Harvey 2 well ZVSP data, Z component, up-going PP waves. 24

Figure 8 The Harvey 2 well ZVSP data, Interactive velocity analysis. 25

Figure 9 The Harvey 2 well ZVSP data, velocity model. 26

Figure 10 The Harvey 2 well ZVSP data, VSP-NMO and corridor stack trace 27

Figure 11 The Harvey 2 well ZVSP, the result of the seismic to well tie (principle reflectors are marked with red dashed lines) 28

Figure 12 The Harvey 3 well: Number of shots per receiver level. 30

Figure 13 The Harvey 3 well correlated ZVSP data 31

Figure 14 The Harvey 3 well direct wave polarisation analysis used to orient horizontal components. 31

Figure 15 The Harvey 3 well ZVSP data after 3C orientation. 32

Figure 16 The Harvey 3 well ZVSP data, Z component, deconvolution and amplitude correction applied. 33

Figure 17 The Harvey 3 well ZVSP data, Z component, up-going PP waves. 34

Figure 18 The Harvey 3 well ZVSP data, Interactive velocity analysis. 35

Figure 19 The Harvey 3 well ZVSP data, velocity model. 36

Figure 20 The Harvey 3 well ZVSP data, VSP-NMO and corridor stack trace. 37

Figure 21 The Harvey 3 well ZVSP, the result of the seismic to well tie (principle reflectors are shown marked with red dashed lines). 39

Figure 22 The Harvey 4 well. Number of shots per receiver level. 41

Figure 23 The Harvey 4 well correlated ZVSP data (X, Y – horizontal components, Z – vertical). 42

Figure 24 The Harvey 4 well direct wave polarisation analysis used to orient horizontal components. ... 43

Figure 25 The Harvey 4 well ZVSP data after 3C orientation. ... 44

Figure 26 The Harvey 4 well ZVSP data, Z component, deconvolution and amplitude correction applied. ... 45

Figure 27 The Harvey 4 well ZVSP data, Z component, up-going PP waves. ... 46

Figure 28 The Harvey 4 well ZVSP data, Interactive velocity analysis ... 47

Figure 29 The Harvey 4 well ZVSP data, velocity model. ... 48

Figure 30 The Harvey 4 well ZVSP data, VSP-NMO and corridor stack trace. ... 49

Figure 31 The Harvey 4 well ZVSP, the result of the seismic to well tie (principle reflectors are shown marked with red dashed lines). ... 50

Figure 32 The Harvey 2 well. Attenuation of up-going waves using FX deconvolution. ... 54

Figure 33 The Harvey 2 well. Amplitude spectra estimations. ... 55

Figure 34 The Harvey 2 well. Amplitude decay at different frequencies. ... 56

Figure 35 The Harvey 2 well. Centroid frequency (top), its deviation (middle) and absolute amplitude decay curves. ... 57

Figure 36 The Harvey 2 well. Centroid frequency (top) and energy decay curves. Q factor estimated in thick layered model. ... 58

Figure 37 The Harvey 2 well. Direct wave amplitude decay curve (red), amplitude decay due to attenuation (black) and amplitude decay curve after Q-compensation (blue). ... 59

Figure 38 The Harvey 3 well. Attenuation of up-going waves using FX deconvolution. ... 59

Figure 39 The Harvey 3 well. Amplitude spectra estimations. ... 60

Figure 40 The Harvey 3 well. Amplitude decay at different frequencies. ... 60

Figure 41 The Harvey 3 well. Centroid frequency (top), its deviation (middle) and absolute amplitude decay curves. ... 61

Figure 42 The Harvey 3 well. Centroid frequency (top) and energy decay curves. Q factor estimated in thick layered model. ... 61

Figure 43 The Harvey 3 well. Direct wave amplitude decay curve (red), amplitude decay due to attenuation (black) and amplitude decay curve after Q-compensation (blue). ... 62

Figure 44 The Harvey 4 well. Attenuation of up-going waves using FX deconvolution. ... 63

Figure 45 The Harvey 4 well. Amplitude spectra estimations. ... 64

Figure 46 The Harvey 4 well. Amplitude decay at different frequencies. 64

Figure 47 The Harvey 4 well. Centroid frequency (top), its deviation (middle) and absolute amplitude decay curves. 65

Figure 48 The Harvey 4 well. Centroid frequency (top) and energy decay curves. Q factor estimated in thick layered model. 66

Figure 49 The Harvey 4 well. Direct wave amplitude decay curve (red), amplitude decay due to attenuation (black) and amplitude decay curve after Q-compensation (blue). 66

Figure 50 Survey layout; Position of available seismic surveys in the area (A). All seismic vintages of a composite line (B). 71

Figure 51 CMP fold coverage. 72

Figure 52 Offset distribution plot and histogram. 73

Figure 53 Refraction statics for all receivers (A) and all source positions (B) displayed in milliseconds.... 74

Figure 54 Raw shot gather 76

Figure 55 Pre-processed shot gather. 77

Figure 56 Interactive velocity analysis, semblance on the left, imaged gather on the right. 78

Figure 57 CDP arbitrary line embedded in regional Harvey 3D grid. 80

Figure 58 PSTM arbitrary section embedded in regional Generation 2 Harvey volume, view from NE. ... 81

Figure 59 PSTM arbitrary section embedded in regional Generation 2 Harvey volume, view from North. 81

Figure 60 PSDM Flowchart. 82

Figure 61 Layer striping of a horizons, showing picked horizon, flatten horizon and RMO picks over semblance plot 83

Figure 62 Final velocity model from PSDM workflow. 84

Figure 63 Comparison of velocities: PSDM (brown), VSP (black) and LOG (red). 85

Figure 64 Final imaged section from PSDM workflow. 86

Figure 65 Isotropic pre-stack migration algorithm. 89

Figure 66 Residual velocity analysis of imaged gathers. 90

Figure 67 Original PSTM volume (top), Generation 2 PSTM volume (bottom). 91

Figure 68 Time slice 750 ms. Original Harvey PSTM volume (left) and Generation 2 Harvey PSTM volume 92

Figure 69 Time slice 1400 ms. Original Harvey PSTM volume (left) and Generation 2 Harvey PSTM volume (right). 93

Figure 70 Harvey the large 3D survey area. 94

Figure 71 Horizons picked on Generation 2 volume with colour corresponding to average similarity. 95

Figure 72 Final velocity model from 3D PSDM 96

Figure 73 Full-stack two-way time composite seismic line with the interpreted horizons and the Harvey 1 well over imposed with gamma ray log. 99

Figure 74 Finally processed and conditioned gathers used for the composite line AVO inversion 101

Figure 75 Two angle-dependant statistical wavelets were extracted from the super gathers. 102

Figure 76 The Harvey 1 well to seismic tie. 103

Figure 77 Low frequency model of the composite line as P-Impedance for the Harvey 1 well to seismic tie. 104

Figure 78 P-impedance – horizontal axis and V_P/V_S – vertical axis logs cross plot. 105

Figure 79 P-impedance – horizontal axis and V_P/V_S – vertical axis logs cross plot. 106

Figure 80 Lithology definition model for the Figure 79 cross plot. 107

Figure 81 AVO inversion analysis for the Harvey 1 well and seismic. 108

Figure 82 P-impedance volume with the Harvey 1 well P-impedance log inserted. 109

Figure 83 V_P/V_S volume with the Harvey 1 well V_P/V_S log inserted. 110

Figure 84 Composite line lithology prediction. 111

Figure 85 Probability of the sand lithology on the composite line. 112

Figure 86 Probability of the shale lithology on the composite line. Harvey-1 is the gamma ray log curve of the Harvey 1 well. 113

Figure 87 Porosity prediction from the inverted P-impedance, for the composite seismic line. 114

Figure 88 High-resolution velocity volume in TWT. P-wave velocity is displayed as the Harvey 1 well colour log. 115

Figure 89 Porosity prediction from the high-resolution tomographic velocities, applied to the composite seismic line. 116

Figure 90 Vertical and horizontal slices through the porosity cube computed from the reflection tomography velocities. 116

Figure 91 Classification of 2 facies types based on gamma radioactivity..... 121

Figure 92 3D distribution of the seismic fold for the large3D seismic data 123

Figure 93 Stochastic well tie at the Harvey 4 well along with a segment of inline 223. 124

Figure 94 Log to seismic correlation at the Harvey 1 well with the reference wavelet extracted from the Harvey 4 well..... 125

Figure 95 Vertical section from the inverted acoustic impedance extracted along crossline 113 passing through the Harvey 4 and close to the Harvey 3 wells. 128

Figure 96 Vertical sections of the mean acoustic impedance obtained from the low SNR (top row) and high SNR scenarios (bottom row). 129

Figure 97 Horizon slice of the mean acoustic impedance cube extracted at the top of Wonnerup Member. 130

Figure 98 The diagram summarizes testing of the number of inversion iterations. 131

Figure 99 Vertical section of the probability of the impermeable facies obtained from the high SNR ... 132

Figure 100 Maps of the probability of the impermeable facies obtained from the high SNR 133

Figure 101 Cross-plot of the well estimates of the total porosity vs log acoustic impedance, ... 134

Figure 102 Vertical and horizontal slices going through the mean acoustic impedance 135

Figure 103 Comparison of the seismic facies probability (1st from the left) with log facies interpretation (2nd to the left) and two realizations of the seismic facies along the Harvey 3 (left), Harvey 4 (middle) and Harvey 1 (right) wells. 137

Figure 104 Comparison of the seismic total porosity 137

LIST OF TABLES

Table 1 The Harvey 2 well VSP acquisition parameters..... 19

Table 2 The Harvey 3 well: VSP acquisition parameters 29

Table 3 The Harvey 4 well: VSP acquisition parameters 40

Table 4 Surface seismic pre-processing flow. 70

Table 5 Post-stack Migration Flow..... 79

Table 6 PSTM workflow. 80

EXECUTIVE SUMMARY

The SW Hub Carbon Capture and Storage (CCS) project is a leading initiative to reduce carbon dioxide emissions in Western Australia. It is a staged project that involves collecting and analysing data and samples from the Lesueur Sandstone formation, to test its feasibility as a CO_2 reservoir. The Lesueur Sandstone lies in the southern Perth Basin and is the type of saline aquifer identified by scientists around the world as a potential CO_2 storage reservoir.

Currently, the SW Hub has been going through a detailed pre-competitive site characterisation. As a part of this process the Harvey 1 stratigraphic well was drilled in 2012 and a 3D seismic survey was acquired in 2013-2014 over a 115 km^2 area in the vicinity of potential future injection sites (Geokinetics, 2014). This survey along with the Harvey 1 well data has been thoroughly analysed in ANLEC R&D Project 7-0314-0231. Since then new sources of the geophysical data became available:

- the new Harvey 2, 3 and 4 wells were drilled and a suite of well-logs have been acquired along with a zero-offset Vertical Seismic Profile (VSP);
- a high-resolution nested 3D seismic surveys around the Harvey 4 well (Urosevic et al., 2014) and, most recently, around the Harvey 3 well (Yavuz et al., 2018)

The objective of the Project 7-0115-0241 (Project) is to fill current information gaps by integrating all available geophysical data. Eventually, we interpreted the data in terms of subsurface distribution of petrophysical properties, relevant for the CO_2 sequestration modelling. These 3D cubes of properties should be used to constrain static and dynamic models, which form a core for feasibility studies of CO_2 sequestration at the SW Hub area.

The analysis started with advanced processing of VSP data. The results of VSP analysis were then used in the reprocessing of the entire 3D seismic dataset plus a composite 2D line that passes in proximity to three Harvey wells and has a relatively dense and uniform distribution of source-receiver offsets. Both of these datasets were then used for stochastic seismic inversion. Underpinning all of these analyses are well logs, which are comprehensively analysed in a separate report corresponding to the Milestone 6 of the Project (Pervukhina et al., 2018) and are not duplicated in this report.

The main findings of the overall study are as follows:

VSP data in the Harvey 2, 3 and 4 wells are of variable quality but sufficient to estimate vertical velocities for constraining the tomographic velocity model for surface seismic data. Anomalous

seismic attenuation (Q=30) is observed in the Yalgorup Member, while the contribution of scattering attenuation is minimal.

A composite line was created through the volumes, which incorporates a previously acquired 2D line with full complement of offsets and passes in proximity to the Harvey 1, 3 and 4 wells. This allowed building a relatively detailed velocity model that provided a sufficiently high quality seismic common-offset gathers and allowed the application of a stochastic Amplitude versus Offset (AVO) inversion. However, this inversion was still anchored at a single well (the Harvey 1 well) as other wells are too shallow for characterisation of the Wonnerup section. In order to validate the results, we compared them with the logs of the Harvey 3 well, which served as a blind test well. The match with this blind well is reasonably good. However, it is unclear if these results could be deemed reliable at such great distances from the Harvey 1 well. In addition, the results are limited to the composite seismic line.

The most comprehensive analysis was performed on the Geokinetics (2014) seismic volume, involving the stochastic rock physics inversion. To this end, the entire volume was first completely reprocessed. This allowed us to produce images far superior to those produced previously, with better reflection continuity and fault delineation. Furthermore, tomographic velocity analysis was undertaken to produce the velocity model for both final imaging and inversion.

The deterministic inversion of the Geokinetics 3D data showed very large uncertainty and hence requires a priori constraints. Hence, a quantitative interpretation workflow was developed, which implemented the Bayesian approach to stochastic seismic inversion. This workflow incorporates prior understanding of the subsurface features. Hence, the inversion gave us an opportunity to test if several geologically plausible hypotheses are consistent with seismic data.

The output of the inversion was controlled by (1) initial model and (2) our subjective estimate of the uncertainty of the initial model, well data and seismic amplitudes. The workflow involved a joint kinematic/amplitude inversion since the initial subsurface seismic model was based on high-resolution velocity analysis that captures both the loading trends derived from the well data and lateral variations of the seismic properties. Given the facies classification in the wells and correlation with petrophysical parameters, we converted the reference inversion output into reservoir characteristics.

The main findings are:

1. Despite the limitations of the Geokinetics (2014) 3D seismic, the inversion confidently delineates the Yalgorup/Wonnerup interface;

2. As expected, this horizon corresponds to the rapid transition of the impermeable rocks to reservoir sandstone. While the probability of the baffles exceeds 70%, it is never close to 100%, and thus, permits lateral discontinuity of the sealing interface along the horizon;

3. Within the sufficient seismic quality areas, we observed two seismic lithology types within Wonnerup:

   a. intense layering in the deeper parts towards western edge of the survey

   b. uniform reservoir – the most typical appearance.

4. We suggest that the quiescent Wonnerup Member may be due to the overlapping depth trends of the reservoir/baffles facies types, so they become seismically indistinguishable. Validation of this suggestion requires additional well information.

1. Introduction

The SW Hub CCS Project is a leading initiative to reduce carbon dioxide emissions in Western Australia. It is a staged project that involves collecting and analysing data and samples from the Lesueur Sandstone formation, to test its feasibility as a CO_2 reservoir. The Lesueur Sandstone lies in the southern Perth Basin and is the type of saline aquifer identified by scientists around the world as a potential CO_2 storage reservoir.

Currently, the SW Hub has been going through a detailed pre-competitive site characterisation. As a part of this process the Harvey 1 stratigraphic well was drilled in 2012 and a 3D seismic survey was acquired in 2013-2014 over a 115 km^2 area in the vicinity of potential future injection sites (Geokinetics, 2014). This survey, along with the Harvey 1 well data has been thoroughly analysed in ANLEC R&D Project 7-0314-0231. Since then new sources of the geophysical data became available:

- the new Harvey 2, 3 and 4 wells were drilled and a suite of well-logs have been acquired along with a zero-offset VSP;
- a high-resolution nested 3D seismic survey around Harvey 4 well (Urosevic et al., 2014).

The objective of the current Project is to fill current information gaps by integrating all available geophysical data. Eventually, we interpreted the data in terms of the subsurface distribution of petrophysical properties that are relevant for the CO_2 sequestration modelling. These 3D cubes of properties should be used to constrain static and dynamic models, which form a core for feasibility studies of CO_2 sequestration at the SW Hub area.

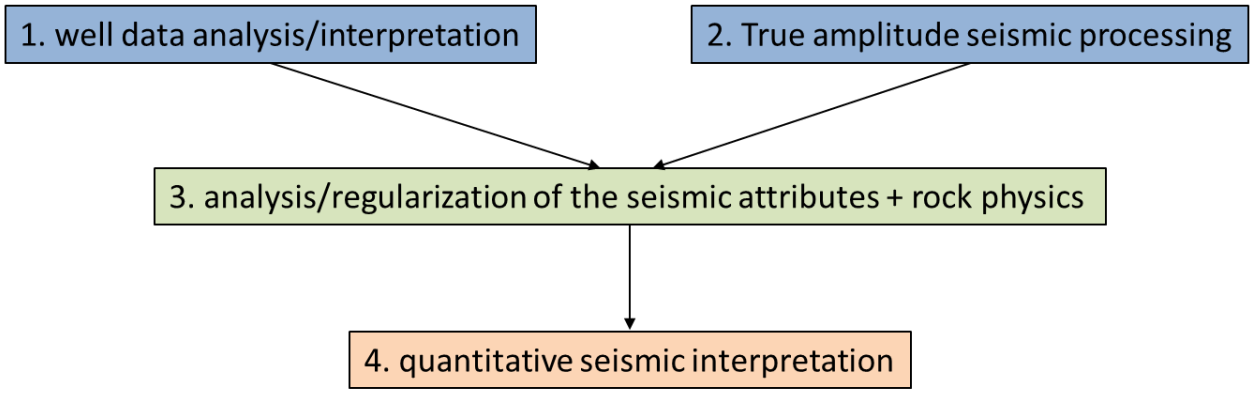


Figure 1 Diagram of the workflow for seismic interpretation to constrain reservoir models.

Once a typical structural interpretation of the geophysical data is completed, a conventional approach to a joint interpretation of geophysical data consists of four major components (Figure 1):

1 well data analysis/interpretation, which results in 1D detailed models of petrophysical/mechanical parameters;
2 seismic data processing to produce a high-quality image of the subsurface structures;
3 analysis/regularization of the seismic attributes and establishing the relationships between the seismic response and rock properties;
4 quantitative seismic interpretation, which aims to spread the 1D well-based models over the 3D volume, relating rock properties distribution to recorded seismic response.

The first two components were conducted independently. Even before the Project commenced, it was obvious that points 3 and 4 – 3D data integration – would be the biggest challenge for building a static geological model at the SW Hub. The success of the workflow largely depends on the amount of available well-data, quality of the recorded seismic amplitudes and adequacy of the joint interpretation engine/model. The target formation, the Lesueur, has a complex structure whose properties are hard to recover properly using available surface seismic and well data:

- the Yalgorup member consists of high-contrast layers of sub-seismic resolution
- the seismic properties of the Wonnerup member change smoothly with depth, which results in absence of reflections amenable to interpretation;
- intense faulting causes significant vertical displacements and dips, which disturb seismic amplitudes and complicate seismic imaging;
- the lateral sizes of geological units and variability of rock properties require a much denser network of wells, than the one formed by the existing Harvey wells;
- the acquired seismic lacks density and coverage required to reliably interpret the recorded amplitudes in a straightforward manner.

In parallel with the present Project, the Department of Mines and Petroleum of Western Australia (now Department of Mines, Industry Regulation and Safety) commissioned the construction of static and dynamic models of the subsurface by ODIN Geosciences ltd (ODIN). Initially, the ODIN geomodelling team used seismic cubes to build a structural framework: pick formation boundaries and trace faults. Petrophysical properties (net-to-gross NG, total porosity ϕ_T, vertical and horizontal permeability κ_V and κ_H etc.) were populated by inter-well interpolation along interpreted seismic horizons. However, reliability of the outcome could potentially be affected by the factors mentioned above: the sparsity of wells (compared with the characteristic lateral dimensions of

geological units) introduces a large uncertainty into the poorly constrained stochastic geological model.

The main goal of the current Project is to develop a methodology that allows for a meaningful seismic-driven 3D static geomodelling, given all the challenges related to the available data. First, we applied advanced processing procedures to get the maximum information out of the available data, implying improvement of the seismic attributes and their relationships to the rock properties. Secondly, we applied stochastic seismic inversion algorithms based on the rock physics modelling.

We first completed a major preparatory work for the stochastic inversion (points 1-3 presented above): data quality control (QC) / systematisation / processing / basic interpretation. Throughout this report, we use the reports of some previous ANLEC R&D projects: Advanced image processing and analysis of the SW Hub 3D Seismic Survey (Pevzner et al. 2015), Nested 3D Seismic Survey to Determine Shallow Features (Urosevic et al., 2014), and Advanced Geophysical data analysis for the SW Hub the Harvey 1 well site (Pevzner et al., 2013).

This Project commenced with the fast track quantitative interpretation of seismic data based largely on deterministic inversion. This fast track work was specifically requested by SW Hub management and with the approval of ANLEC R&D and was accomplished in close consultation with ODIN. This work was presented in the report on Milestone 2 (Glubokovskikh et al., 2016a). Further analysis of the VSPs, advanced well log analysis and the pilot magnetotelluric study along with true amplitude processing and advanced deterministic seismic inversion were presented in the report on Milestone 4 (Glubokovskikh et al., 2016b). Since then, advanced well log analysis and stress analysis work has been completed and the final report presented as the report on Milestone 6 (Pervukhina et al., 2018), and is included in this report as Appendix C.

The main conclusion of the seismic inversion work done as part of Milestone 4 (Glubokovskikh et al., 2016b) was that deterministic inversion produced a very large uncertainty and thus stochastic inversion was required in order to

- incorporate a priori constraints;
- incorporate knowledge of spatially variable seismic data quality and
- estimate the uncertainty of the results.

Thus, the quantitative interpretation of the seismic data in this report focuses on stochastic seismic inversion. Two separate paths were explored in this regard. AVO inversion is only possible where a full range of seismic offset is available. The offset distribution in the large 3D

volume is too patchy, and in the nested Harvey 4 survey is too limited for such inversion. Thus, such inversion was only attempted on a composite line, which incorporated a 2D line passing close to the Harvey 1 well and elements of the Harvey 3 and 4 nested surveys passing in proximity to Harvey 3 and Harvey 4 wells. Data processing and imaging along this line is presented in section 3.1, and stochastic AVO inversion in section 4. However, despite the irregular offset distribution, the large 3D seismic volume was still amenable to post-stack stochastic acoustic inversion. This work is presented in section 5. The deterministic seismic inversion presented as part of the Milestones 2 and 4 has been entirely superseded in the current report and therefore is not duplicated here. The work on VSP analysis (that helped constrain tomographic velocities in section 3), previously presented as part of Milestone 4 report (Glubokovskikh et al., 2016b) and is reproduced in this report for completeness (section 2).

The report follows a logical sequence starting with a detailed analysis of VSP data (section 2), the result of which forms one of the inputs into seismic processing and imaging (in section 3), which in turn produces input into AVO inversion along the composite 2D line (section 4) and stochastic acoustic inversion of the 3D volume (section 5).

2. Advanced VSP Processing

VSP data contains downhole recordings of seismic waves excited by a surface source. At the SW Hub area, VSPs were shot with the source close to the boreholes, which is called Zero-Offset VSP (ZVSP). The main goals of the ZVSPs are

- the estimation of 1D distribution of P and S-wave velocity in the seismic frequency range (for site characterisation and future seismic survey planning);
- the estimation of seismic attenuation (site characterisation / optimisation of processing of surface seismic);
- Seismic to well tie: surface seismic events are attributed through the ZVSP to log interpretation;
- the estimation of seismic anisotropy (stress characterisation / fault seal detection / optimisation of seismic processing)

This report covers the processing and analysis of ZVSPs in the Harvey 2, 3 and 4 wells. The processing flow is very similar for the three wells, thus we present details only for the Harvey 2 well, while the results for each well are described independently. We explain additional processing steps when required.

The dataset contains:

- Three-component (3C) ZVSP data acquired in the Harvey 2 well covering the interval 15 -1347.4 m. The data was initially acquired as a VSProwes ACQ (Avalon Sciences Ltd., http://avalonsciences.com/) project and was converted to SEG-Y format by Halliburton (Fadhli, 2015).
- 3C ZVSP data acquired in the Harvey 3 well covering the interval 85 -1530 m. The data was initially acquired as a VSProwes ACQ (Avalon Sciences Ltd., http://avalonsciences.com/) project but was converted to SEG-Y format by Halliburton (Human, 2015).
- 3C ZVSP data acquired in the Harvey 4 well covering the interval 85 -1760 m. The data was initially acquired as a VSProwes ACQ (Avalon Sciences Ltd., http://avalonsciences.com/) project but was converted to SEG-Y format by Halliburton (Roseno, 2015).
- Log data in the Harvey 2 well, including P and S velocity logs.
- Log data in the Harvey 3 well, including density and P velocity logs.
- Log data in the Harvey 4 well, including density and P velocity logs.

- The large and Nested Harvey 4 3D seismic datasets.

2.1. The Harvey 2 well

ZVSP data was acquired in the Harvey 2 well by Halliburton (Fadhli, 2015). Important survey parameters are provided in Table 1. Several shots were recorded for each receiver interval, the actual number varied from 5 to 10. Due to random noise on one of the tool's channels, more shots acquired for the bottom part of the borehole. Dual control panel was changed with a backup to resolve this issue (Fadhli, 2015).

Table 1 The Harvey 2 well VSP acquisition parameters.

General Survey Parameters	
Survey date	23/02/2015
Well coordinates	392052.65 E, 6347141.74 N
Surface elevation	15.4 m above MSL
Reference level elevation	16.05 m above MSL
Receiver parameters	
Downhole tool	3C,Dual ASR, 2 downhole shuttles, Sensor: OYO SMC2400-OMNI-15HZ
Receiver depth range (MD, m)	15 – 1347.4
Receiver step (m)	15
Record length	20000 ms
Sampling interval	1 ms
Source parameters	
Source position (from the well)	Easting 34.3 m, Northing 52.8 m
Source reference elevation	15.4 m above MSL
Source depth below SRE	0 m
Source type	Vibroseis Univib 26000 lb
Sweep Length	12000 ms
Start Frequency	8 Hz
End Frequency	120 Hz
Sweep Type	Linear
Start Taper Period	250 ms
End Taper Period	250 ms
Source control system	Pelton
External delay	0 ms

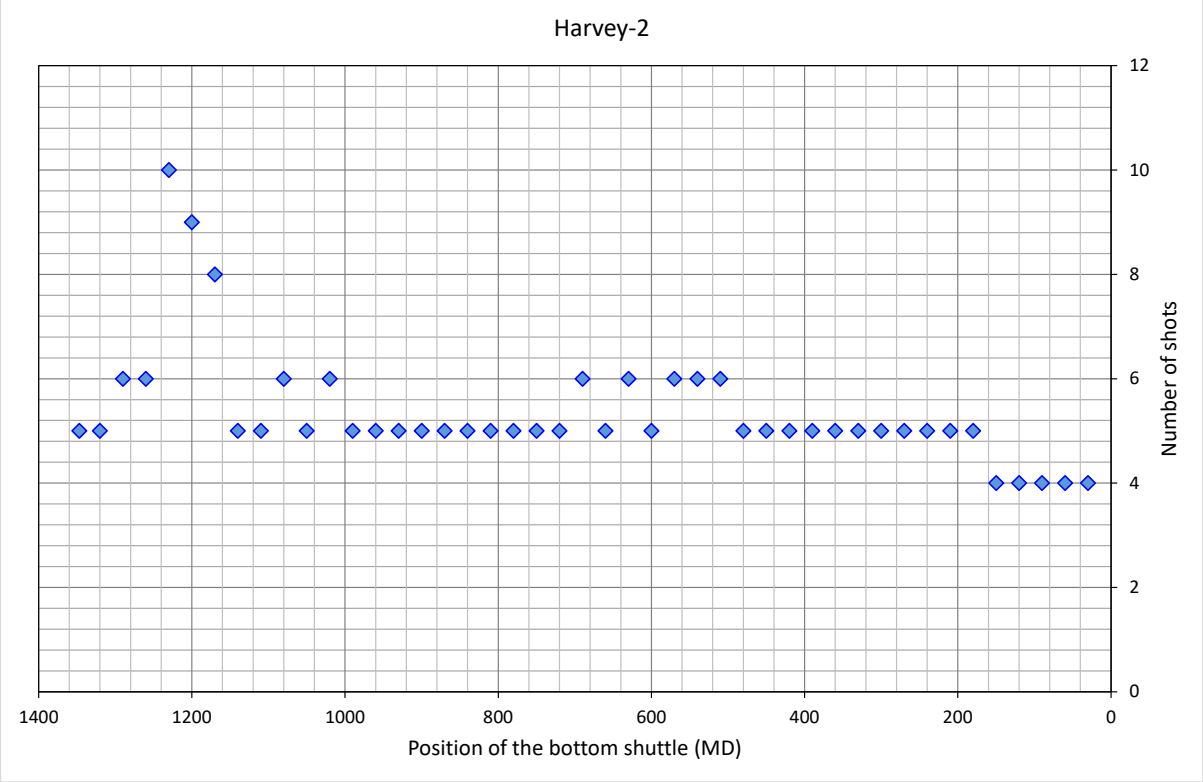


Figure 2 Number of shots per receiver level in the Harvey 2 well.

The ZVSP data was processed in RadExPro Advanced (DECO Geophysical) software package. Several routines were performed using purposely designed Matlab/Octave codes.

The general processing flow that was used is listed below:

- Data input, geometry
- Statics, vertical stacking
- Amplitude recovery
- Deterministic deconvolution
- Wavefield separation
- Velocity survey processing
- Normal move-out (NMO) correction
- Corridor stack

The general processing was followed by additional steps aimed at a well-tie and an estimation of seismic attenuation and anisotropy.

The data was loaded directly from shot records (SEG-Y files) provided by Halliburton. The coordinates of the source and receiver positions, relative to the well head, were obtained from the observer logs and surveying report. The Harvey 2 well ZVSP data was acquired using a vibroseis

(Inova Univib) seismic source. The parameters of the sweep signal are presented in Table 1. First raw data were loaded into Radexpro database and correlated with the sweep parameters, then geometry was assigned to seismic records.

Several shots per receiver location (Figure 2) were recorded during the acquisition to be able to perform stacking for improving signal-to-noise ratio (SNR) of seismic data. Before vertical stacking, traces were checked for quality. Noisy channels were muted before stacking. The result of the stacking is presented in Figure 3.

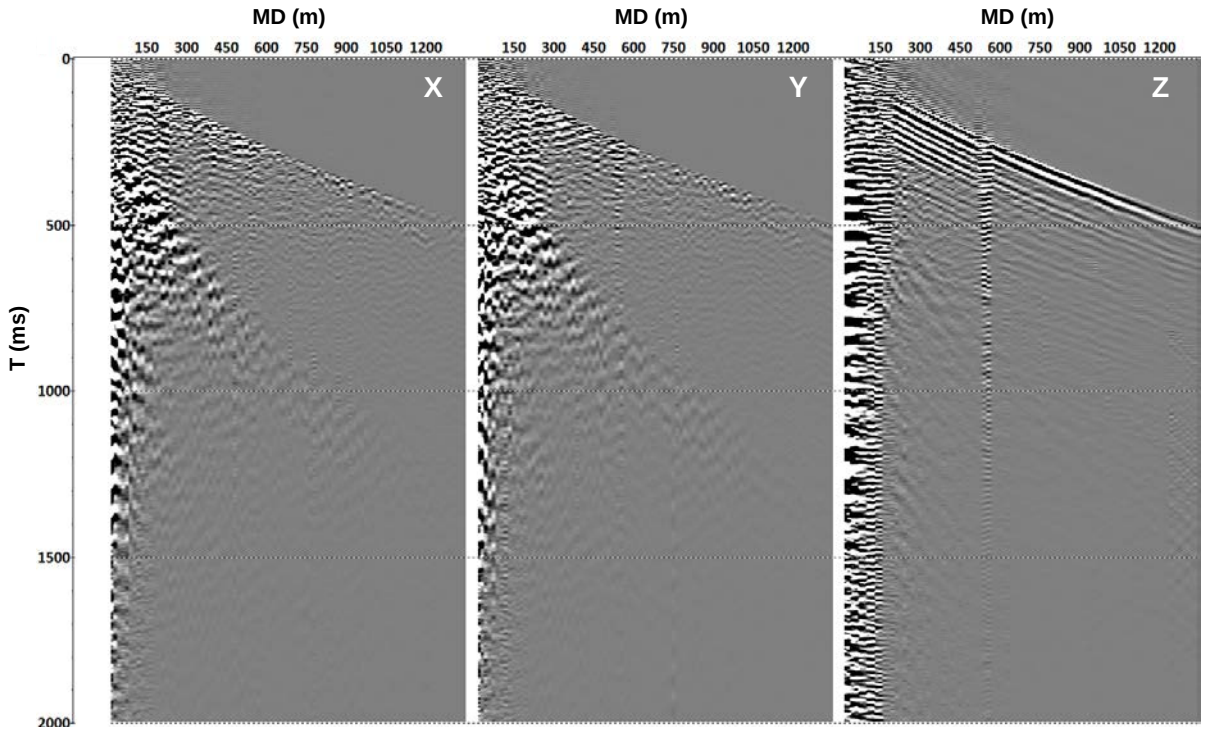


Figure 3 The Harvey 2 well correlated ZVSP data (X, Y – horizontal components, Z – vertical).

As no dedicated orientation device was used to acquire the data, we performed the polarisation analysis of the direct P-wave to orient horizontal components.

To QC the orientation of the tool, we compared the estimated polarisation of the direct P-wave with the angle between the vertical axis and the direction from source to receiver (Figure 4).

The result of the orientation is shown in Figure 5. The horizontal component contained significant shear waves energy generated by the source as well as PS converted waves, which. could be used for shear wave velocity profile estimation. A geological structure is observed on each component that starts at around 1000 m depth (marked by red arrow in Figure 5), which could be interpreted as a reflection from the F10 fault plane.

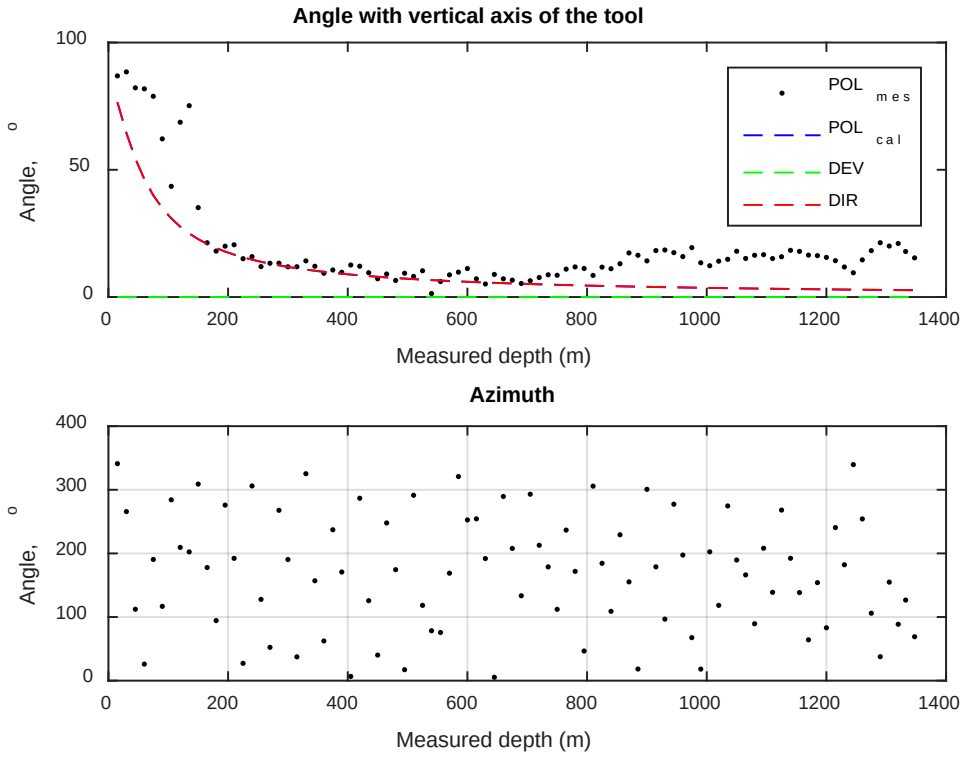


Figure 4 The Harvey 2 well direct wave polarisation analysis used to orient horizontal components. Top plot: Black dots – measured polarization of a P-wave in respect to a vertical axis of the VSP tool; Blue dash line – calculated polarization P-wave in respect to a vertical axis of the VSP tool; Blue dash line – calculated polarization P-wave in respect to a vertical axis of the VSP tool; Green dash line – well inclination; Red dash line – angle between a vertical direction and the direction of a P-wave propagation. Bottom plot: estimated rotation azimuth of the radial (X) component.

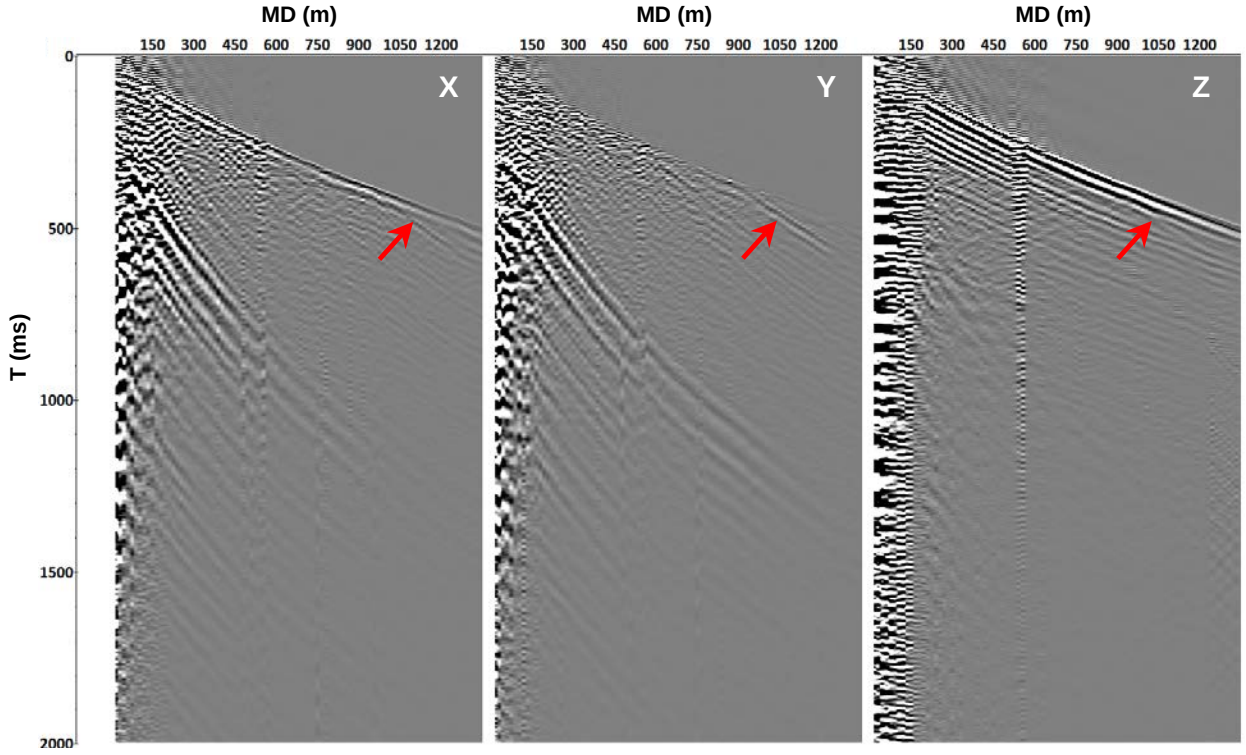


Figure 5 The Harvey 2 well ZVSP data after 3C orientation. Red arrows indicate reflection from the fault plane.

To compensate for the amplitude decay due to divergence of the wavefront, a single gain function (t^2) was used.

Deterministic deconvolution using down-going P-waves as an estimate of the wavelet was used to correct the phase of the wavelet to zero and broaden the amplitude spectrum. The depth range below 210 m was used to estimate the wavelet because the upper part of the record was contaminated with ringing. The length of the wavelet used for deconvolution was 236 ms. Depth levels 525-570 m were also excluded from the further analysis since they were contaminated by noise caused by the well design. **Figure 6** shows the vertical component of the Harvey 2 well ZVSP data after the amplitude correction and deconvolution.

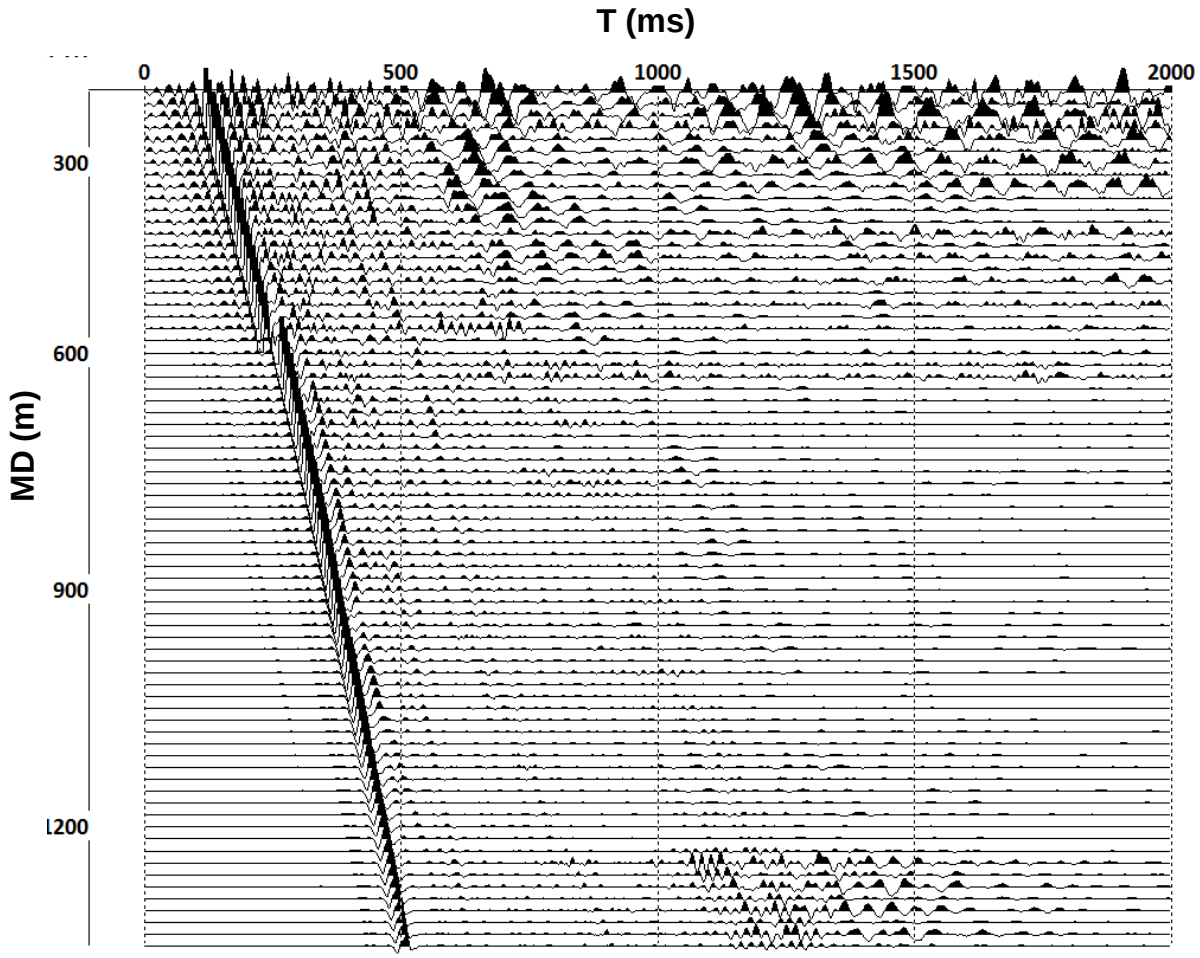


Figure 6 The Harvey 2 well ZVSP data, Z component, deconvolution and amplitude correction applied.

Each unwanted component of the wavefield (such as downgoing P and PS waves, tube waves etc.) was sequentially subtracted from the seismogram via the application of an alpha-mean

trimmed 2D filter along its travel time curve in rejection mode. The results only contains the down-going P wave.

We suppressed the random noise by mean filtering along the PP events and a bandpass filter (5-10-50-125 Hz, zero-phase, Ormsby). A significant part of the record above the 500 m measured depth (MD) is contaminated with remaining surface wave noise. Unfortunately, it was not viable to apply 2D filters with a directivity pattern sufficiently narrow to exclude all of them without damaging up-going PP waves. However, the well tie process remains unaffected by these events as they appear only at late times and thus might be excluded from the corridor stack. Figure 6 shows up-going PP wavefield of the vertical component.

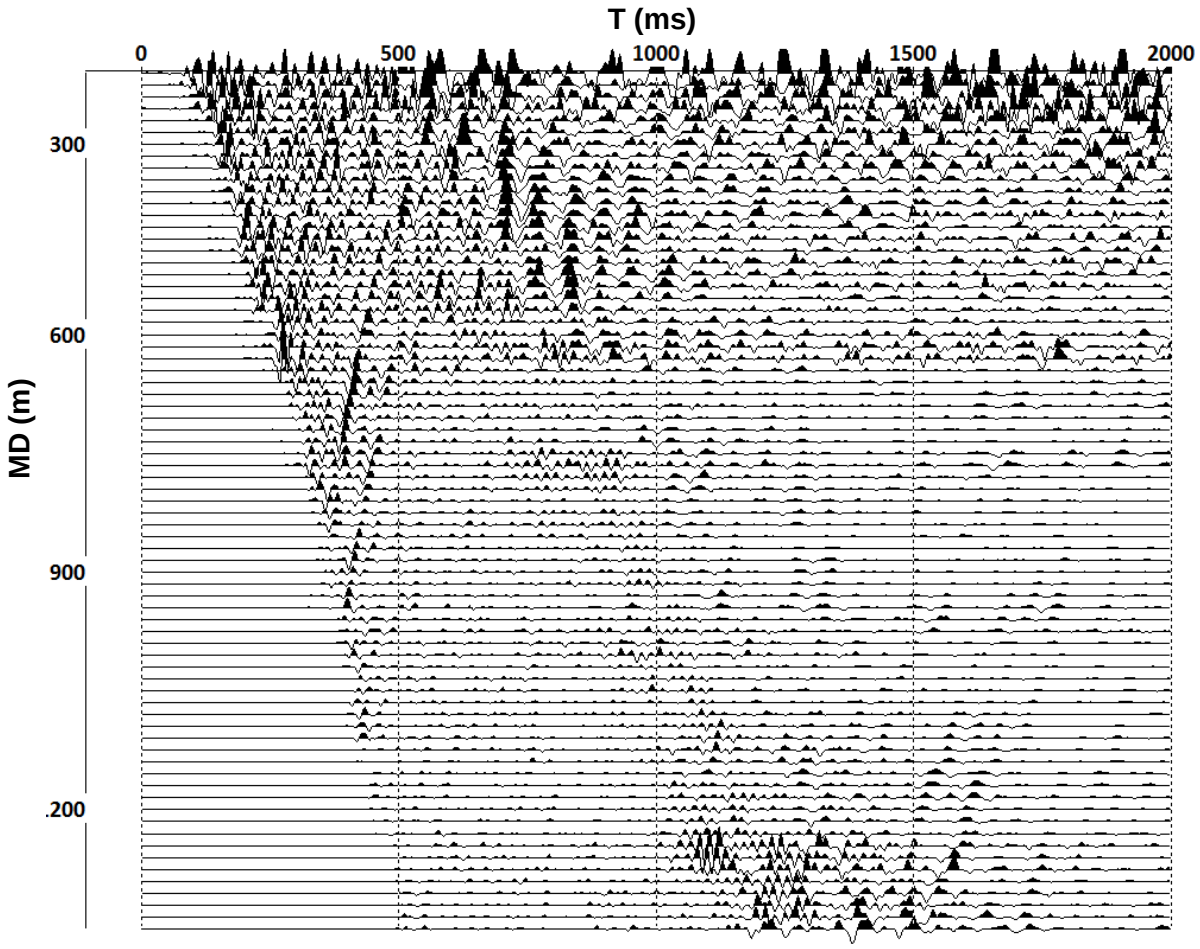


Figure 7 The Harvey 2 well ZVSP data, Z component, up-going PP waves.

To derive the two way travel time curve as a function of depth and also estimate interval P-wave velocities, an interactive tool (Advanced VSP Display) was used (Figure 8). To estimate the boundaries between the layers, the following criteria was used:

1. Positions of reflections,
2. Bending of the two way travel time curve, and
3. Log data

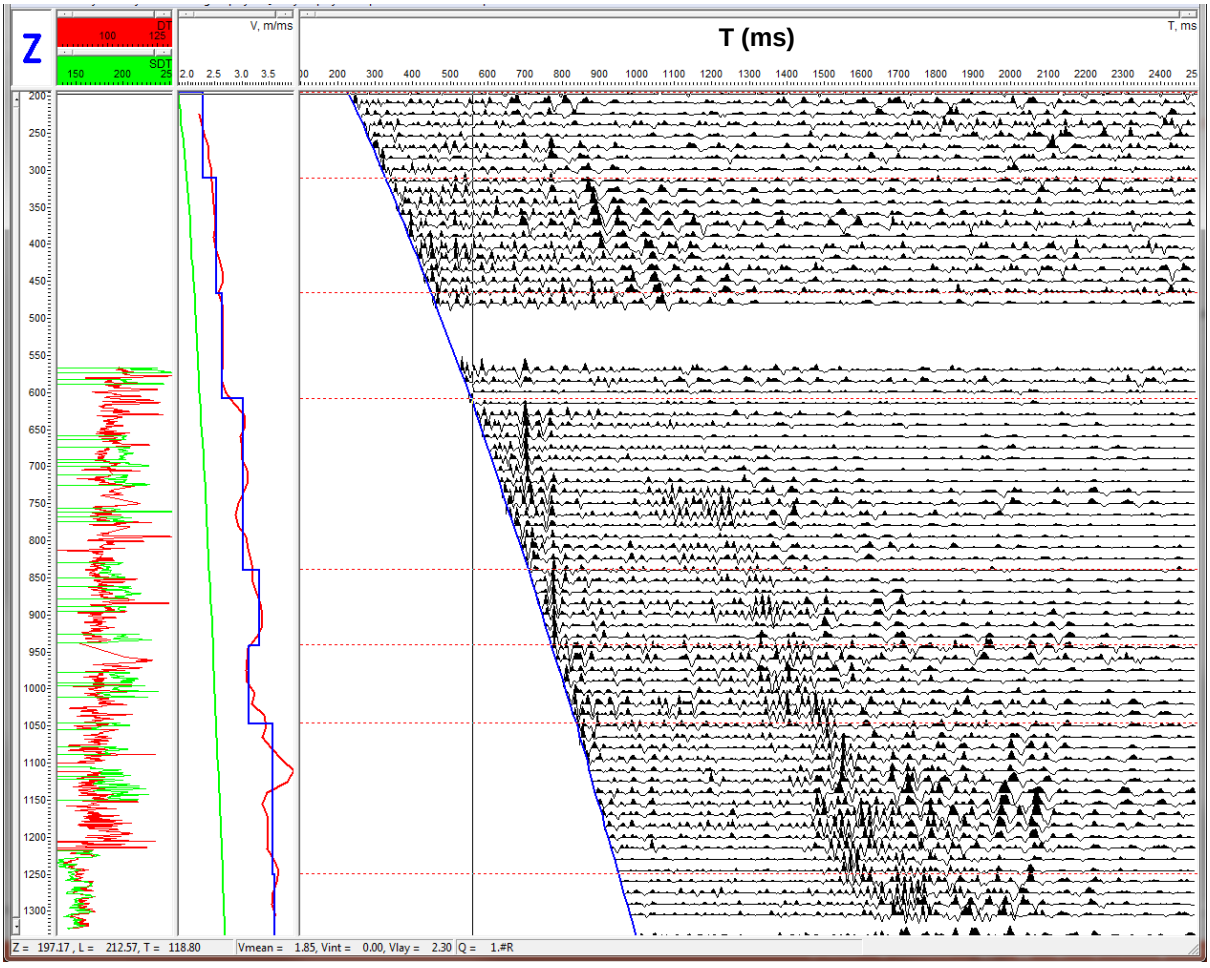


Figure 8 The Harvey 2 well ZVSP data, Interactive velocity analysis.

Strong source-generated shear waves were observed in the horizontal component after the 3C orientation of the VSP tool. They were used to estimate the S-wave velocity profile in a similar way.

The result of the velocity model processing is shown in Figure 9. Tables with the derived check shot data and velocity values are presented in Appendix A.

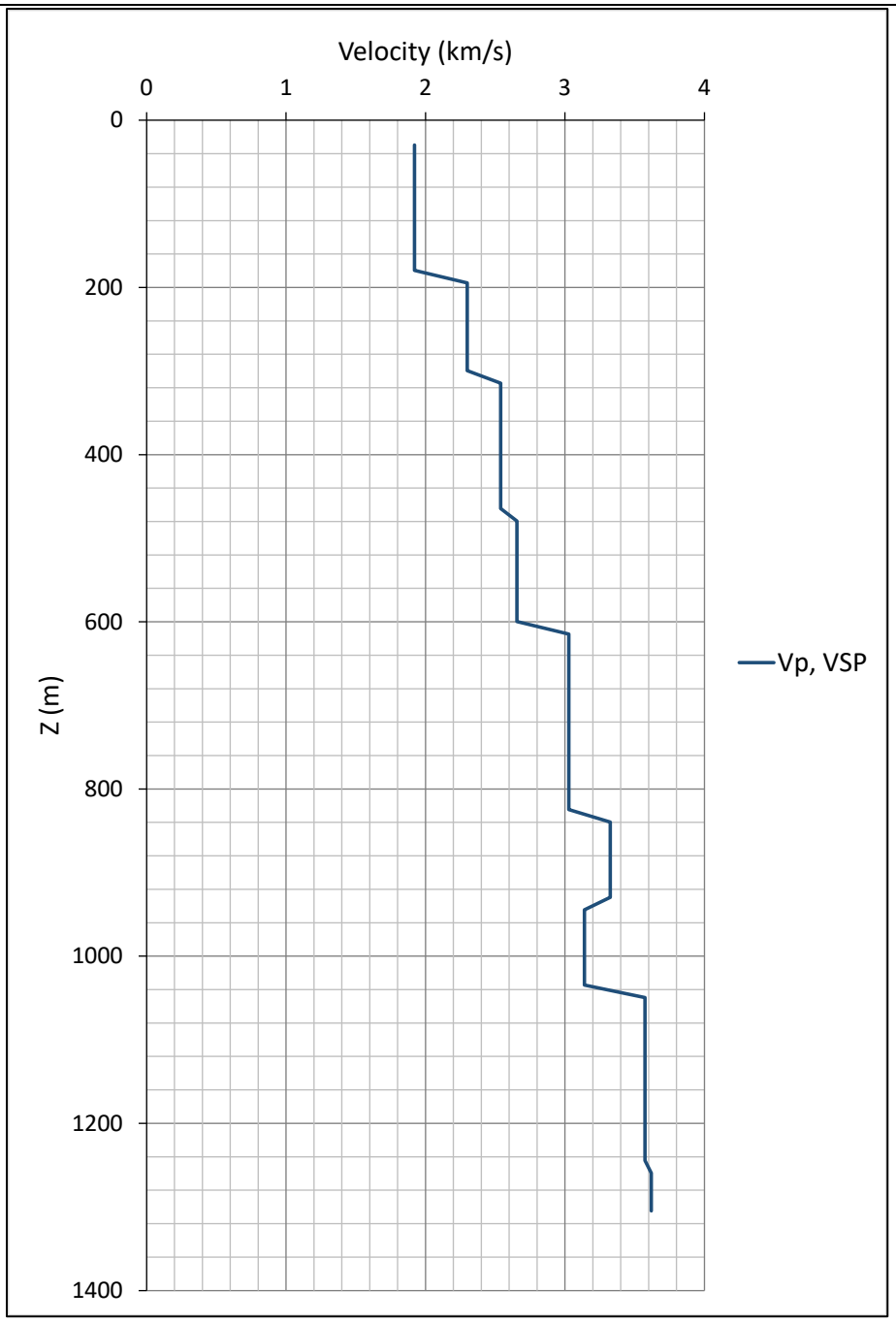


Figure 9 The Harvey 2 well ZVSP data, velocity model. Blue curve represents layer velocities derived through processing of travel time curves for direct P waves.

The result of the NMO correction of the up-going PP waves and the corridor stack trace are presented in Figure 10. The blue and red lines show the time gate used to compute the corridor stack trace.

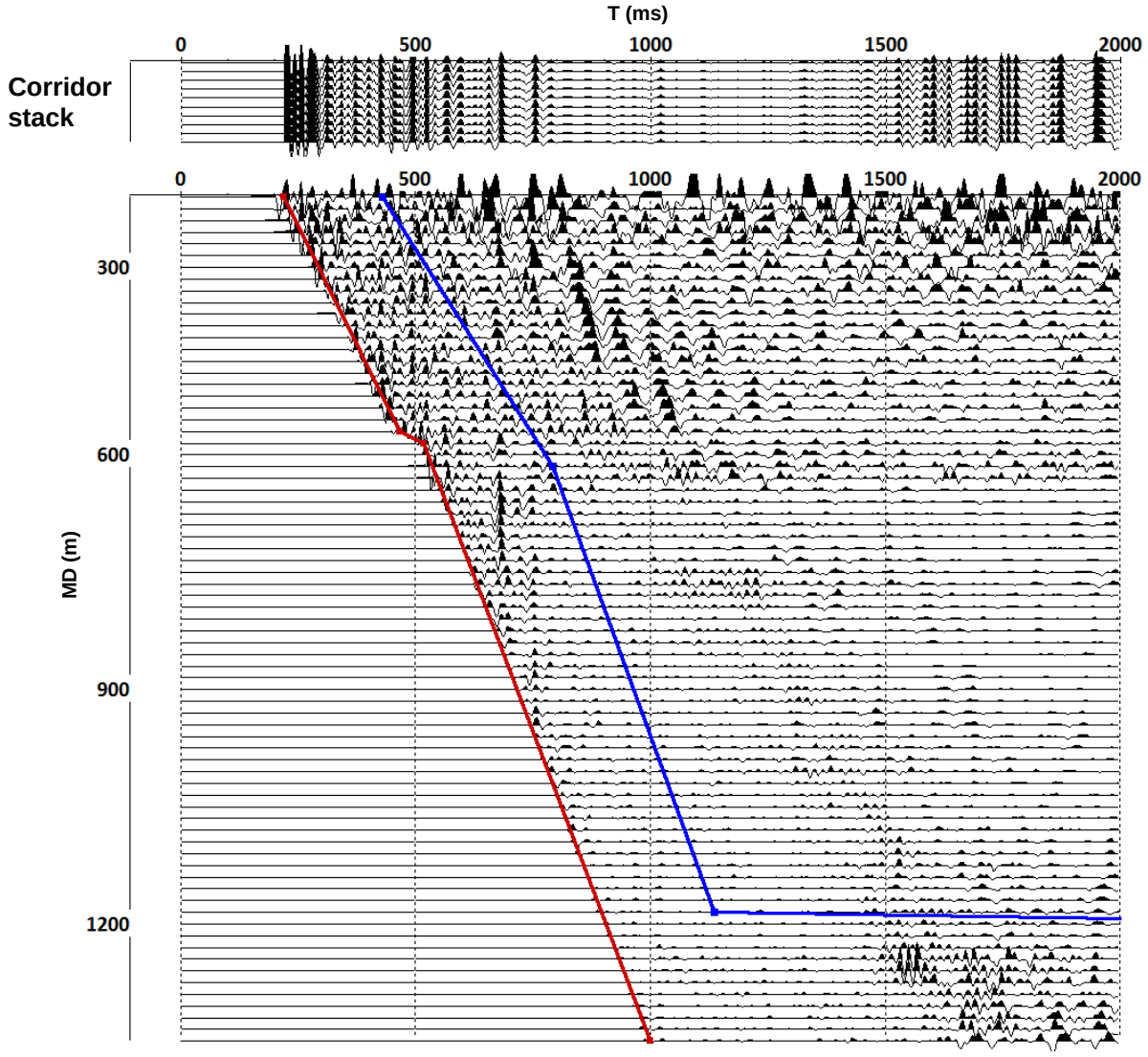


Figure 10 The Harvey 2 well ZVSP data, VSP-NMO and corridor stack trace

The Harvey 2 well is located at the intersection of inline 1241 and crossline 5272 of the large 3D seismic. The PSTM seismic cube is obtained for the datum of 40 m with replacement velocity 2.5 km/s. The actual time shift between the seismic data and corridor stack was computed by taking into account a VSP datum of 15.4 m and matching two seismic records. Total shift is 25.68 ms.

Results of the well tie using the corridor stack trace are presented in Figure 11. All major reflectors can be traced from VSP to surface seismic data. Corresponding check-shot table is provided in Appendix A.

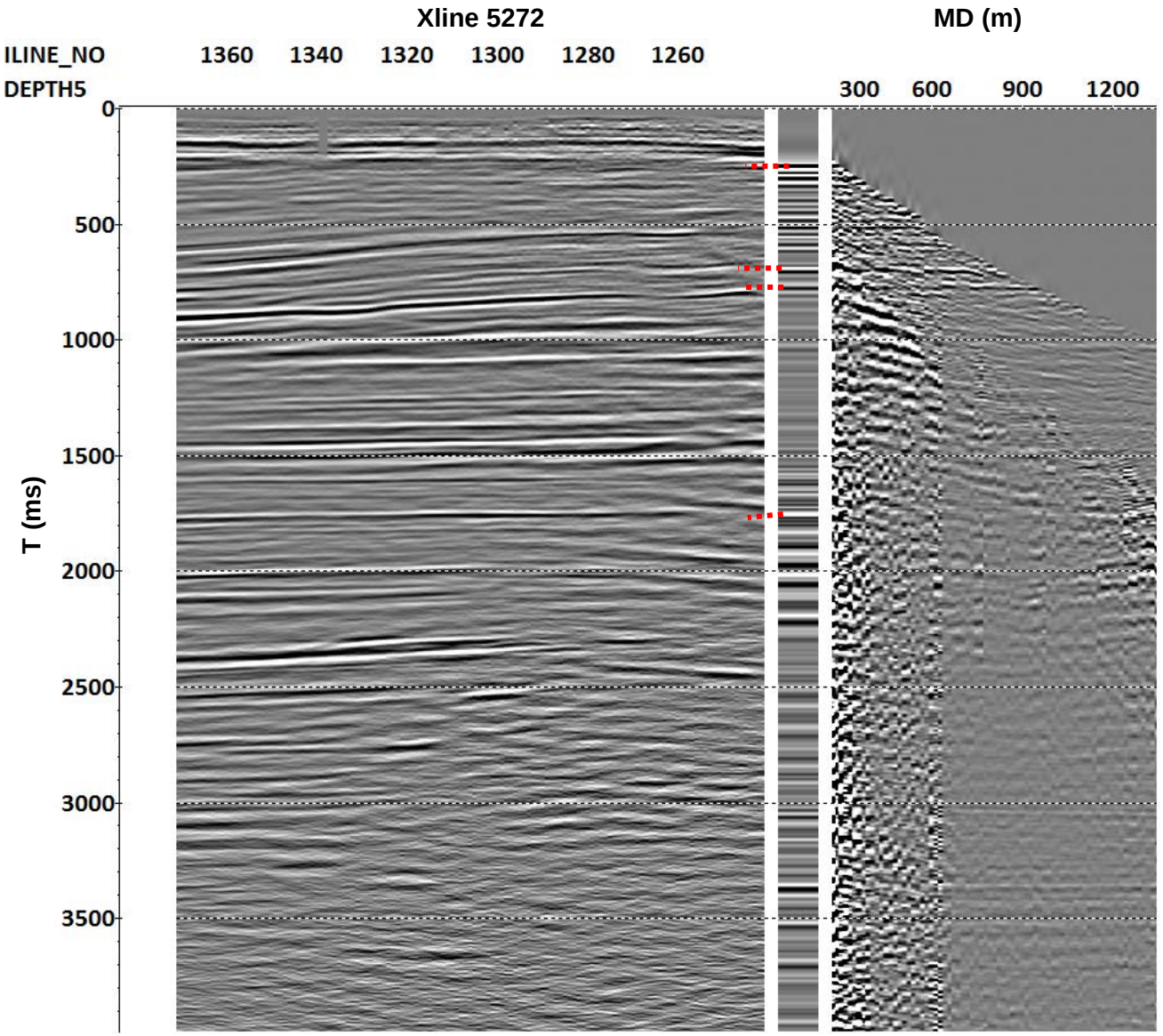


Figure 11 The Harvey 2 well ZVSP, the result of the seismic to well tie (principle reflectors are marked with red dashed lines)

2.2. The Harvey 3 well

ZVSP data was recorded in the Harvey 3 well by Halliburton (Human, 2015). The main recording parameters are provided in Table 2. Several shots were recorded for each receiver interval (Figure 12), the actual number varied from 3 to 4 (Human, 2015).

Table 2 The Harvey 3 well: VSP acquisition parameters

General Survey Parameters	
Survey date	24/01/2015
Well coordinates	387392.24 E, 6343895.95 N
Surface elevation	20.0 m above MSL
Reference level elevation	20.2 m above MSL
Receiver parameters	
Downhole tool	3C,Dual ASR, 2 downhole shuttles, Sensor: OYO SMC2400-OMNI-15HZ
Receiver depth range (MD, m)	85 – 1530
Receiver step (m)	15
Record length	18000 ms
Sampling interval	1 ms
Source parameters	
Source position (from the well)	Easting 18 m, Northing 76 m
Source reference elevation	20.2 m above MSL
Source depth below SRE	0 m
Source type	Enviro VIB
Sweep Length	12000 ms
Start Frequency	8 Hz
End Frequency	120 Hz
Sweep Type	Linear
Start Taper Period	250 ms
End Taper Period	250 ms
Source control system	Pelton
External delay	0 ms

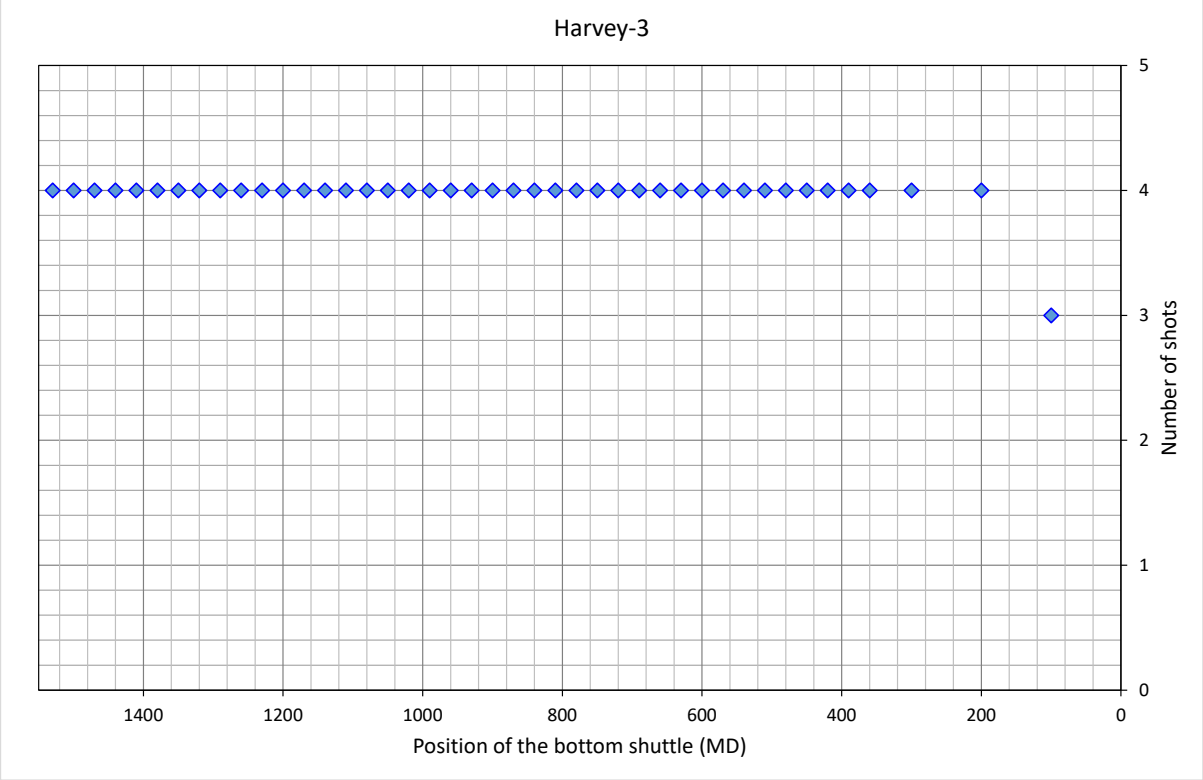


Figure 12 The Harvey 3 well: Number of shots per receiver level.

The data was loaded directly from shot records (SEG-Y files) provided by Halliburton. The coordinates of the source and receiver positions, relative to the well head, was obtained from the observer logs and surveying report. The Harvey 3 well ZVSP data was acquired using a vibroseis (Inova Univib) seismic source. The parameters of the sweep signal are presented in Table 2. First raw data was loaded into Radexpro database and correlated with the sweep, then geometry was assigned.

Several shots per receiver location (Figure 12) were stacked to increase SNR. Before the stacking, the data were QCed and noisy channels removed. The result of the stacking is presented in Figure 13.

VSP tools (horizontal component) was oriented using a polarisation analysis of the direct P-wave.

The comparison of the estimated P-wave polarisation with the angle between the vertical axis and the direction from source to receiver is shown in Figure 14. The result of the orientation is show in Figure 15.

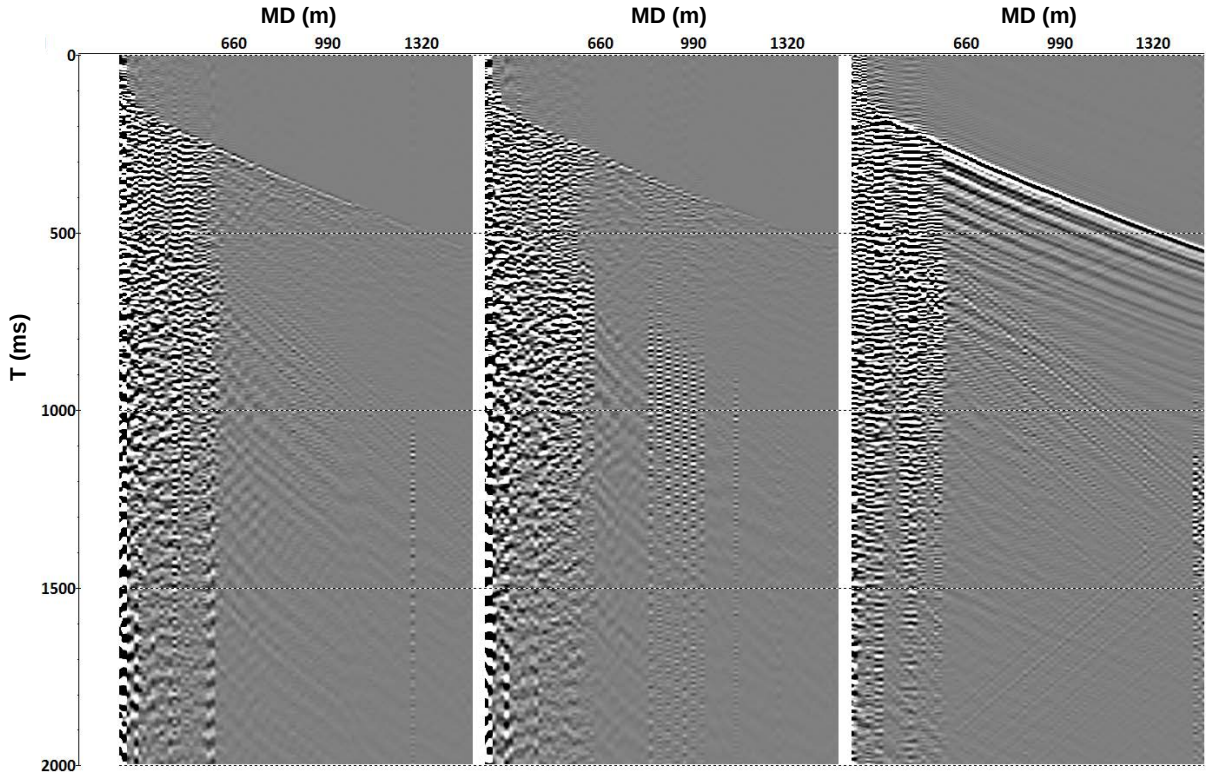


Figure 13 The Harvey 3 well correlated ZVSP data(X, Y – horizontal components, Z – vertical).

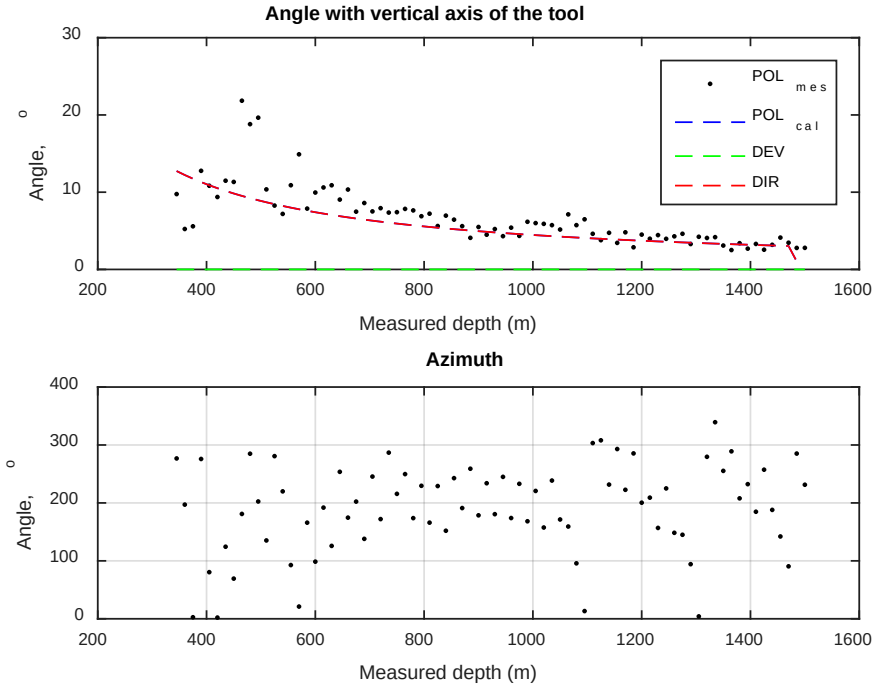


Figure 14 The Harvey 3 well direct wave polarisation analysis used to orient horizontal components. Top plot: Black dots – measured polarization of a P-wave in respect to a vertical axis of the VSP tool; Blue dash line – calculated polarization of a P-wave in respect to a vertical axis of the VSP tool; Green dash line – well inclination; Red dash line – angle between a vertical direction and the direction of a P-wave propagation. Bottom plot: estimated rotation azimuth of the radial (X) component.

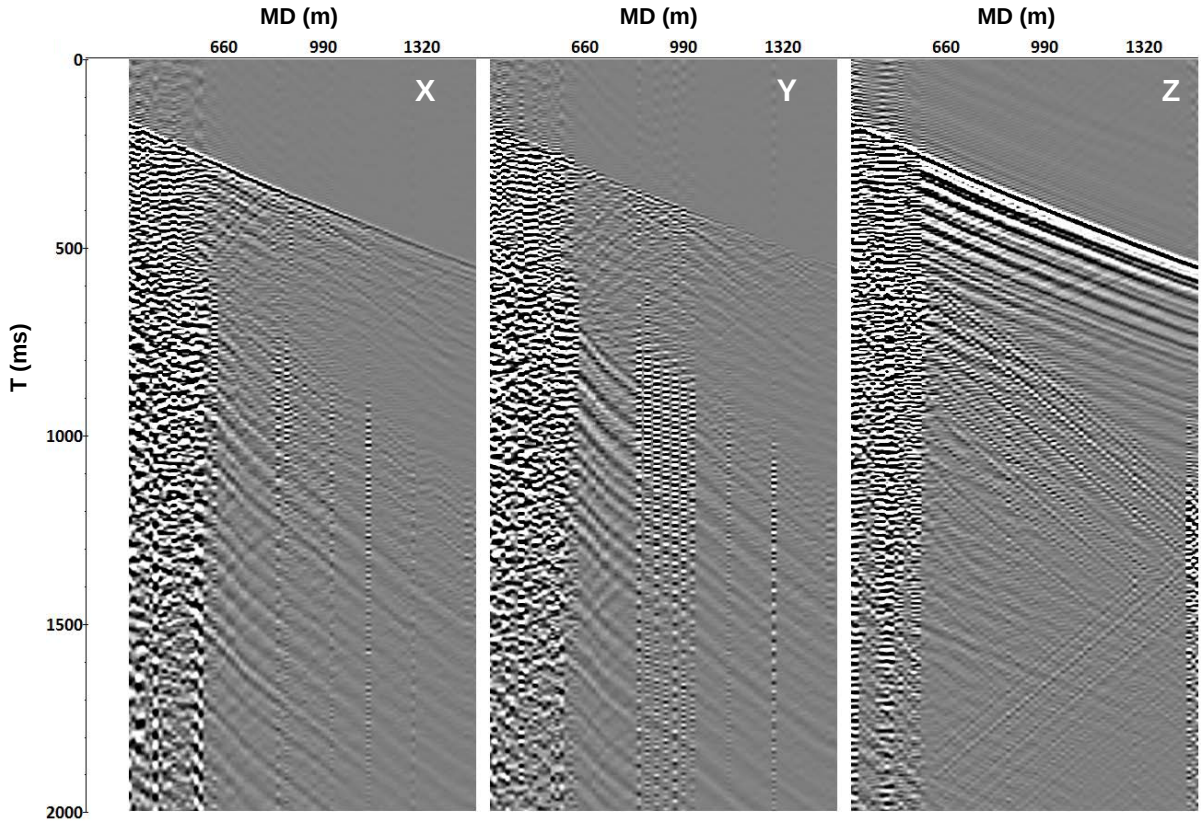


Figure 15 The Harvey 3 well ZVSP data after 3C orientation.

To compensate for the amplitude decay due to divergence of the wavefront, a single gain function (t^2) was used.

Deterministic deconvolution using down-going P-waves as an estimate of the wavelet was used to correct the phase of the wavelet to zero and widen the amplitude spectrum. The depth range below 615 m was used to estimate the wavelet because the upper part of the record was contaminated with ringing. The length of the wavelet used for deconvolution was 375 ms. Depths above 585 m were also excluded from the further analysis due to extreme ringing. Figure 15 shows the vertical component of the Harvey 3 well data after the amplitude correction and deconvolution.

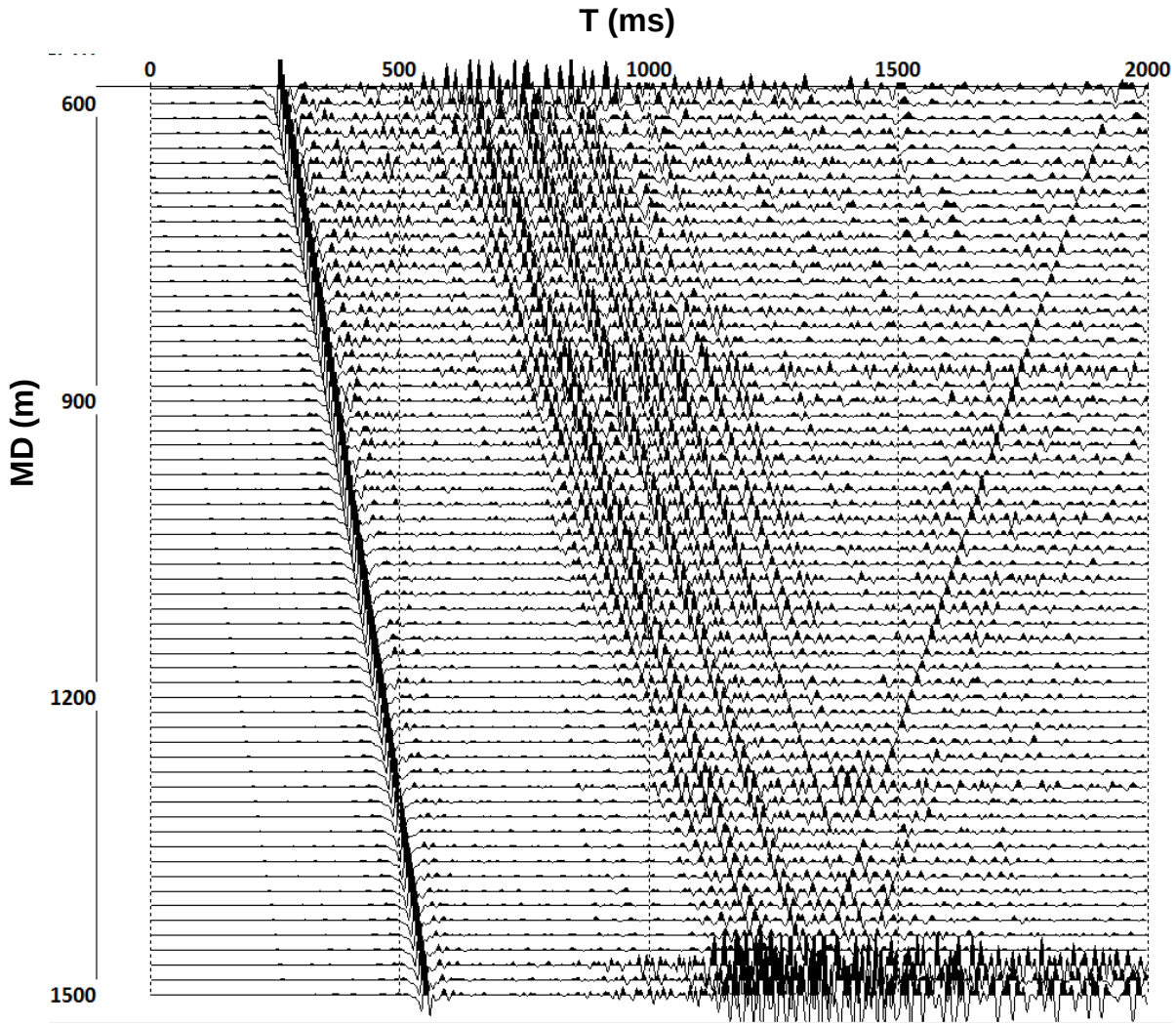


Figure 16 The Harvey 3 well ZVSP data, Z component, deconvolution and amplitude correction applied.

A set of 2D filters (9 to 17 traces depending on the events, alpha-mean trimmed with 50% rejection) in the T-X domain were applied in order to separate the up-going PP waves. Each unwanted component of the wavefield, such as down-going P and PS waves, tube waves, etc., were sequentially subtracted from the seismogram via the application of an alpha-mean trimmed 2D filter along its travel time curve in rejection mode. A bandpass filter (5-10-50-125 Hz, zero-phase, Ormsby) was applied at the final stage of processing. Figure 16 shows up-going PP wavefield of the vertical component.

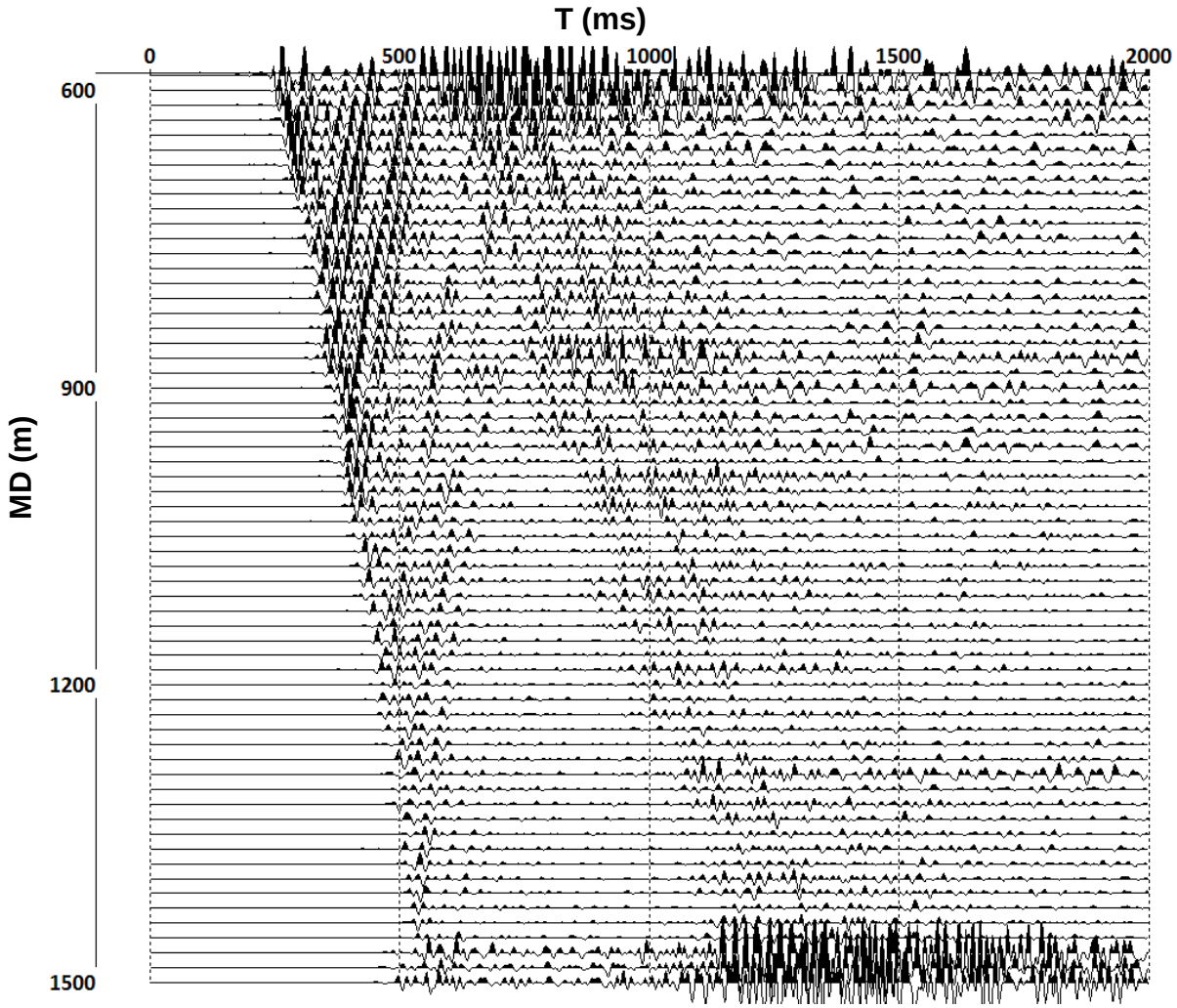


Figure 17 The Harvey 3 well ZVSP data, Z component, up-going PP waves.

To derive the two way travel time curve as a function of depth and also estimate interval P-wave velocities, an interactive tool (Advanced VSP Display) was used. To estimate the boundaries between the layers, the following criteria was used:

1. Positions of reflections,
2. Bending of the two way travel time curve, and
3. Log data

The result of the velocity model survey processing is shown in Figure 19. Tables with the derived check shot data and velocity values are presented in Appendix A.

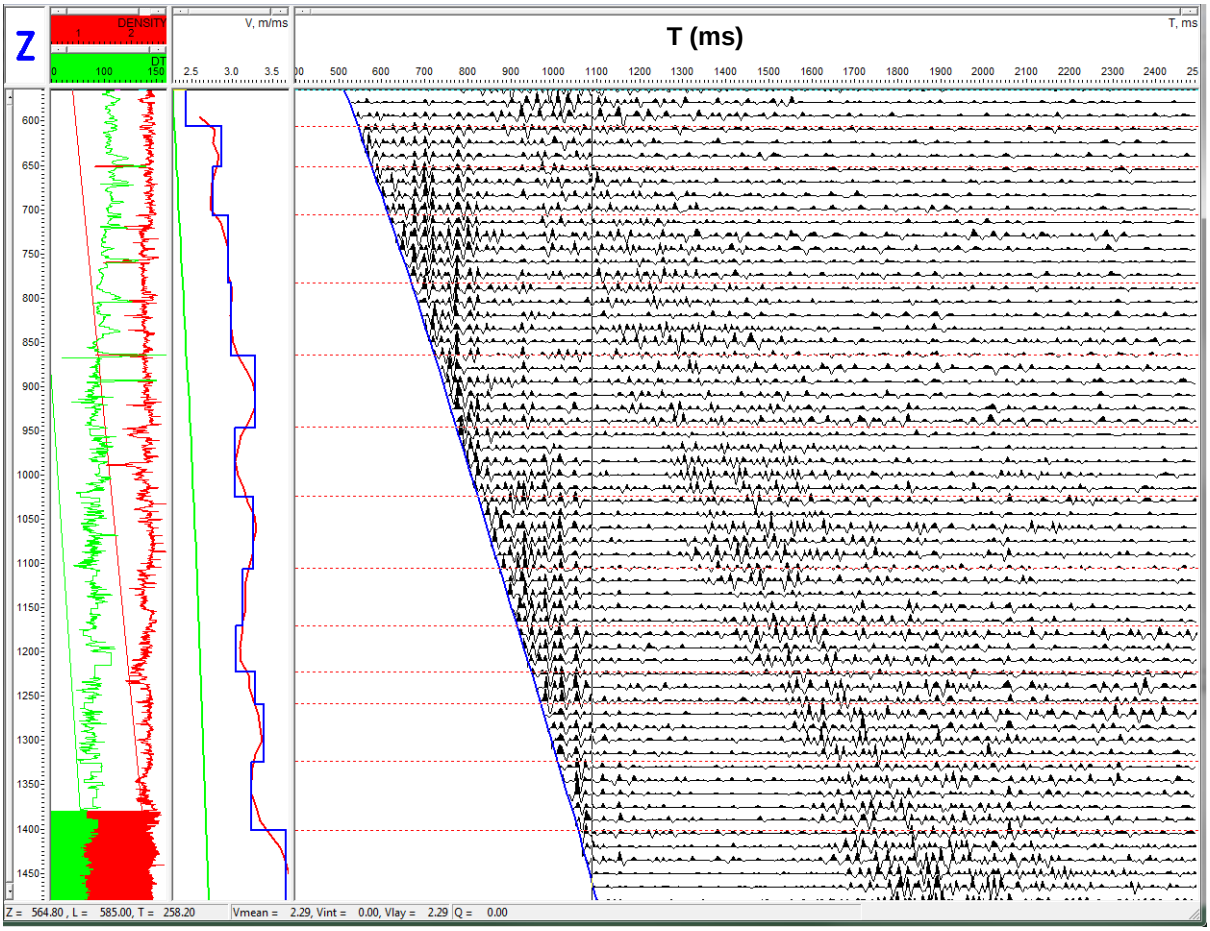


Figure 18 The Harvey 3 well ZVSP data, Interactive velocity analysis.

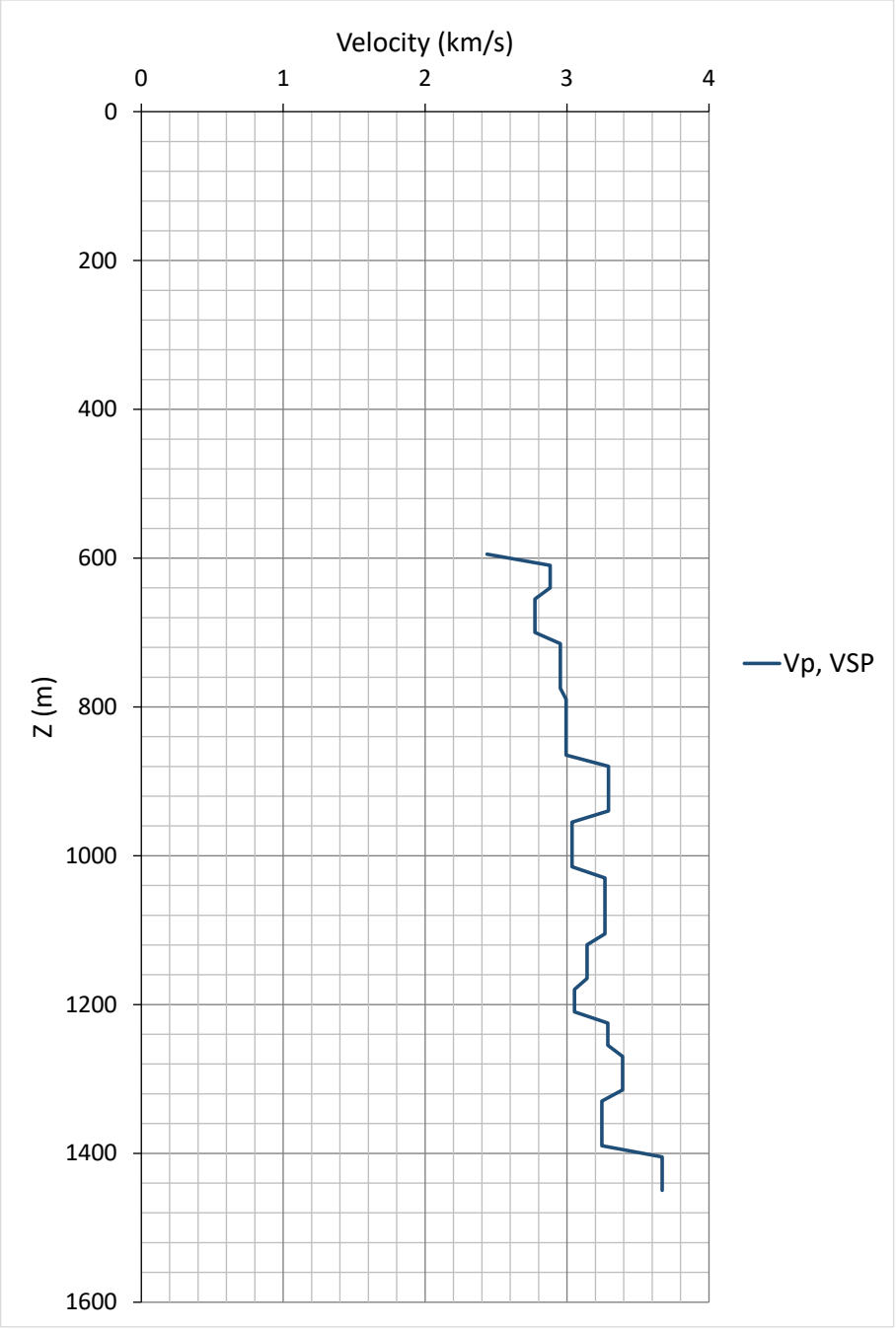


Figure 19 The Harvey 3 well ZVSP data, velocity model. Blue curve represents layer velocities derived through processing of travel time curves for direct P waves.

The result of the NMO correction of the up-going PP waves and the corridor stack trace are presented in Figure 20. The blue and red lines show the time gate used to compute the corridor stack trace.

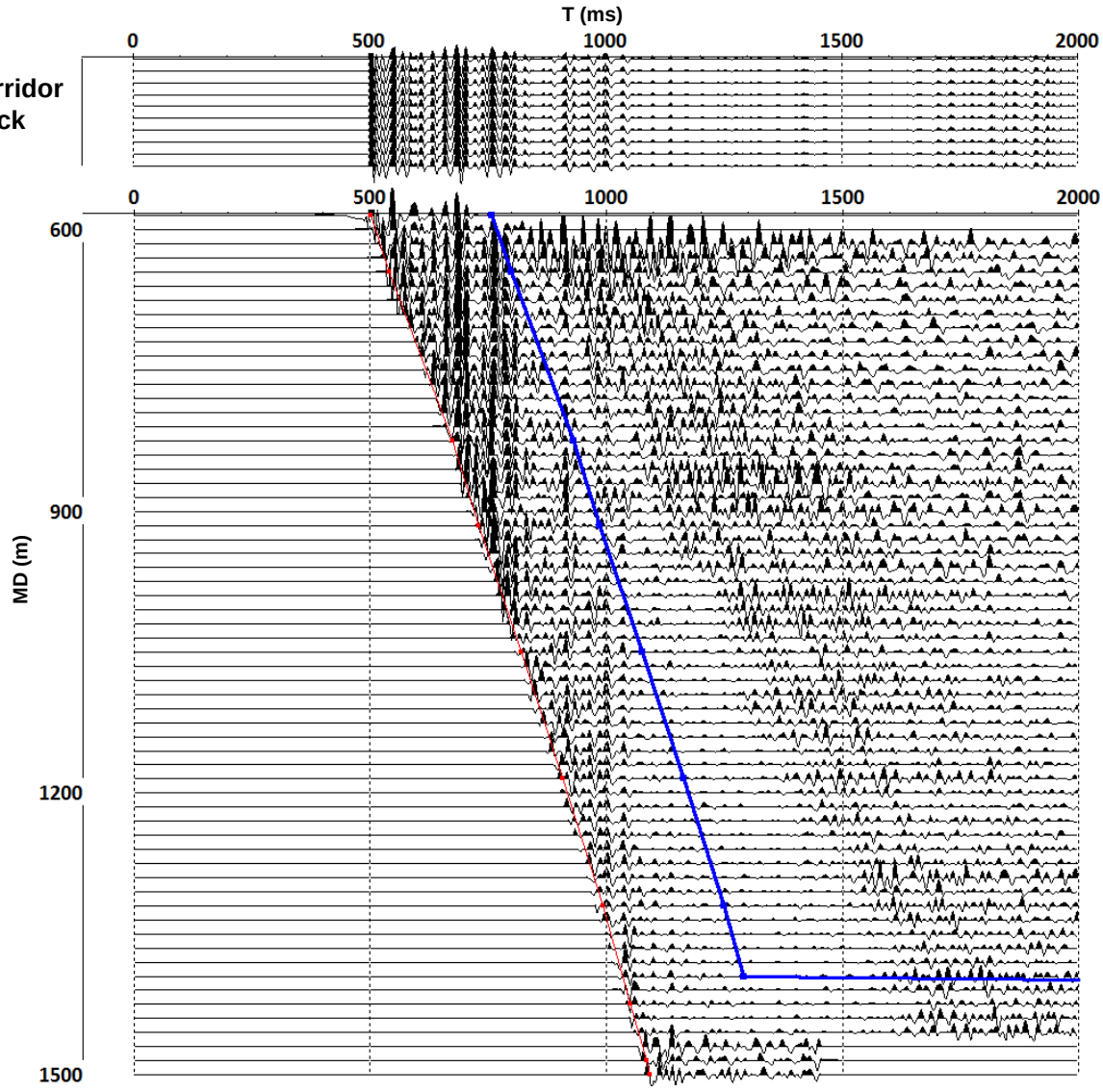


Figure 20 The Harvey 3 well ZVSP data, VSP-NMO and corridor stack trace.

The Harvey 3 well is located at the intersection of Inline 1112 and Xline 5086 of the 3D PSTM seismic cube. The seismic cube was computed for the datum of 40 m with replacement velocity 2.5 km/s. The actual time shift between the seismic data and corridor stack was computed by taking into account VSP datum of 20.2 m and matching two seismic records. The total shift was 21.84 ms.

Results of the well tie using the corridor stack trace are presented in Figure 21. All major reflectors can be traced from VSP to surface seismic data. A corresponding check-shot table is provided in Appendix A.

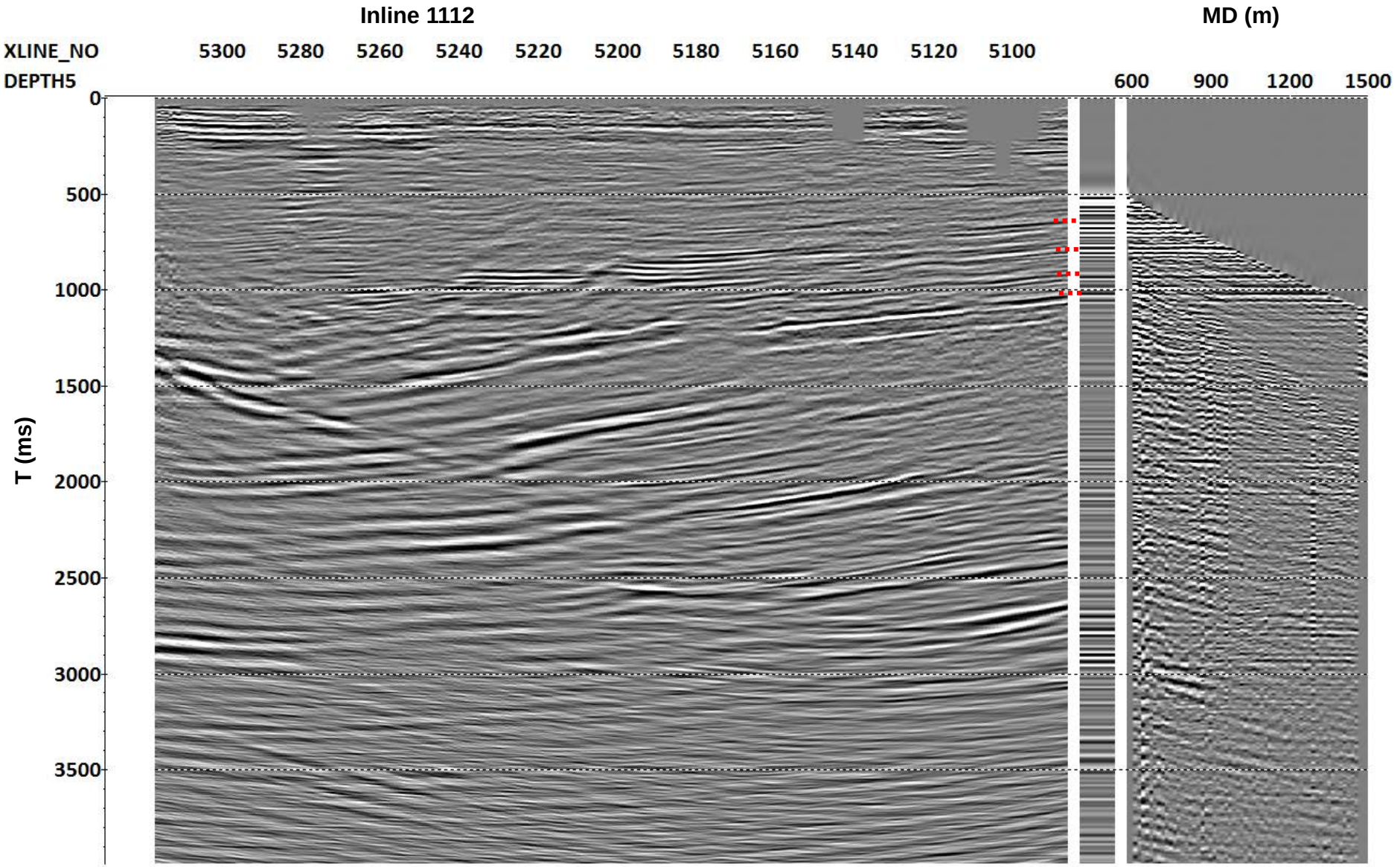


Figure 21 The Harvey 3 well ZVSP, the result of the seismic to well tie (principle reflectors are shown marked with red dashed lines).

2.3. The Harvey 4 well

ZVSP data was recorded in the Harvey 4 well by Halliburton (Roseno, 2015). The main recording parameters are provided in Table 3.

Table 3 The Harvey 4 well: VSP acquisition parameters

General Survey Parameters	
Survey date	18/04/2015
Well coordinates	389946.08 E, 6343842.51 N
Surface elevation	15.89 m above MSL
Reference level elevation	19.89 m above MSL
Receiver parameters	
Downhole tool	3C,Dual ASR, 2 downhole shuttles, Sensor: OYO SMC2400-OMNI-15HZ
Receiver depth range (MD, m)	85 – 1760
Receiver step (m)	15
Record length	18000 ms
Sampling interval	1 ms
Source parameters	
Source position (from the well)	Easting 66.1 m, Northing -48.0 m
Source reference elevation	15.8 m above MSL
Source depth below SRE	0 m
Source type	Inova UNIVIB
Sweep Length	12000 ms
Start Frequency	8 Hz
End Frequency	120 Hz
Sweep Type	Linear
Start Taper Period	250 ms
End Taper Period	250 ms
Source control system	Pelton
External delay	0 ms

Several shots were recorded for each receiver interval (Figure 22), the actual number varied from 4 to 14. The high number of shots in the middle of the borehole was caused by communication problems with the vibrator; a radio was replaced to resolve the issue. (Roseno, 2015).

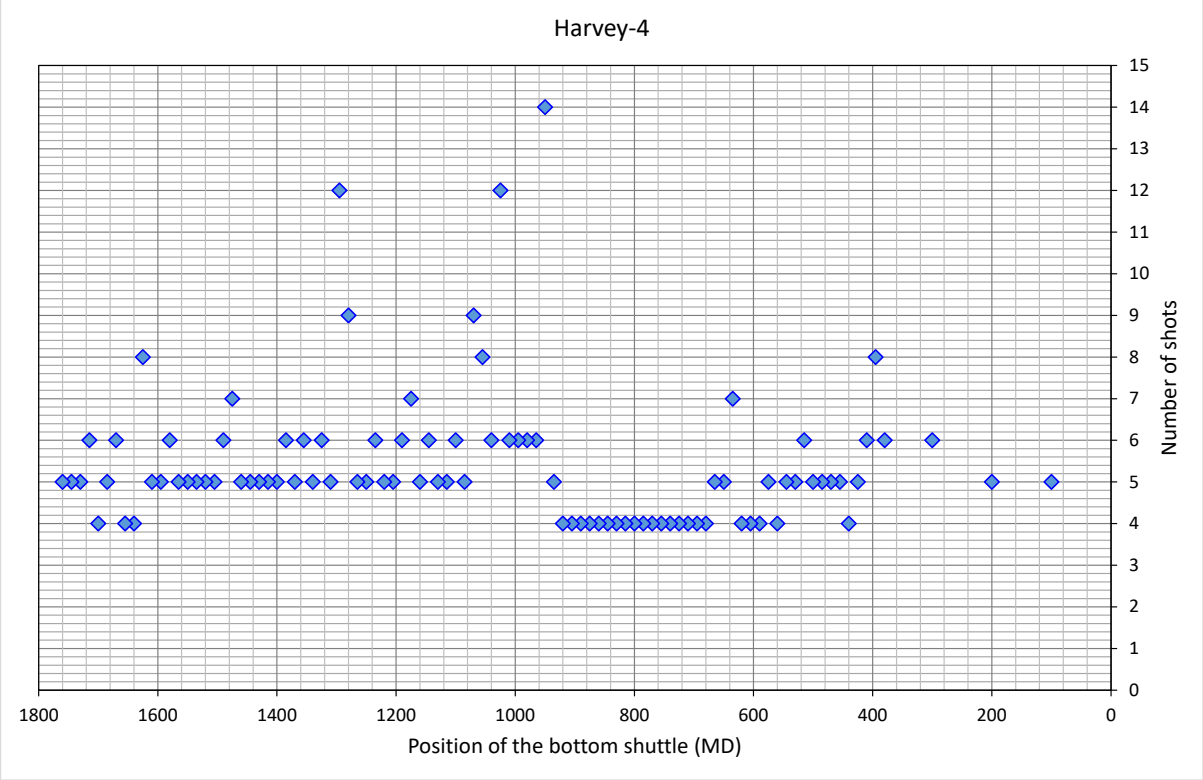


Figure 22 The Harvey 4 well. Number of shots per receiver level.

The data was loaded directly from shot records (SEG-Y files) provided by Halliburton. The coordinates of the source and receiver positions, relative to the well head, were obtained from the observer logs and surveying report. The Harvey 4 well ZVSP data was acquired using vibroseis (Inova Univib) seismic source. Parameters of the sweep signal are presented in Table 3. First, raw data was loaded into Radexpro database and correlated with sweep parameters, then geometry was assigned to seismic records.

Several shots per receivers' location (Figure 22) have been recorded during the acquisition to be able to perform stacking for improving SNR of seismic data. Before vertical stacking of traces QCed. Noisy channels were muted before stacking and the results of which are presented in Figure 23.

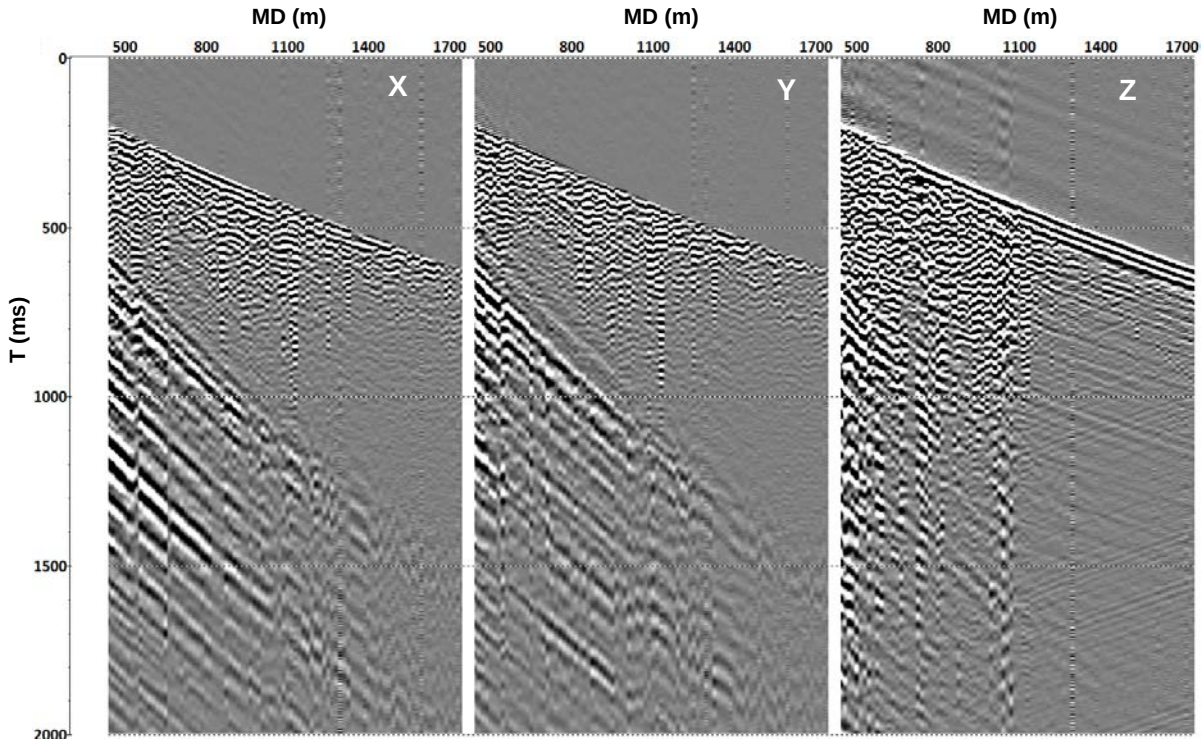


Figure 23 The Harvey 4 well correlated ZVSP data (X, Y – horizontal components, Z – vertical).

VSP tools (horizontal component) were oriented using a polarisation analysis of the direct P-wave.

Comparison of the estimated dip angle of polarisation of the direct P-wave with the angle between the vertical axis and the direction from source to receiver is shown in Figure 24. The result of the orientation is show in Figure 25.

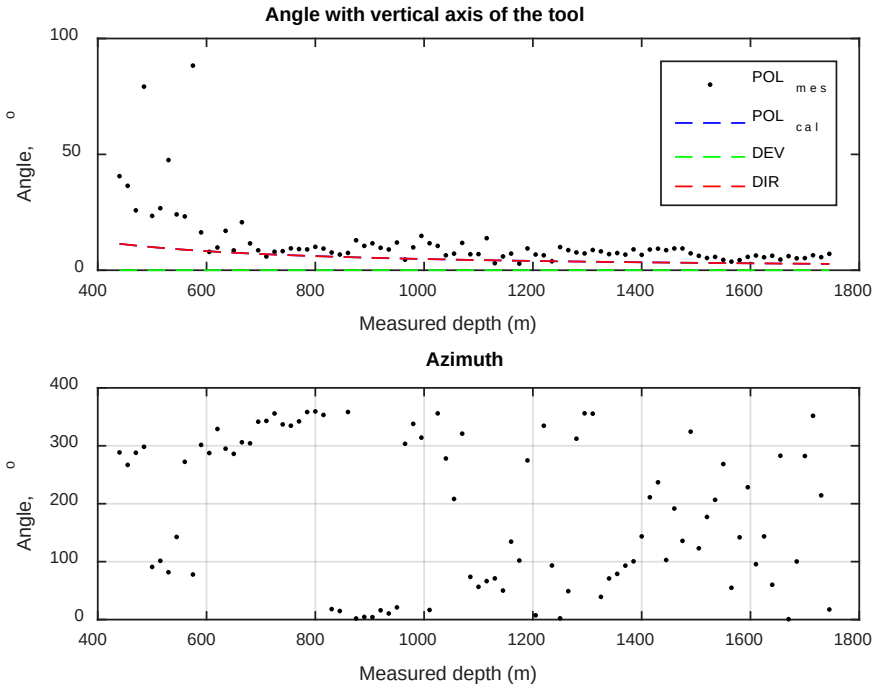


Figure 24 The Harvey 4 well direct wave polarisation analysis used to orient horizontal components. Top plot: Black dots – measured polarization of a P-wave in respect to a vertical axis of the VSP tool; Blue dash line – calculated polarization of a P-wave in respect to a vertical axis of the VSP tool; Green dash line – well inclination; Red dash line – angle between a vertical direction and the direction of a P-wave propagation. Bottom plot: estimated rotation azimuth of the radial (X) component.

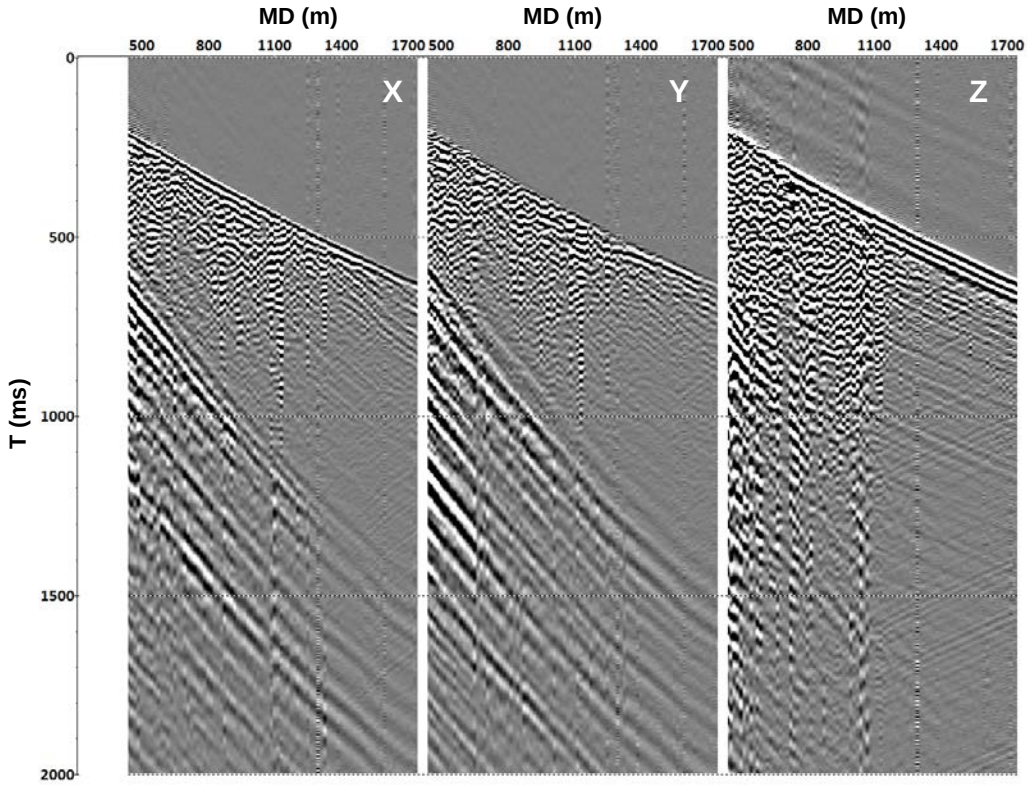


Figure 25 The Harvey 4 well ZVSP data after 3C orientation.

To compensate the amplitude decay due to divergence of the wavefront, a single gain function (t^2) was used.

Deterministic deconvolution using down-going P-waves as an estimate of the wavelet was used to correct the phase of the wavelet to zero and widen the amplitude spectrum. The depth range below 1160 m was used to estimate the wavelet because this part of the record is largely free of noise. The length of the wavelet used for deconvolution was 95 ms. Depths above 440 m were also excluded from the further analysis due to extreme ringing. Figure 26 shows the vertical component of the Harvey 4 well data after the amplitude correction and deconvolution.

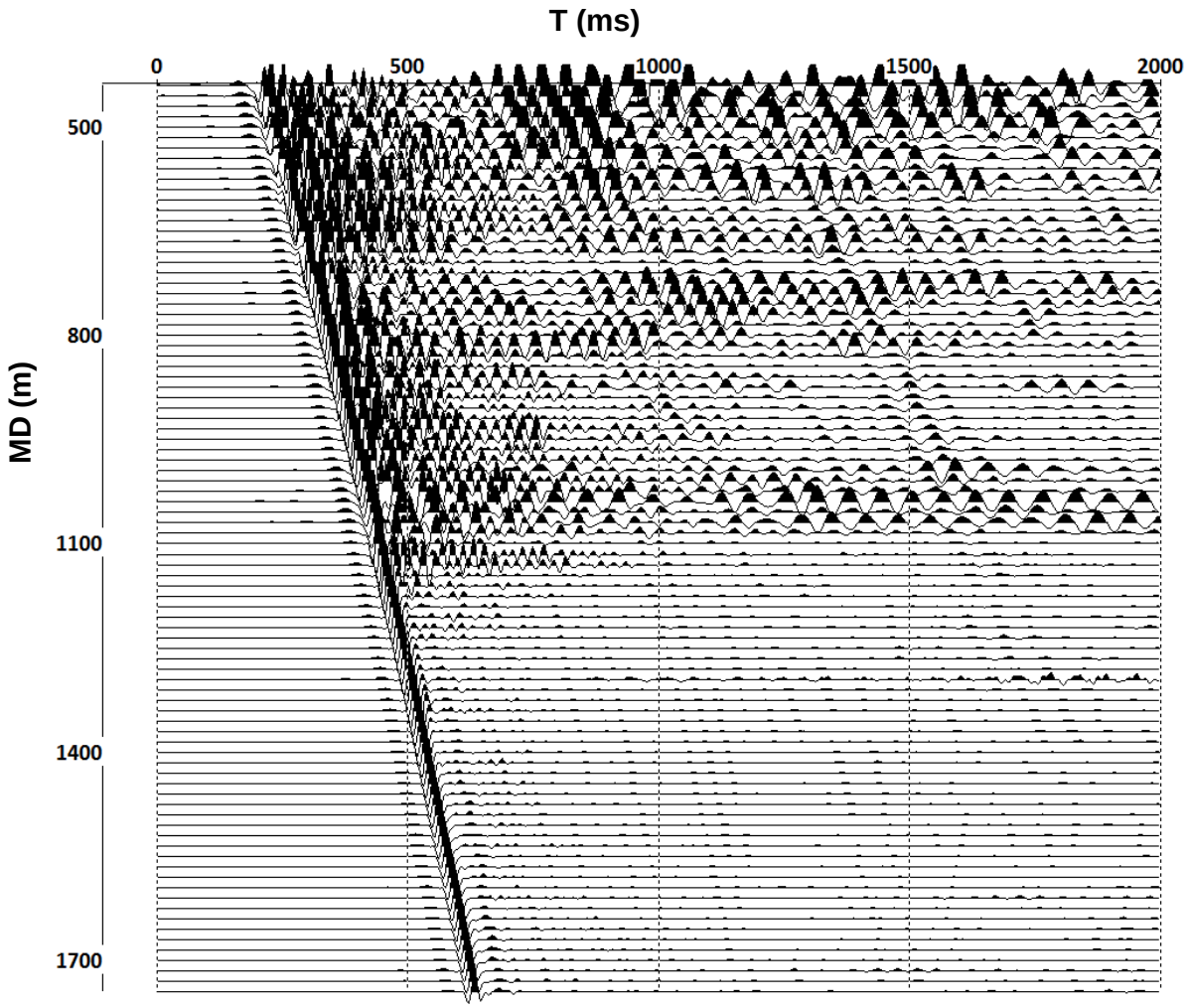


Figure 26 The Harvey 4 well ZVSP data, Z component, deconvolution and amplitude correction applied.

A set of 2D filters (11 traces, alpha-mean trimmed with 50% rejection) in the T-X domain were applied in order to separate the up-going PP waves. Each unwanted component of the wavefield, such as down-going P and PS waves, tube waves, etc., was sequentially subtracted from the seismogram via the application of an alpha-mean trimmed 2D filter along its travel time curve in rejection mode. A bandpass filter (5-10-80-90 Hz, zero-phase, Ormsby) was applied at the final stage of processing. Figure 27 shows up-going PP wavefield of the vertical component.

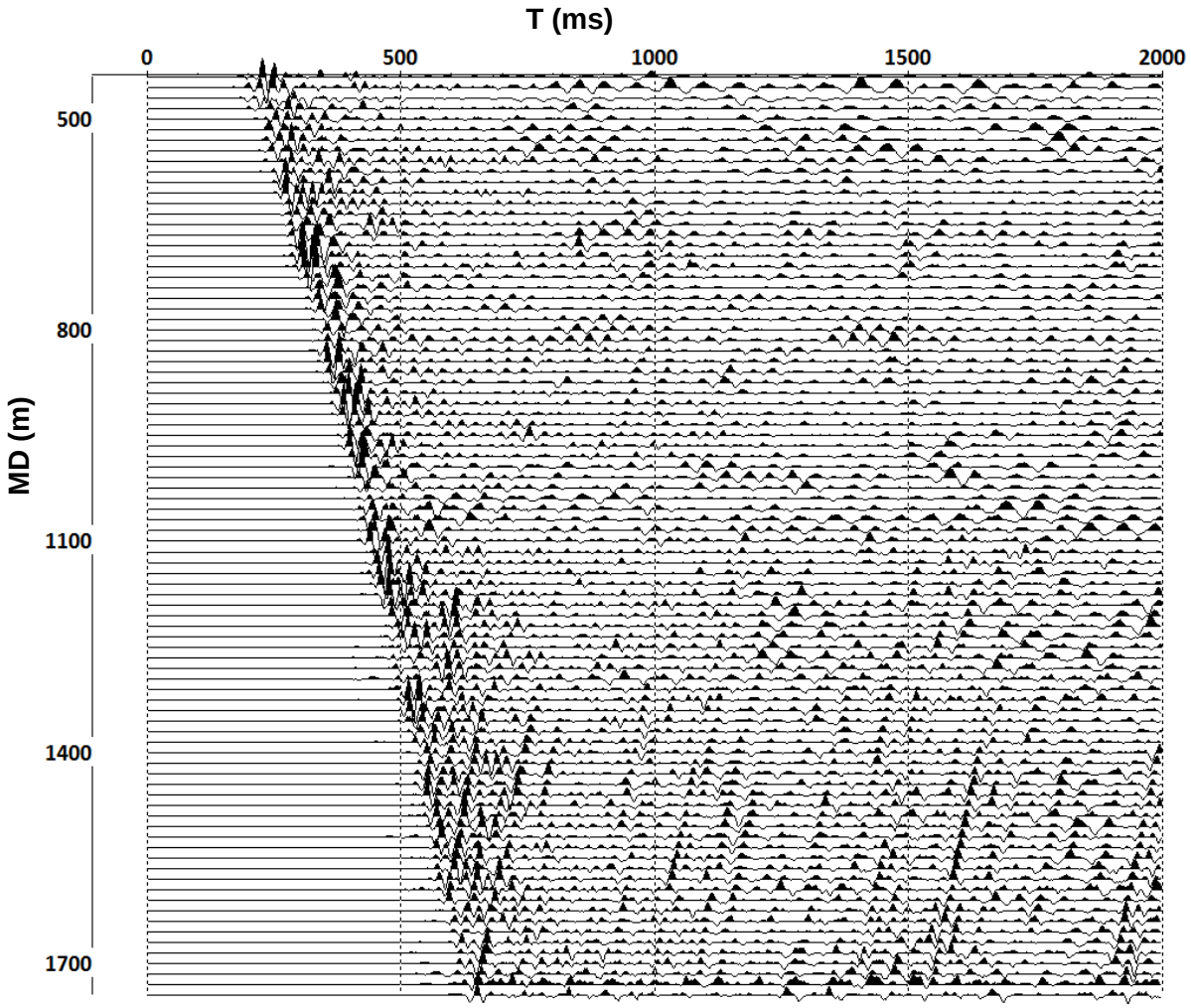


Figure 27 The Harvey 4 well ZVSP data, Z component, up-going PP waves.

To derive the two way travel time curve as a function of depth and also estimate interval P-wave velocities, an interactive tool (Advanced VSP Display) was used (Figure 28). To estimate the boundaries between the layers, the following criteria was used:

1. Positions of reflections,
2. Bending of the two way travel time curve, and
3. Log data

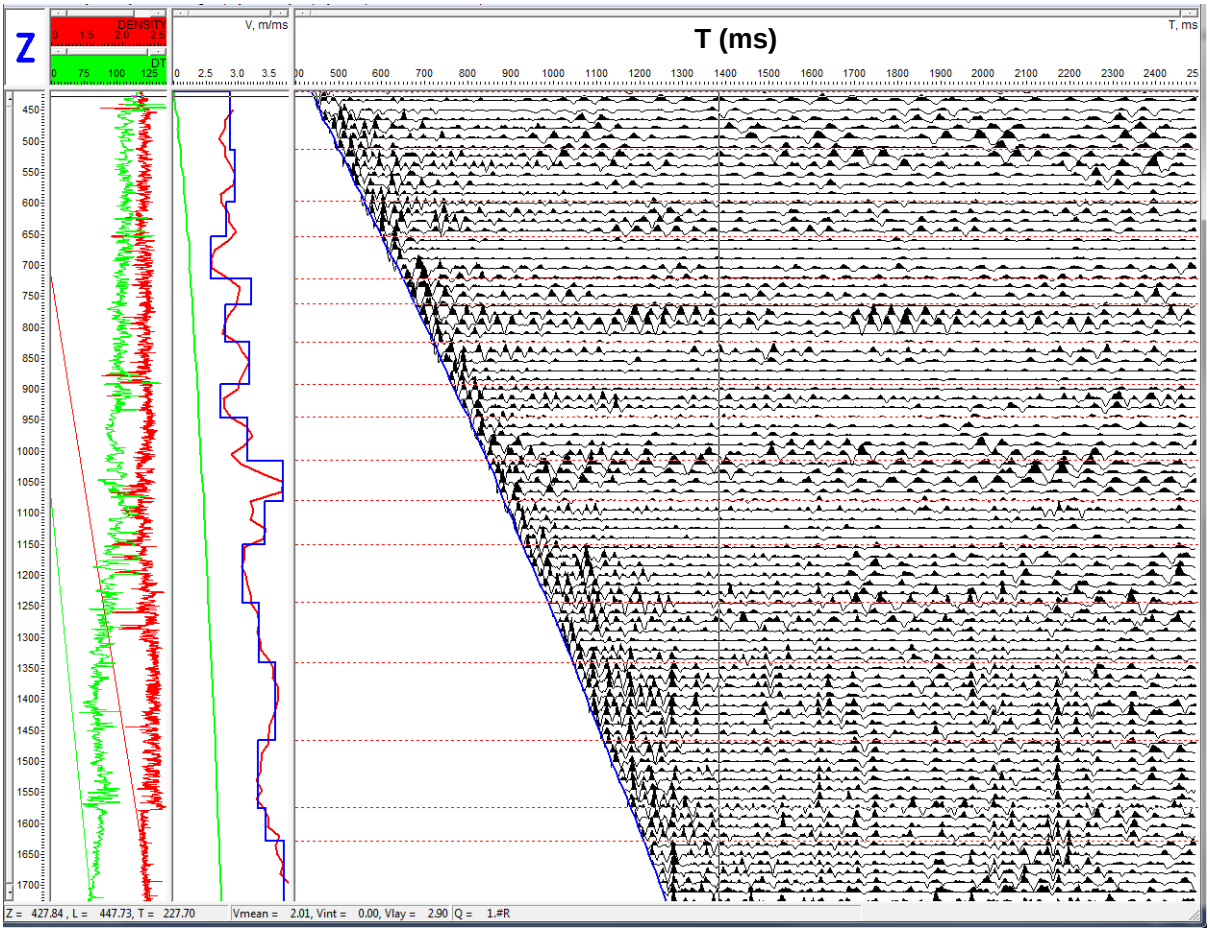


Figure 28 The Harvey 4 well ZVSP data, Interactive velocity analysis

The result of the velocity model survey processing is shown in Figure 29. Tables with the derived check shot data and velocity values are presented in Appendix A.

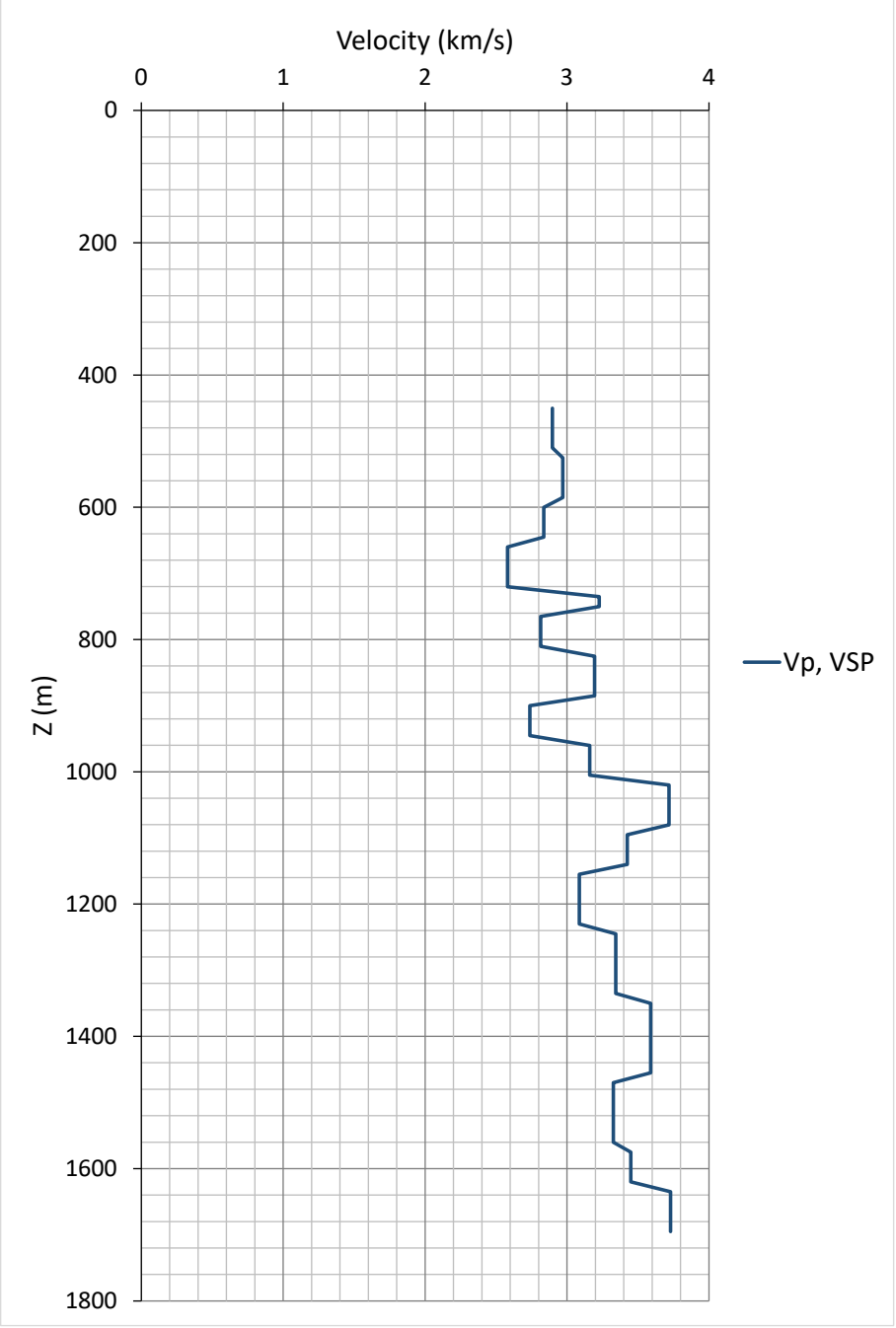


Figure 29 The Harvey 4 well ZVSP data, velocity model. Blue curve represents layer velocities derived through processing of travel time curves for direct P waves.

The result of the NMO correction of the up-going PP waves and the corridor stack trace are presented in Figure 30. The blue and red lines show the time gate used to compute the corridor stack trace.

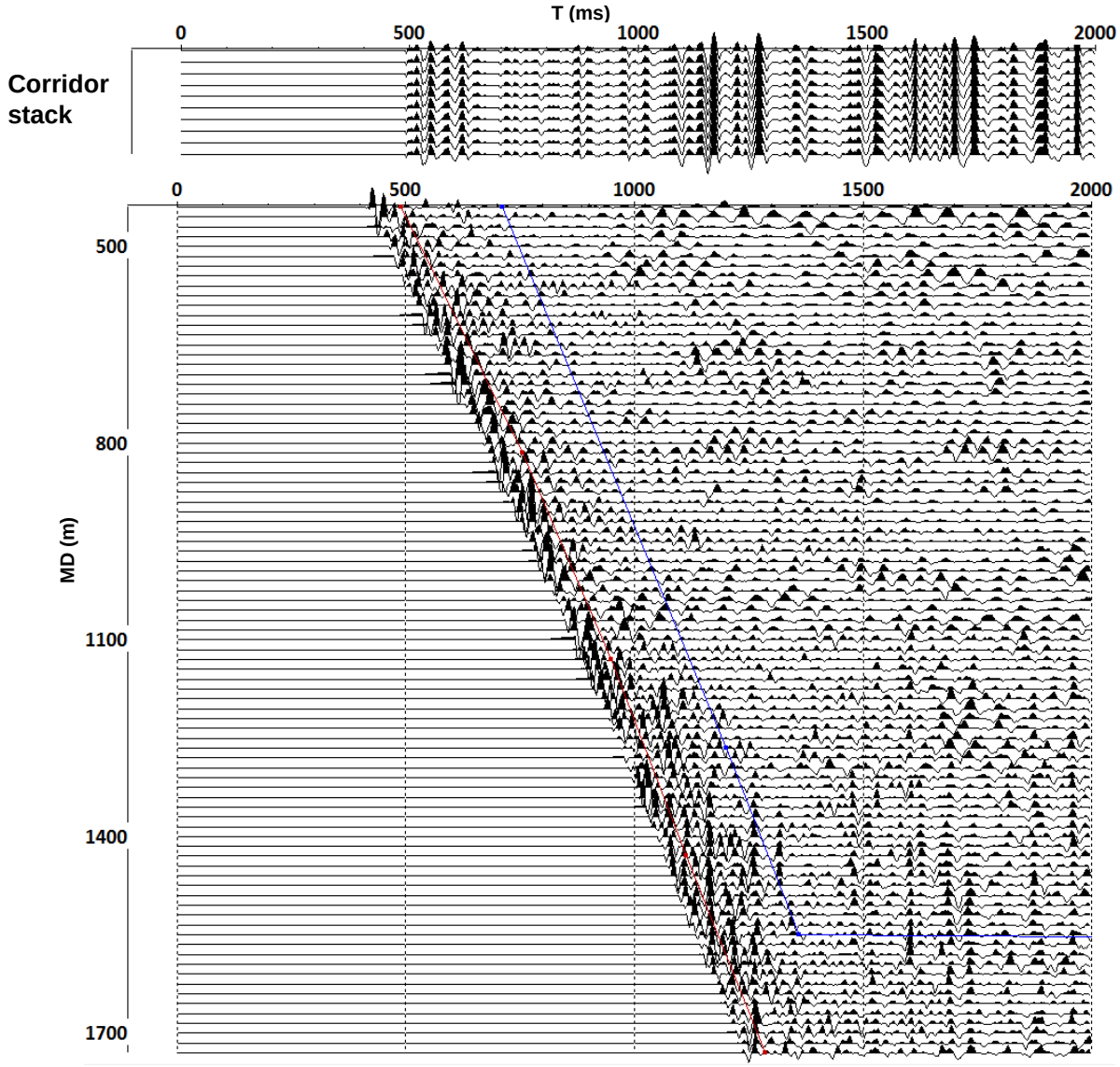


Figure 30 The Harvey 4 well ZVSP data, VSP-NMO and corridor stack trace.

The Harvey 4 well is located at the intersection of Inline 1109 and Xline 5188 of the 3D PSTM seismic cube. A seismic cube was computed for the datum of 40 m with replacement velocity 2.5 km/s. The actual time shift between the seismic data and the corridor stack was computed by taking into account a VSP datum of 15.89 m and matching the two seismic records. Total shift is 25.28 ms.

Results of the well tie using the corridor stack trace are presented in Figure 31. All major reflectors can be traced from VSP to surface seismic data. Corresponding check-shot table is provided in Appendix A.

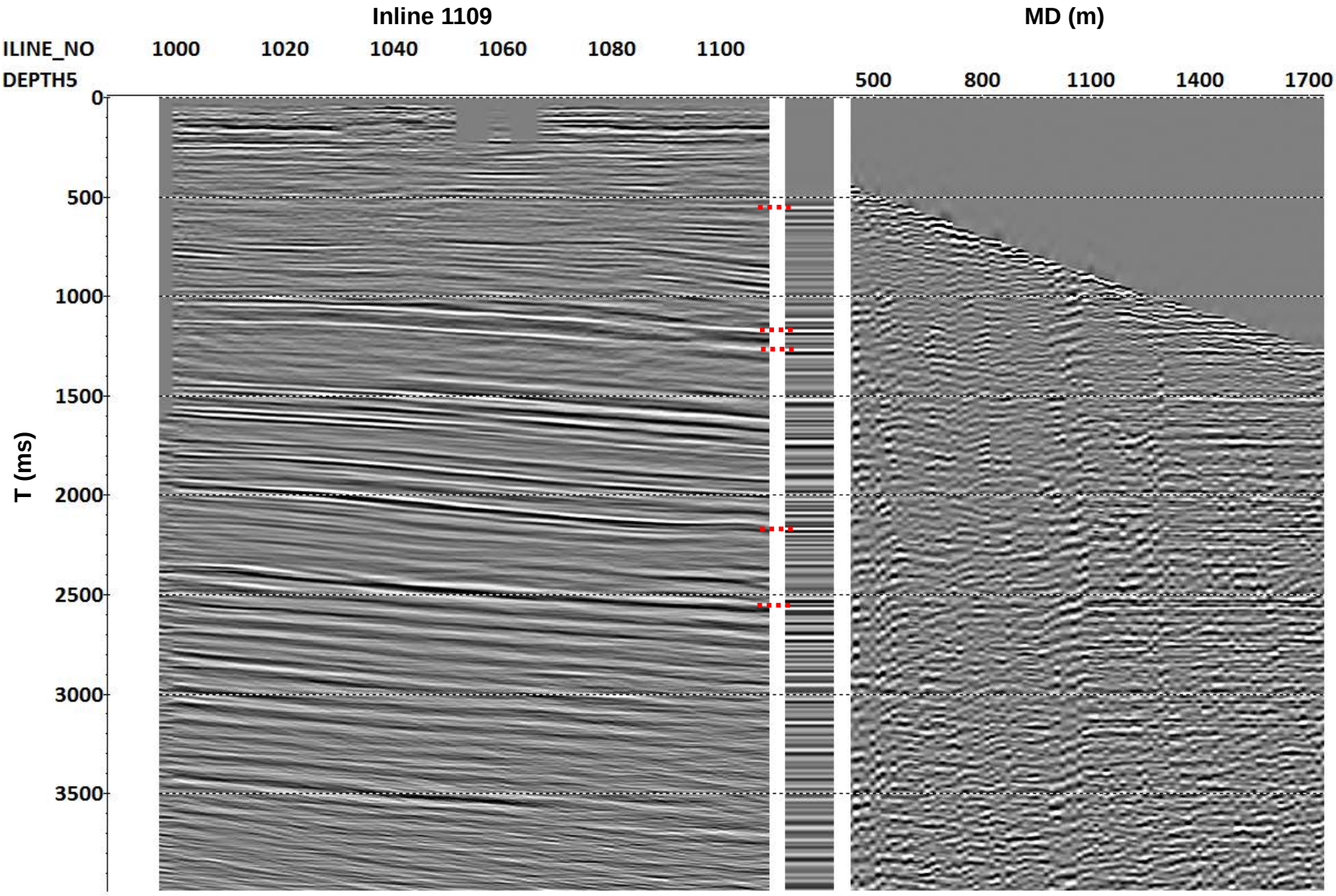


Figure 31 The Harvey 4 well ZVSP, the result of the seismic to well tie (principle reflectors are shown marked with red dashed lines).

2.4. Estimation of attenuation

Knowledge of the attenuation of seismic signals propagating through a medium is essential for reliable processing and interpretation of 3D seismic data. The main factors responsible for the decay of seismic amplitudes are divergence of the wavefront, scattering, attenuation and transmission losses (Hatton et al. 1986). VSP provides a great opportunity to study in-situ changes in the amplitude and shape of seismic waves. In order to estimate attenuation from the VSP data, we assume that propagation of the seismic wave can be described with linear system theory (Quan and Harris 1997). In this theory, the amplitude spectrum $S_R(f)$ of a direct wave recorded by a receiver located at a given depth is given by the equation:

$$S_R(f) = G(f)D \cdot H(f)S_0(f), \tag{28}$$

where f is frequency; $G(f)$ is a factor including instrument response, source coupling, receiver coupling, radiation pattern and frequency-independent transmission losses; D is a factor responsible for wavefront divergence; $S_0(f)$ is the amplitude spectrum of the emitted wave; and $H(f)$ describes the attenuation effect. To describe the attenuation effect $H(f)$, we can use the following notation (Quan and Harris 1997):

$$H(f) = \exp\left(-f \int_{ray} \alpha_0 dl\right), \tag{29}$$

where α_0 is the attenuation coefficient. This coefficient is related to the quality factor Q: $\alpha_0 = \pi/(Qv)$, where v is the velocity of the wave. This relation implies that both Q and v are independent of frequency.

The attenuation (equation 28) affects both amplitude and shape of the wavelet propagating in the medium. Several methods can be employed to estimate Q or the attenuation coefficient from the zero-offset VSP data.

We used the centroid frequency shift method to estimate the apparent attenuation from VSP data. We chose this method for its stability in the presence of random noise (Pevzner et al. 2012). The method was proposed by Kuc et al. (1976) and adopted for geophysical applications by Quan and Harris (1997) and involves measuring changes in centroid frequency and variance in order to estimate the Q factor. Quan and Harris (1997) defined centroid frequency measured at the receiver as

$$f_R = \frac{\int_0^{\infty} f \cdot S_R(f) df}{\int_0^{\infty} S_R(f) df} \tag{30}$$

and variance as

$$\sigma_R^2 = \frac{\int_0^{\infty} (f - f_R)^2 \cdot S_R(f) df}{\int_0^{\infty} S_R(f) df}, \tag{31}$$

where $S_R(f)$ is the amplitude spectrum of a direct wave recorded by a receiver located at a given depth.

For an amplitude spectrum given by the Gaussian function, a centroid frequency shift between a pair of receivers located along the ray path is

$$\frac{(f_{R1} - f_{R2})}{\sigma_{R1}^2} = \int_{ray} \frac{\pi}{Qv} dl \tag{32}$$

The centroid frequency shift method is based on a fact (equation 32) that the centroid frequency of the propagating wave decreases linearly with the travelled distance and the ratio is proportional to the attenuation coefficient. In this methodology qualitative analysis of the attenuation can be carried out by visual inspection of the centroid frequency shift curves; layers with a constant attenuation coefficient will have a constant slope. To avoid underestimated Q^{-1} values in layers with high attenuation and/or the large spatial distances between the receivers, the modification is implemented in this method. In equation 32, the average variance for the source-receiver (or receiver-receiver) pair in the denominator instead of the variance of the amplitude spectrum at the source (or top receiver):

$$2\frac{(f_{R1} - f_{R2})}{\sigma_{R1}^2 + \sigma_{R2}^2} \approx \int_{ray} \frac{\pi}{Qv} dl \tag{33}$$

This modification allows obtaining Q^{-1} with less than 5% error in most practical scenarios.

2.4.1. *The Harvey 2 well*

Here we describe the workflow which was used to estimate attenuation parameters along the boreholes. Only the vertical component of 3C VSP data was used for this purpose. The workflow is demonstrated using the data from the Harvey 2 well. The same approach was applied to the two wells.

The main workflow consists of the following stages:

1. Data conditioning.
2. Computation of attributes related to attenuation, such as the centroid frequency and amplitude decay curve.
3. Estimation of Q for the thick-layered model.

ZVSP data had to be conditioned prior to estimation of attenuation parameters in order to:

- Suppress all waves in the analysis window except for the down-going direct wave
- Compensate amplitude decay for wavefront divergence

Presence of up-coming waves in the analysis window can affect the amplitude spectrum estimation. Here we used F-X deconvolution (Canales 1985). To do this, we first applied a static correction to flatten the arrivals of the direct wave. In this case, upcoming waves was treated by F-X deconvolution as random non-predictable noise and removed from the seismogram. The actual parameters used were: a minimum frequency of 0 Hz, a maximum frequency of 180 Hz, a length of filter of 3-5 samples and a pre-whitening of 15%. We calculated and analysed the residuals to ensure that FX deconvolution was applied correctly to the data (e.g. most of the up-going energy is suppressed but no significant damage is done to the shape of the down-going waves). Figure 32 shows the results before and after the FX deconvolution and the difference. An event (red arrow on the right panel) related to a reflection can be observed from a fault plane (likely F10 fault) that causes interference with direct wave (red arrow on the centre panel). This interference could affect the reliability of the attenuation estimation.

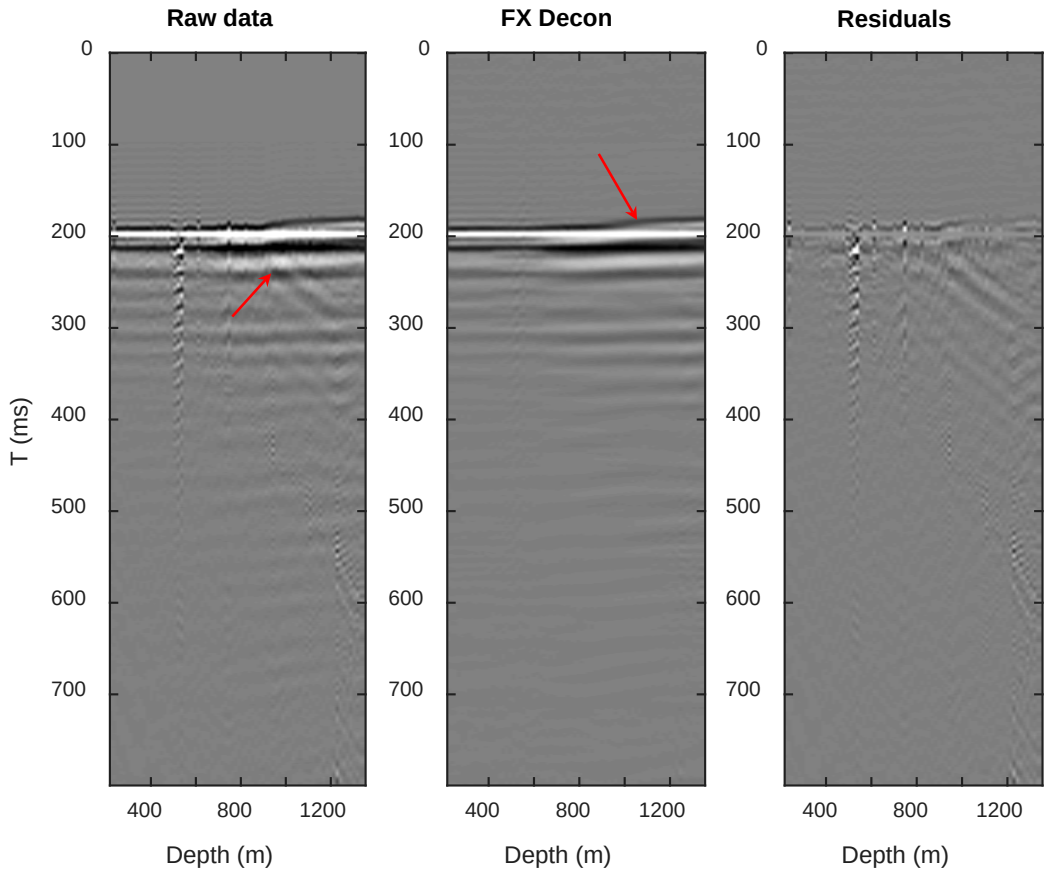


Figure 32 The Harvey 2 well. Attenuation of up-going waves using FX deconvolution. From left to right: original data, result of FX deconvolution and the difference. Red arrows indicate the events related to the interference with the wavefield reflected from a fault plane.

The next stage was to produce the amplitude spectra of the time-domain traces using FFT in the time window around the direct wave. After some testing, we decided to use a time window of about 300-400 ms as it gave a good spectral resolution. Hence, we did not include the part of the record with a poor S/N ratio. To further reduce the influence of the interference with up-going waves, we smoothed the spectra along the depth axis using a running average (window size is 3 traces x 1 sample) (Figure 33). Next, we applied a divergence correction.

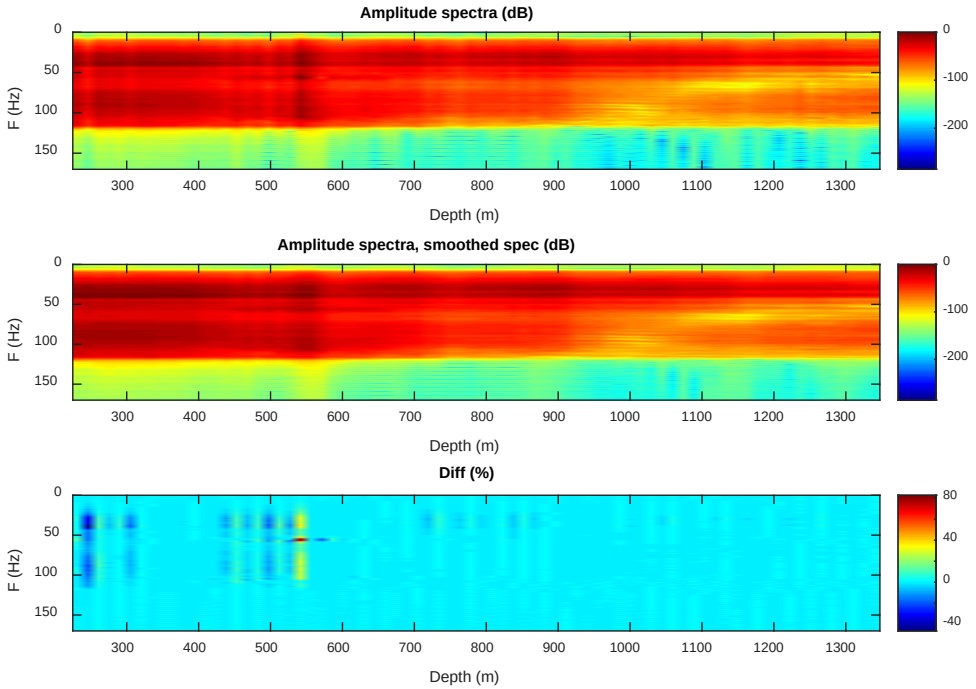


Figure 33 The Harvey 2 well. Amplitude spectra estimations. Top – amplitude spectra, middle – smoothed amplitude spectra, bottom – relative difference.

We then analysed amplitude decay at different frequencies (Figure 34) and computed the centroid frequency and the square root of its variance (Figure 35). We used the square root of the variance the 'deviation' instead of the variance as it had the same units as frequency.

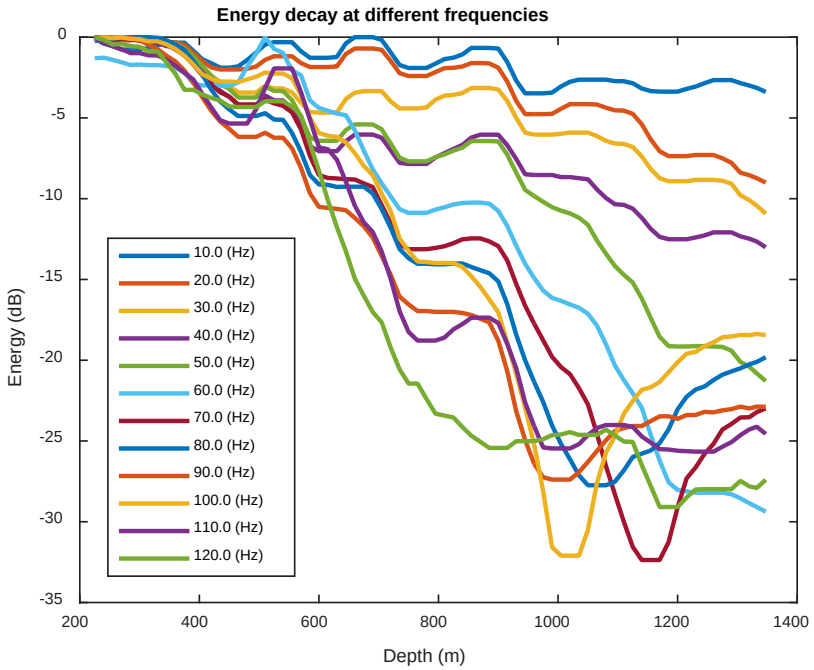


Figure 34 The Harvey 2 well. Amplitude decay at different frequencies.

Figure 35 allows the qualitative detection of layers with significant attenuation as these layers should be characterised by the increased dip of the curves corresponding to higher frequencies. The centroid frequency decay and centroid frequency variance curves were used to obtain interval Q values, and the amplitude decay curve – to QC our estimates. Amplitude decay can be computed from Q estimates using equation (29). Agreement between amplitude decay computed from estimated Q and directly from seismograms is a good indicator of the quality of Q estimates.

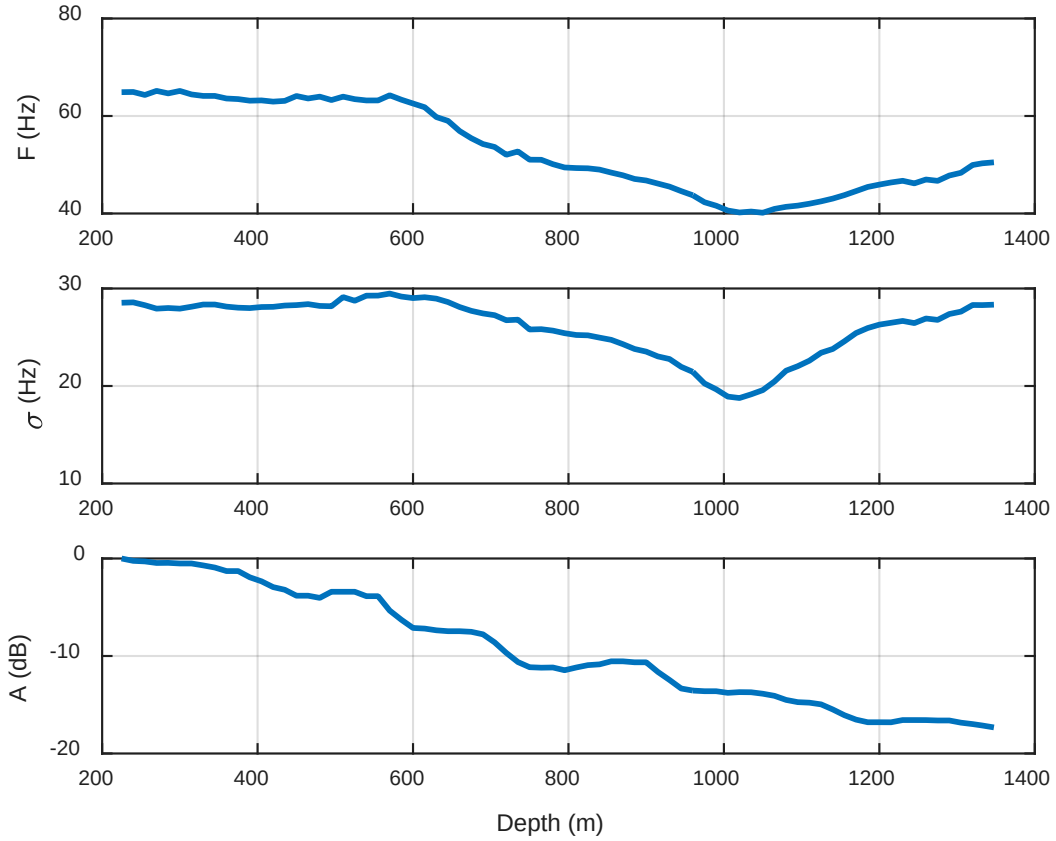


Figure 35 The Harvey 2 well. Centroid frequency (top), its deviation (middle) and absolute amplitude decay curves.

To obtain the layered Q^{-1} model, we used a modified centroid frequency shift approach (equation 33). Results of such an inversion are presented in Figure 36. We can conclude that for the thick layers Q-1 values was reconstructed reasonably well. Although the disruptive effects of the interference at the bottom part of the record and influence of ringing (due to the well design) at the top part are quite noticeable, we can conclude that the large estimated value of the apparent attenuation of Q=17 is reliable. This part of the centroid frequency curve is related to the lower part of the Yalgorup formation.

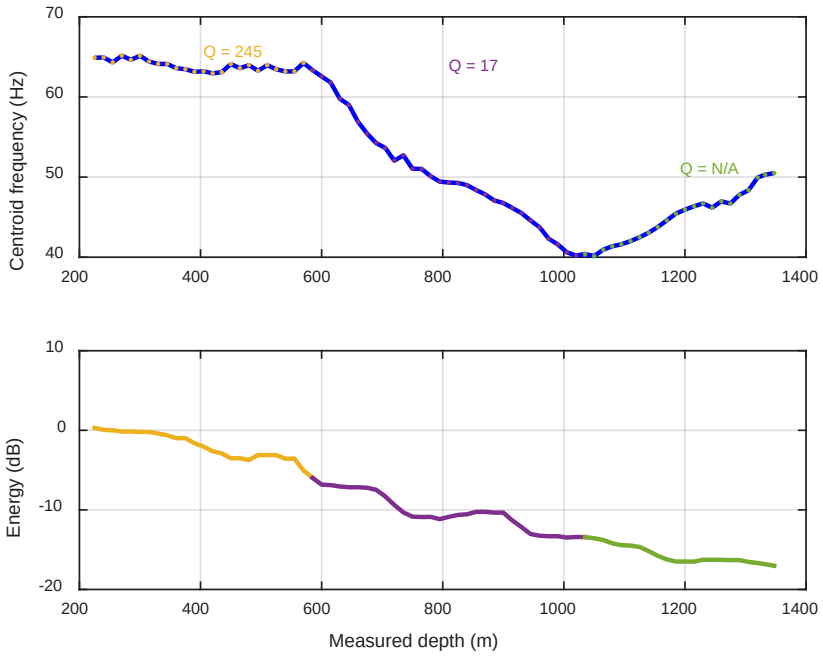


Figure 36 The Harvey 2 well. Centroid frequency (top) and energy decay curves. Q factor estimated in thick layered model.

In order to QC these estimates, we computed direct wave amplitude decay due to attenuation and compared it to actual amplitude decay curves corrected for the wave front divergence (Figure 37). These two curves match with less than 2 dB discrepancy most of the time. A large discrepancy can be noted below ~1000 m due to interference with the fault plane reflection and at the top part due to ringing caused by the well design.

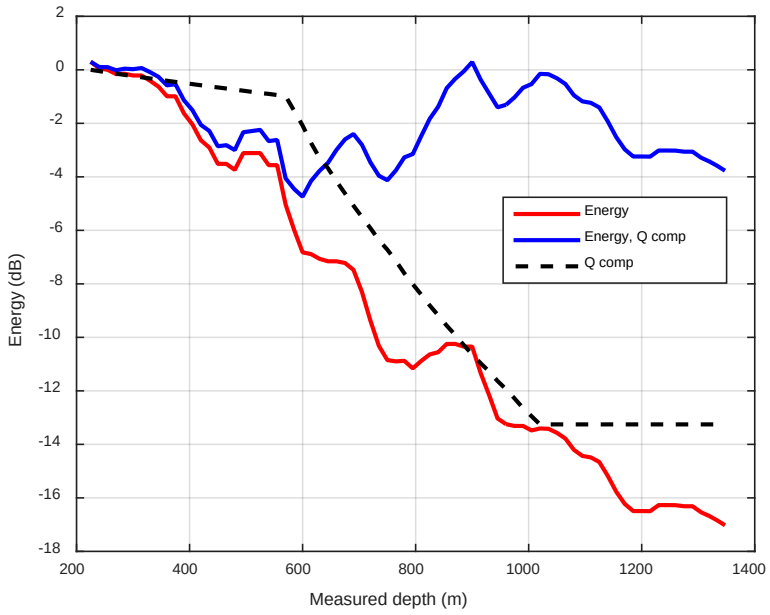


Figure 37 The Harvey 2 well. Direct wave amplitude decay curve (red), amplitude decay due to attenuation (black) and amplitude decay curve after Q-compensation (blue).

2.4.2. *The Harvey 3 well*

The same workflow was applied to the Harvey 3 well data to estimate apparent attenuation. First the up-going energy was suppressed using FX deconvolution (Figure 38) and the amplitude decay due to the wavefront divergence was compensated.

Figure 40 demonstrates the amplitude decay at different frequencies. A sharp decay of high frequencies (> 80 Hz) from ~ 1000 m depth downwards is observed.

The results of the implementation of the centroid frequency shift method are shown in Figure 41.

Estimation of the apparent attenuation in a thick layered model is shown in Figure 42. The layer with high attenuation Q=40 is related to the lower part of Yalgorup formation.

The results of the attenuation compensation are presented in Figure 43.

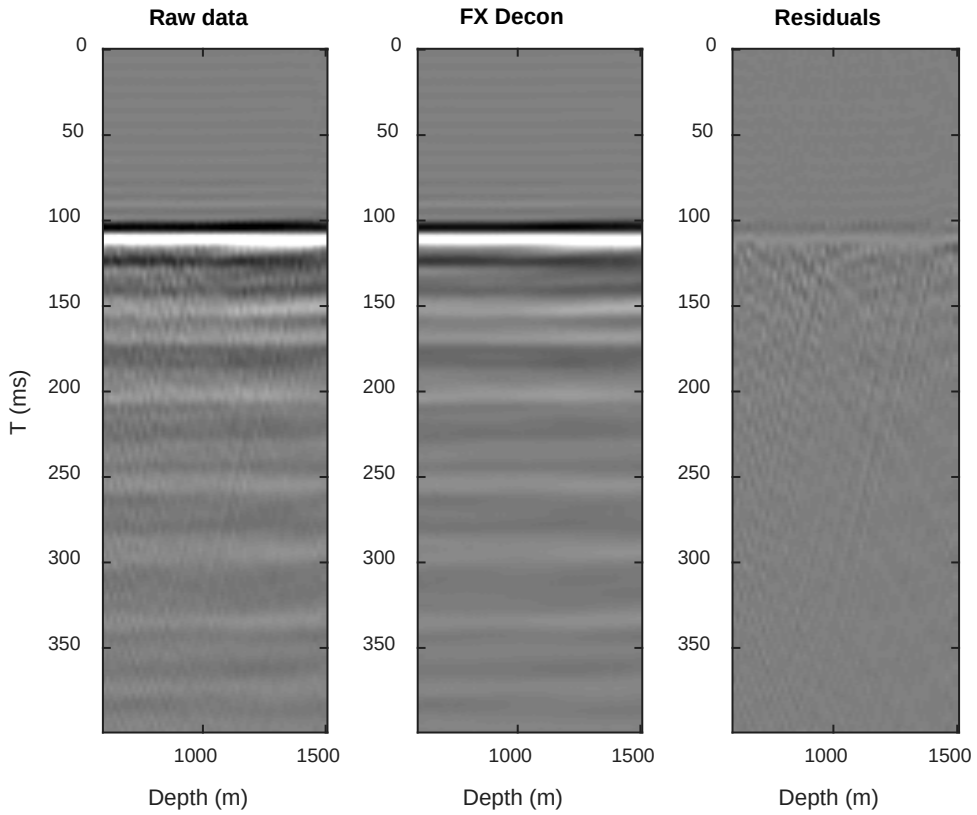


Figure 38 The Harvey 3 well. Attenuation of up-going waves using FX deconvolution. From left to right: original data, result of FX deconvolution and the difference.

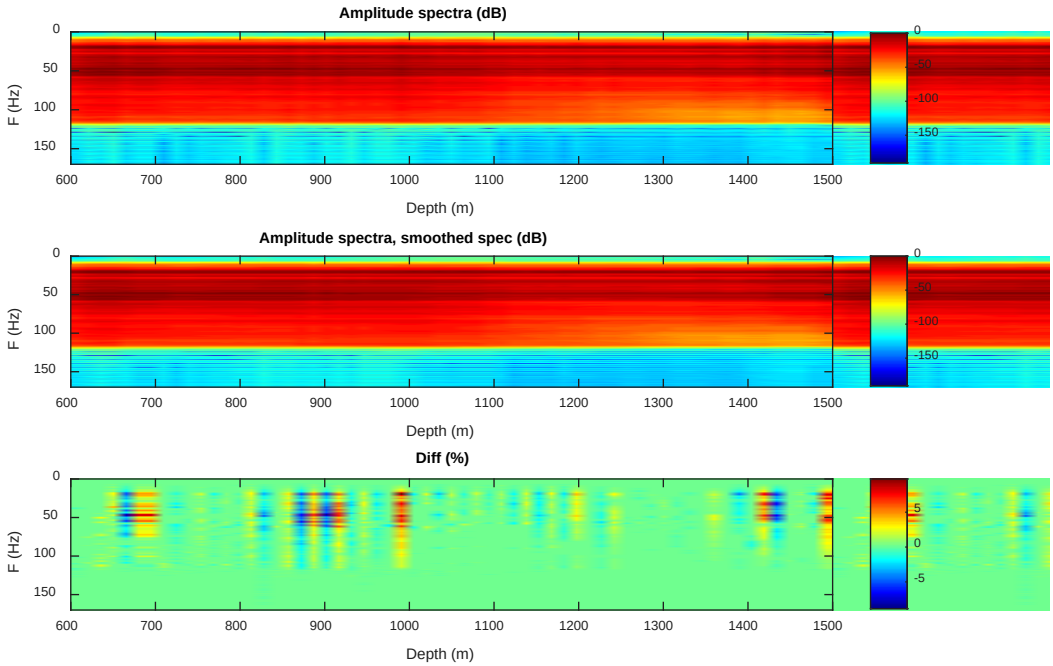


Figure 39 The Harvey 3 well. Amplitude spectra estimations. Top – amplitude spectra, middle – smoothed amplitude spectra, bottom – relative difference.

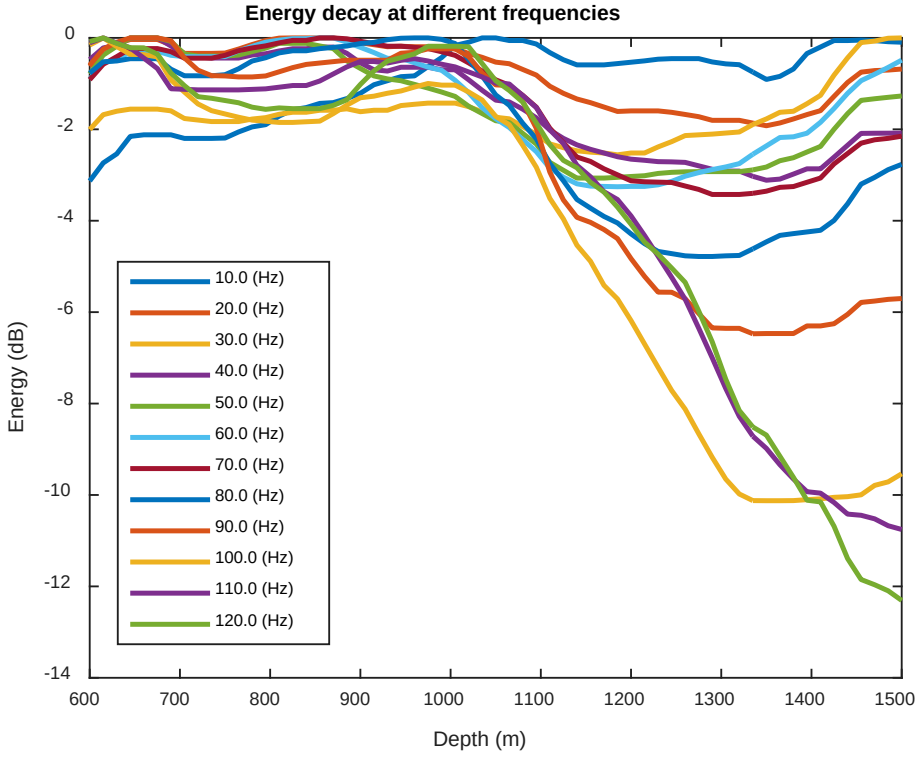


Figure 40 The Harvey 3 well. Amplitude decay at different frequencies.

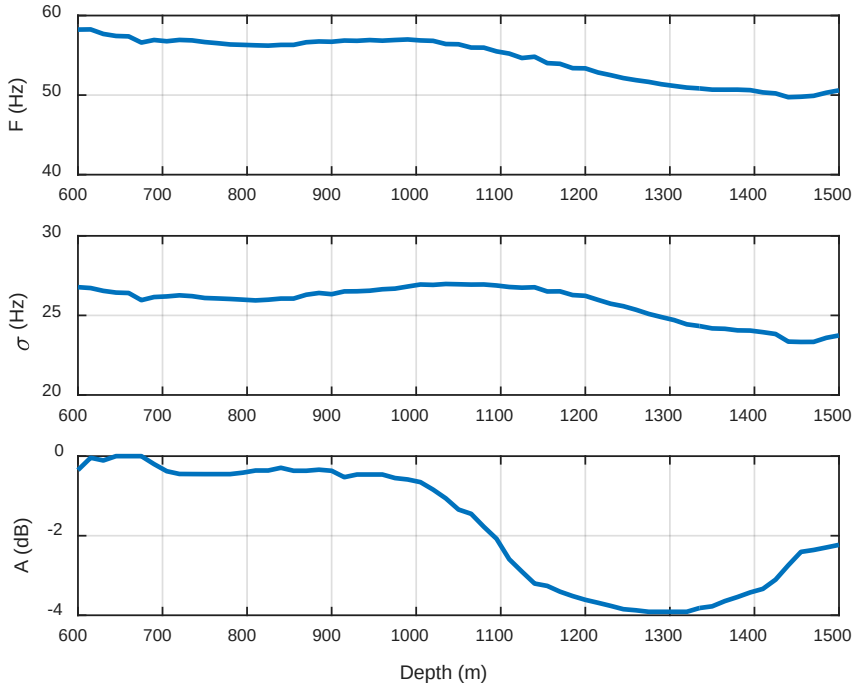


Figure 41 The Harvey 3 well. Centroid frequency (top), its deviation (middle) and absolute amplitude decay curves.

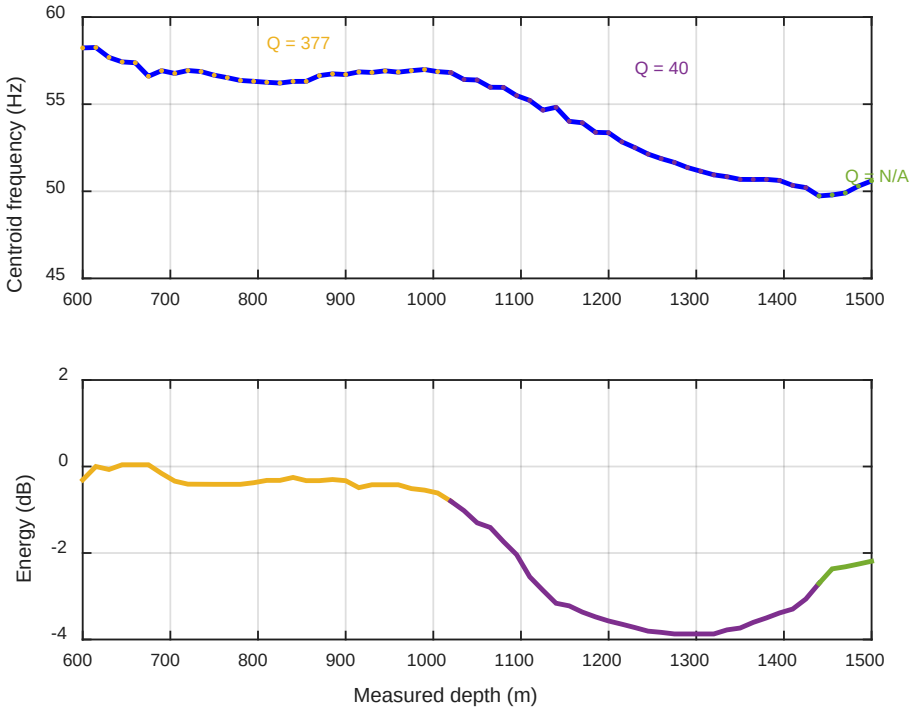


Figure 42 The Harvey 3 well. Centroid frequency (top) and energy decay curves. Q factor estimated in thick layered model.

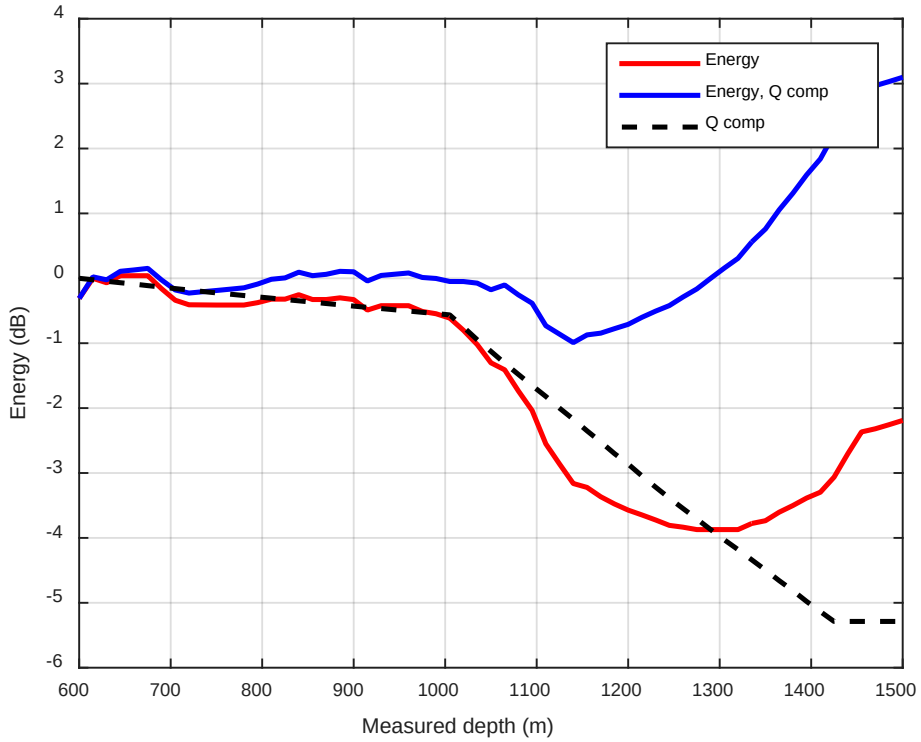


Figure 43 The Harvey 3 well. Direct wave amplitude decay curve (red), amplitude decay due to attenuation (black) and amplitude decay curve after Q-compensation (blue).

2.4.3. *The Harvey 4 well*

The same workflow was applied to the Harvey 4 data to estimate apparent attenuation. First the up-going energy was suppressed using FX deconvolution (Figure 44) and the amplitude decay due to the wavefront divergence was compensated.

Figure 45 shows the amplitude spectra of the down-going energy.

Figure 46 demonstrates the amplitude decay at different frequencies. A sharp decay of high frequencies (> 80 Hz) from ~ 1300 m depth downwards is observed.

The results of the implementation of the centroid frequency shift method are shown in Figure 47.

The estimation of the apparent attenuation in a thick layered model is shown in Figure 48. The layer with high attenuation Q=40 is related to the lower part of Yalgorup formation.

The results of the attenuation compensation are presented in Figure 49.

In conclusion, we see that the Yalgorup formation experiences high attenuation of seismic signal in all three wells: the Harvey 2 well Q=17, the Harvey 3 well Q=40, and the Harvey 4 well Q=40.

To improve 3D seismic processing results such a level of the signal attenuation had to be taken into account.

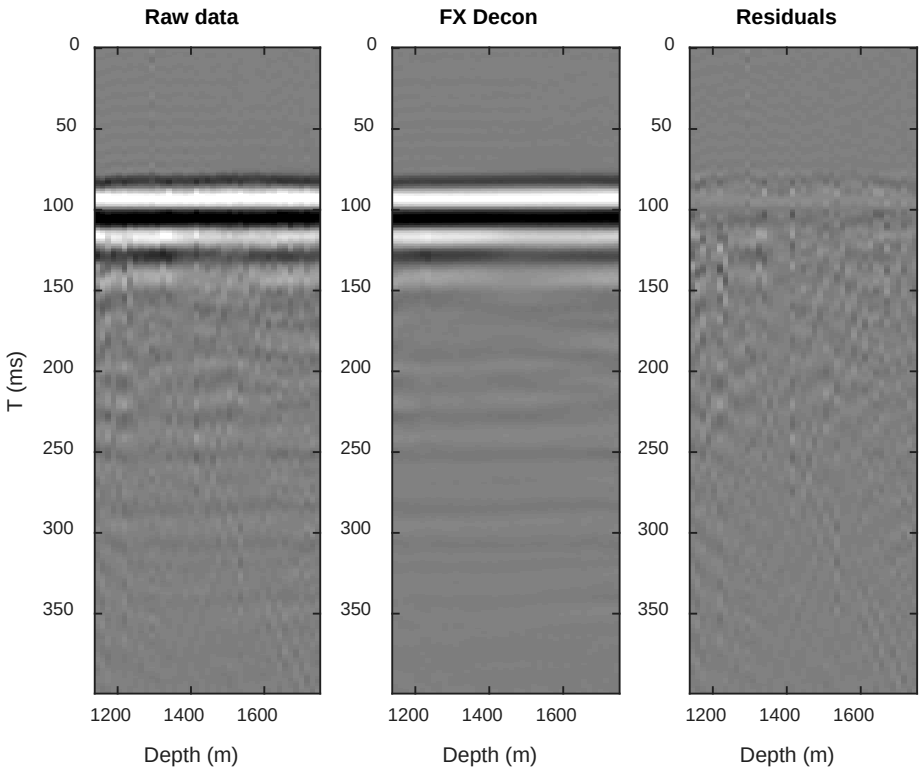


Figure 44 The Harvey 4 well. Attenuation of up-going waves using FX deconvolution. From left to right: original data, result of FX deconvolution and the difference.

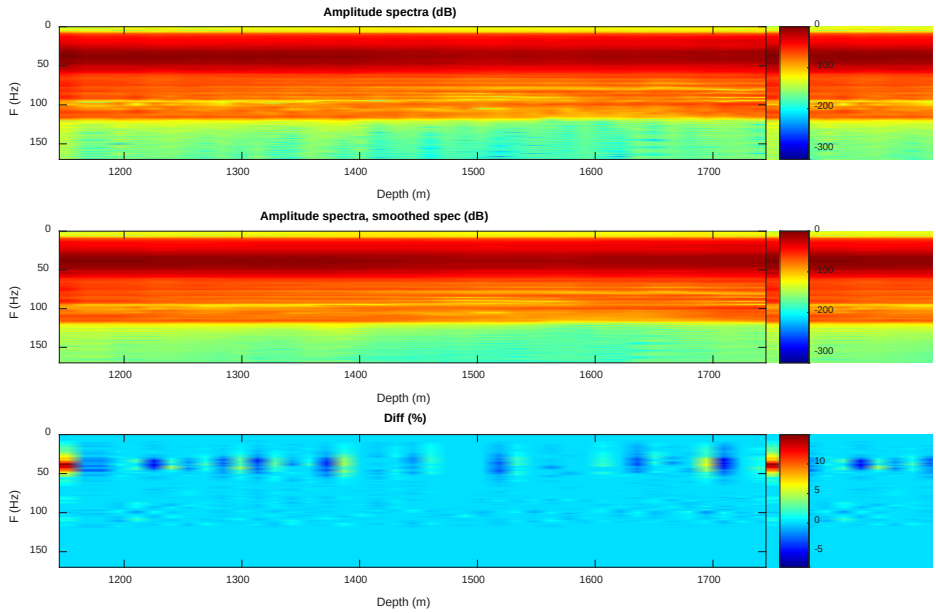


Figure 45 The Harvey 4 well. Amplitude spectra estimations. Top – amplitude spectra, middle – smoothed amplitude spectra, bottom – relative difference.

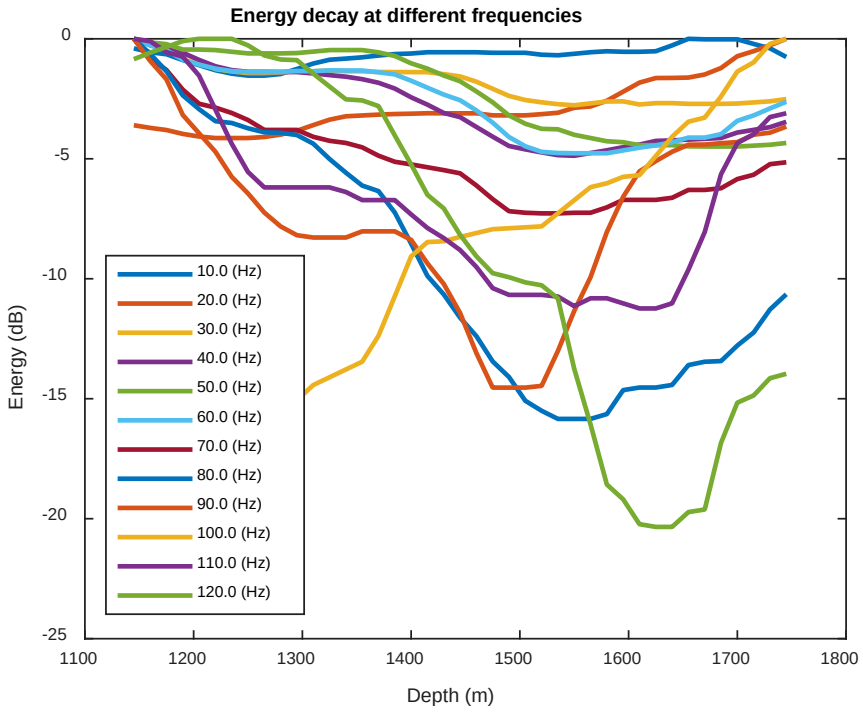


Figure 46 The Harvey 4 well. Amplitude decay at different frequencies.

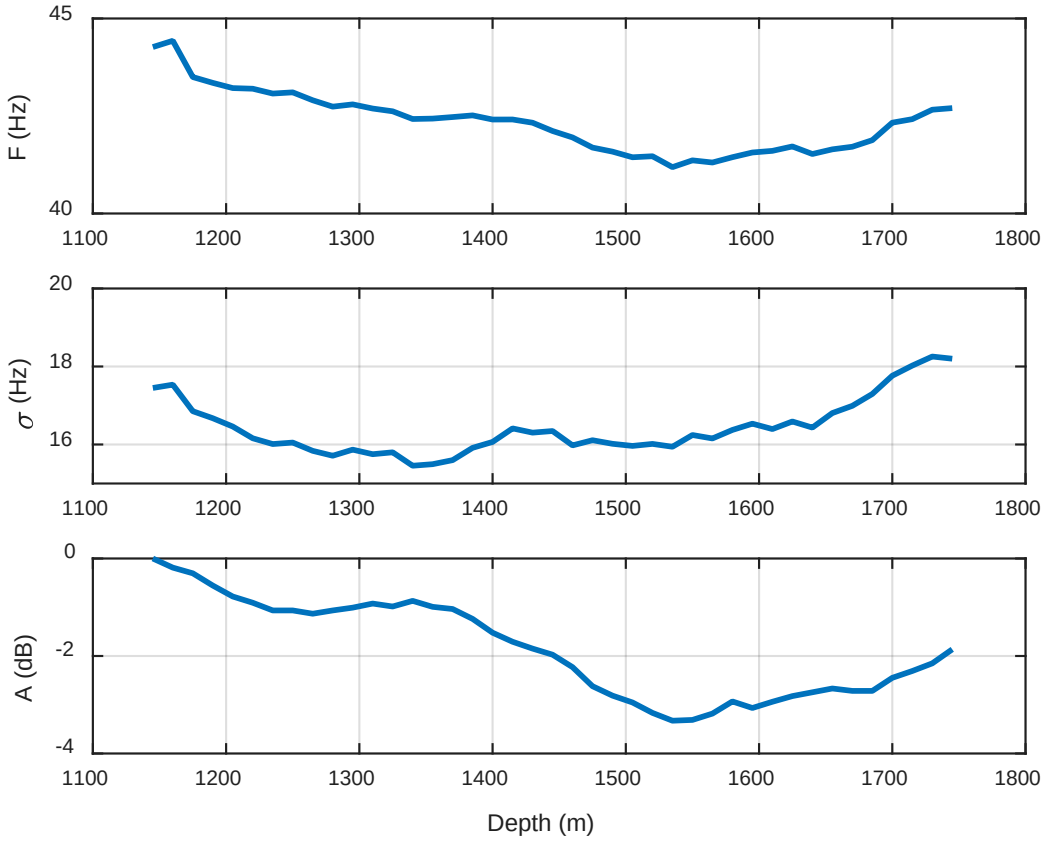


Figure 47 The Harvey 4 well. Centroid frequency (top), its deviation (middle) and absolute amplitude decay curves.

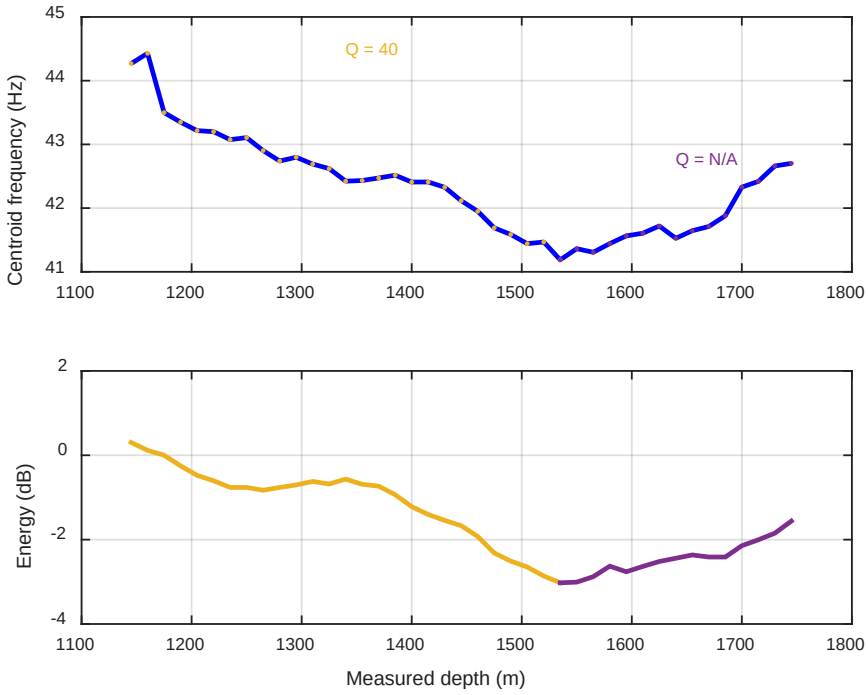


Figure 48 The Harvey 4 well. Centroid frequency (top) and energy decay curves. Q factor estimated in thick layered model.

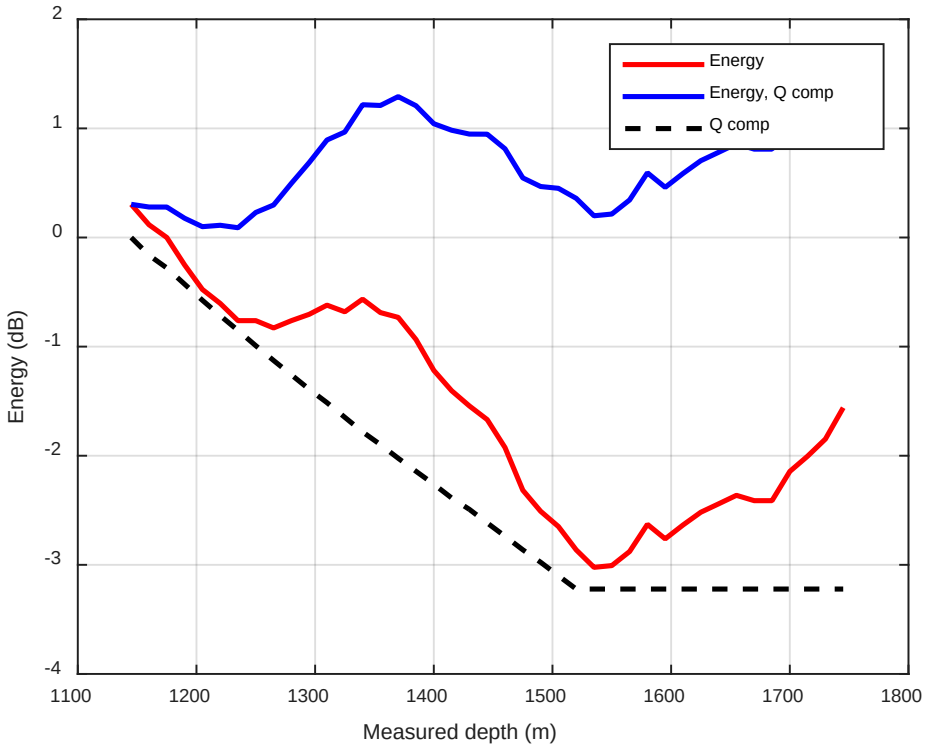


Figure 49 The Harvey 4 well. Direct wave amplitude decay curve (red), amplitude decay due to attenuation (black) and amplitude decay curve after Q-compensation (blue).

2.5. Conclusions

The ZVSP data were of satisfactory quality for a conventional analysis and interpretation, except for the Harvey 4, which had a significant interval contaminated by noise. We were able to recover reliable time-depth relations for the Yalgorup and Wonnerup members, which significantly helped with the well-tie. The interval velocities were used to stabilize migration velocities and sonic logs.

VSP data quality in the Harvey 2 and Harvey 4 wells is varied. Some of the datasets (the Harvey 3 & 4 wells) are contaminated with the tube waves. A well tie using VSP data was performed using both the corridor stack trace and the full field after NMO correction specifically to avoid mixing tube wave remnants with true reflections.

The Harvey 2 well contains prominent signature of the intersecting fault (Fault 10), which leads to a conclusion that the borehole seismic (such a 3D VSP survey) can be effective for fault characterisation in the area. The Harvey 4 well also intersected a fault (Fault 7), but it is not as clearly seen on seismograms due to unfavourable geometry of source-receiver locations with respect to the fault plane. Nevertheless, the interference still occurs because of the presence of the fault as can be observed during the study of the attenuation (on amplitude decay curves for different frequencies and centroid frequency graphs, Figure 46 and Figure 47) resulting in negative Q estimates. Acquisition of 3D VSP data was required for better characterisation of faults in the vicinity of a well.

Seismic attenuation retrieved from ZVSP in all of the Harvey wells features the same pattern: high attenuation in the Yalgorup member (Q ~30) and negative values in the Wonnerup. The negative values of the attenuation have been observed due to the interference of the downgoing energy from a source with reflected/refracted energy from the sub-vertical features (such as steeply dipping faults). So far, we are not ready to interpret these values in terms of rock properties. However, it is a clear sign of complex structure of the Yalgorup member, which should be taken into account during both seismic processing and interpretation.

3. Seismic Data Processing and Imaging

In order to improve subsurface characterisation of the proposed SW Hub area a large 3D seismic reflection survey was acquired by the Department of Mines and Petroleum, Western Australia in December 2012 – April 2014 (Geokinetics, 2014). The survey is officially known as DMPWA 2013 Harvey-Waroona 3D seismic survey, for simplicity in this report we refer to it as the large 3D seismic survey.

The survey has undergone a thorough analysis by Pevzner et al. (2015). But that work focused on the detailed reconstruction of the subsurface structure – faults, horizons and global geobodies. This goal does not require careful preservation of the relative seismic amplitudes. Even the opposite is true - if a particular seismic event is detected it should be highlighted to facilitate spatial correlation of the events. Thus, the final seismic images are inappropriate for the quantitative interpretation of the amplitudes. To overcome this issue, the Milestone 4 report presented the processing steps that we have undertaken to get so-called true-amplitude seismic data suitable for quantitative interpretation.

Furthermore, although the large 3D survey has undergone thorough analysis, there is a room for improvement, including attempts to improve seismic coverage of the poorly covered zones, which in turn might improve the reliability of reservoir characterisation. This task was specifically requested by the SW Hub management and incorporated into this Project as part of Variation 3.

In addition, the large 3D volume still had extremely uneven seismic offset distribution and thus precluded the application of any offset dependent reservoir characterisation, such as AVO analysis. To address this problem, it was decided to create a composite seismic line, based on the 2D line passing close to the Harvey 1 well, combined with elements of the Harvey 3 and Harvey 4 nested survey (and hence passing in proximity to these wells). This composite line is expected to have a more even distribution of seismic offsets and hence is expected to be more suitable for AVO inversion. Processing and imaging of this composite line was also incorporated into the Project as part of Variation 3.

This chapter describes complete processing and imaging flow for the 2D composite line followed by complete reprocessing and true-amplitude imaging of the large 3D volume.

3.1. Composite line

To model the distribution of paleosols, lenses of high clay content, which are assumed to serve as baffles for CO_2 upward migration a pre-stack depth migration (PSDM) was attempted on

Harvey seismic data. PSDM was applied on the southern half of Harvey generation 2 regional 3D seismic data and available 2D seismic lines. An arbitrary 2D line was extracted from existing 2D and 3D surveys that connected Harvey 1, 3 and 4 wells (Figure 50).

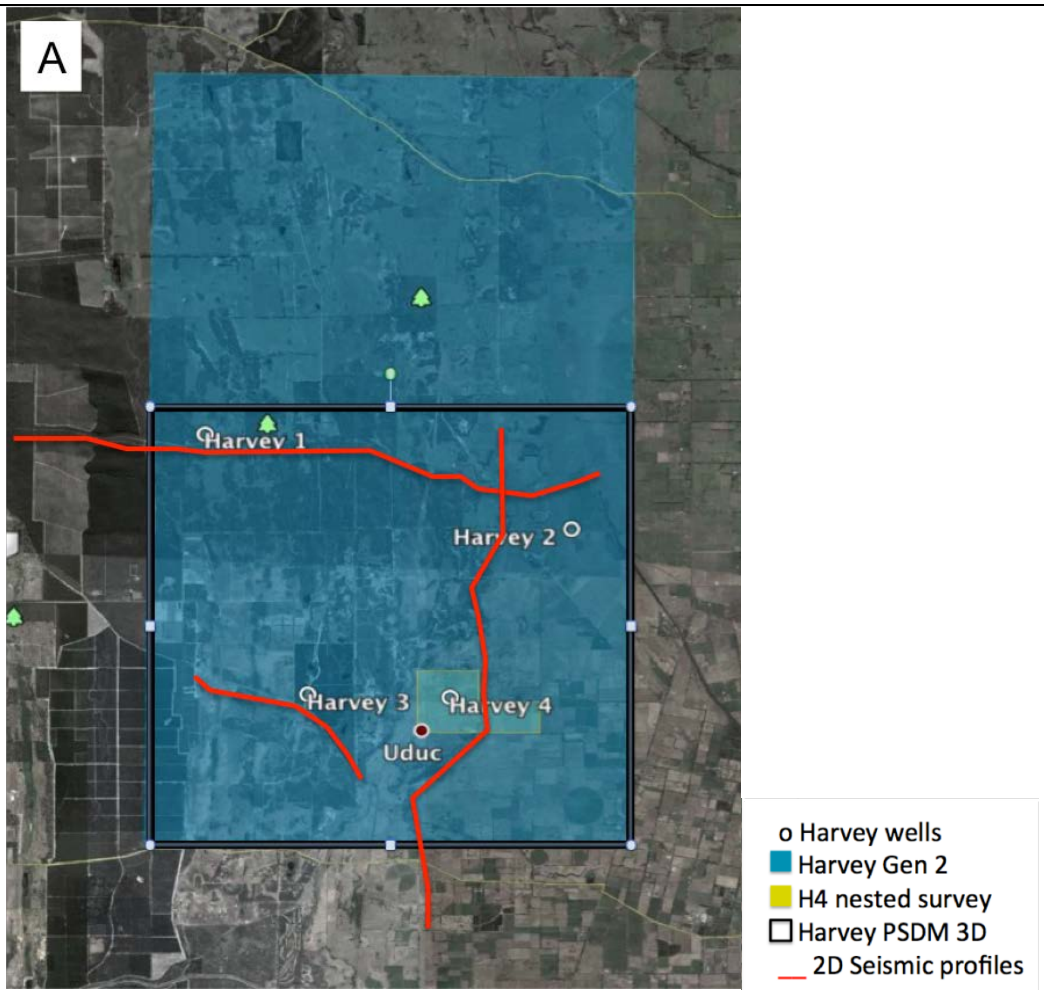
The subsequent pre-processing flow is displayed in Table 4. The main stages of the surface seismic data processing are the application of static corrections and SNR improvement so that the initial velocity analysis could be better accomplished. In the final depth imaging, the layer stripping method and tomography inversion were utilized on PSDM image gathers to obtain a reliable high-resolution velocity field.

Firstly, 2D and 3D seismic geometries were loaded into the SeisSpace processing software and reformatted to the internal format. 2D crooked line geometry assignment was used to calculate CDP binning information, source-receiver offsets and azimuths. Following the geometry assignment to the database, and the accuracy of the geometry verified. The data was binned using the inline bin size of 25 m, which resulted in a fold map and mean offset plot displayed in Figure 50 and Figure 51. Diagrams illustrated satisfactory offset distribution. However, it was also observed that offset normalisation was imperative prior the pre-stack time migration (PSTM).

The trace editing was conducted in an automatic routine. The compensation for the amplitude loss was followed by the root mean square (RMS) threshold energy value calculation. This allowed us to determine the traces with abnormally high amplitude values (typically 10:1 amplitude ratio computed for the selected time window), which were eliminated from further processing. Some traces were detected to have noise bursts. To eliminate those traces, a Time-Frequency Domain (TFD) noise rejection was used to isolate the noise bursts and replaced them with the median spectral amplitudes calculated from 11 adjacent traces. The detailed processing flow is illustrated in Table 4 Surface seismic pre-processing flow.

Table 4 Surface seismic pre-processing flow.

Procedure	**Parameters**
Data conversion	SEG-D data Input and conversion to Seispace internal format
Geometry assignment	Applied from SPS files
Binning	Inline bin size 25 m
Trace Editing	Kill bad traces
Air Blast Attenuation	Attenuation mode for air velocity at 330 m/s
Refraction Statics	Final datum elevation – 40 m, Replacement Velocity – 2200 m/s
Residual Static	Application of refraction and residual statics
Deconvolution	Zero phase spiking, Operator length – 80ms, Operator 'white noise' level – 0.1%
Band-pass Filtering	4-12-150-250 (Hz)
Surface wave noise attenuation	Velocity 1100m/s, frequencies 1-60Hz
Automatic Gain Control (display purposes)	500ms



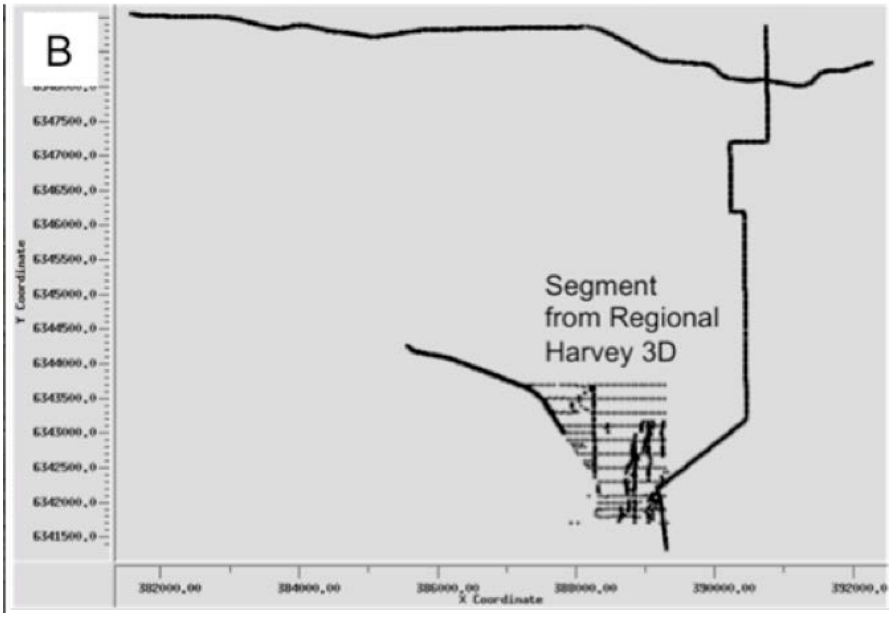


Figure 50 Survey layout; Position of available seismic surveys in the area (A). All seismic vintages of a composite line (B).

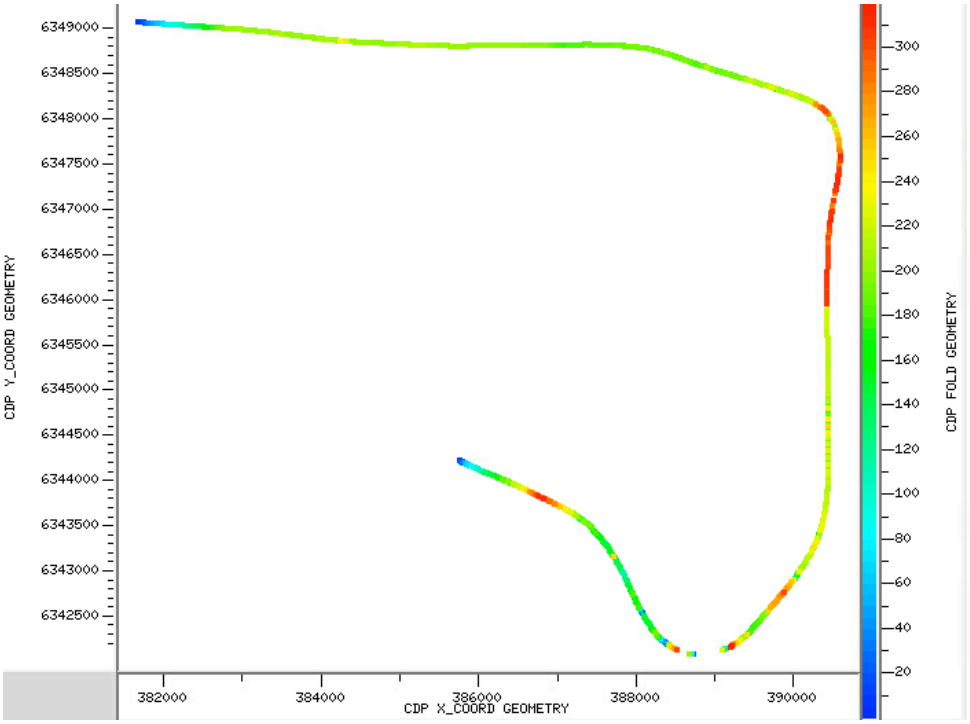


Figure 51 CMP fold coverage. Blue colour corresponds to low fold and red colour corresponds to a high fold of over 300 traces in a single bin.

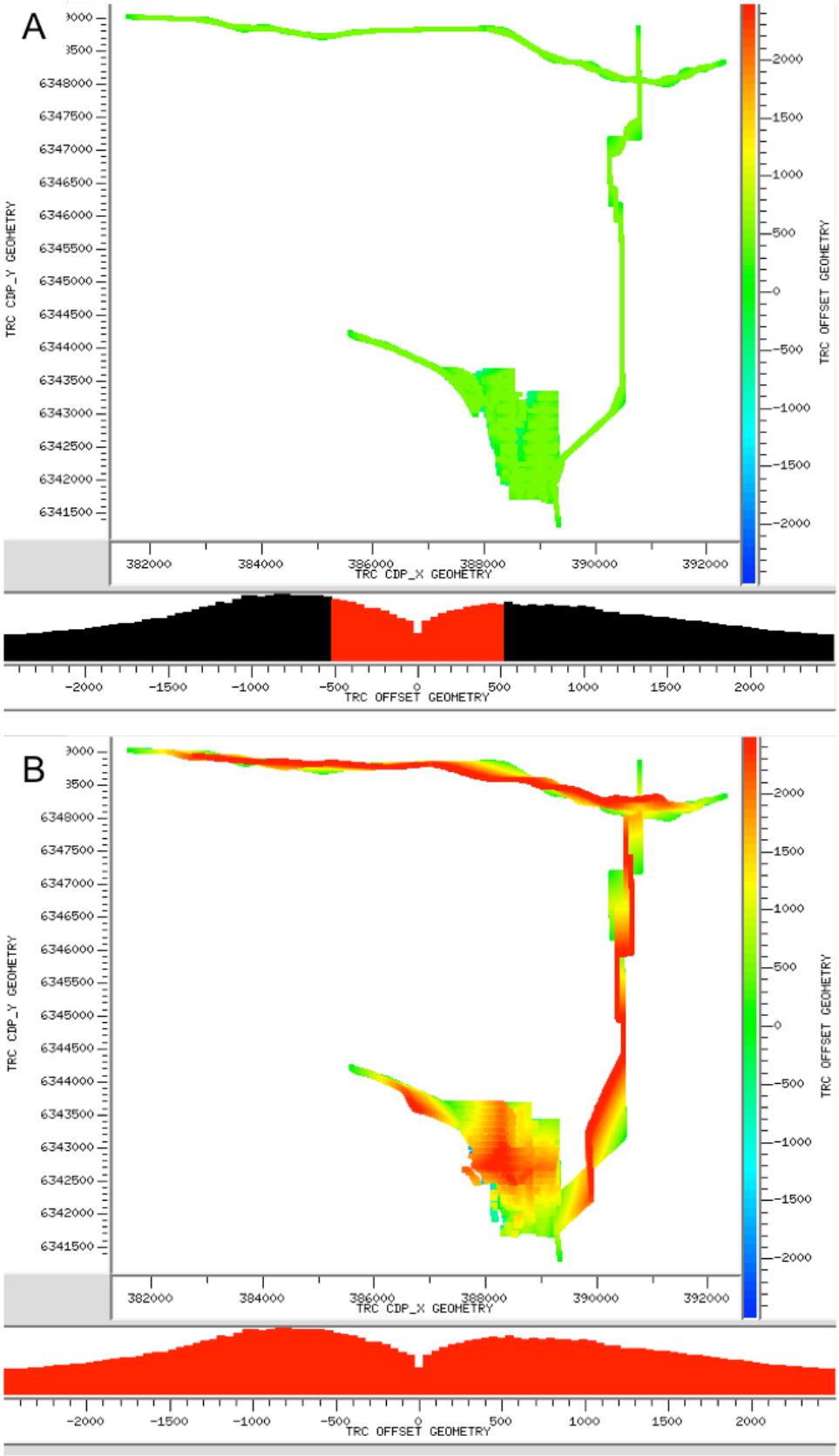


Figure 52 Offset distribution plot and histogram. Highlighted near source-receiver offset (0 - 500 m) (A). Highlighted all offsets (B).

Gentle topographic and weathering variations over the survey area were corrected with a refraction static correction. For the selected seismic datum of 40 m, and a replacement velocity of 2200 m/s, the total variations in delay times are illustrated in Figure 53. Following the application of refraction statics, residual statics were applied.

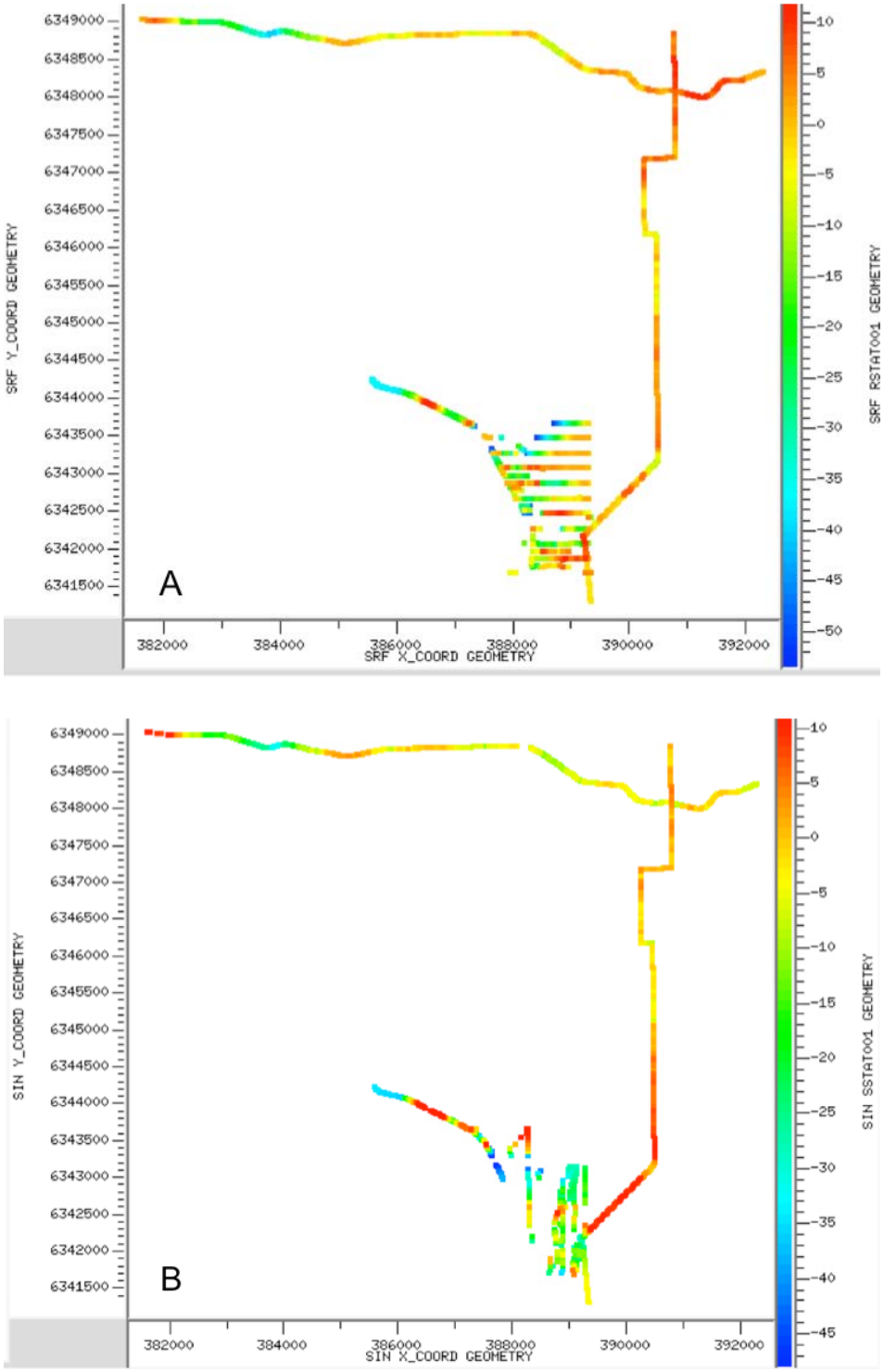


Figure 53 Refraction statics for all receivers (A) and all source positions (B) displayed in milliseconds

3.1.1. *Signal to Noise Ratio (SNR) improvement*

Ambient noise was suppressed through the process of stacking. However, the effectiveness of this suppression was proportional to the fold of data. Stacking was not as effective in suppressing the source-generated coherent noise. The main types of coherent noise were air blast, surface or Rayleigh waves and refracted waves (P and converted S-waves). Additional problems arose from the multiple reflections or simply “multiples”. Air blast attenuation routine (2D operator) using an air-wave velocity of 330 m/s was applied to attenuate the waves propagating across the receiver spread through the air. Surface waves were attenuated with the frequency-wavenumber (F-K) based routine that operates using the apparent slopes. For an F-K application, the frequency range was limited to the surface wave frequency range which minimised the signal distortion. To precondition the data for this 2D filtering operation, each 3D shot was decomposed into a sequence of 2D shots, arranged by the receiver line number and sorted from maximum negative to maximum positive offset. Subsequently, we applied deconvolution to attenuate short period multiples and improve the shape of the wavelet. This also increased the temporal resolution. After the tests with several algorithms, a predictive deconvolution was selected. The deconvolution operator length was initially estimated using an autocorrelation function computed across selected shots. The performance could be assessed in two ways:

I. by the visual inspection of the continuity and reflectivity of the direct and reflected waves and

II. by the shape of autocorrelation curve obtained with the application of several different deconvolution routines.

Eventually, an operator length of 80 ms was chosen. Deconvolution was followed by the broad bandpass filtering (4-12-100-120 Hz). The purpose of this filter was to remove low-frequency deconvolution artefacts such that high frequencies were unaffected. Illustration of a shot record before and after preliminary processing is shown in Figure 54 and Figure 55.

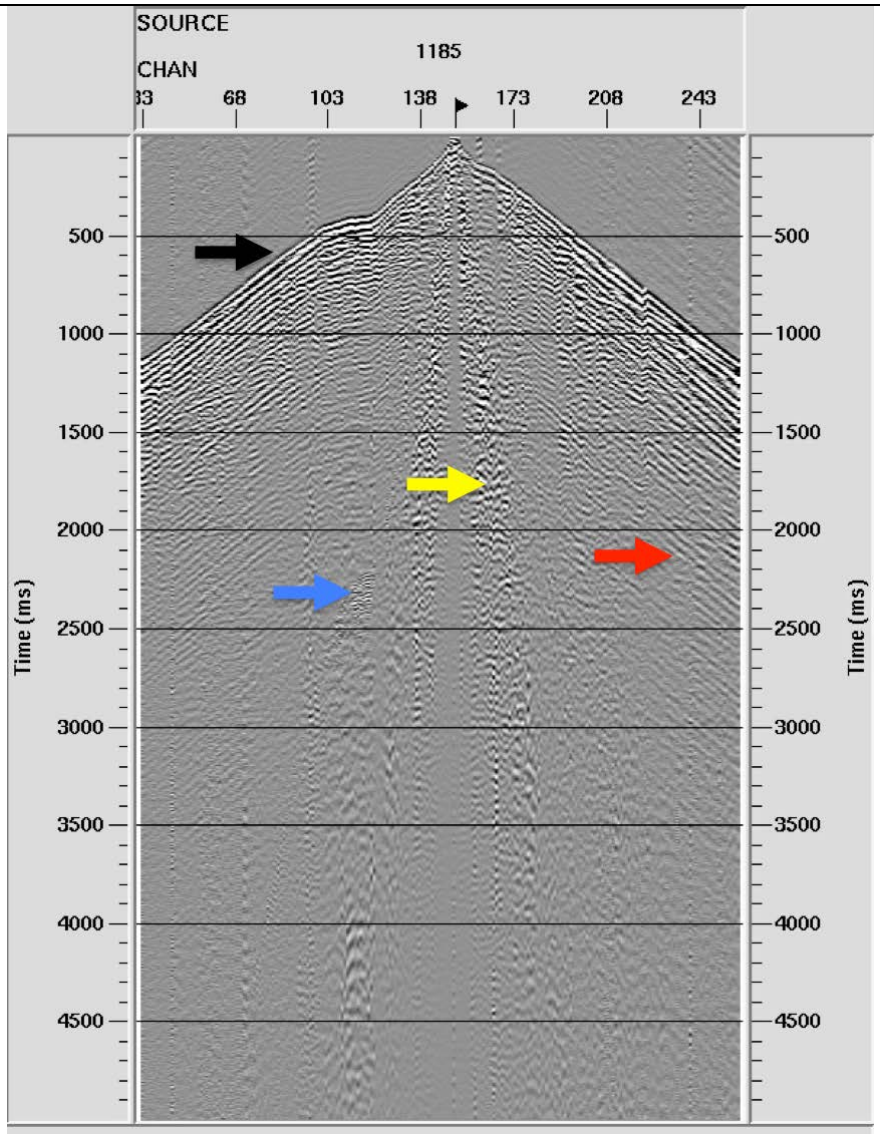


Figure 54 Raw shot gather: black arrow – refracted P-waves, yellow arrow-surface waves, red arrow-refracted converted waves, blue arrow-air blast.

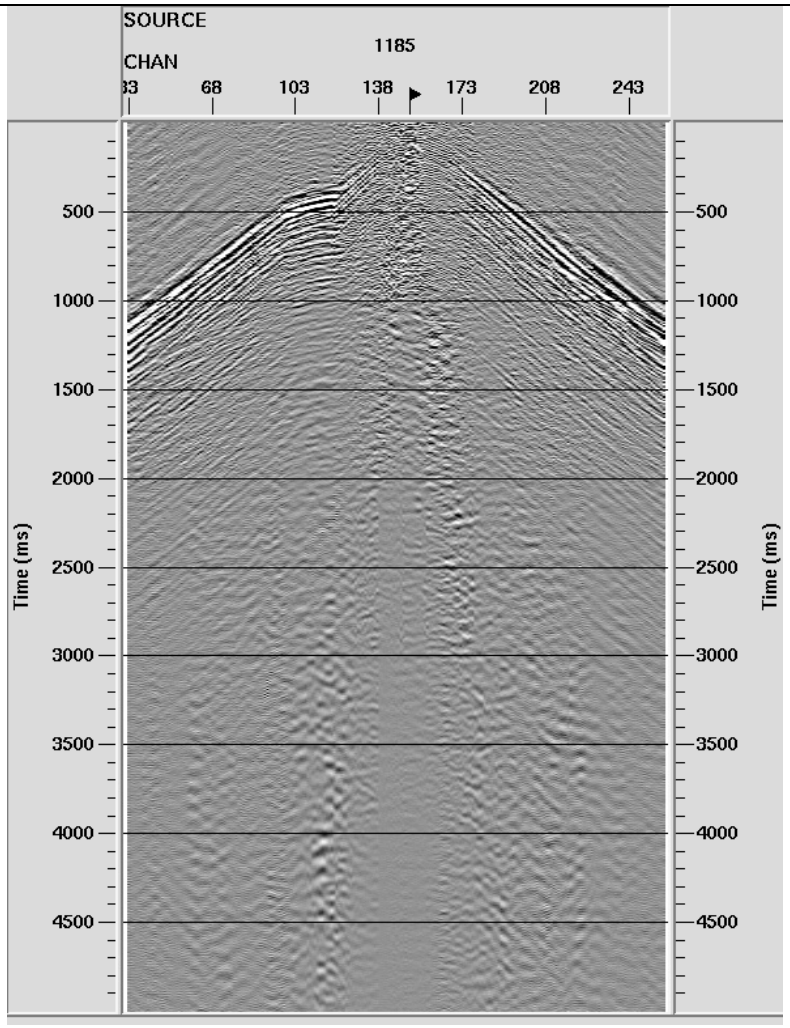


Figure 55 Pre-processed shot gather.

3.1.2. *Velocity analysis*

Velocity analysis, particularly semblance based interactive velocity analysis, requires further SNR improvement. For that purpose, the bandpass filter was temporarily narrowed to 8-14-50-70 Hz. This allowed us to reduce the contribution of random noise at the high end of the spectra. Further signal enhancement was achieved 3D super-gathers generation using 5 CDPs in the in-line direction, respectively. Two velocity analysis passes were performed. The initial velocity field was built upon the information provided by the 2D reflection seismic survey acquired in 2013. Regular offset distributions used for the 2D seismic profile enabled a reliable estimate of the initial velocity field. Hence, we used this velocity field as a guide. The 2D velocity field was subsequently extended to 3D space and refined to condition the data for residual static corrections. An example of the velocity spectra (semblance) or so-called interactive velocity (IVA) analysis is illustrated in Figure 56.

The second stage of the velocity analysis accounted for the dip-dependency of the stacking velocities after the application of a dip move-out correction (DMO). This field was subsequently utilised for stacking and post-stack migration. The same velocity field was also used for the initial PSTM run. In the first iteration, PSTM was conducted on a pre-processed dataset in the offset domain. Subsequent iterations of PSTM updated to build the final velocity field. This velocity field was utilised for the last PSTM run to produce the final seismic image.

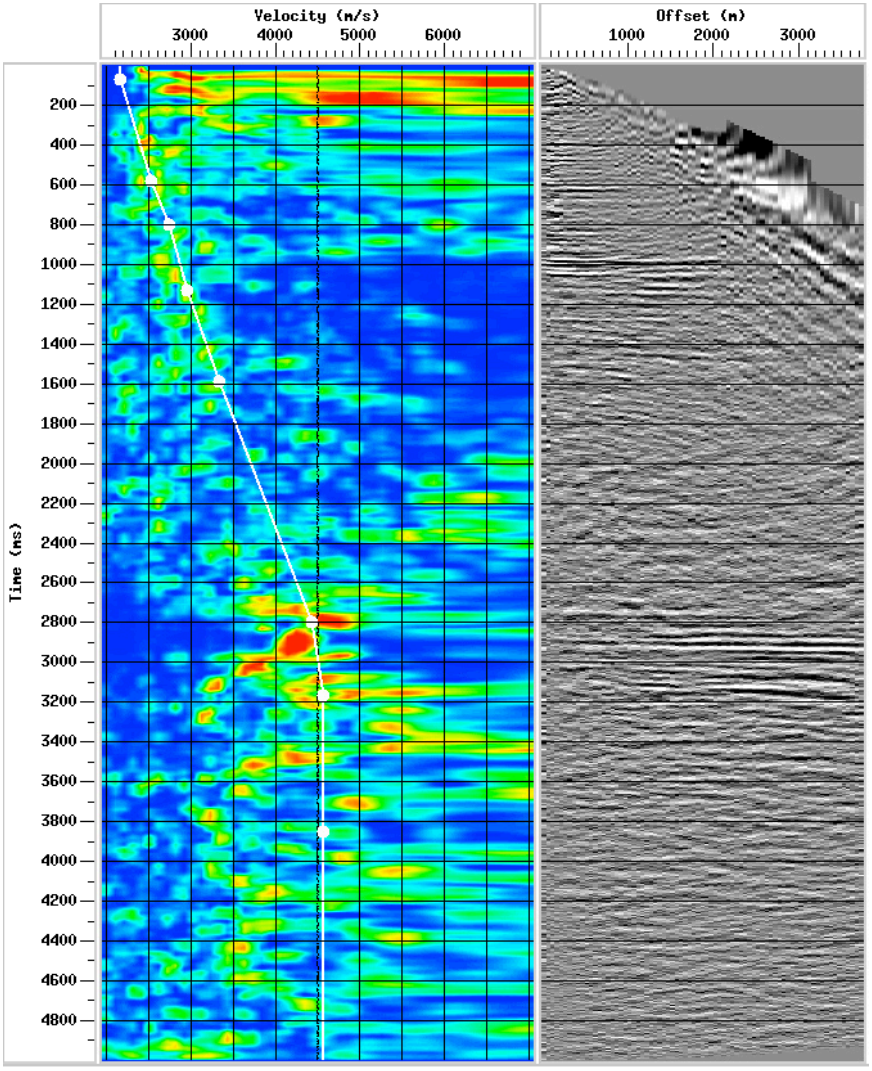


Figure 56 Interactive velocity analysis, semblance on the left, imaged gather on the right.

3.1.3. *Pre-stack time imaging*

The post stack migration flow is shown in Table 5. The key steps in this flow are the applications of DMO prior to stacking, and F-XY deconvolution after CDP stacking that enhance the signal significantly.

Table 5 Post-stack Migration Flow.

Procedure	Parameters
Data input	Pre-processed dataset
NMO Iteration I	Velocity field I (from legacy 2D survey)
DMO to Gathers 3D Iteration I	Offset binning: 25/50/2500
Velocity analysis	Compute velocity field II
NMO Iteration II	Velocity field II
DMO to Gathers 3D Iteration II	Offset binning: 25/50/2500
60% stretch mute	Post-NMO top mute
Band-pass filter	8-16-80-100 (HZ)
3D stack	Normalisation scalar 0.5
FXY deconvolution	Window 200/800ms
Post-stack migration	Velocity field II converted to interval velocities
Display Filters	8-16-70-90 (HZ)
Depth conversion	Velocity field II converted to average velocity
SEGY output	Standard SEG Rev1

The imaging using the Kirchhoff integral solution was applied on the pre-processed offset gathers, without a DMO correction. Typically, in the first pass of migration, many of the reflection events are not accurately imaged. This points to the errors in the initial velocity model that requires refinement of the velocity model in an iterative manner. Since our initial velocity model is already a reasonably good approximation of the true velocities, a single iteration is observed to be sufficient to produce the correct image gathers. Post-migration processes were applied to image gathers including the elimination of extrapolated migration swings and the application of a bandpass filter. The workflow for pre-stack migration is shown in Table 6. To reduce migration swings, an aperture of 30^0 and migration distance of 4000 m was used in pre-stack imaging. Final PSTM results are illustrated in Figure 57 - Figure 59.

Table 6 PSTM workflow.

Procedure	**Parameters**
Data input	Pre-processed dataset
Velocity datuming	Moving seismic and velocities to final datum
PSTM run I	Offset binning: 25/50/2500, aperture 30^0, distance 4000m.
Velocity analysis	Compute velocity field
PSTM Iteration I	Offset binning: 25/50/2500, aperture 30^0, distance 4000m.
60% stretch mute	Post-NMO top mute
3D stack	Normalisation scalar 0.5
FXY deconvolution	Window 200/800ms
SEGY output	Standard SEG Rev1

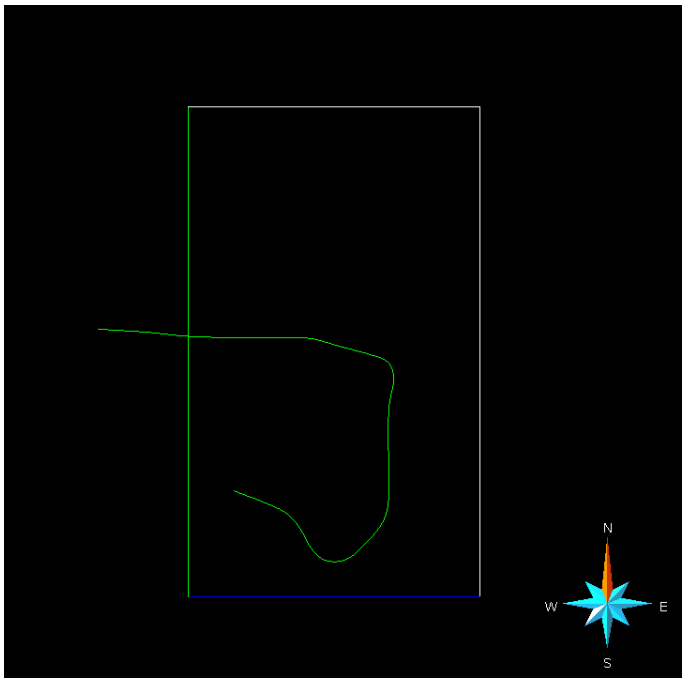


Figure 57 CDP arbitrary line embedded in regional Harvey 3D grid.

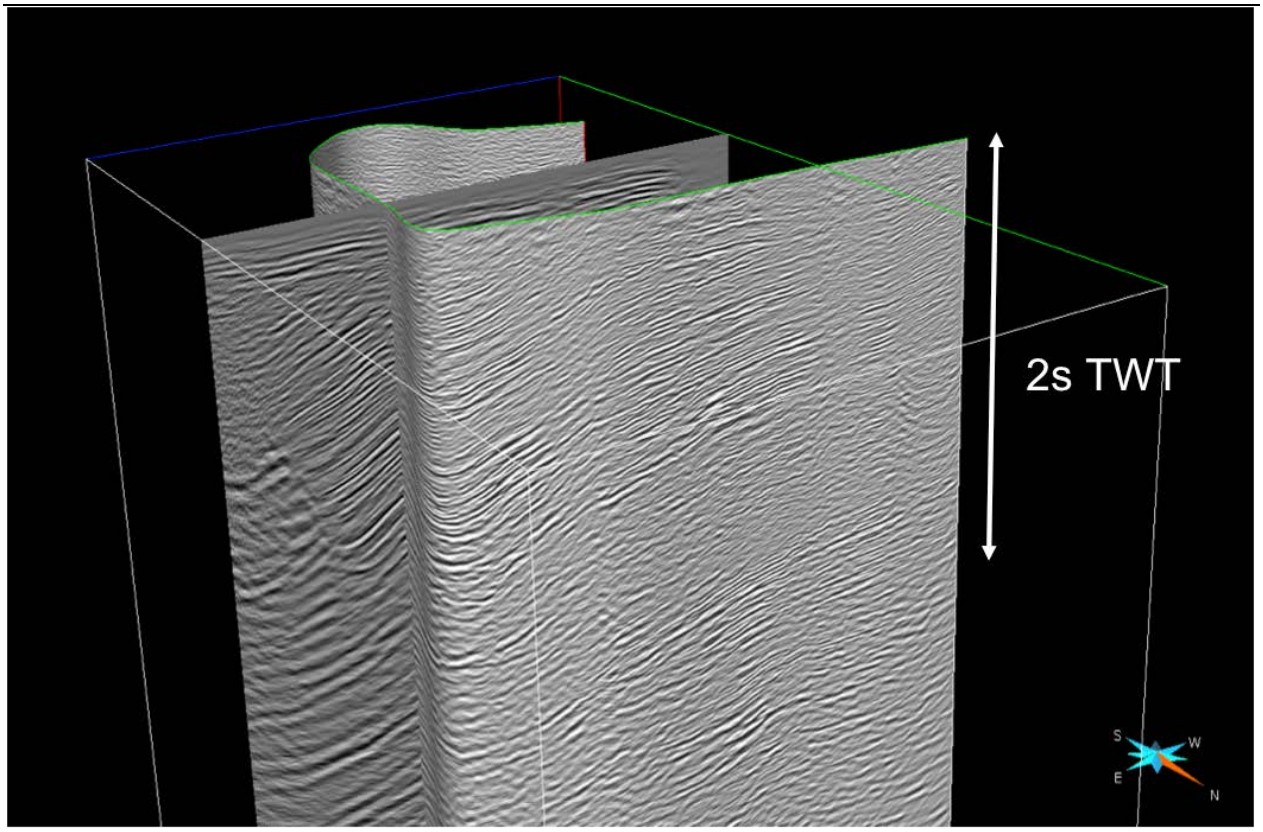


Figure 58 PSTM arbitrary section embedded in regional Generation 2 Harvey volume, view from NE.

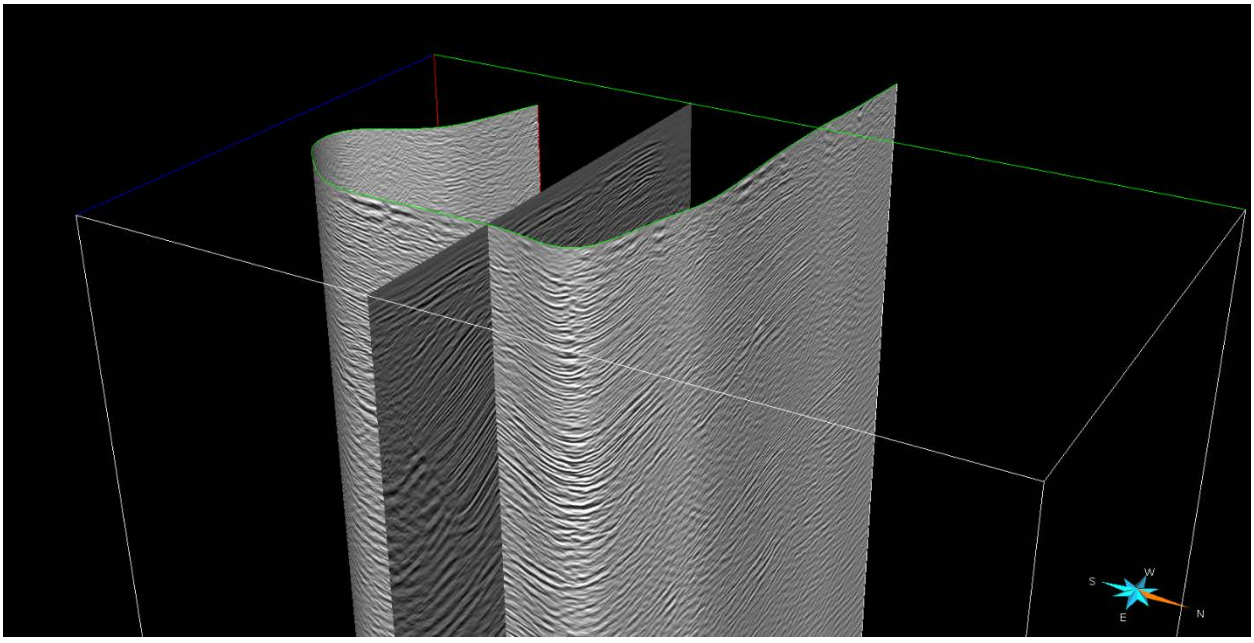


Figure 59 PSTM arbitrary section embedded in regional Generation 2 Harvey volume, view from North.

The intersection of PSTM images of the arbitrary line and Harvey 3D volume shows a good correlation (Figure 58 and Figure 59). The arbitrary image has a comparable resolution and reflectivity to the Generation 2 3D PSTM volume.

3.1.4. *Pre-stack depth imaging*

For many years, migration was the finishing step of the seismic processing sequence, feeding directly into maps of structure and stratigraphy. Nowadays, migration is much more likely to be an intermediate step, feeding information into other seismic processes. Migrated amplitudes re used for AVO analysis, velocity model building and for other forms of seismic attribute analysis.

Kirchhoff's integral solution to the wave equation was used for PSDM. It is capable of imaging reflected arrivals from 90^0 angles and beyond as turning rays. Kirchhoff migration allows direct ray-tracing in the velocity model and is robust enough to properly handle diverse geometries of different vintages.

Depth imaging of arbitrary line dataset was constrained by physical property measurements in the Harvey 1, 3 and 4 well drill logs, which significantly increased the accuracy of initial velocity model. The PSDM algorithm is illustrated in Figure 60.

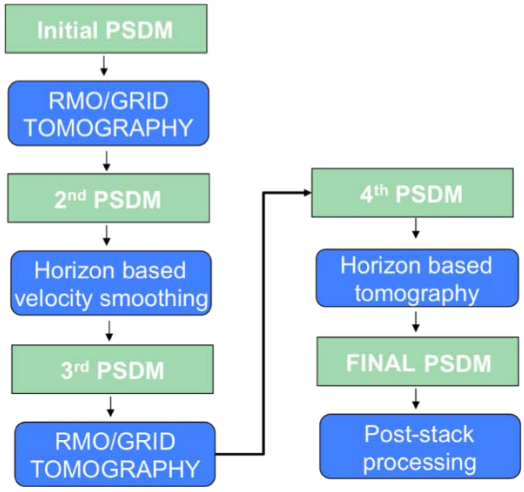


Figure 60 PSDM Flowchart.

The layer stripping method was used to perform residual move-out (RMO) followed by tomography. The method included parameterisation of velocity within each layer of the structural model as either constant interval velocity or a linear function. The velocity field was updated using PSDM gathers for a set of target horizons over the Project area. Residual depth delays at horizon boundaries for all layers were then extracted from the imaged gathers. Tomographic analysis methods were used for the final updates of velocity/structural model. The travel-time tomography projects the offset-dependent RMO along ray paths, joining the subsurface location and the source and receiver locations (Stork, 1992). Iterations of these analyses continued until the pre-stack depth gathers were flat for the horizon events (Figure 61).

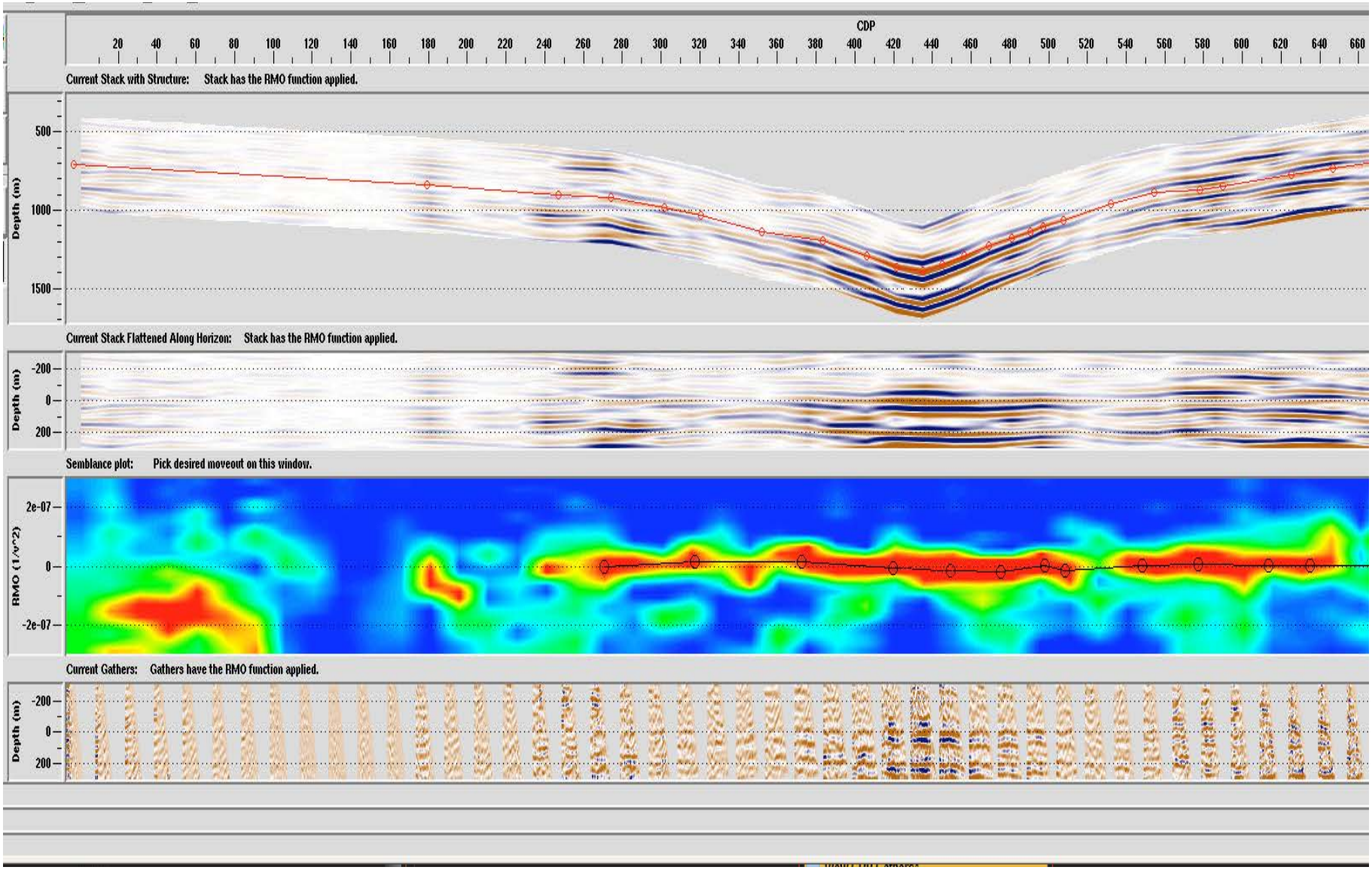


Figure 61 Layer striping of a horizons, showing picked horizon, flatten horizon and RMO picks over semblance plot

The last iteration of RMO application and tomography produced the final velocity model, Figure 62.

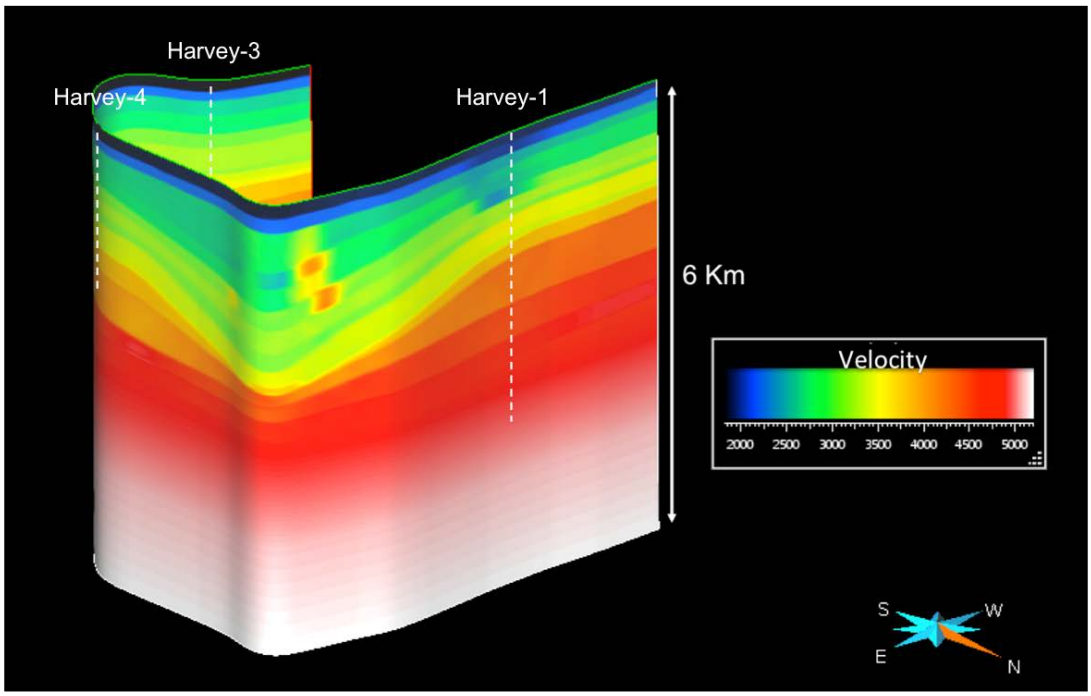


Figure 62 Final velocity model from PSDM workflow.

The VSP and sonic logs from the wells were used to constrain the initial velocity field used in PSDM process. The comparison of final PSDM velocity and velocities from wells are illustrated in Figure 63. By construction, the PSDM velocities are, on average, consistent with VSP and well log velocities, but smoother than VSP velocities. This is because VSP velocities were obtained from direct waves, which were densely sampled in depth and retained higher frequencies due to one-way propagation.

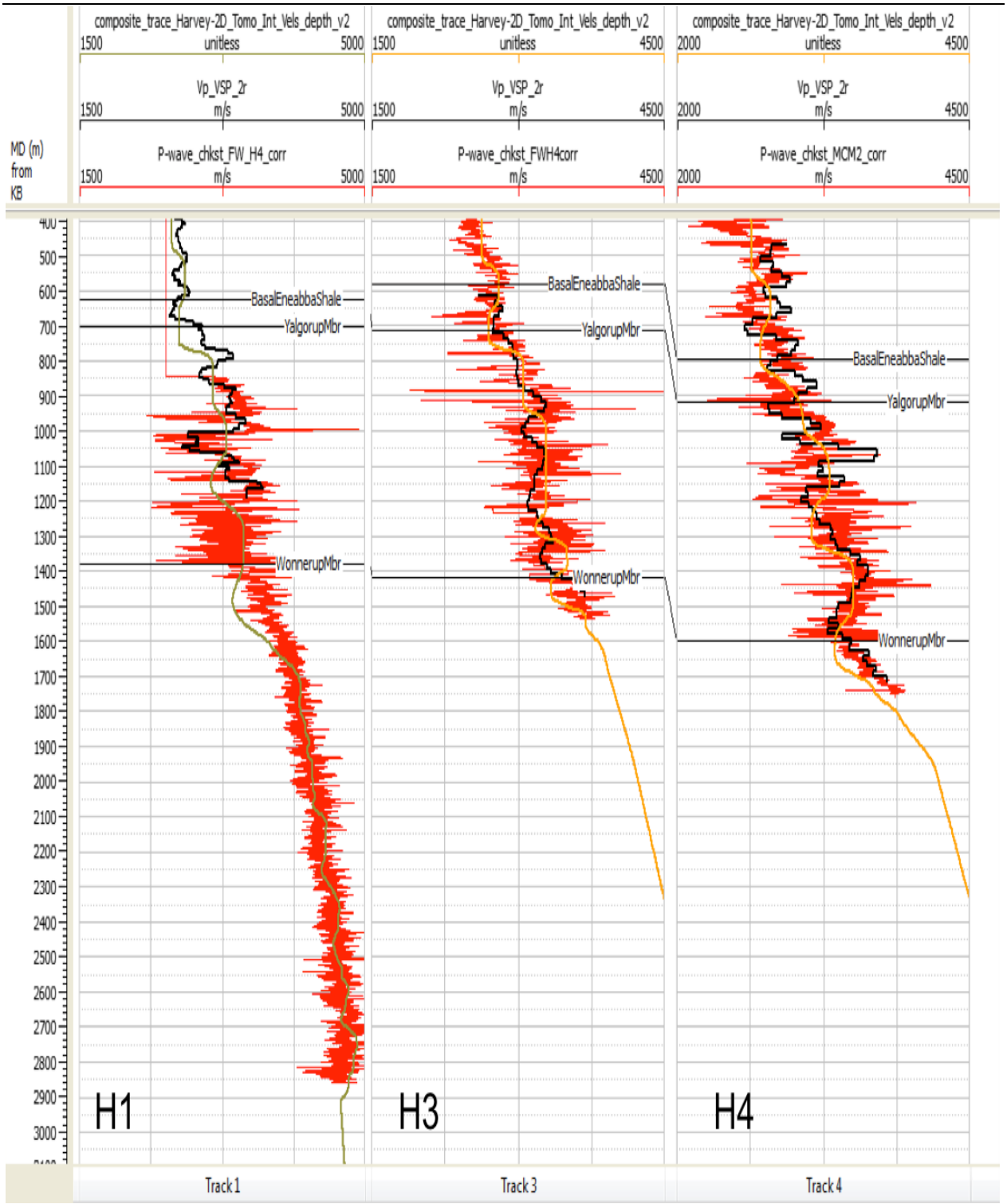


Figure 63 Comparison of velocities: PSDM (brown), VSP (black) and LOG (red).

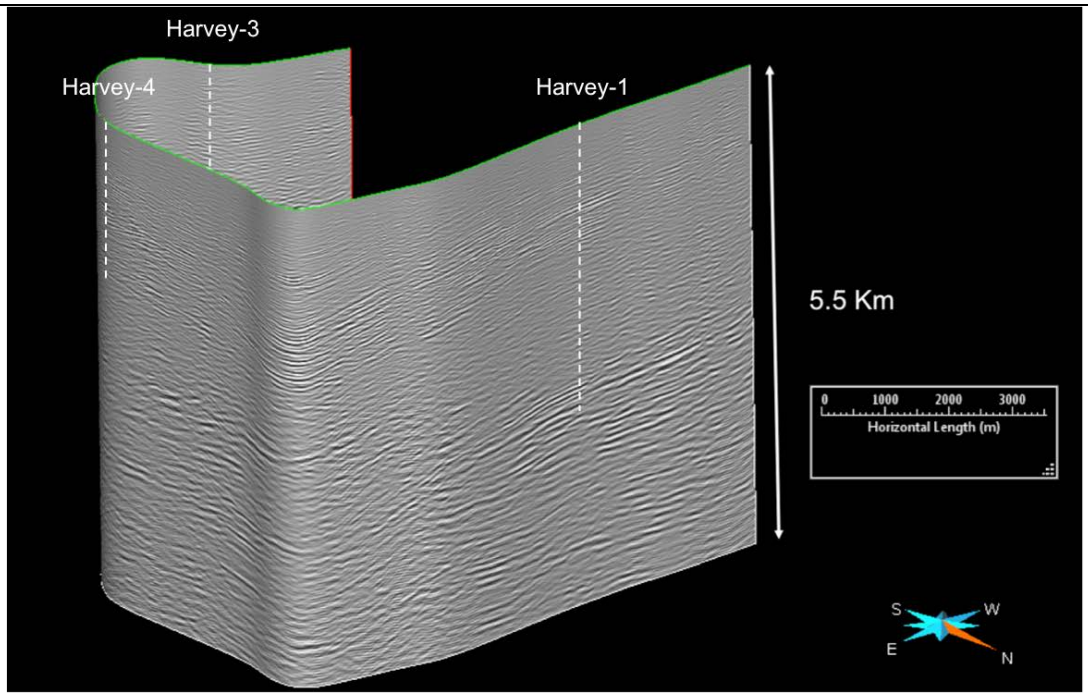


Figure 64 Final imaged section from PSDM workflow.

The resulting image from the PSDM process is illustrated in Figure 64. Both PSDM results (velocity and the image) are expected to be of a strategic importance for the containment studies, development of the dynamic model and establishment of the injection.

3.1.5. *Conclusions*

The motivation for building an arbitrary line from existing 2D and 3D data in Harvey area was its proximity to existing wells: the Harvey 1, 3 and 4 wells. With the advantage of relatively regular fold/offset distribution of 2D seismic and the availability of downhole property measurements, it was expected that depth imaging would achieve a high-resolution with a more accurate velocity model that would be used in QI. The resulting final velocity model shows a good correlation with both velocity measurements from wells and velocities from surface seismic. The intersection of final arbitrary seismic image with 3D seismic volume shows a good correlation.

3.2. Reprocessing of Harvey 3D – Generation 2 volume

The Harvey 3D regional survey was shot in 2013 over approximately 100 km^2 to characterise the future CO_2 sequestration site. Unfortunately, environmental restrictions and lack of land access permissions created many obstacles and which resulted in "no data" zones. This created a problem for characterisation of the reservoir and uncertainties with the static model. Although the large 3D survey has undergone a number of iterations of processing (Pevzner et al., 2015) there is room for improvement, including attempts to improve seismic coverage of the poorly covered zones, which might improve the reservoir characterisation. This is the motivation for reprocessing of data and creation of Generation 2 Harvey 3D volume.

The Generation 2 processing flow included:

1. Data validation

2. Geometry validation/correction/application/QC

4. Automatic Refraction Statics Calculation and Application

5. Model Based Noise Attenuation

6. Random noise Attenuation trace editing/spatial filtering

7. Deconvolution

8. True relative amplitude recovery

9. First Velocity Analysis

10. Residual Statics

11. Second detailed Velocity Analysis

12. Data regularisation, interpolation and non-stretch NMO

13. PSTM (with and without AGC)

14. CDP stack and Post-stack processing

15. Time-depth conversion

16. SegY output (time and depth)

Model-Based Noise Attenuation (MBNA) is principally a noise analysis followed by a subtraction process. The data acquired in this Project contain significant amount of unwanted coherent noise the main components of which are ground roll and air-blast. In this process, the noise was both analysed and then separated from the original record in the shot domain. The separation was implemented by isolating the wave number and frequency characteristics of the coherent noise in contrast to the primary energy. This would produce a residual template from which a final separation can take place. In this phase, windowed mean amplitudes were calculated, and where amplitudes of samples exceed a user-specified ratio to the mean, those amplitudes were modulated and output to a final template. All amplitudes of samples that are smaller than the mean of the user-specified ratio were not allowed to pass to the final template. It was this final template that was then used to perform a direct subtraction from the original input shot. The MBNA process has significantly increased the reflectivity of the generation 2 data especially in the top 1s of TWT.

To address the problem of the variable fold of coverage and offset distribution within the 3D bins, acquired data was regularised by the implementation of the following process.

Firstly, traces within input ensembles were assigned to a user-specified grid in which the offset range and increment is based on the original acquisition geometry. Within each bin and offset compartment, over or under population may occur. Following this procedure, it is likely that some bins within individual offset volumes will be empty. For the second step of the regularization procedure, these holes were filled using an interpolation procedure. Empty bins were automatically identified and then infilled using a local tau-p trace interpolation. Original data in occupied bins is unchanged by this step. Furthermore, to achieve the maximum use of recorded data non–stretch NMO was used to minimise the mute at far offsets. The process has significantly reduced gap size in the “no-go” areas and improved the overall resolution, Figure 68 and Figure 69.

3.2.1. *Pre-stack time imaging*

Due to geological complexity, conventional DMO correction followed by post-stack migration was insufficient to handle the lateral changes in the velocity field. Therefore, a pre-stack time migration was attempted to aid in handling the complex velocity field. The basic steps in the 3D pre-stack time migration workflow are illustrated below.

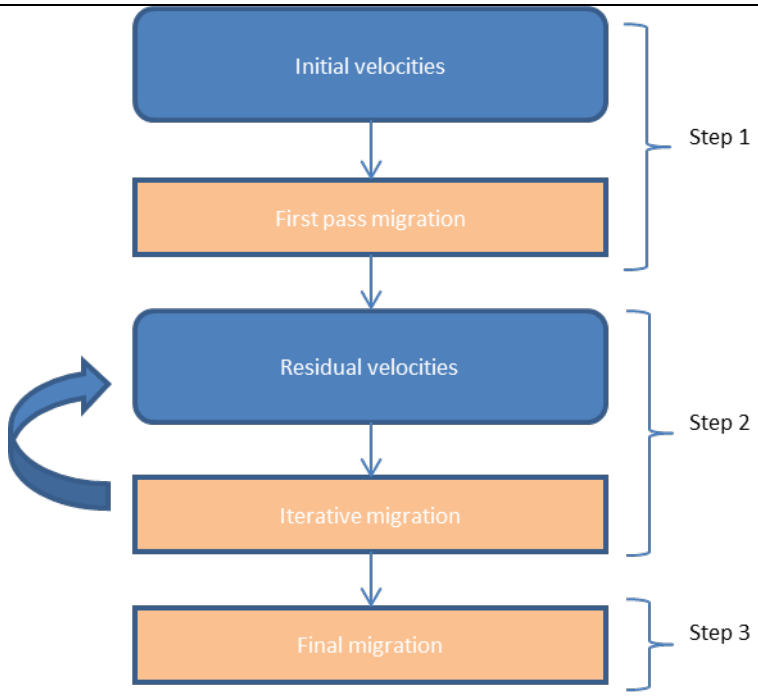


Figure 65 Isotropic pre-stack migration algorithm.

- Step 1: The construction of velocity model from downhole information and 1st pass of pre-stack time migration;
- Step 2: The residual velocity model modification, using subsequent iterations of pre-stack time migration;
- Step 3: The final migration;

Step 1 involved the building of the initial velocity model followed by the first iteration of pre-stack time migration. Typically, some of the reflection events in the imaged gathers produced by the first pass of migration were not properly imaged. This suggests errors in the initial velocity model, which required updates to properly image the gathers.

Step 2 used one or more iterations of residual velocity analysis on image gathers. The residual velocity error, or move out, was determined by analysis of the gathers. This analysis proposed the changes to the original velocity model that imaged the gathers more precisely. Once the velocity model was updated it was once more used in the pre-stack time migration to produce revised image gathers. These gathers were once again analysed and, if additional correction was required, the velocity updating process was repeated, as shown in the Figure 66.

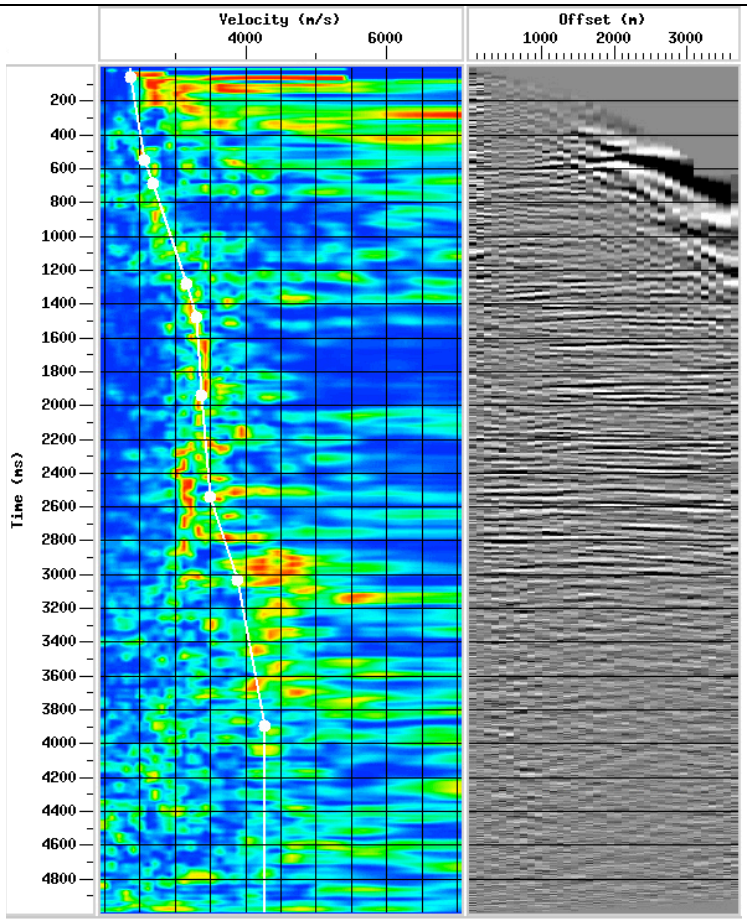


Figure 66 Residual velocity analysis of imaged gathers.

Upon achieving satisfactory imaging of the gathers, Step 3 was performed. This step involves pre-stack time migration of the full dataset using the final velocity model. After the final migration, several post-migration processes were applied to the data. These include radon filtering, scaling and calibration of the volume to tie at known well markers.

Good results were achieved using the velocity model from image gathers in the final migration. The final step in the seismic data processing was to use the information from well logs to convert the seismic volumes from two-way travel time to depth. Comparison of PSTM volumes of original processing and Generation 2 volumes is illustrated in Figure 67. The reflectivity is greatly improved in the top 1s of TWT, as well as the resolution and the clarity of faults.

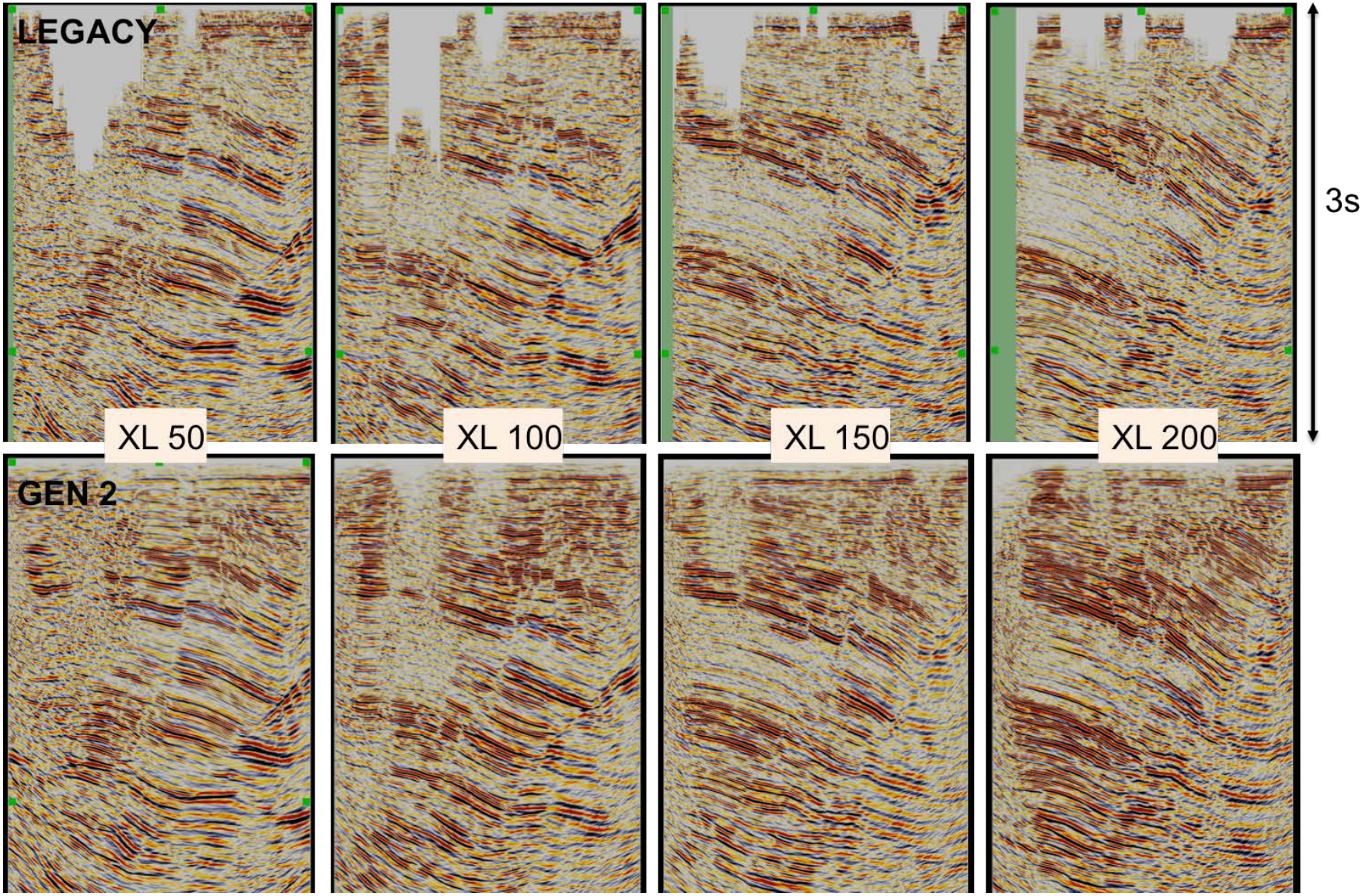


Figure 67 Original PSTM volume (top), Generation 2 PSTM volume (bottom). The illustration of 4 cross-line sections, before and after reprocessing.

The time slices below also confirm enhanced reflectivity, increased SNR and successful implementation of data interpolation.

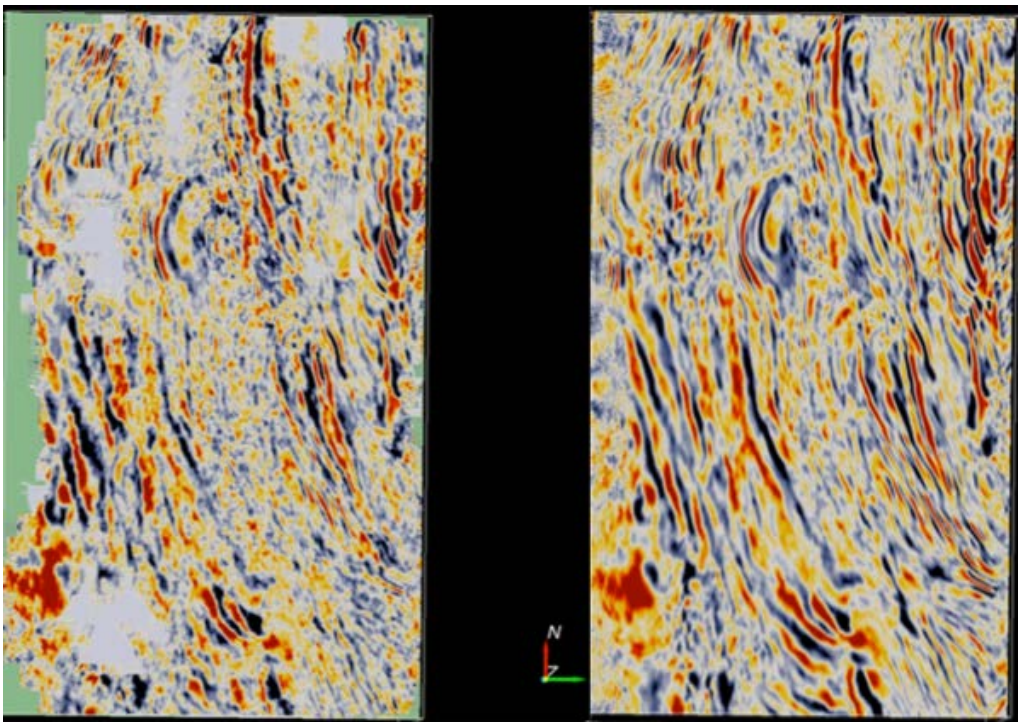


Figure 68 Time slice 750 ms. Original Harvey PSTM volume (left) and Generation 2 Harvey PSTM volume

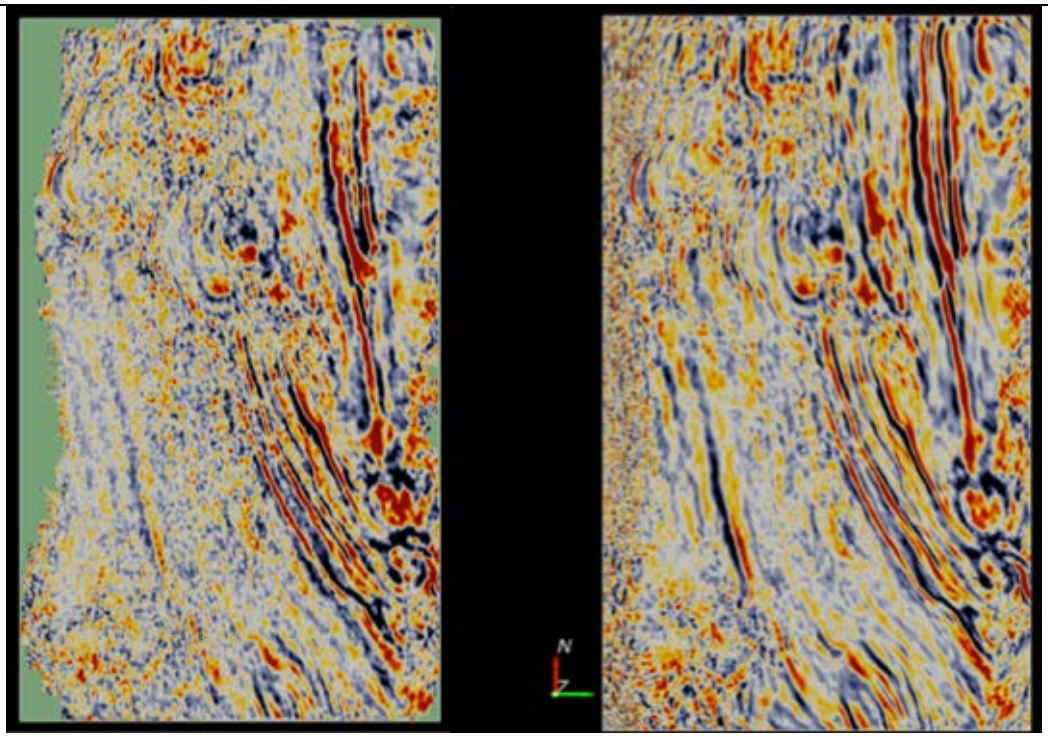


Figure 69 Time slice 1400 ms. Original Harvey PSTM volume (left) and Generation 2 Harvey PSTM volume (right).

3.2.2. *Velocity model building using PSDM on Generation 2 Harvey data*

In the past, compromises were made because of limitations in computing power and the need to generate a timely result. The algorithms used in the previous processing tended to include initial post-stack time migration methods that are not capable of fully accommodating lateral velocity variations. Time-migration is a process, which collapses diffractions and moves dipping events toward the true position. It assumes that the diffraction shape is hyperbolic and ignores ray bending at velocity boundaries of non-horizontal layers. It is fast and resistant to errors (sometimes up to 10%) in the velocity model (Stewart 2015).

Depth migration has the potential to compute the correct diffraction shape assuming that the initial velocity model is correct. Pre-stack depth migration has potential to provide an error estimate of the migrated result. Depth imaging typically takes ten times longer to run than time migration and is sensitive to small velocity errors, i.e. required to be within 1% (Stewart 2015).

The area of investigation is southern half of the full Harvey 3D survey, covering the existing well locations, Figure 70. The primary aim of PSDM is to build an accurate velocity model.

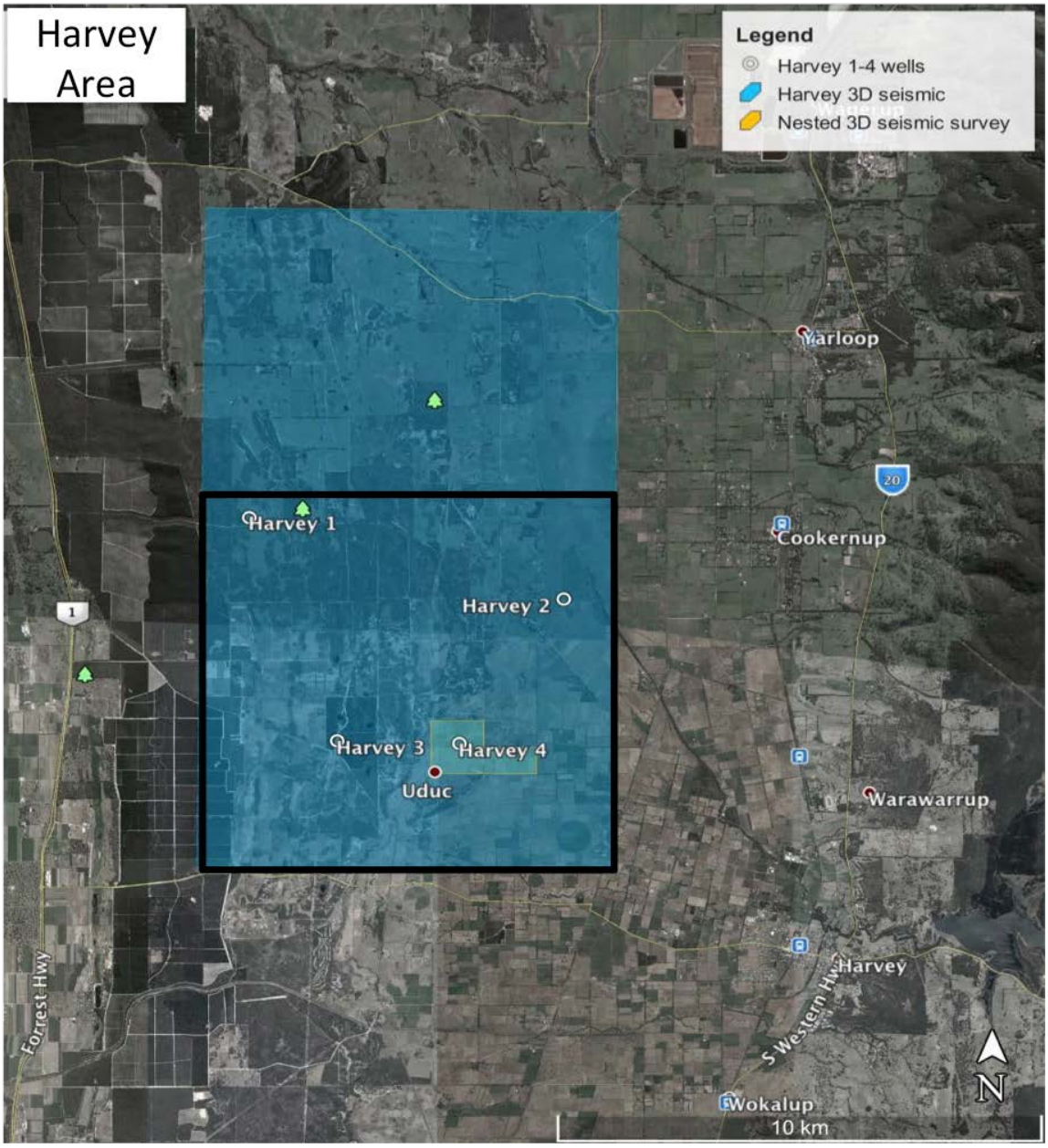


Figure 70 Harvey the large 3D survey area. Highlighted in a black line is area under investigation (PSDM).

Ray based Kirchhoff's integral solution to the wave equation was the algorithm used for PSDM. It is the most widely used depth imaging technique in the industry, capable of imaging reflected arrivals from 90^0 angles and beyond as turning rays. Kirchhoff migration allows direct ray-tracing in the velocity model, which can generate more accurate travel times and therefore improve the positioning of the image. It is robust enough to handle fold/offset variations in the survey.

The initial velocity field for PSDM was constrained by physical property measurements and VSP velocities from the Harvey 1, 2, 3 and 4 well logs, which significantly increased the precision. The PSDM algorithm further included RMO picking along existing horizons and tomography to achieve

final updates of velocity/structural model. The horizons used for velocity model building are illustrated in Figure 71.

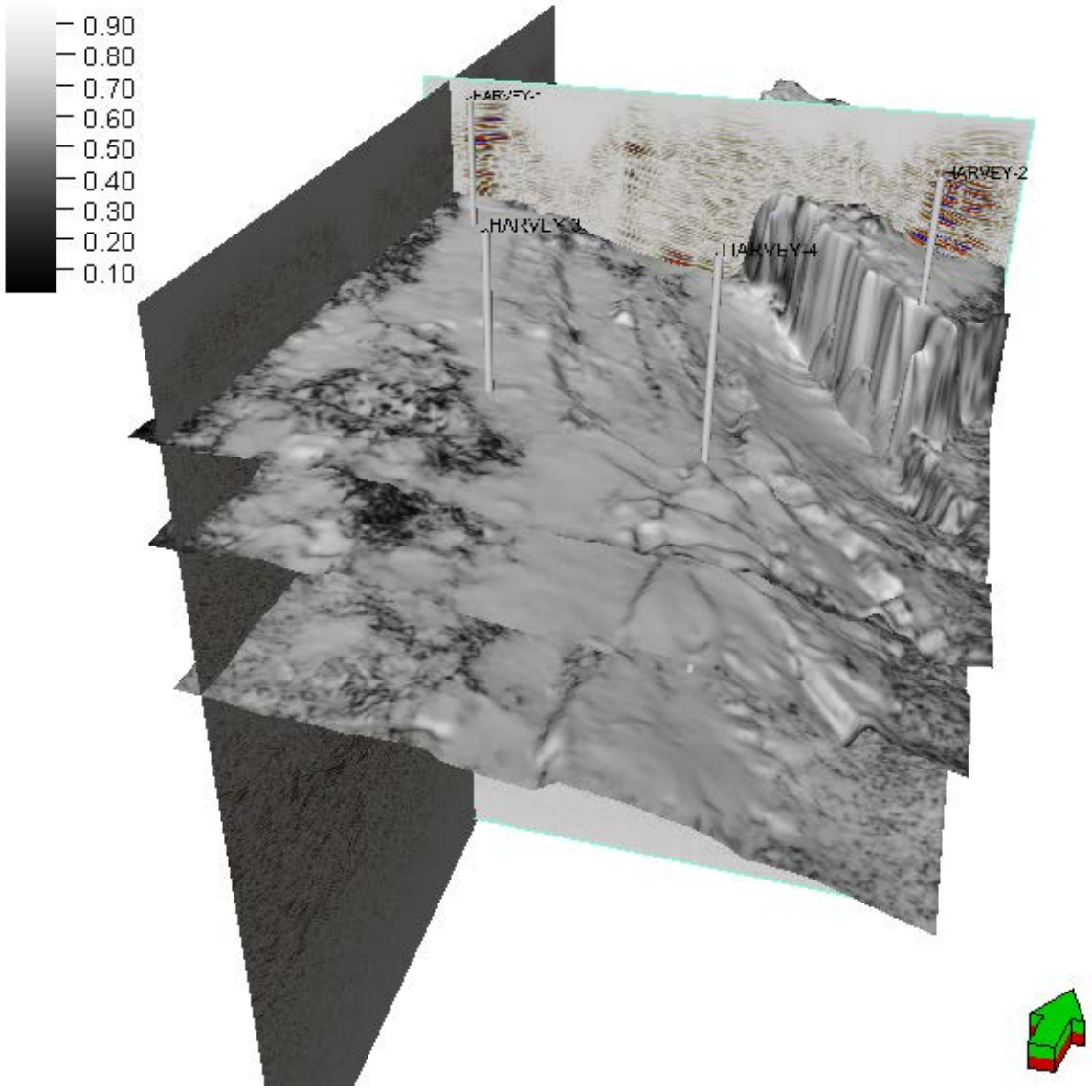


Figure 71 Horizons picked on Generation 2 volume with colour corresponding to average similarity. Yalgorup (top), Wonnerup (middle) and Sabina (bottom) horizons.

With tomography updates, the velocity estimation process was finalised, and the final velocity model was ready to be used for seismic inversion and interpretation.

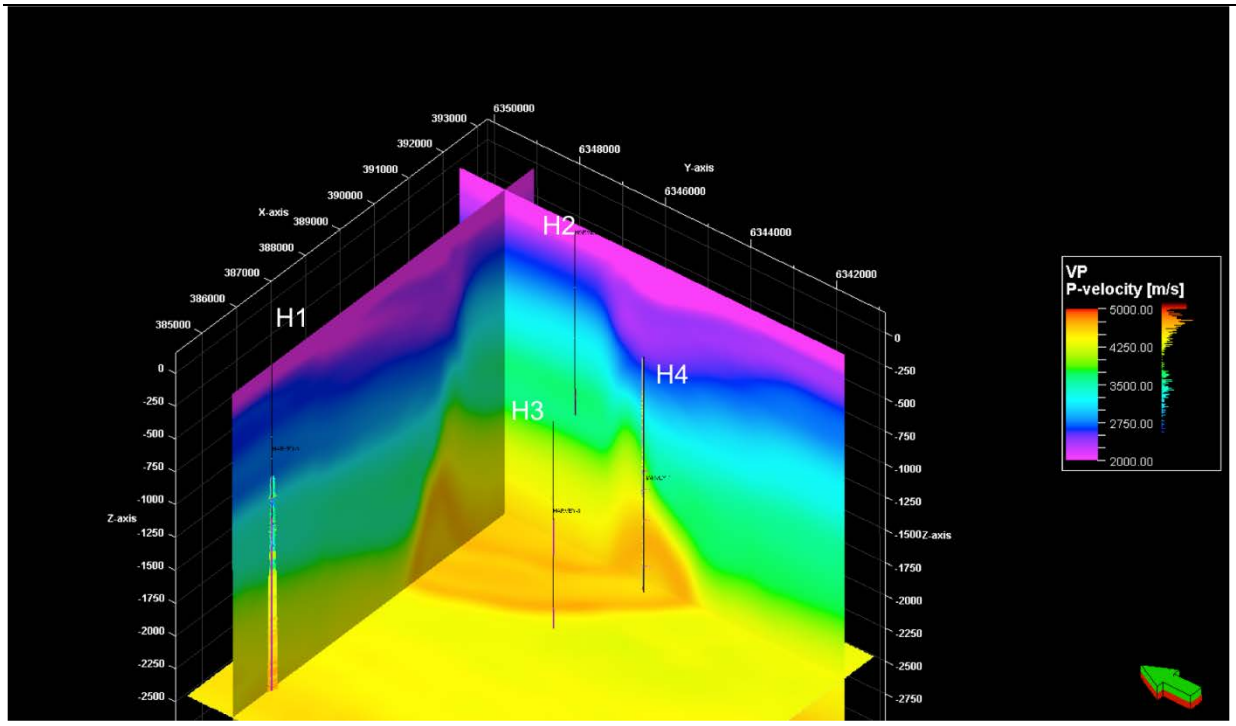


Figure 72 Final velocity model from 3D PSDM, with highlighted positions of existing wells.

3.2.3. *Conclusions*

Reprocessing of Harvey data was challenging due to highly irregular offset/fold distribution. For this reason, preserving relative amplitudes was an even more difficult task. Nevertheless, with proper offset regularisation techniques in place, combined with the SNR and velocity improvement, the reprocessing produced very good quality images. Preserved relative amplitude volume was created for stratigraphic interpretation, well tie and subsequent AVO analysis. Amplitude balanced volume was produced as a preferred product for the structural analysis.

A comparative analysis is conducted between generation 2 PSTM data cube against to the original Harvey PSTM volume. The improvements in Generation 2 cube manifest themselves in higher resolution, reflection strength and continuity. Faults are clearer and more obvious. More specifically, Generation 2 processing included further whitening of the amplitude spectrum, which improved vertical resolution. Advanced de-noising techniques made final image clearer. Velocity improvement made structures in the final image sharper. Interpolation techniques have brought more information in “no go” zones. Where the information could not be recovered the data retains its noisy character.

The fault detection cannot be fully achieved with the low-resolution seismic data in shallow depths. Therefore, it is recommended that high-resolution surveys, similar to the the Harvey 3 and Harvey 4 nested 3D surveys were considered where future drilling or injection is to take place. A good result was achieved after merging nested surveys over the Harvey 3 and Harvey 4 wells and Generation 2 volume. This retained the resolution of nested survey and coverage of regional 3D Harvey survey.

Downhole property measurements and VSP was used in the PSDM process to obtain accurate velocity volume in the southern half of Harvey 3D survey. Although the 3D velocity model lacked resolution in comparison with arbitrary line velocities, the model covered a larger area and is considered to be useful for the quantitative interpretation process. Perhaps the most promising application of depth imaging in a complex geological environment is the application of interpretational knowledge and skills during the velocity-estimation process. This process requires a geological aspect to accompany the seismic analysis, giving us the opportunity to target drilling activities more accurately.

4. Stochastic AVO Seismic Inversion along the Composite Line

While a deterministic inversion technique obtains an optimal solution of the inverse problem, the stochastic inversion technique attempts to describe the potential variability of the inverse solutions. Unlike deterministic inversion, therefore, a stochastic inversion does not provide a single 'optimal' solution. Multiple realisations of the subsurface impedance are generated, the synthetic from which all tie the seismic as well as honouring both the well data, the statistical properties of the impedances as well as any spatial model constraints. Given a sufficient number of realisations, an average of these solutions is close to the deterministic or best estimate inversion. (Simms and Bacon 2014).

The main reason for using AVO inversion was that it makes the prediction of the lithology and properties more informative due to using an additional shear velocity component. The Wonnerup Member of the Triassic Lower Lesueur Formation is the potential reservoir with a predominantly sand lithology, and the Yalgorup Member of the Triassic Upper Lesueur Formation is the potential seal and is characterised by the presence of a sand and shale lithology. These two members are the main focus of the AVO inversion with lithology prediction of the shale and sand. Porosity prediction of sand for the potential reservoir for CO_2 injection is another objective.

Ideally AVO inversion should be performed on the 3D seismic cubes. However, the patchy geometry and the offset distribution in the large survey and limited offset ranges in the nested survey made such approach inapplicable. The best that could be done on the large 3D cube is stochastic poststack acoustic inversion. This is discussed in the next chapter. Here, we instead attempt to perform a stochastic AVO inversion on the composite 2D seismic line (Figure 50) described in section 3.1.

Three 2D volumes were produced in the inversion: (1) Probabilistic lithology prediction of the sand and shale, (2) Sand porosity predictions calculated from velocity, and, (3) Sand porosity prediction calculated from P-Impedance (Figure 84, Figure 87, and Figure 89).

Additionally, a 3D pseudo-porosity cube was calculated using 3D high-resolution PSDM velocity cube (Figure 90).

4.1. Workflow and data conditioning.

HampsonRussell CGG software was used for inversion and DUG (DownUnder GeoSolutions) Insight software was used for seismic interpretation, pre-processing and data conditioning for the AVO inversion.

Full-stack two-way time seismic section along the composite line was used in the interpretation of the three horizons, which were tied to the Harvey 1 well (Figure 73). The Harvey 3 and the Harvey 4 wells are 300 m to 450 m away from the line respectively, and were not used in the inversion process. The Harvey 3 well was considered to be the blind well for the lithology prediction (Figure 84).

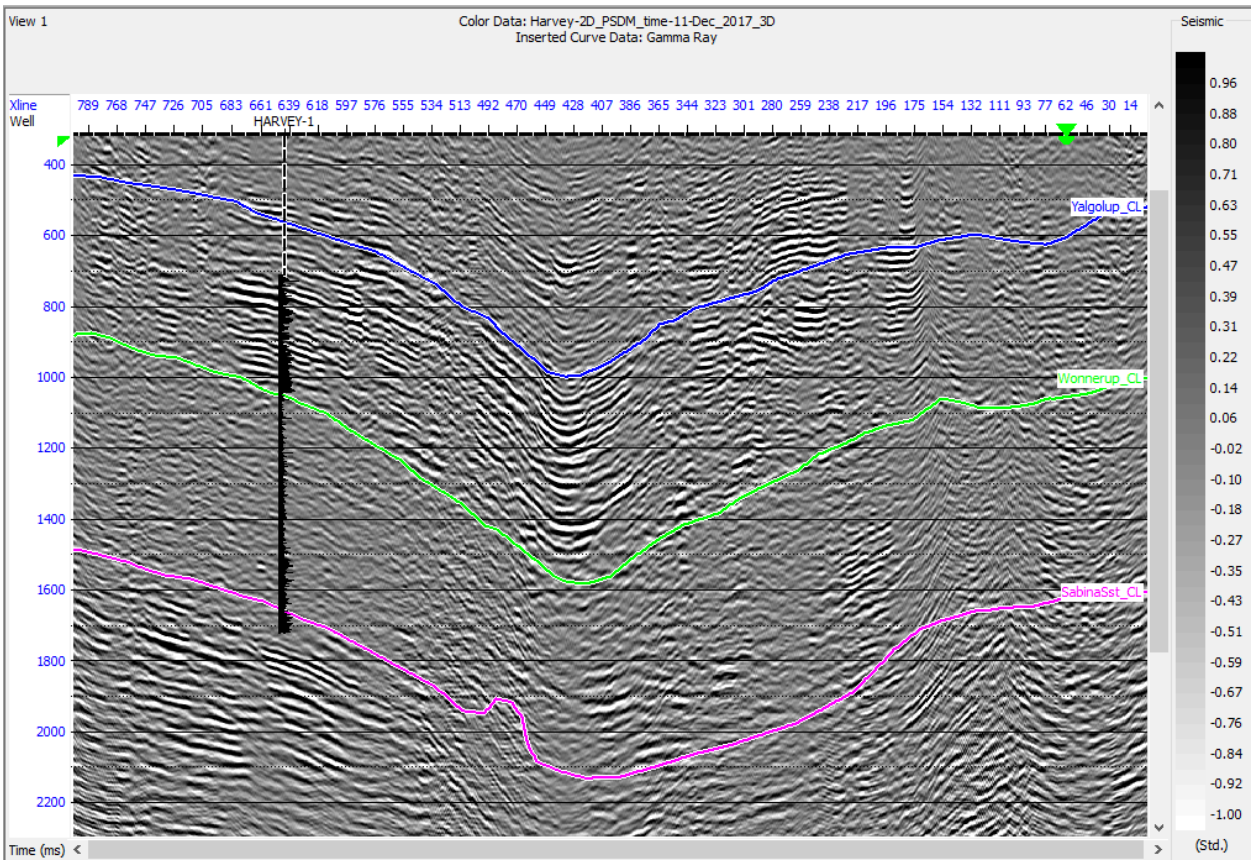


Figure 73 Full-stack two-way time composite seismic line with the interpreted horizons and the Harvey 1 well over imposed with gamma ray log. Three horizons are Near Top Yalgorup Member - blue, Near Top Wonnerup Member – green an Near Top Sabina Sandstone - pink.

Workflow:

Processing and conditioning of the seismic data:

1. Residual moveout removal (RMO).
2. Muting
3. Creating supergathers

AVO inversion:

1. Extracting the statistical wavelet.
2. Well correlation.

3. Initial model Building.
4. Inversion analysis.
5. Calculating the P-impedance and • V_P/V_S volumes.
6. Computing conditional probability of the lithology prediction using Bayesian classification scheme.
7. Porosity prediction.

RMO is the process that flattens gathers by aligning peaks and troughs horizontally. RMO parabolic correction was applied to the gather offset volume by calculating shifts every 50 m.

Inner – 10-degree and outer – 35-degree mutes were applied for the angle gathers. A surgical mute was also applied to minimise the effect of the ground roll (Figure 74).

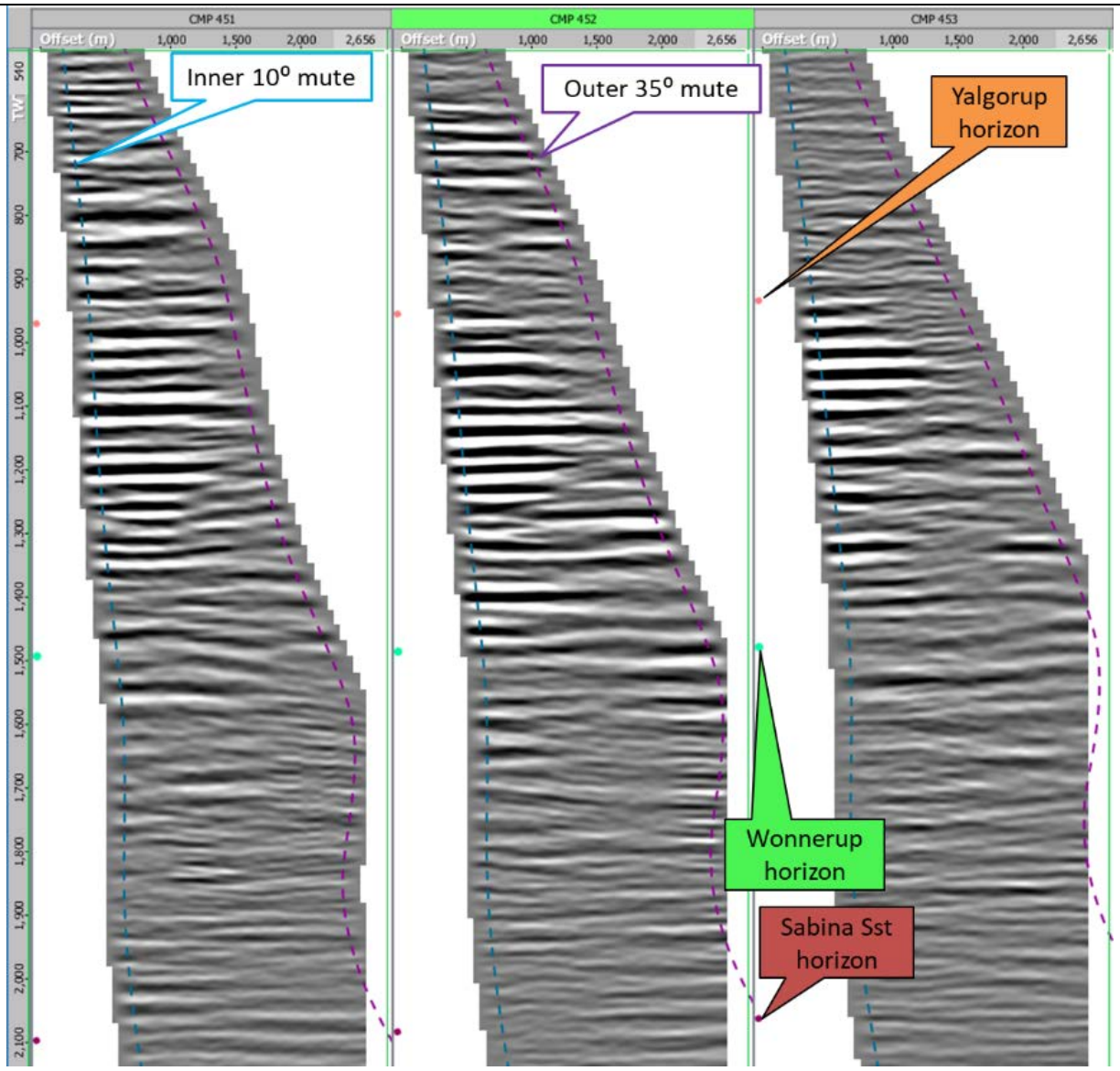


Figure 74 Finally processed and conditioned gathers used for the composite line AVO inversion (CMP 447, 452 and 457).

Supergathers were created for five angles; 15, 19, 23, 27 and 31 degrees using mean calculation.

4.2. Data QC and Well to Seismic Tie.

The Harvey 1 well logs were used in well correlation. Two angle-dependant statistical zero phase wavelets were extracted from the supergathers for the angle range of 13-23^0 and 23-33^0. These wavelets were used for the AVO inversion. Wavelets were extracted along the single trace closest to the Harvey 1 well within top Yalgorup and base Wonnerup Members (Figure 75).

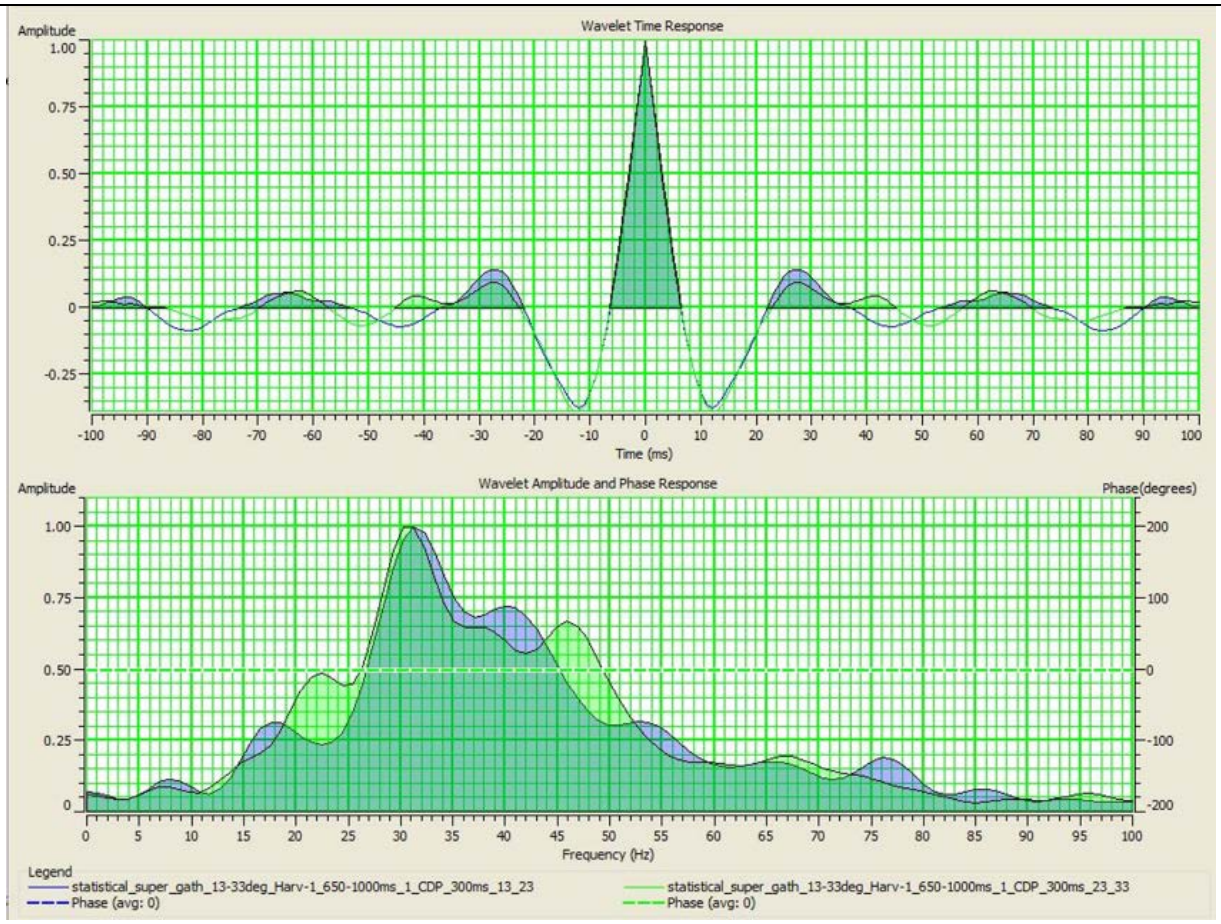


Figure 75 Two angle-dependant statistical wavelets were extracted from the super gathers. Wavelet length is 300 ms. Blue is for 13-230 and grin is for 23-330

Time to depth conversion of the Harvey 1 well to seismic was achieved with the combination of the check-shot survey 0-1189 MDKB and sonic log data 1208-TD MDKB. The best seismic to the well tie was achieved with a bulk time shifting -41 ms of the logs using zero-offset synthetic. (Figure 76). Good correlation of the well logs to seismic was observed in the upper part of the Yalgorup Member. In the lower part, the correlation was poor, probably due to wash-outs in the shaly section of the lower part of the Yalgorup, which made the density log noisy.

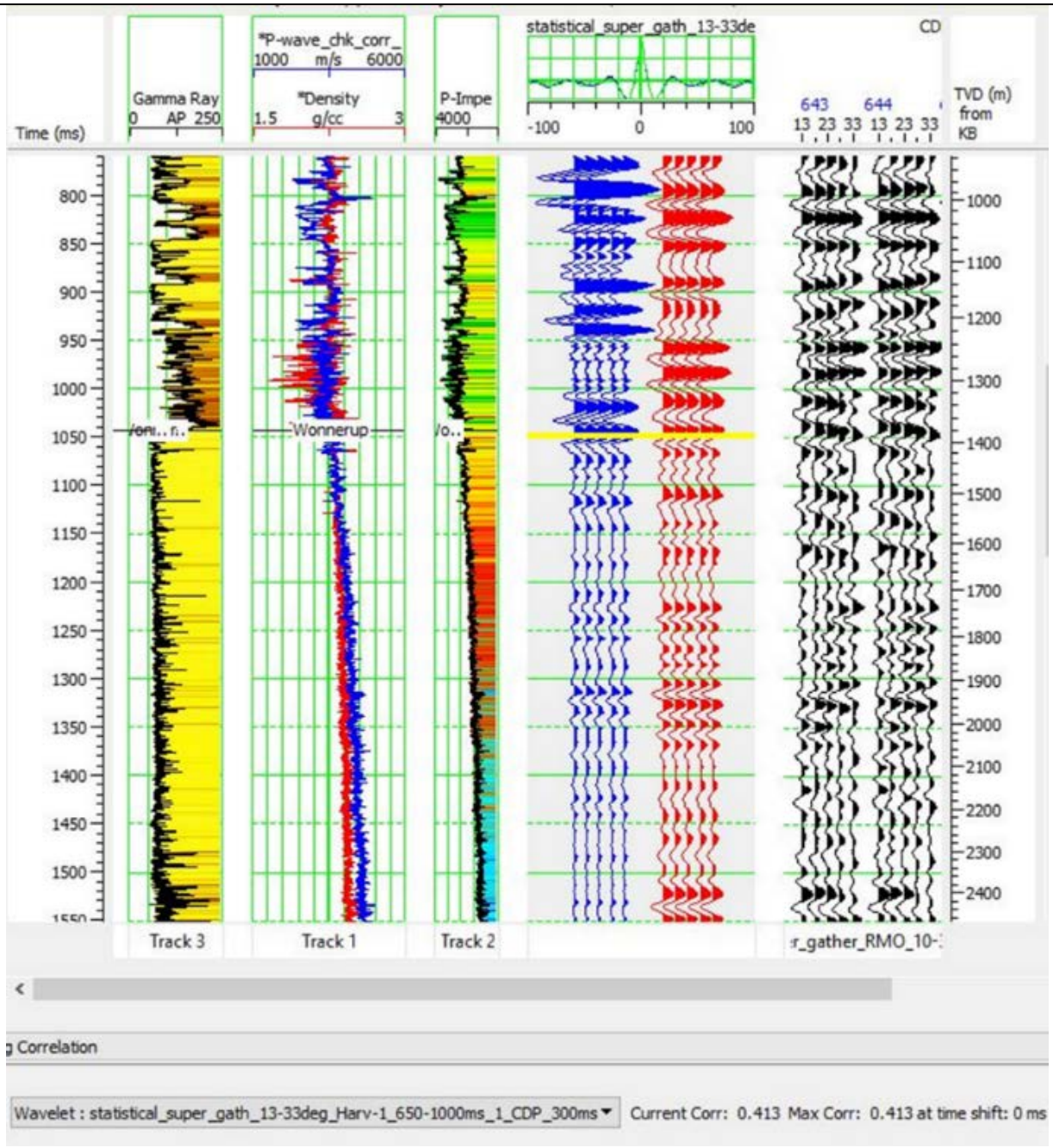


Figure 76 The Harvey 1 well to seismic tie. Blue traces are zero-offset synthetic, red are near-offset seismic trace and black are the super gather traces.

An initial low-frequency model was built using supergather data, three interpreted horizons and the Harvey 1 well logs. For this purpose, a low-pass frequency filter was applied to pass the frequencies up to 10 Hz and filter out the frequencies above 15 Hz (Figure 77).

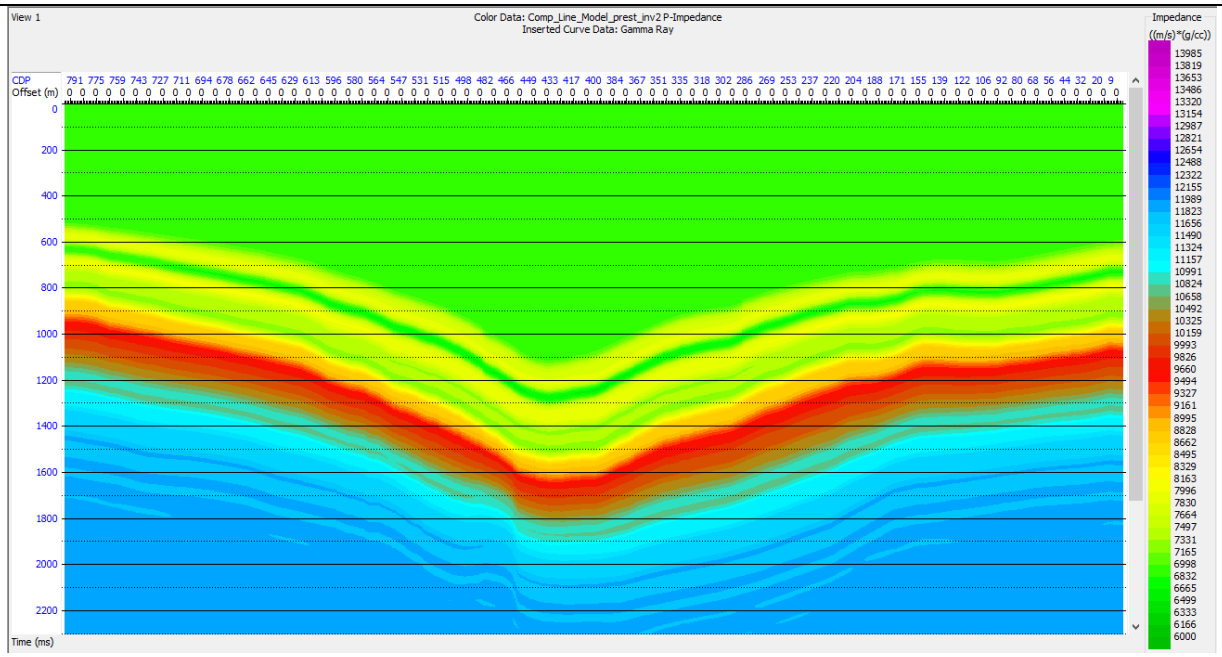


Figure 77 Low frequency model of the composite line as P-Impedance for the Harvey 1 well to seismic tie.

4.3. Rock physics model and inversion analysis.

P-impedance and V_P/V_S logs are presented as the cross plot (Figure 78) and were used for the rock physics model. A distinction was observed in the clustering between the low impedance, high V_P/V_S shales and high impedance, low V_P/V_S sands. There were some high impedance shale points falling into sand defined ellipse cluster on the cross plot. This shale was hard to distinguish on the predicted lithology log and mainly relates to the Lower Yalgorup section with an unreliable density log and the Wonnerup Member where shales are only a few meters thick and therefore below seismic resolution (Figure 79 and Figure 80). Hence, a two-lithology model was used for inversion (Figure 78).

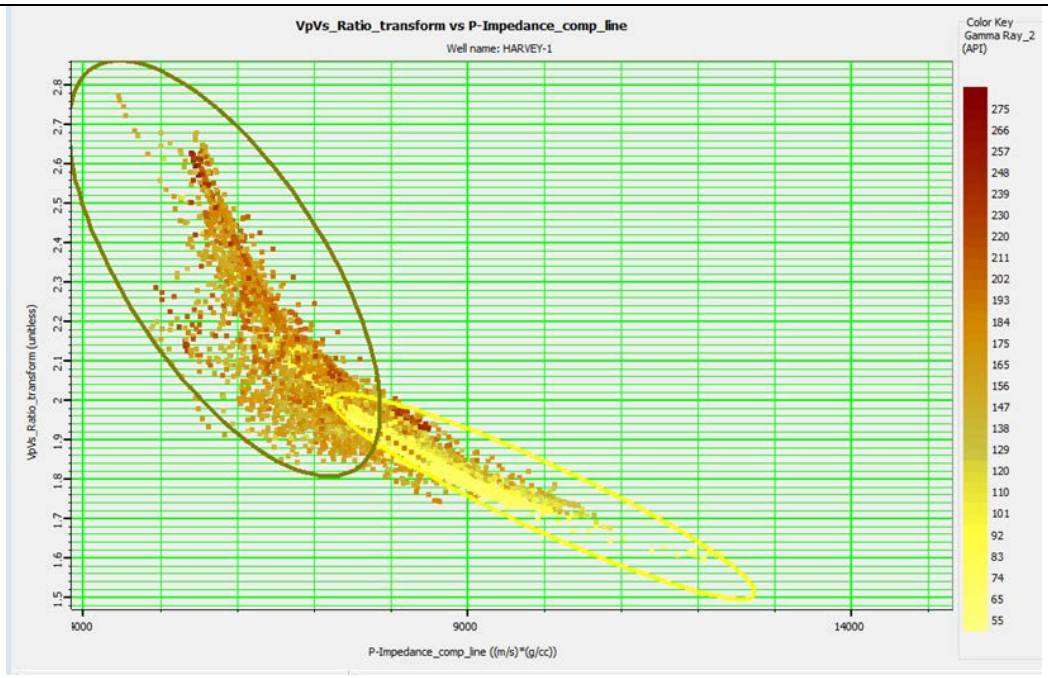


Figure 78 P-impedance – horizontal axis and V_P/V_S – vertical axis logs cross plot. Yellow ellipse identifies sand lithology and green ellipse – shales. Gamma ray is the colour scale.

The AVO inversion analysis is shown in Figure 81. The left panel shows the inverted logs P-Impedance, S-Impedance, density and V_P/V_S as red curves and original logs in blue. On the right, seismic synthetics traces in red, super gather traces in black and the errors in red. Although the error had a high value of 0.51 due to noisy data, the correlation coefficient was quite high: 0.86. Two angle dependant wavelets were used for the analyses and to run the inversion for the full volume with maximum iterations 100. The resulted P-impedance and V_P/V_S volumes are displayed in Figure 82 and Figure 83.

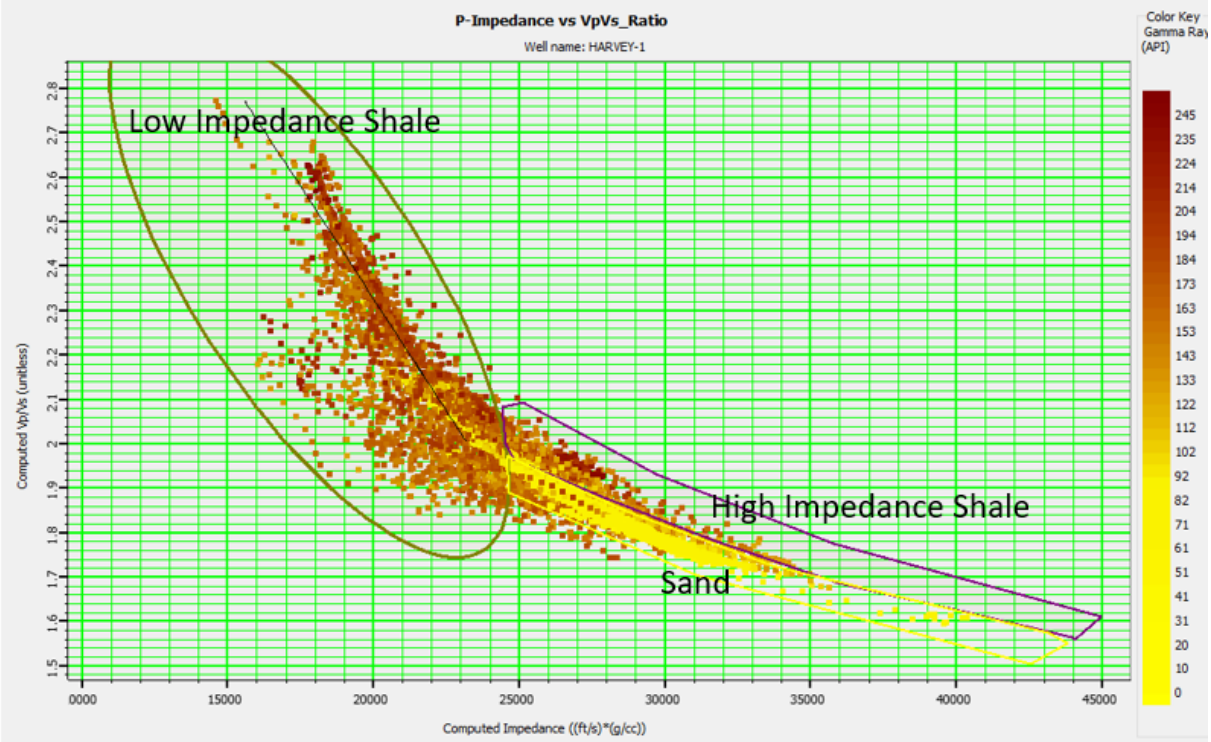


Figure 79 P-impedance – horizontal axis and V_P/V_S – vertical axis logs cross plot. Yellow ellipse identifies sand lithology and green ellipse – shales. Gamma ray is the colour scale. This lithology zones were used in Figure 80 logs lithology definition model.

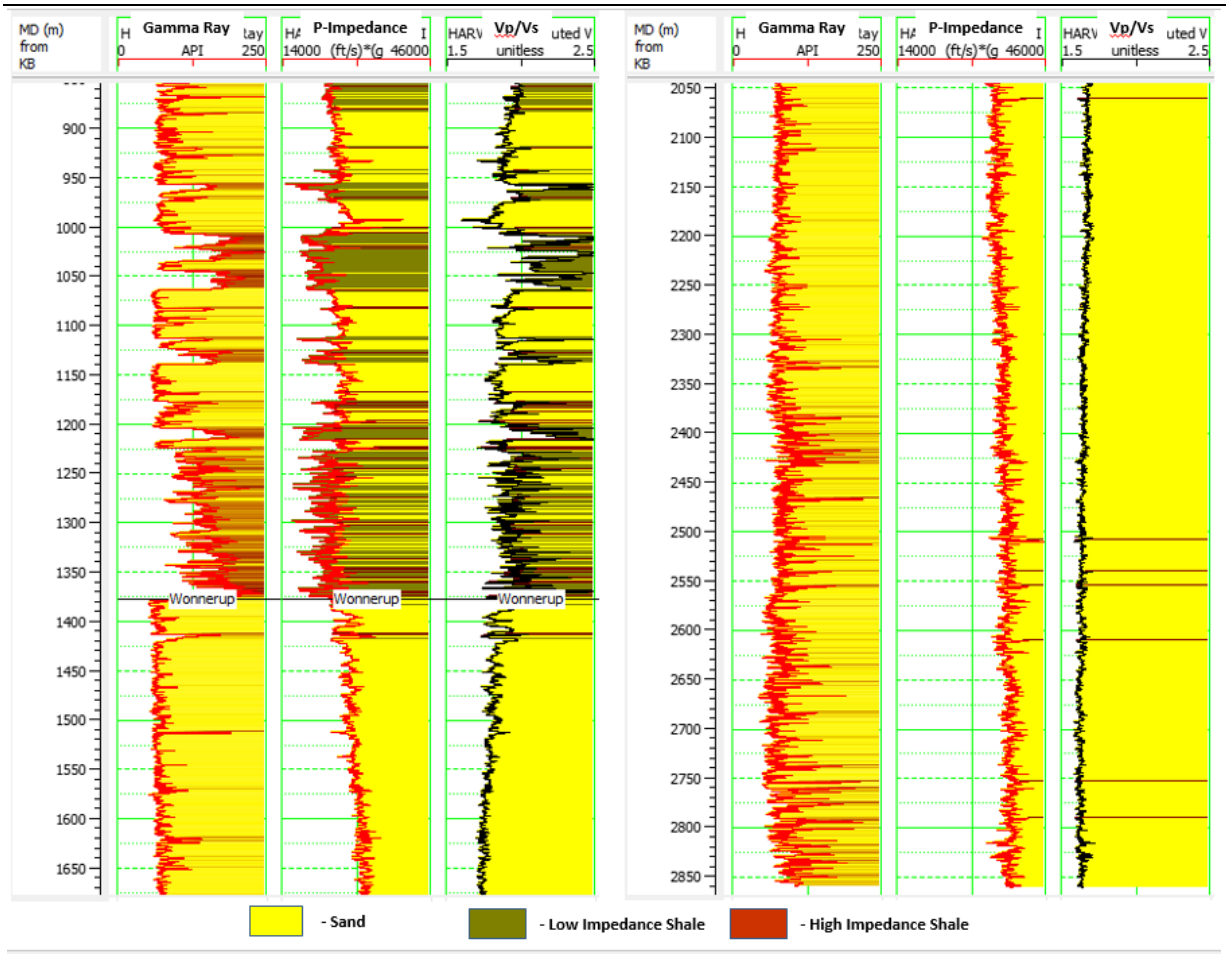


Figure 80 Lithology definition model for the Figure 79 cross plot.

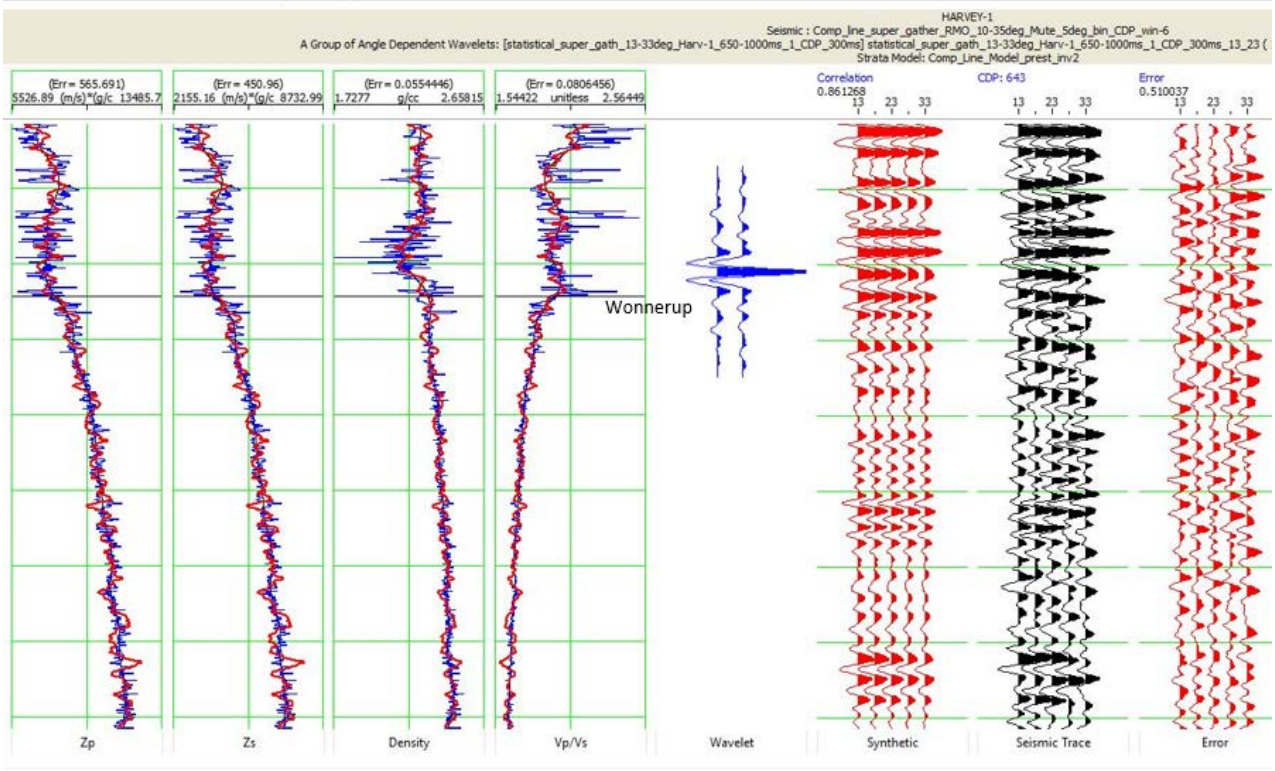


Figure 81 AVO inversion analysis for the Harvey 1 well and seismic.

Hampson-Russell LithoSI tool uses a Bayesian classification scheme, which computes both the conditional probability and a priori probability for each class using the well logs. It uses P-impedance, V_P/V_S volumes, and well logs for a defined lithology model. LithoSI can use several classes or lithologies, each with its probability distribution function (pdf). In our case, we had two classes: sand and shale shown in the Figure 78. The results of the lithology prediction are displayed in the Figure 84. The lithology prediction for the blind Harvey 3 well did not match with the gamma ray log within the upper part of the Yalgorup Member. This is probably due to the absence of this part of the log in the Harvey 1 well. The rest of the prediction provided a better match with the log. It should be noted that the well is 300 m away from the line. Figure 85 and Figure 86 show the probability of the predicted sand and shale respectively. The predicted results from the composite line indicated that the Yalgorup Member has mainly shaly lithology with two apparently continuous shale sequences. The low shale sequence is 150-200 m thick interbedded with the sand lithology. The upper shale sequence is 60-80 m thick predicted as a continuous monolithic shale without sand inclusions. These shale layers can probably act as a seal for the injected CO_2. The Wonnerup Member is predicted as sandy lithology with no shale. The shale lithology or “paleosols” were not predicted as they are below the seismic resolution of this method.

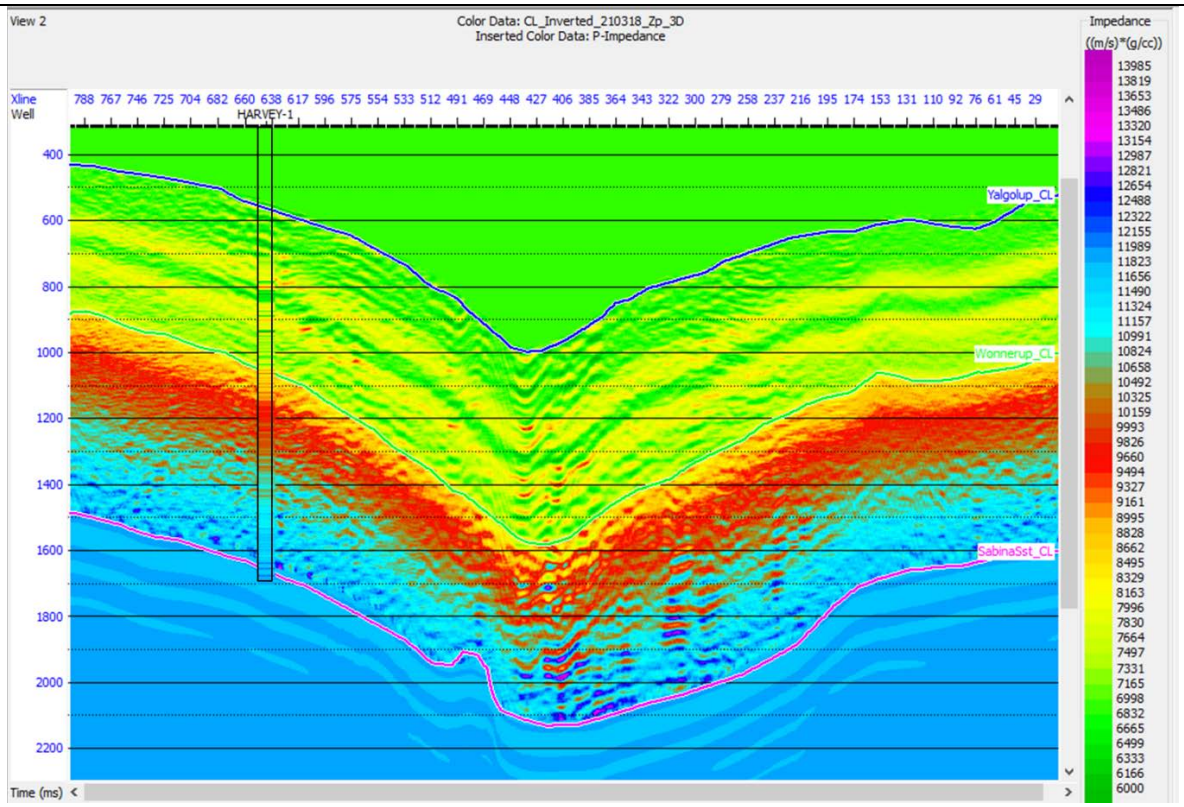


Figure 82 P-impedance volume with the Harvey 1 well P-impedance log inserted.

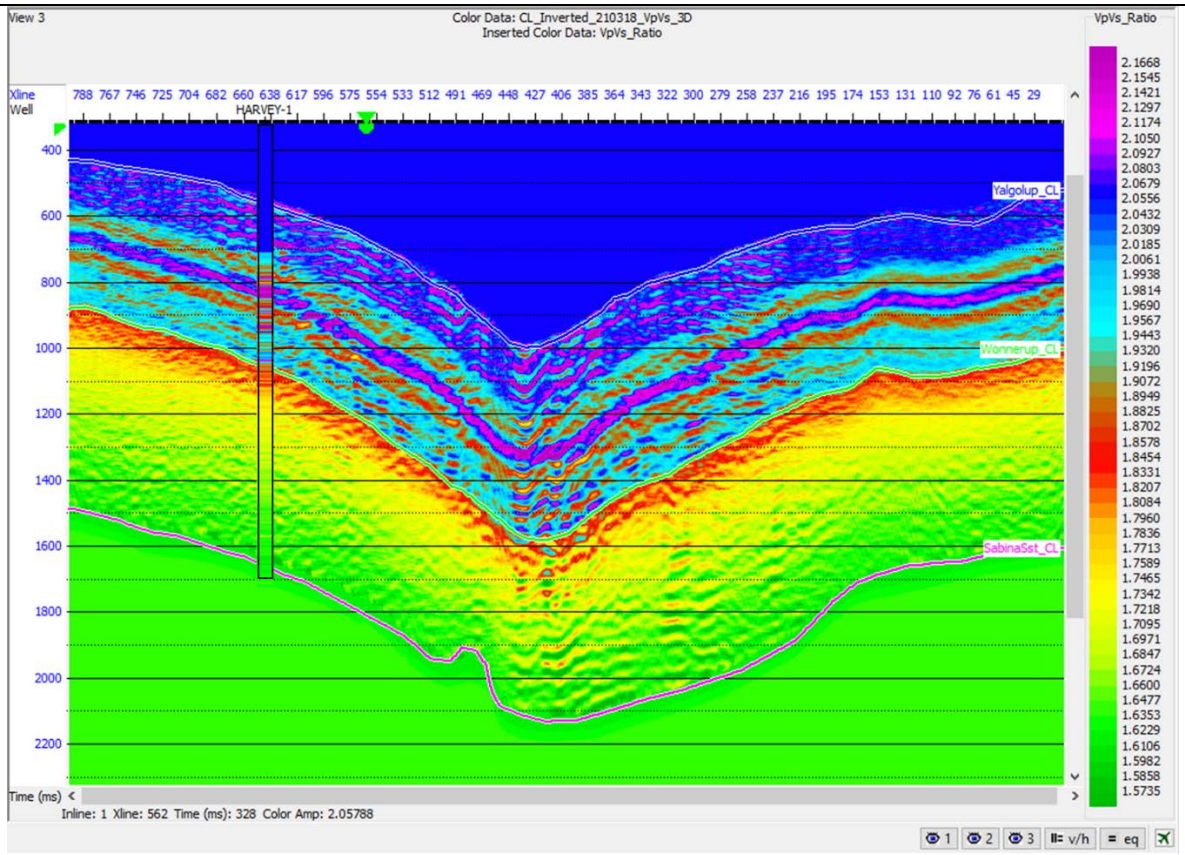


Figure 83 V_P/V_S volume with the Harvey 1 well V_P/V_S log inserted.

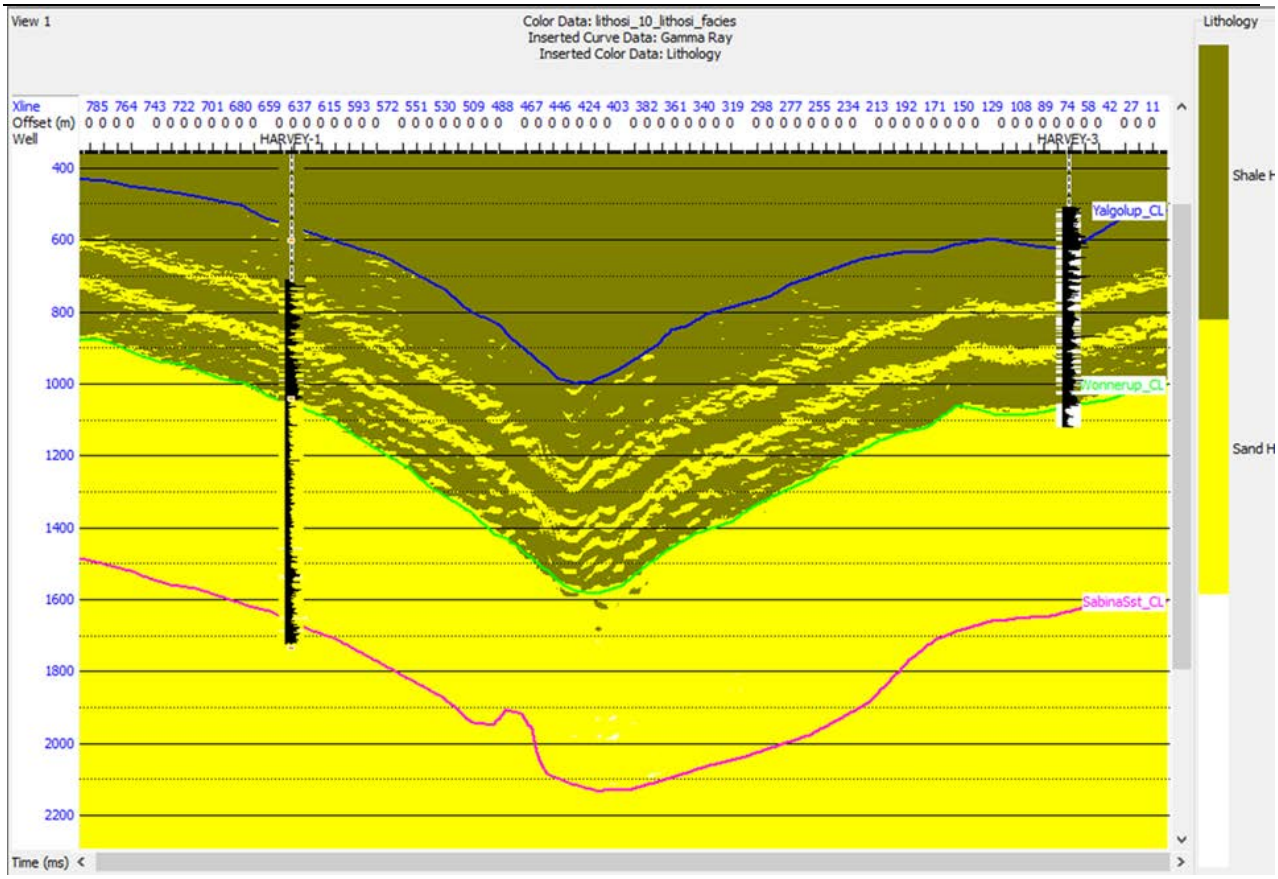


Figure 84 Composite line lithology prediction. The black curve of the Harvey 1 well is the gamma ray log and inserted colour is lithology log. The Harvey 3 is a blind well with black curve as the gamma ray log.

Two approaches were used for calculating sand porosity.

1. The standard approach of sand porosity prediction from acoustic impedance volume using the correlation between the acoustic impedance and porosity from well logs (Figure 87).
2. The alternative approach was to compute porosity from the tomographic PSDM velocity volume (section 3). The velocities along the composite line are shown in Figure 88 and the resulting porosity in Figure 89. This alternative approach gives much lower spatial resolution. However, it is entirely based on seismic data (reflections from below Yalgorup), in contrast to the impedance based predictions, which essentially extrapolates the Harvey 1 well using seismic information. As such, the velocity based porosity prediction, although of much lower resolution, may be more reliable at large distances from the Harvey 1 well, and could also be applied to the 3D velocity volume obtained from the seismic cubes (section 3.2.2).

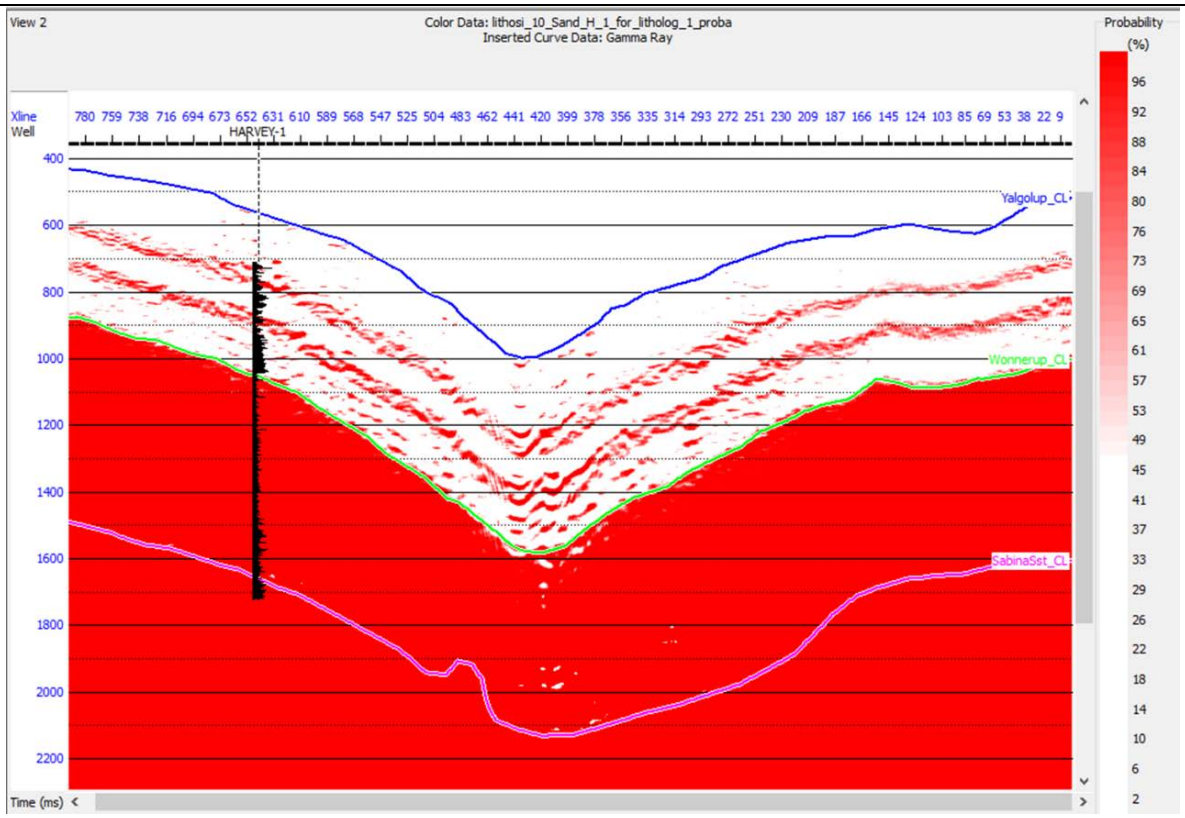


Figure 85 Probability of the sand lithology on the composite line. Harvey-1 is the gamma ray log curve of the Harvey 1 well.

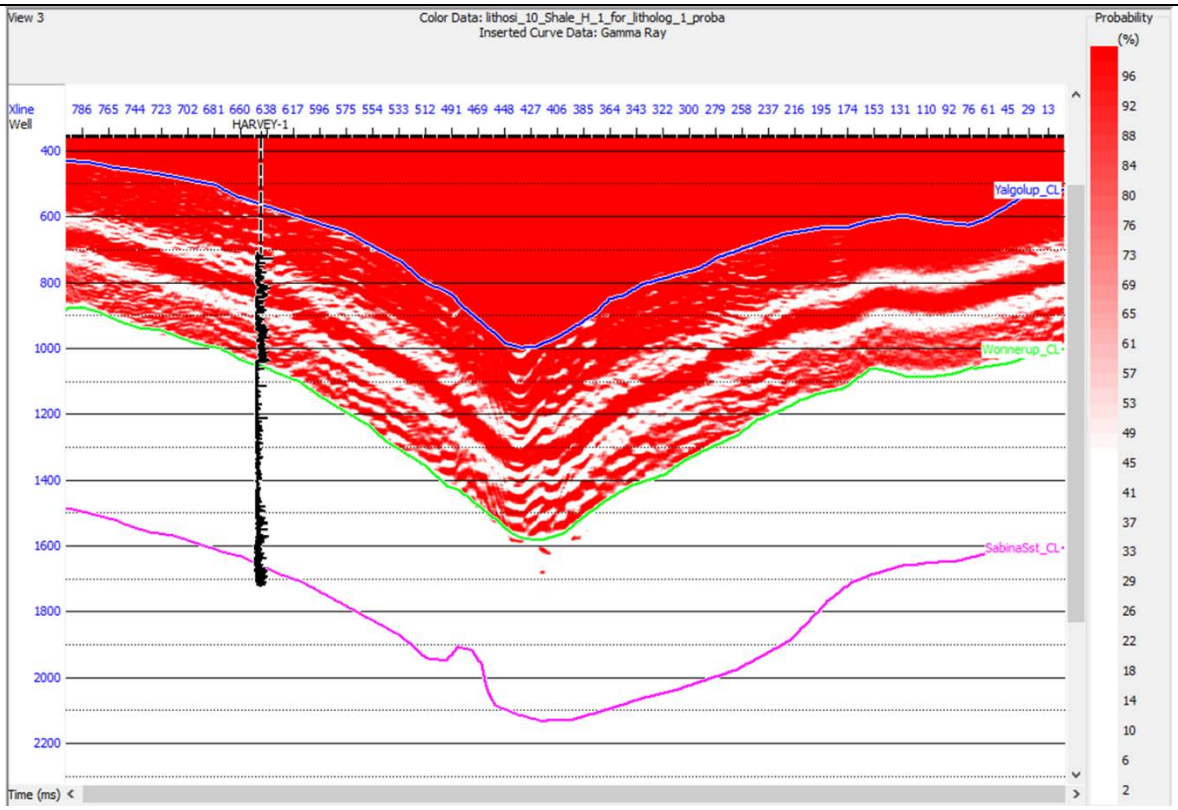


Figure 86 Probability of the shale lithology on the composite line. Harvey-1 is the gamma ray log curve of the Harvey 1 well.

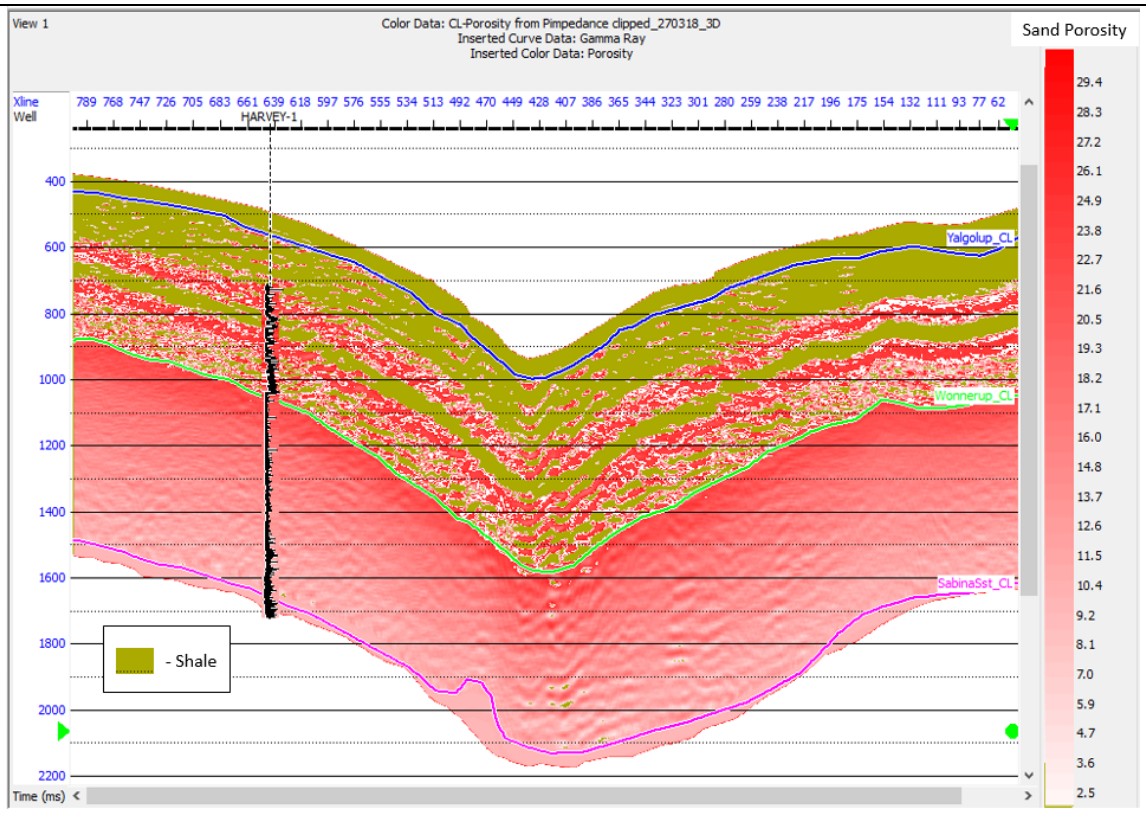


Figure 87 Porosity prediction from the inverted P-impedance, for the composite seismic line. In the Yalgorup we show the predicted shale facies (with credibility of the false-positive prediction < 5%), which is assumed to lack any effective porosity.

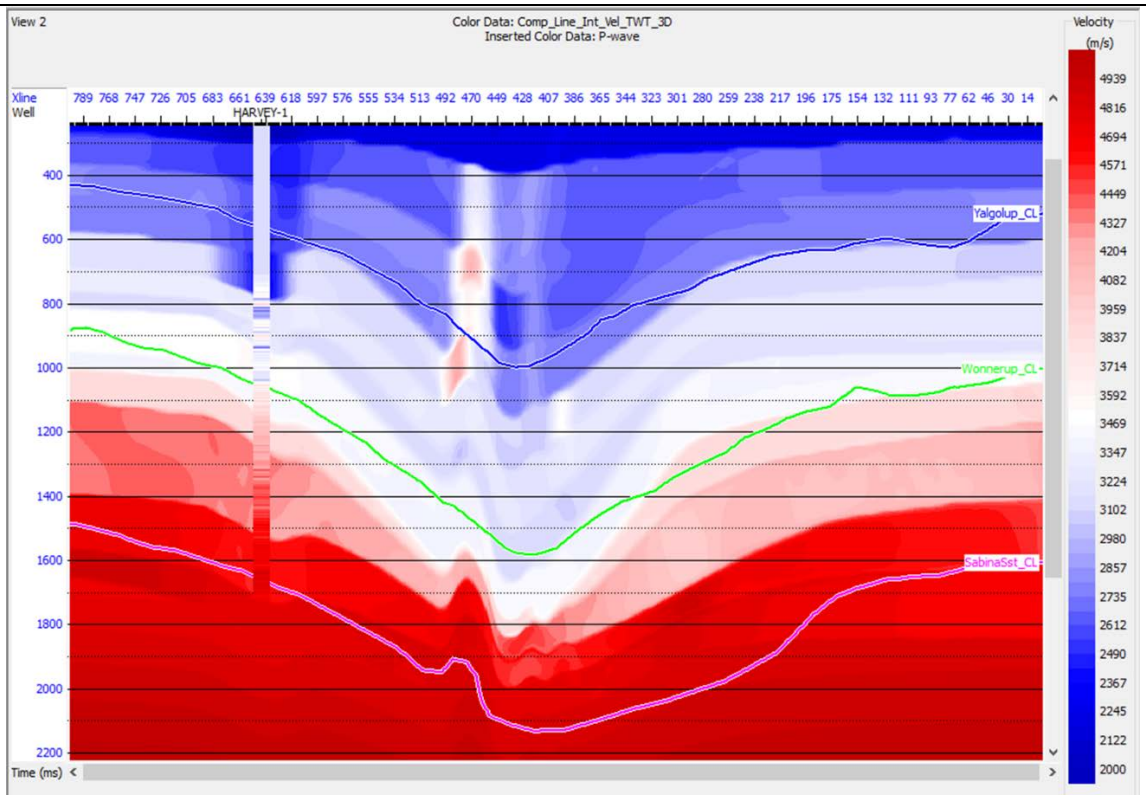


Figure 88 High-resolution velocity volume in TWT. P-wave velocity is displayed as the Harvey 1 well colour log. Note the shallow problem anomalies at 400-1150 ms due to surface acquisition/conditions problem.

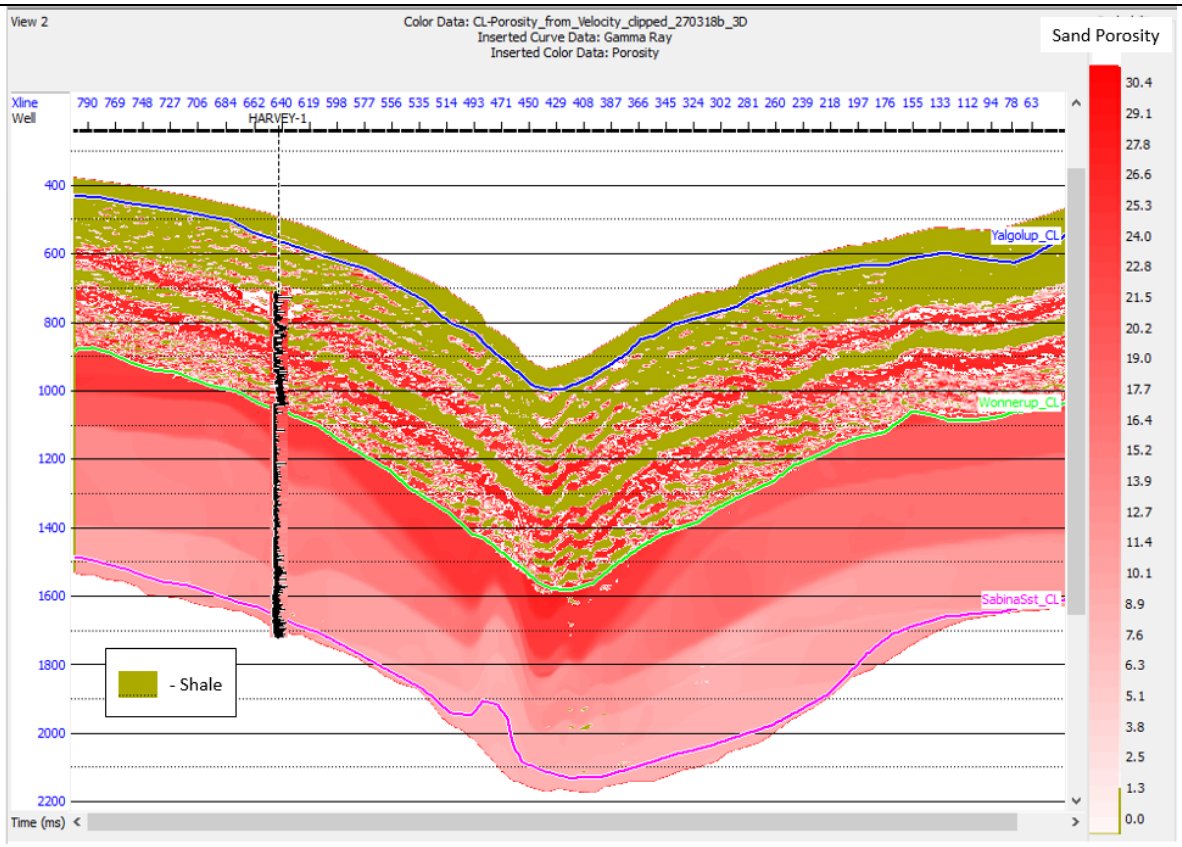


Figure 89 Porosity prediction from the high-resolution tomographic velocities, applied to the composite seismic line. In the Yalgorup we show the predicted shale facies (with credibility of the false-positive prediction < 5%), which is assumed to lack any effective porosity.

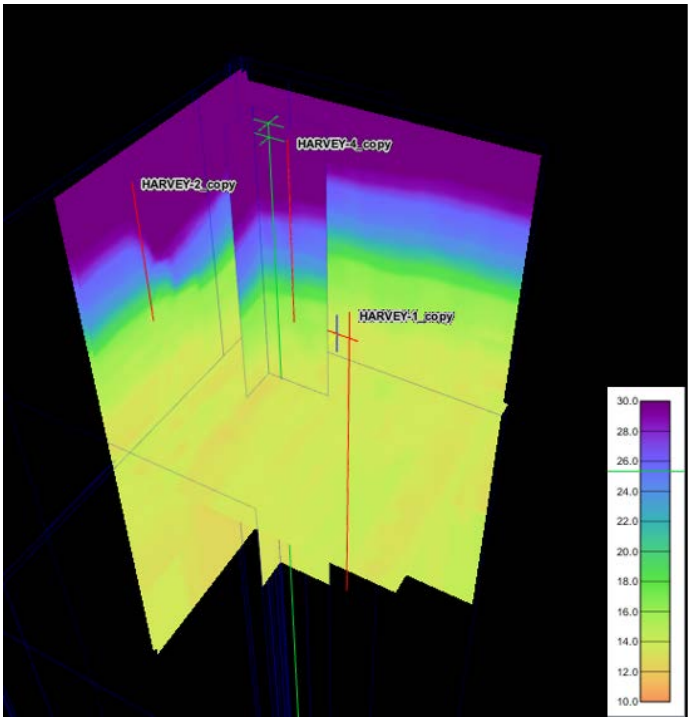


Figure 90 Vertical and horizontal slices through the porosity cube computed from the reflection tomography velocities. Note the smooth structure of the porosity, which resulted from the low resolution of the velocity analysis.

4.4. Conclusions

Stochastic AVO inversion was applied to the composite seismic line. To this end, we produced partial angle gathers within the range of 10^0 to 35^0. The petrophysical interpretation of the inversion relies on the Harvey 1 well logs. Two lithology classes were used for lithology prediction: the low impedance, high V_P/V_S shales and high impedance, low V_P/V_S sands within Yalgorup and Wonnerup Members. We used two methods in predicting sand porosity: standard approach, which uses the P-impedance volume and an alternative approach using high-resolution PSDM velocity volume.

The Wonnerup Member is predicted to have a sand lithology only. The lithology of the Yalgorup Member is predicted predominantly as shale interbedded with sand. It has two continuous thick shale layers.

We recommend the use of high density grid of 2D seismic data for quantitative interpretation in the areas with the restricted land access.

5. Stochastic Seismic Inversion of the Large 3D Survey

This section presents the seismic inversion workflow and the results obtained from the SW Hub seismic data. Essentially, any seismic inversion algorithm converts recorded seismic amplitudes into a distribution of rock properties. A conventional inversion algorithm retrieves seismic contrasts in the subsurface, which then may be 'integrated' into seismic properties distribution. The properties are then transformed into petrophysical properties required by a reservoir geomodeller (e.g., Avseth et al. 2000).

The large 3D seismic provides the only means to build a geological model of the SW Hub area. A number of studies have attempted the prediction of the reservoir properties using the survey (e.g., Strachan et al., 2016; Glubokovskikh et al. 2016b; Strachan 2018). Unfortunately, all of these studies concluded that the data quality precludes building a reliable model of the subsurface properties. Even structural interpretation is ambiguous in some areas.

Clearly, seismic processing cannot compensate for the limitations of the acquisition geometry completely, but Generation 2 volume described in this report (section 3) has improved SNR of the imaged data compared with previously interpreted seismic cubes (Pevzner et al. 2013; Glubokovskikh et al. 2016b). The latest data set has already been used for static geomodelling by Strachan (2018). The 'high-resolution' cube allowed the geomodelling team to refine structural framework of the subsurface, such as:

- intra-Wonnerup and intra-Yalgorup horizons were added;
- new fault picking was done with higher confidence.

Quantitative interpretation of the 'amplitude-preserved' seismic was not successful: most of the amplitude anomalies obtained were interpreted as overprints of the acquisition geometry.

Then, Glubokovskikh et al (2018) performed a systematic quality assessment of the large 3D seismic cubes. To this end, the authors computed an extensive set of seismic attributes that are commonly-used for stratigraphic mapping and the prediction of petrophysical properties. The attributes had no clear spatial patterns other than the ones related to the variable seismic fold (density of the source-receiver pairs) and major faults. Hence, any quantitative interpretation that relies only on amplitudes – such as deterministic seismic inversion - would have very high uncertainty.

Having established that the quality of seismic amplitudes is relatively low, we could still obtain useful information from seismic inversion. However, instead of sample-based estimation of the seismic properties, we implemented a stochastic seismic inversion to assess the credibility of particular features of the subsurface model (Dvorkin, Gutierrez, and Grana 2014). Such formulation relaxes the requirements on the accuracy at a particular sample obtained in one realization of the inverted model but rather focuses on detection of patterns that occur more frequently in the ensemble of the inversions and form consistent spatial patterns.

Another benefit of stochastic inversion is related to the regularization of the inverted models. The regularization is an essential part of any quantitative interpretation method, but Bayesian framework provides a solid approach for incorporating both prior beliefs about the subsurface *and* the seismic data quality (Sen and Stoffa 2013). Thus, depending on the seismic quality at a particular location the inverted model is either driven by the seismic data or ignores noisy amplitudes and clings to the prior model.

Glubokovskikh et al. (2018) have tested feasibility of the probabilistic approach to the seismic inversion using the composite 2D seismic line and nested seismic surveys around the Harvey 1 and the Harvey 4 wells. The authors imposed strong rock physics constraints on the inversion algorithm and varied the 'trustworthiness' of the seismic amplitudes to classify the Yalgorup and Wonnerup member of the Lesueur sandstones into baffles and reservoir facies. Eventually, the study identified zones of increased concentration of the baffles around the the Harvey 1 well, despite the fact that accurate predictive mapping of the facies was deemed impossible.

In the following section, we develop a workflow for stochastic inversion that would integrate geophysical studies of the SW Hub Project in order to refine existing geomodels of the subsurface. We focus on aspects of the subsurface that have been extensively studied since the large 3D seismic was acquired:

- the distribution of the impermeable facies - baffles - at the transition between the Yalgorup and Wonnerup Members of the Lesueur sandstones;
- the cause of the quiescent seismic image within Wonnerup Member;
- the nature of the weak reflections observed within some parts of the Wonnerup member.

5.1. Inversion algorithm

A probabilistic approach to the seismic inversion employs minimization of the objective function

$$E[\mathbf{m}] = (\mathbf{y} - f[\mathbf{m}])^T C_d^{-1} (\mathbf{y} - f[\mathbf{m}]) + (\mathbf{m} - \bar{\mathbf{m}})^T C_m^{-1} (\mathbf{m} - \bar{\mathbf{m}}), \quad (34)$$

with respect to $\mathbf{m}$ (inverted seismic parameters of the subsurface with initial guess $\bar{\mathbf{m}}$). $\bar{\mathbf{m}}$ integrates all prior beliefs about distribution of the seismic properties – lateral variation, loading trends, facies abundance etc. The first term accounts for the mismatch between the observed seismic data **y** and the inverted model, which is transformed into synthetic seismic data through convolutional modelling $f[\mathbf{m}]$.

Equation 34 shows how data quality controls the credibility of the inversion outcome through C_d and C_m. C_d depends on the noise model and SNR – quality of the seismic data. C_M quantifies reliability of the initial model of the subsurface. Essentially, the C matrices contain acceptable magnitudes of the mismatch between the data and model for a particular seismic sample. The higher the SNR the less the mismatch would be tolerated by the inversion algorithm. In the limit of zero C_d, the objective function equals to zero for $\mathbf{m}=\bar{\mathbf{m}}$ and hence the initial model is not modified.

5.1.1. *A priori seismic model*

Traditionally, an initial model is built using structural interpretation to guide interpolation of the well data. Given the complexity of the SW Hub site, the available set of wells is too sparse for a reliable initial model. High-resolution velocity analysis (section 3.2.2) refined the initial low-frequency model through analysis of the travel-time curves. The resultant model was used as an initial guess $\bar{\mathbf{m}}$ for the stochastic seismic inversion, which may be regarded as a joint kinematic/amplitude seismic inversion.

Estimation of the uncertainty of the model is relatively straightforward. First of all, the minimization of the objective function should have enough freedom to capture the variability of the seismic properties. Figure 91a compares estimated seismic velocities against the sonic logs. All the three wells have similar patterns: (1) the Yalgorup Member is rather heterogeneous while (2) the Wonnerup Member has a relatively smooth V_P sonic log which has a good agreement with reflection tomography results. Glubokovskikh et al. (2018) proposed a plausible explanation for such behaviour: the depth trends of the seismic properties overlap in the Wonnerup Member for reservoir and non-reservoir facies (see Figure 91b), thus reducing contrasts between the rock types, and making the curves smoother.

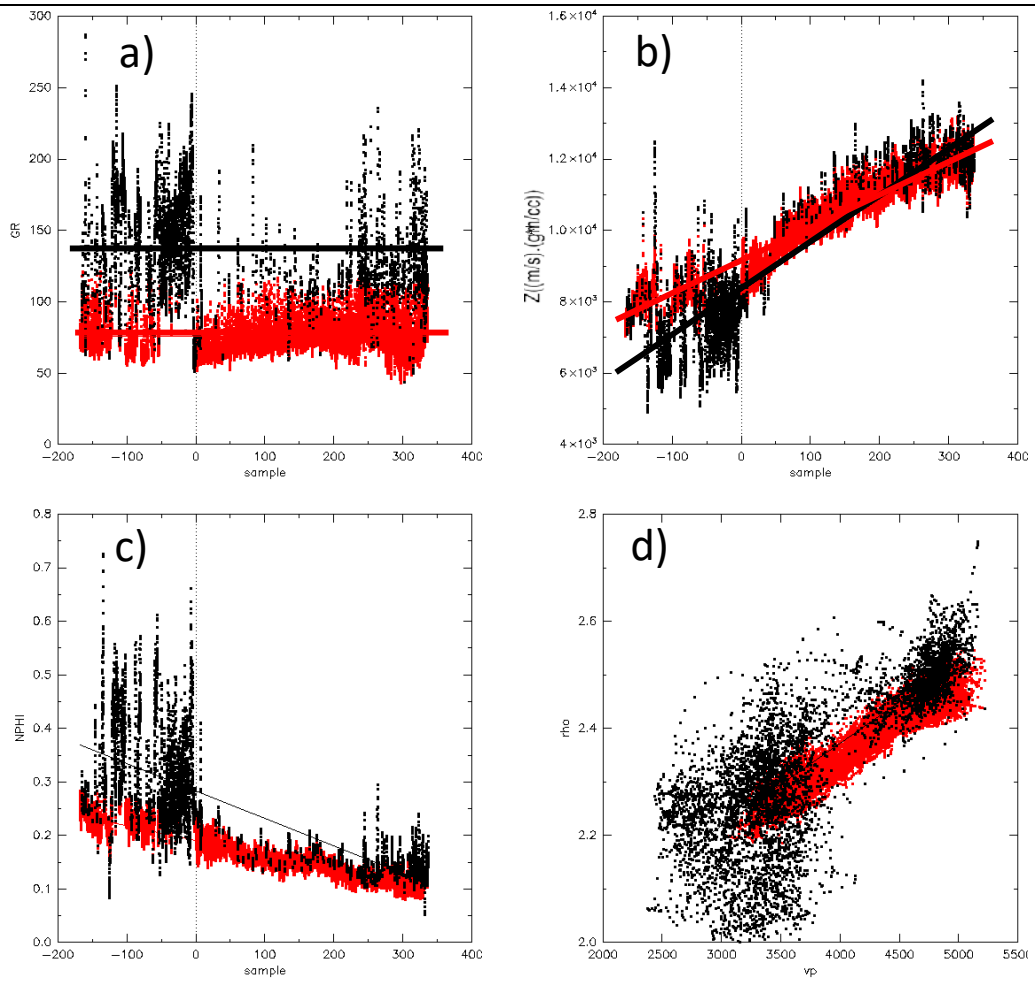


Figure 91 Classification of 2 facies types based on gamma radioactivity (a) and acoustic impedance (b), neutron porosity (c) and sonic and density (d) logs in the Harvey 1 well. The results obtained by the Expectation-Maximization algorithm with 2 facies types. The loading affects the impedance linearly. Horizontal axis represents samples of the logs converted into TWT where zero corresponds to the top Wonnerup Member. (See for details Glubokovskikh et al. 2018)

5.1.2. *Uncertainty of the seismic data*

Quantitative characterisation of the SNR of seismic data is much more complicated than estimation of C_m. The issue arises due to the unavailability of a noiseless signal that would serve as a reference to measure the noise level. In fact, even definition of the SNR varies depending on a problem under consideration. Here, we use the ratio of signal RMS amplitude to noise RMS because this ratio is naturally related to the C_d.

A conventional approach to estimation of the seismic SNR compares a trace extracted from final seismic image at a well location to actual structure of the subsurface obtained from the well data. For the SW Hub data set, the match is relatively low for all four wells. This mismatch can be caused by violation of basic assumptions behind the well tie:

- A 1D approximation may oversimplify an intensely faulted SW Hub subsurface;
- the well logs have intervals of poor quality, and thus might not represent the ground truth model;
- the source signature may be affected significantly by scattering and intrinsic attenuation as was indicated by Glubokovskikh et al. (2016b).

All these assumptions are essential for the inversion algorithm, based on equation 34, that we used for seismic inversion. Hence, we consider the well tie quality as an appropriate measure of the seismic SNR, which incorporates not only the quality of seismic data but also modelling errors (due to errors in log data and inadequacy of the 1D convolutional forward model).

An issue remains with the spatial interpolation of the SNR values derived at the well locations. Glubokovskikh et al. (2018) showed that the quality of the large 3D seismic is controlled by the seismic fold. In Figure 92, we see that only the Harvey 2 and the Harvey 4 are located in a relatively high-fold area. We focus on the analysis of the Harvey 4 well, because the Harvey 2 well belongs to a completely different geological setting characteristic of the Lesueur sandstones beyond the Fault 10.

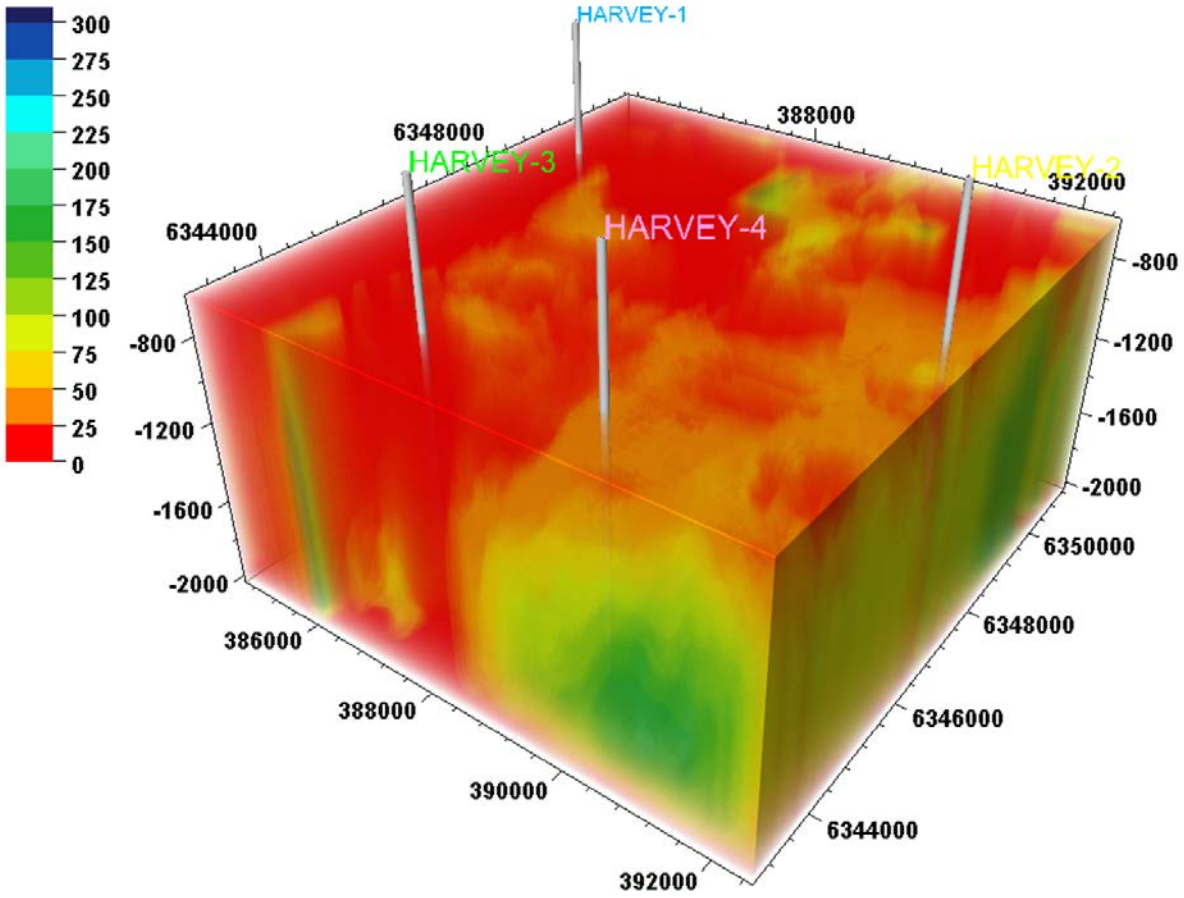


Figure 92 3D distribution of the seismic fold for the large3D seismic data (from Glubokovskikh et al. 2018).

Traditionally, the correlation between the actual and synthetic trace is used as a measure of a well tie (e.g., Walden and White 1998). There is no rigorous theory behind the translation of the correlation to our definition of the SNR, and thus we extracted the wavelets and estimated the well tie based on the Bayesian algorithm developed by Gunning and Glinsky (2005). **Figure 93** shows the well tie display for the Harvey 4 well. A poor match between the traces is noticeable even visually and amounts to a SNR of ~ 1.2, which corresponds to a ~50% correlation coefficient. The most severe discrepancy occurs at the intersection between Fault 7 and the borehole at ~1000ms. The reference points for the seismic-to-log correlation was chosen from the top of the Yalgorup and Wonnerup members. Seismic impedance (the left track in **Figure 93**) shows a clear change of seismic character at these boundaries (trend and variance) that manifests itself in the seismic response – easily detectable strong events in the vicinity of the Harvey 4 well. This is a strikingly different outcome from the known issue of identifying the top of Yalgorup in the Harvey 1 well.

Given the extracted wavelet, we estimated the SNR at the Harvey 1 and Harvey 3 wells. The fold effect results in a SNR ~ 0.2 around these wells (see, e.g., Figure 94).

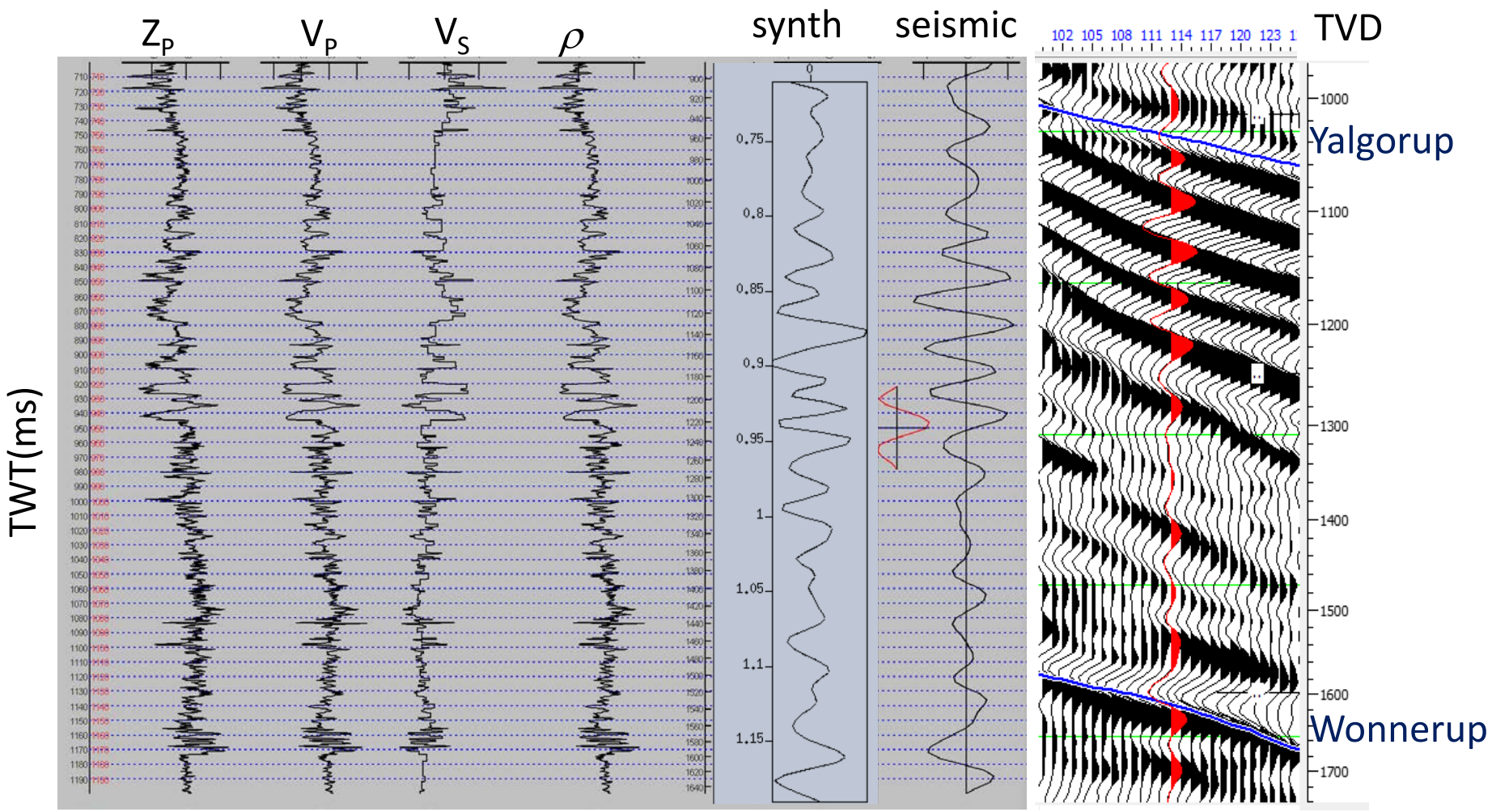


Figure 93 Stochastic well tie at the Harvey 4 well along with a segment of inline 223.

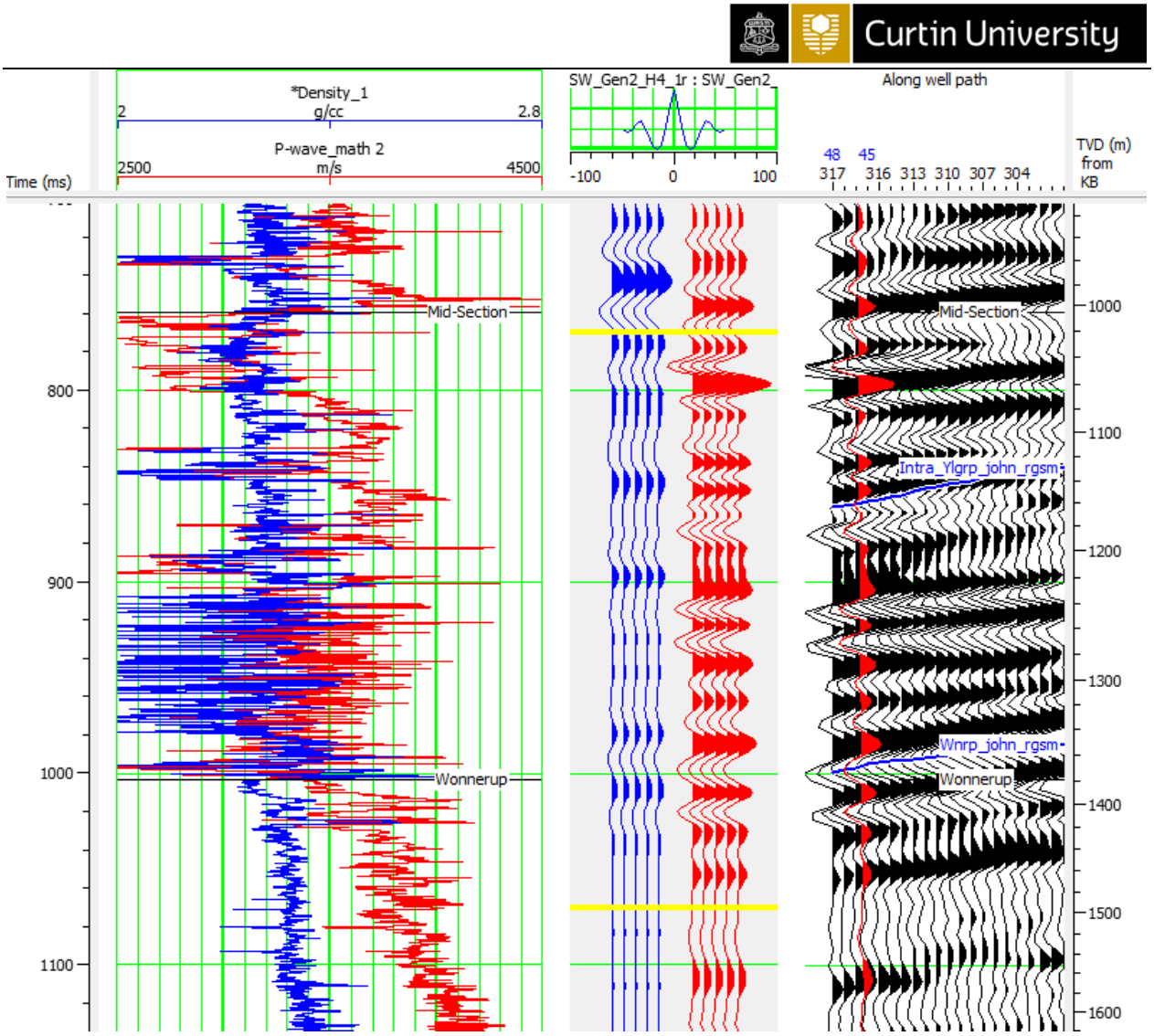


Figure 94 Log to seismic correlation at the Harvey 1 well with the reference wavelet extracted from the Harvey 4 well (done in Hampson Russell v.10.2). Besides the matching seismic horizons, correlation between the seismic and logs is ~ 25%, which is extremely low.

5.1.3. *Final parameters of the inversion algorithm*

Here we summarize the findings from the above subsections and formalize them into specific settings of the stochastic seismic inversion of the large 3D seismic volume.

First of all, the well ties in the Harvey 1 and Harvey 4 wells show a good match at the reference reflections – top Wonnerup and/or Yalgorup Members. The correlation deteriorates away from the strong seismic events. This is a common feature for all wells at the SW Hub site, which complicates the estimation of the SNR of the seismic data: the value varies laterally and vertically. In general, the SNR is low, but some of the seismic events have a stable appearance throughout the seismic cube and thus allow for a more reliable interpretation of their amplitudes. Such patterns should be picked up by the stochastic sampling of the plausible inverted models.

Secondly, high-resolution velocity analysis provides a rather reliable initial model of the subsurface that is conditioned to the sonic logs from the Harvey wells and VSP data. The standard deviation of the sonic data can be used as a measure of the model uncertainty, which is estimated as ~10% within the Yalgorup Member and ~4% - the Wonnerup Member. In addition, C_m describes the rate of vertical variations of the model – essentially, how similar adjacent samples should be, which are also computed based on the sonic logs. We use an exponential variogram with 2m correlation length.

Eventually, we designed three scenarios of the stochastic inversion algorithms that have the same initial model but differ in the values of the seismic SNR – term C_d in equation 34:

- Pessimistic scenario: the SNR is constant and equals 0.2;
- Optimistic scenario: the SNR is constant and equals 1.2;
- Reference scenario: the SNR computed varies from 0.2 to 1.5 laterally and vertically as a function of the seismic fold.

According to a particular value of the SNR, the seismic trace would have a particular weight in the optimization process. In the first scenario, we were likely to recover the initial model modified only where the seismic had really strong and consistent events. The optimistic SNR case was driven by the seismic data to a larger extent, regardless of the estimated data quality. The reference scenario used the seismic amplitudes where they were more reliable and relaxed the expectations from the seismic where the seismic fold is low.

5.2. Interpretation of the inversion results

We applied to the large 3D seismic a stochastic inversion workflow implemented in Hampson-Russel Software v. 10.2 that has all of the necessary functions described above. Figure 95 shows a typical output of the inversion for the inline 113 passing through the Harvey 3 and Harvey 4 wells. The mean acoustic impedance in Figure 95a is obtained by averaging of 100 realizations (we discuss the number of iterations below). Each of the realizations satisfies equation 34 within the specified accuracy. This example gives an idea of the uncertainty of a conventional deterministic inversion. Having an ensemble of the realizations, we may detect the most reliable events in the seismic data that persist in the realizations. These events feature consistently strong amplitudes and their seismic response may be well described by the extracted source wavelet.

We began with the constant seismic SNR scenarios. Figure 96 compares the mean acoustic impedance inverted for the low and reference seismic SNR. As expected, the reference case results in much more detailed impedance cubes. However, top of the Wonnerup Member is clearly visible in the low SNR section between The Harvey 3 and Harvey 4 wells, which suggests a higher

credibility for the continuous seismic boundary between the two formations at this location. **Figure 97** shows horizon slices through the mean acoustic impedance volumes along the top Wonnerup Member. It should be noted that, there is a more mild variation of the impedance when the SNR varies spatially. The inversion 'avoids' big contrasts unless we observe very strong kicks in the seismic.

5.2.1. *Lithological classification*

As the ultimate goal of the stochastic inversion is petrophysical characterisation of the reservoir, we focus on the mean facies volume as the main convergence criterion. Given the only inverted value is acoustic impedance, we classify facies types based on the sign of dZ_P - deviation of the acoustic impedance from the initial trend. Figure 91 suggests that the negative dZ_P within the Yalgorup Member and positive dZ_P in the Wonnerup Member should be associated with the baffles facies.

The number of iterations is an important parameter that controls the outcome of the stochastic inversion algorithm. This value depends on the data quality and complexity of the subsurface. One can estimate the number of iterations empirically using convergence of the ensemble average of the inverted parameters. From the test inversion runs shown in **Figure 98**, we considered that 100 realizations was enough.

The lithological nature of the boundary could be predicted from the ensemble of dZ_P realizations. According to the facies classification, we may compute the probability of a particular facies at a given sample as a frequency of the occurrence in the ensemble. Figure 99 and Figure 100 show a consistent continuous shale/sand interface between the Wonnerup and Yalgorup Members. The probability sections are overlaid by a transparent fold section to compare the probability values for the high SNR inversion against the reference scenario. We see that reduction of the fold shifts the probabilities to 0.5 – i.e. the facies type is a toss of a coin. Comparison of the probabilities in Figure 99a and Figure 99b in the vicinity of the Harvey 3 well illustrates the point.

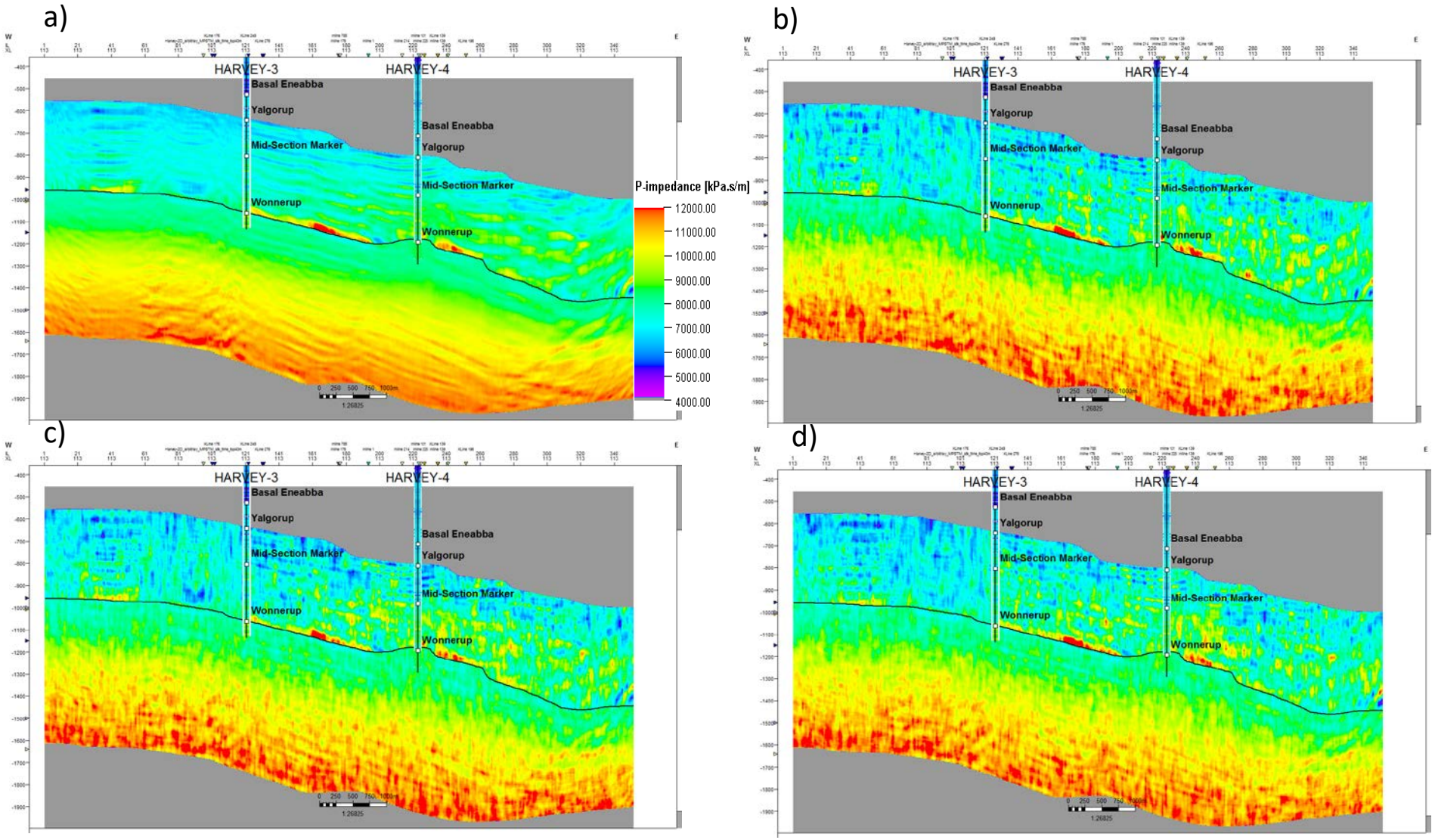


Figure 95 Vertical section from the inverted acoustic impedance extracted along crossline 113 passing through the Harvey 4 and close to the Harvey 3 wells. Shown are the mean impedance (a), and stochastic realizations # 12(b), # 25(c) and #50 (d), which resulted in a very similar level of agreement between the synthetic and actual seismic data.

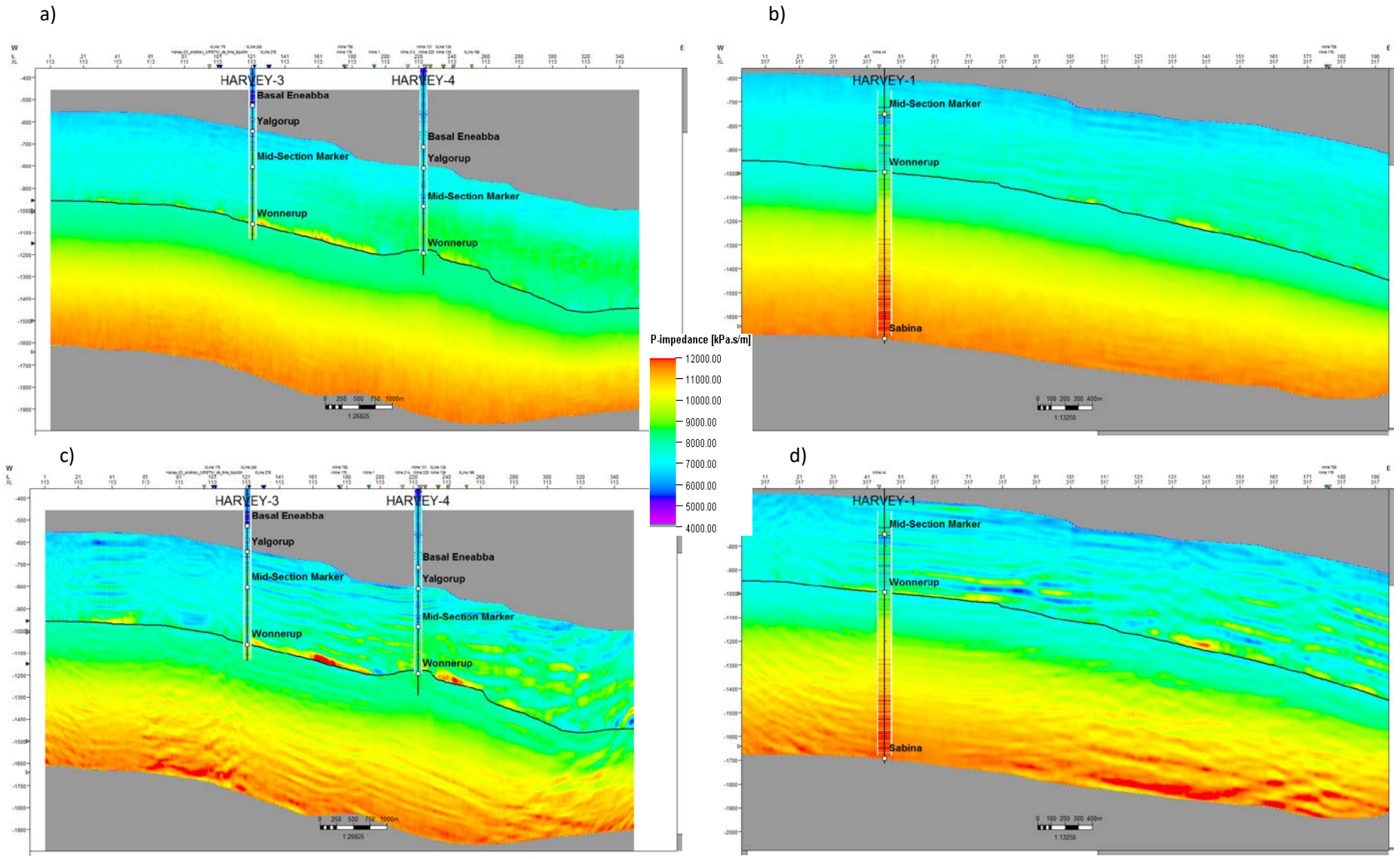


Figure 96 Vertical sections of the mean acoustic impedance obtained from the low SNR (top row) and high SNR scenarios (bottom row). The sections are extracted along crossline 113 (left column) and 317 (right column). Note the effect of seismic uncertainty estimate: the higher it is the closer to initial guess is the inverted model.

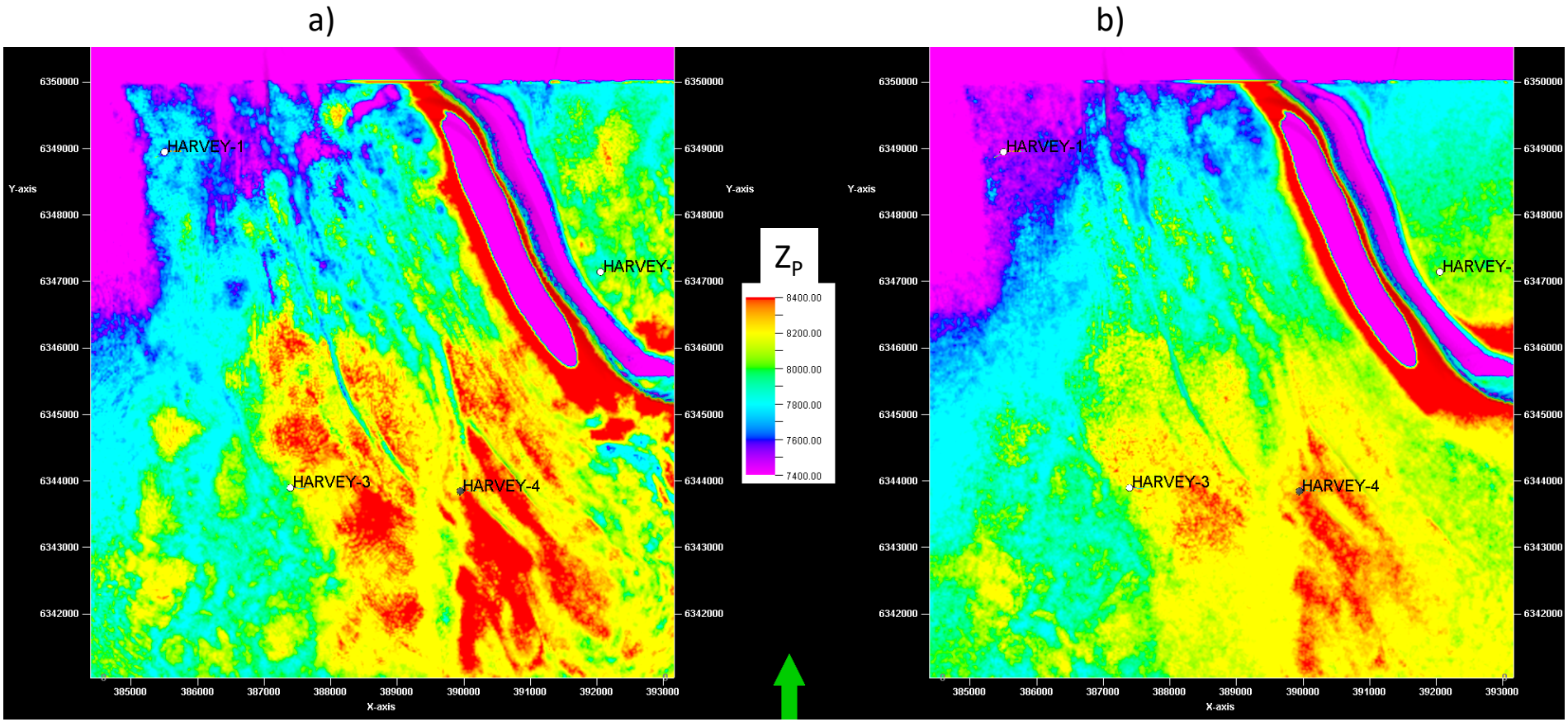


Figure 97 Horizon slice of the mean acoustic impedance cube extracted at the top of Wonnerup Member. The presented inversion scenarios are high SNR (a) and variable SNR (b). Note the effect of non-uniform seismic uncertainty: the latter map has more mild variation of the acoustic impedance that correspond to strong events that might be matched well using the extracted source wavelet.



Figure 98 The diagram summarizes testing of the number of inversion iterations. We chose the integral facies volume as a criterion of convergence. We see that after 10 realizations integral facies volume and its standard deviation stabilize. We ran the inversion with 100 realizations in order to reduce the uncertainty of the mean estimates at each trace.

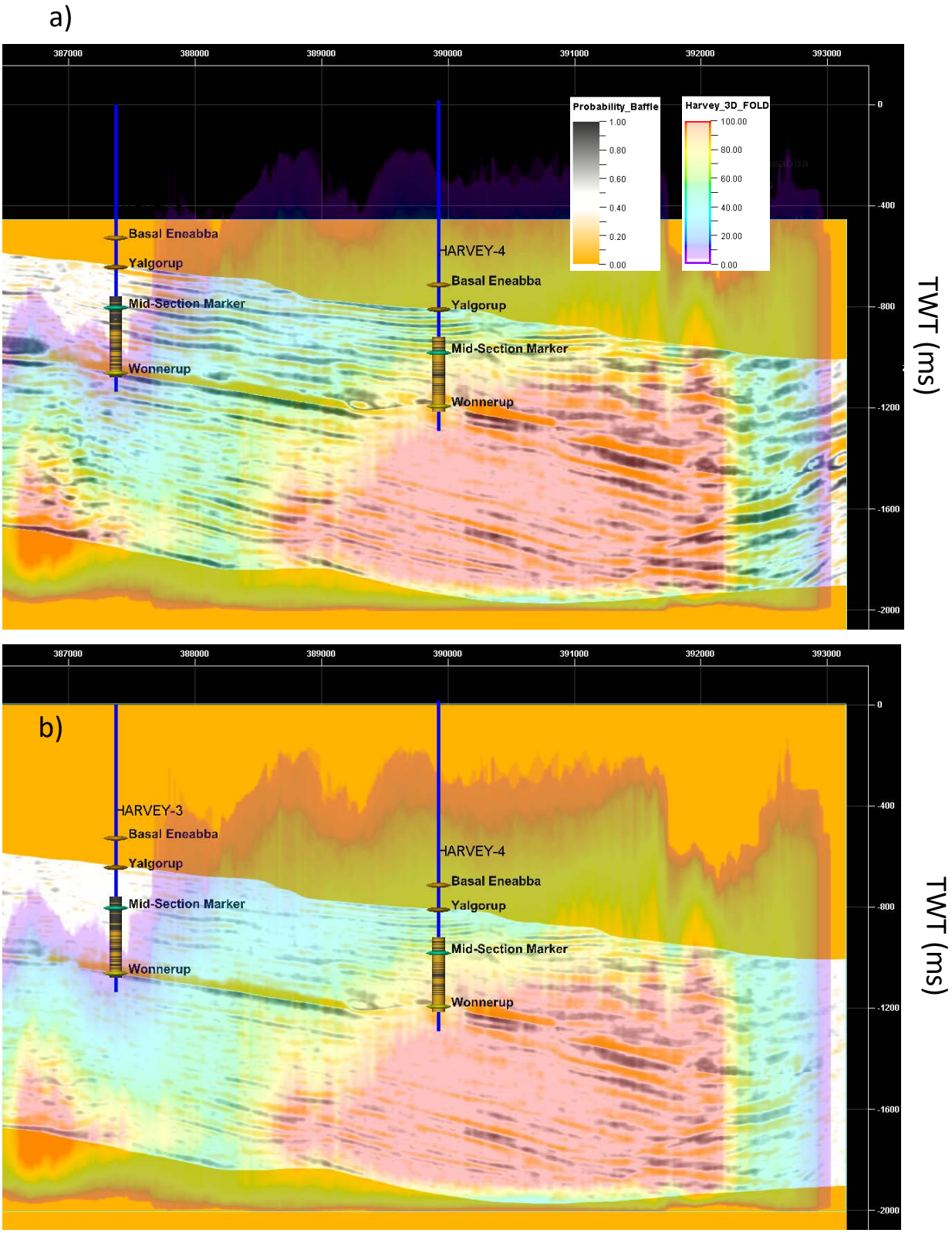


Figure 99 Vertical section of the probability of the impermeable facies obtained from the high SNR (a) and variable SNR scenario (b). Note the effect of non-uniform seismic uncertainty: section (b) has more intervals with the probability of 0.5 (facies is unknown).

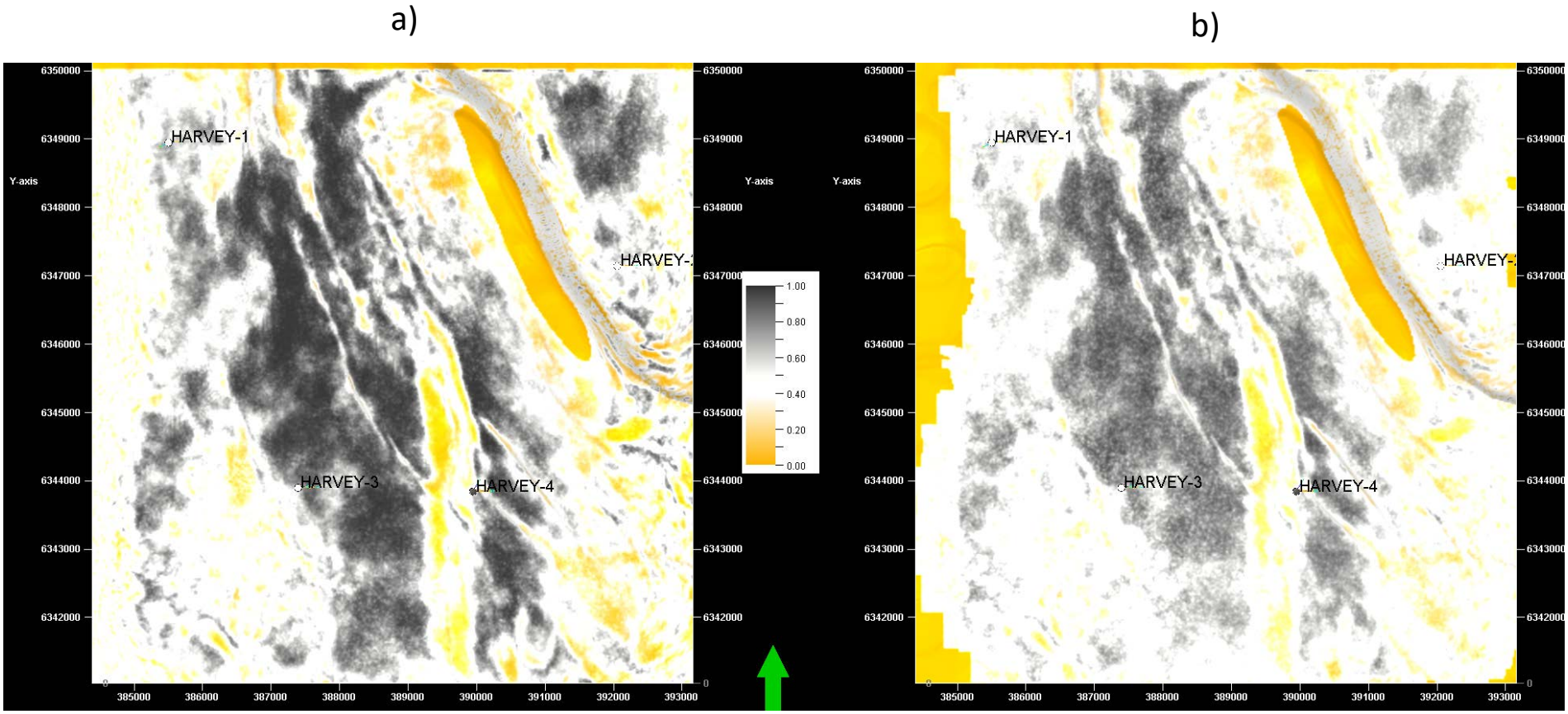


Figure 100 Maps of the probability of the impermeable facies obtained from the high SNR (a) and variable SNR scenario (b). Note the effect of non-uniform seismic uncertainty: section (b) has more intervals with the probability of 0.5 (facies is unknown), and the map features a bias towards 0.5 in general.

5.2.2. *Porosity prediction*

Accumulated experience with the SW Hub data suggests a consistent relationship between the acoustic impedance and the total porosity estimates from log data within deeper parts of the Lesueuer sandstones (see, e.g., Pervukhina et al. 2018). Figure 101 presents crossplot of the total porosity PHIT vs Z_P computed from the logs. The trend line is a least-square estimate of a polynomial function given the data in the light blue cloud (the outliers mainly belong to intervals of washouts and errors in log readings). Since non-linear terms are negligible, we applied the same linear regression to the entire impedance volume:

$$PHIT = 0.48 - 3.15 \cdot 10^{-5} \cdot Z_P \,, \tag{35}$$

The result looks geologically plausible (see **Figure 102**b):

- The transition from the Yalgorup to Wonnerup Member comprises a layer of reduced porosity that corresponds to the shaly baffles facies;
- The Wonnerup member represents a gradually changing porosity with interbeds of decreased porosity where the seismic layering is consistently observed.

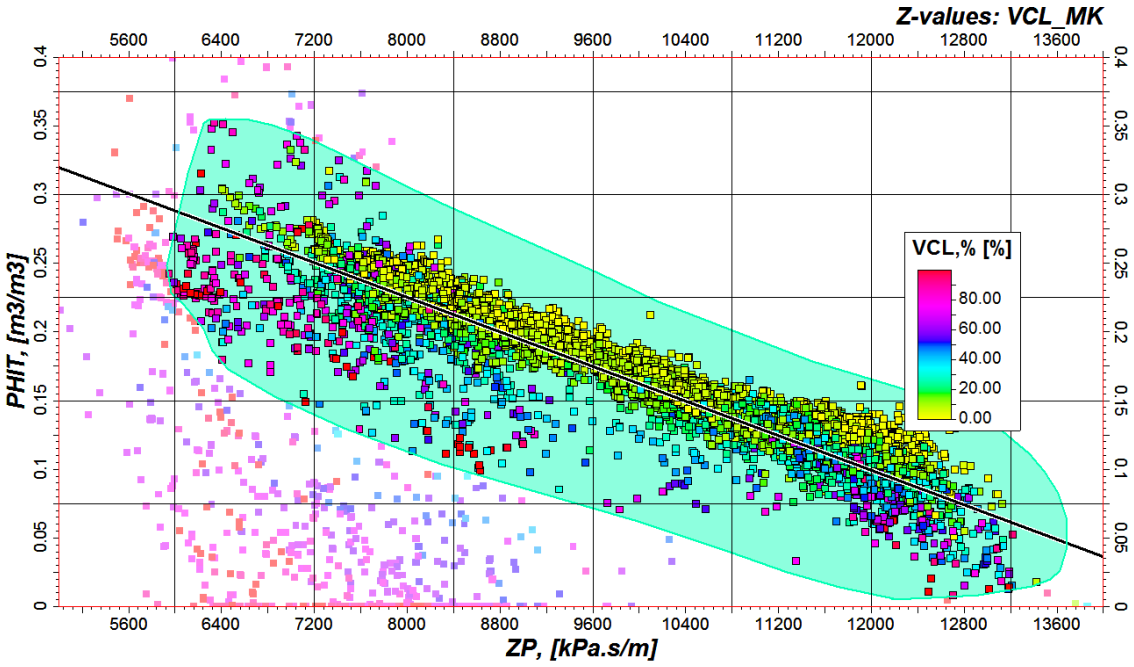


Figure 101 Cross-plot of the well estimates of the total porosity vs log acoustic impedance, the colour denotes the value of log estimate of VCL. A light-blue bubble comprises the values used in the regression (black line). The rest of the values correspond to pure shales and intervals of erroneous logs.

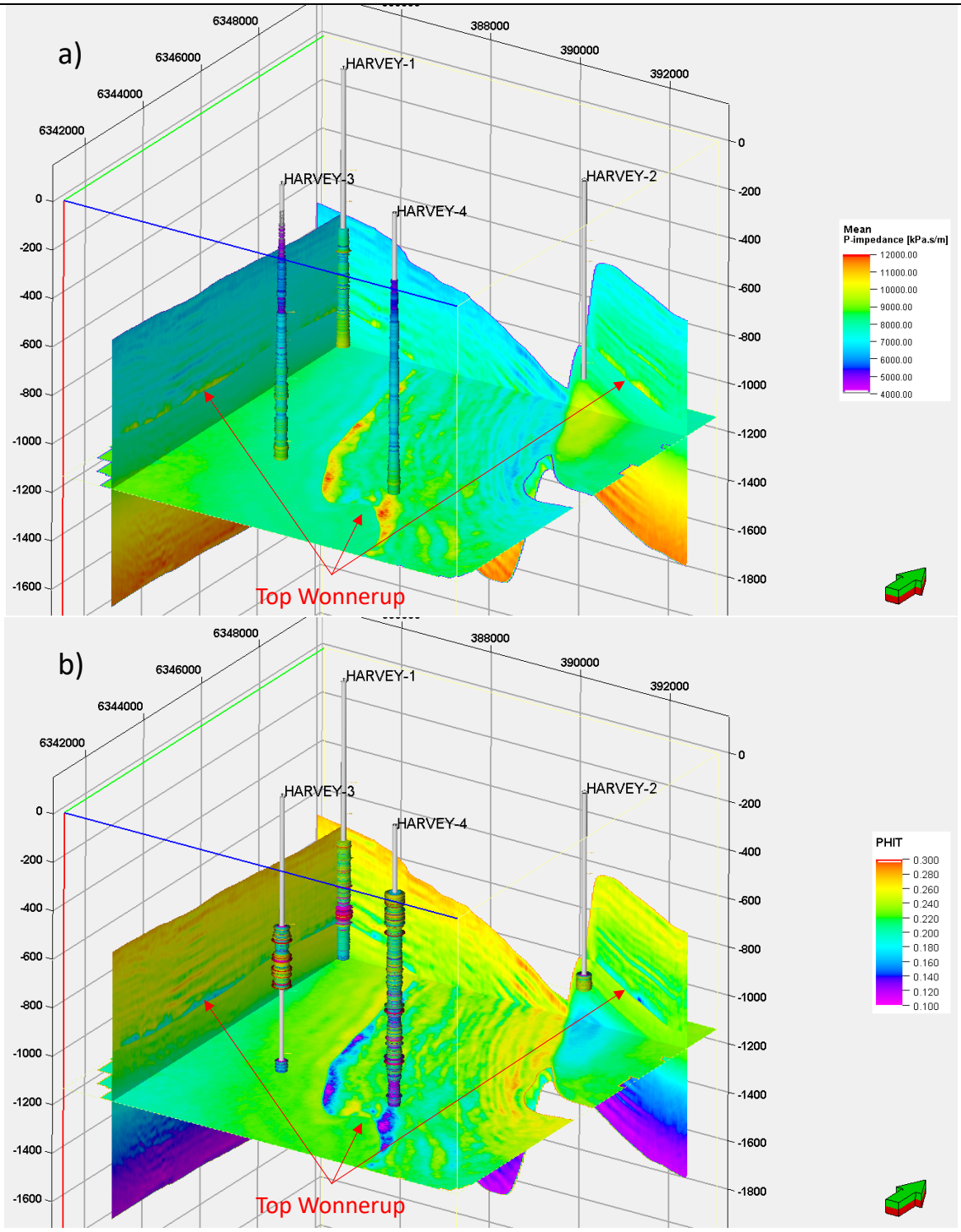


Figure 102 Vertical and horizontal slices going through the mean acoustic impedance (a) and total porosity (b) obtained from the variable SNR scenario.

5.2.3. *Comparison with the well data*

The stochastic inversion is calibrated on the available well data:

- Indirect use of the well data through:
  - well ties and wavelet extraction;
  - facies classification criteria derived from the facies interpretation of a suite of logs;
  - porosity transformation calibrated on the log data;
- Increased weight of the initial model in the vicinity of the well location.

Hence, one of the criteria for assessment of the inversion quality is agreement with the wells. Nonetheless, we may not expect a perfect match because of the incompatible difference of resolutions and lack of the seismic quality.

Figure 103 compares facies interpretation in the the Harvey 1, Harvey 3 and Harvey 4 wells by Glubokovskikh et al. (2018) against seismic facies prediction obtained for the variable SNR scenario. In general, the seismic prediction is of relatively low resolution and misses several relatively thick packages of baffles. However, the geobodies detected have a high confidence. The seismic inversion picks up the baffles/reservoir transition at the top of the Wonnerup Member even at the the Harvey 3 well location, where the section is mainly uninformative due to the high seismic uncertainty. An intra-Yalgorup interface is also marked with an increased probability of baffles.

To illustrate the essence of the probabilistic approach to the seismic interpretation, we compare the probability of baffles with two particular realizations that were drawn from it in **Figure 103**. For example, we see that the seismic data suggests a higher concentration of the baffles at the interface, but the realizations do not necessarily have a baffles body along the boreholes. This means that a discontinuous top of the Wonnerup Member allows the matching of the seismic response and the initial model with sufficient accuracy.

Figure 104 compares the seismic prediction for total porosity against the porosity estimated from the logs. The Harvey 3 well has very limited interval of the porosity logs. The other two wells show a reasonable agreement apart from an interval of noisy logs at the bottom of the Yalgorup Member, where the log porosity estimates appear to be unreliable.

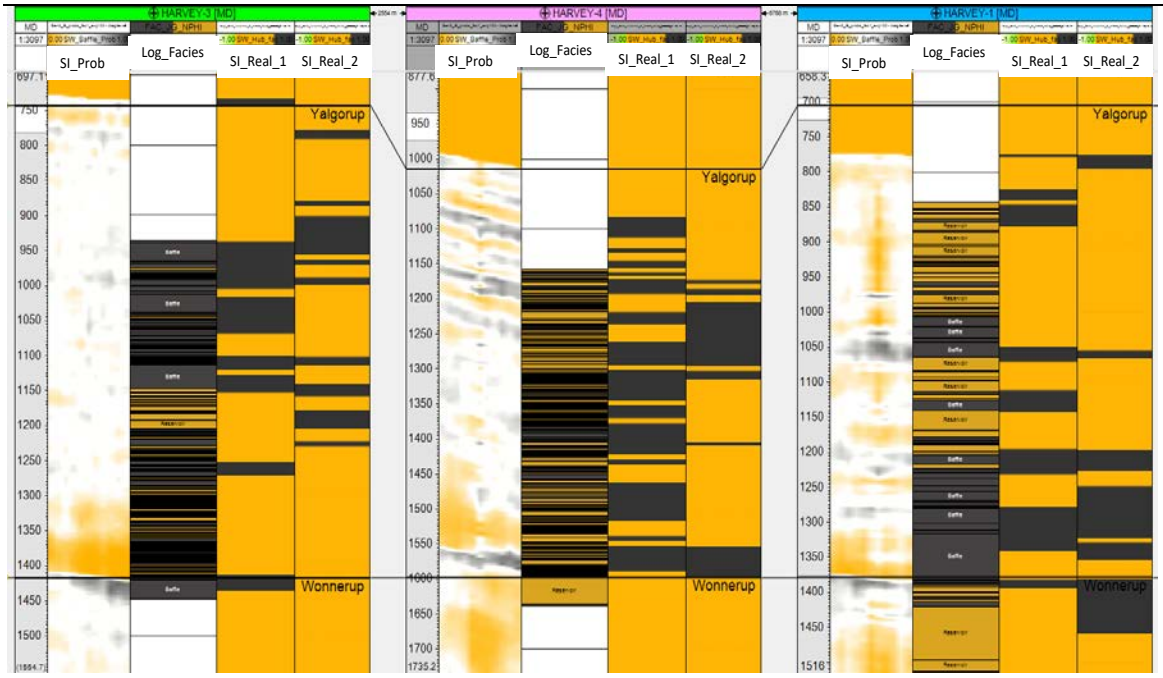


Figure 103 Comparison of the seismic facies probability (1st from the left) with log facies interpretation (2nd to the left) and two realizations of the seismic facies along the Harvey 3 (left), Harvey 4 (middle) and Harvey 1 (right) wells.

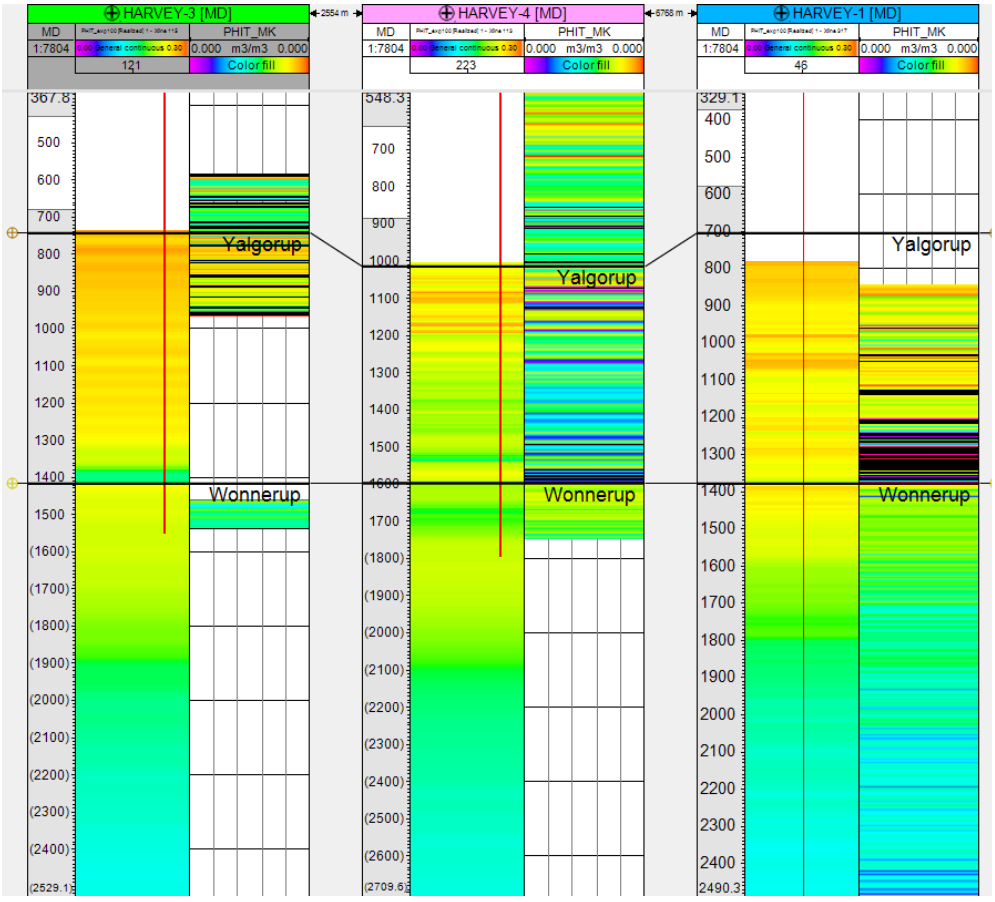


Figure 104 Comparison of the seismic total porosity (1st from the left) with the log estimates along the Harvey 3 (left), Harvey 4 (middle) and Harvey 1 (right) wells.

5.3. Conclusions

Since the seismic data quality is deemed to be too low and too variable for straightforward seismic inversion, we have modified the seismic inversion concept to reduce ambiguity of the seismic reservoir characterization at the expense of the detail of property estimates. To this end, we developed a quantitative interpretation workflow for the large 3D seismic, which implements the Bayesian approach to stochastic seismic inversion. The workflow incorporates naturally our prior beliefs about the subsurface, and hence, we used the inversion as a testing tool for different geologically plausible hypotheses.

The output of the inversion is controlled by (1) initial model and (2) our subjective estimate of the uncertainty of the initial model, well data and seismic amplitudes.

1. Our workflow may be considered a joint kinematic/amplitude inversion since the initial subsurface seismic model is based on high-resolution velocity analysis that captures both the loading trends derived from the well data and lateral variations of the seismic properties.
2. Estimates of the seismic uncertainty are derived from the well logs to seismic correlation. The point estimates at the wells were distributed into the 3D volume using the seismic data quality cube based on the seismic fold. Then, we examined three scenarios that reflect different levels of confidence in the seismic data:
    a. Low SNR results in a very smooth model almost identical to the input reflection tomography velocities, where the only prominent additional feature appears at the top of the Wonnerup Member;
    b. High SNR scenario gives much more seismically-driven features: mid-Yalgorup marker, layering in the Wonnerup Member towards eastern part of the survey (closer to the Fault 10, e.g., around The Harvey 4 etc);
    c. Variable SNR – the reference case that combines the results of the previous two scenarios in order to avoid interpretation of strong seismic features with low credibility.

Given the facies classification in the wells and correlation with petrophysical parameters, we converted the reference inversion output into petrophysical reservoir prediction. The main findings are:

1. Despite the limitations of the large 3D seismic, we still can confidently detect the Yalgorup/Wonnerup interface;

2. As expected, this horizons correspond to the rapid transition of the impermeable rocks to reservoir sandstone. While the probability of the baffles exceeds 70%, it is never close to 100%, and thus would allow for lateral discontinuity of the horizon;
3. Within the sufficient seismic quality areas within Wonnnerup, we observed two types of seismic lithology prediction:
    a. intense layering in the deeper parts towards western edge of the survey
    b. uniform reservoir – the most typical appearance.
4. We suggest that the quiescent Wonnerup Member may be due to the overlapping depth trends of the reservoir/baffles facies, so they become seismically indistinguishable.

6. Overall Conclusions

This report describes the workflow and presents the results of the comprehensive analysis of geophysical data in SW Hub area, aimed at estimating rock property distribution within the Lesueur formation. The analysis started with advanced processing of VSP data. The results of VSP analysis were then used in the reprocessing of the entire 3D seismic dataset plus a composite 2D line that passes in proximity to the three Harvey wells and has a relatively dense and uniform distribution of source-receiver offsets. Both of these datasets were then used for stochastic seismic inversion. Underpinning all of these analyses are well logs, which were comprehensively analysed in a separate report corresponding to Milestone 6 of this Project (Pervukhina et al., 2018) and are not duplicated in this report.

The main findings of the overall study are as follows:

VSP data in the Harvey 2, 3 and 4 wells are of variable quality but sufficient to estimate vertical velocities for constraining the tomographic velocity model for surface seismic data. Anomalous seismic attenuation (Q=30) is observed in the Yalgorup Member, while the contribution of scattering attenuation is minimal.

A composite line was created through the volumes, which incorporates a previously acquired 2D line with full complement of offsets and passes in proximity to the Harvey 1, 3 and 4 wells. This allowed building a relatively accurate detailed velocity model that provided a sufficiently high quality of the seismic common-offset gathers and allowed application of the stochastic AVO inversion. However, this inversion is still anchored at a single well (the Harvey 1 well) as the other wells are too shallow for the characterisation of the Wonnerup section. Although the results match the logs in the blind well (the Harvey 3 well) reasonably well, it is unclear if these results can be deemed reliable at such great distances from the Harvey 1 well. In addition, by design the results are limited to the composite seismic line.

The most comprehensive analysis was performed on the Geokinetics (2014) seismic volume, involving the stochastic rock physics inversion. To this end, the entire volume was first completely reprocessed and produced images far superior to those produced previously, with better reflection continuity and fault delineation. Furthermore tomographic velocity analysis was undertaken to produce the velocity model for both final imaging and inversion.

The deterministic inversion of the Geokinetics 3D data showed very large uncertainty and hence requires a priori constraints. To this end, a quantitative interpretation workflow was developed,

which implements the Bayesian approach to stochastic seismic inversion. The workflow incorporates naturally prior understanding about the subsurface, and hence, the inversion was used as a testing tool for different geologically plausible hypotheses.

The output of the inversion is controlled by (1) initial model and (2) our subjective estimate of the uncertainty of the initial model, well data and seismic amplitudes. The workflow is a joint kinematic/amplitude inversion since the initial subsurface seismic model is based on high-resolution velocity analysis that captures both the loading trends derived from the well data and lateral variations of the seismic properties. Given the facies classification in the wells and correlation with petrophysical parameters, we converted the reference inversion output into reservoir characteristics.

The main findings are:

1. Despite the limitations of the Geokinetics (2014) 3D seismic, the inversion confidently delineates the Yalgorup/Wonnerup interface;

2. As expected, this horizon corresponds to the rapid transition from the impermeable rocks to reservoir sandstone. While the probability of the baffles exceeds 70%, it is never close to 100%, and thus, allows for lateral discontinuity of the sealing interface along the horizon;

3. Within the sufficient seismic quality areas, we observed two seismic lithology types within Wonnnerup:

    a. intense layering in the deeper parts towards western edge of the survey

    b. uniform reservoir – the most typical appearance.

4. We suggest that the quiescent Wonnerup Member may be due to the overlapping depth trends of the reservoir/baffles facies types, so they become seismically indistinguishable. Validation of this suggestion requires additional well information.

REFERENCES

Canales, L. L., 1985, Random Noise Reduction: *Geophysics* 50, 329-329.

Commader, P. 2013 Groundwater resources of the Lesueur carbon storage project area (SW Hub); Government of Western Australia: A report for: Department of Mines and Petroleum and Department of Land and Australian Government Department of Resources, Energy and Tourism (http://www.dmp.wa.gov.au/Documents/Community-Education/SW_Hub_Groundwater.pdf)

Connolly, P., 1999. Elastic Impedance: The Leading Edge, vol. 18, no. 4, p. 438-452.

Dvorkin, J., M. A. Gutierrez, and D. Grana. 2014, Seismic Reflections of Rock Properties: Cambridge University Press

Fadhli, M., 2015, Borehole Seismic Field Report Zero Offset VSP in 2, Halliburton for Department of Mines and Petroleum, Government of Western Australia, pp26.

Geokinetics (Australasia) Pty Ltd, 2014, 2013 Harvey-Waroona 3D Seismic Survey, Final report, 136 p

Glubokovskikh, S., Ziramov, S., Urosevic, M., Pervukhina, M., and B. Gurevich, 2016a. The Lesueur, SWH: Improving seismic response and attributes. Fast-track quantitative interpretation for South West Hub. Milestone 2 Report, ANLEC R&D Project – 7-0115-0241.

Glubokovskikh, S., M.Pervukhina, R. Pevzner, B. Harris, K. Tertyshnikov, S. Ziramov, T. Müller, L. Esteban, M. Urosevic, A. Pethick, R Schaa, B. Gurevich, 2016b, The Lesueur, SWH: Improving seismic response and attributes, Milestone 4 Report, ANLEC R&D Project 7-0115-0241.

Gunning, J., Kemper, M., Saussus, D., Pelham A. and E. Fitzgerald (2013). A Tour of Optimisation Methods for Facies Estimation in AVO Seismic Inversion Using Markov Random Fields. 75th EAGE Conference & Exhibition incorporating SPE EUROPEC.

Gunning, J., & Glinsky, M. E. (2004). Delivery: an open-source model-based Bayesian seismic inversion program. Computers & Geosciences, 30(6), 619-636. doi: http://dx.doi.org/10.1016/j.cageo.2003.10.013

Hatton, L., J. Makin and M. H. Worthington, 1986, Seismic data processing: theory and practice: Blackwell Scientific, ISBN 0632013745.

Hortle, A., Ricard, L., Zhang, Y., Schaubs, P., Harris, B., Pethick, A., Shaa, R., Glubokovskikh, S., Bona, A., Pevzner, R.; Egorov, A.; Madadi, M., 2017, Feasibility of monitoring an injected CO2 plume at the South West Hub project site. ANLEC R&D Project 7-0314-0232 Milestone 3 Report.

Human, T., 2015, Borehole Seismic Field Report Zero Offset VSP in Harvey-3, Halliburton for Department of Mines and Petroleum, Government of Western Australia, pp26

Kuc, R., Schwartz, M., and von Micsky, L., 1976. Parametric Estimation of the Acoustic Attenuation Coefficient Slope for Soft Tissues, in *IEEE Ultrasonic Symposium Proceeding*, pp. 44-47 (IEEE Cat. #76H 1120-5SU).

Pervukhina, M., Esteban, L., Müller, T., Zhang, Y. and Schaubs, P., Gurevich, B., (2018). The Lesueur, SW Hub: Advanced well log analysis, constraints for the stress field and geomechanical modelling of CO2 injection, Milestone 6 Report, ANLEC R&D Project 7-0115-0241

Pevzner, R., Langhi, L., Shragge, J., Ziramov, S., Potter, T., Tetyshnikov, K., Bona, A., and M. Urosevic, 2015. Advanced processing and analysis of South West hub 3D seismic data. ANLEC R&D Report (7-0314-0231).

Pevzner, R., Lumley, D., Urosevic, M., Gurevich, B., Bóna, A., Alajmi, M.A., Shragge, J., Pervukhina, M., Mueller, T., Shulakova, V., 2013. Advanced geophysical data analysis at Harvey-1: storage site characterization and stability assessment. ANLEC R&D project number 7-1111-0198.

Pevzner, R., Muller, T., Galvin, R., and Gurevich, B., 2012, Estimation of attenuation from zero-offset VSP data: CO2CRC Otway Project case study: SEG Technical Program Expanded Abstracts, v. 31.

Quan, Y.L. and Harris, J.M., 1997, Seismic attenuation tomography using the frequency shift method. Geophysics 62, 895-905.

Roseno, E., 2015, Borehole Seismic Field Report Zero Offset VSP in Harvey-4, Halliburton for Department of Mines and Petroleum, Government of Western Australia, pp26

Simm, R., and M. Bacon. 2014, Seismic Amplitude: An Interpreter's Handbook: Cambridge University Press.

Stewart S., 2015, Seismic Processing Version 1. [Online] Available: http://www.xsgeo.com/index.html

Stork, C., 1992, Reflection tomography in the postmigrated domain: GEOPHYSICS, 57, 680–692.

Strachan, J. et al., 2016. Odin Reservoir Consultants: Static Model of the Harvey Area. Final Report for the Departments of Mines and Petroleum of Western Australia. DMP/2016/4.

Strachan, J., 2018. Odin Reservoir Consultants: Updated Static Model of the Harvey Area. Presentation to researchers.

Urosevic, M., Ziramov, S., Pevzner, R., 2015, Acquisition of the Nested 3D seismic survey at Harvey. ANLEC R&D Project 7-1213-0224 Final report, Curtin University, 36 pp.

Walden, A. T., and R. E. White. 1998, Seismic wavelet estimation: a frequency domain solution to a geophysical noisy input-output problem. IEEE Transactions on Geoscience and Remote Sensing, 36, no. 1,287-297. doi: 10.1109/36.655337.

White, R., Simm, R. & Xu, S. 1998. Well tie, fluid substitution and AVO modelling: a North Sea example. Geophysical Prospecting 46, 323-346.

Yavuz, S., Ziramov, S., Shulakova, V., Tertyshnikov, K., Langhi, L., Bona, A., R. Pevzner and M. Urosevic (2018). Potential for preferential flow through faults and fractures. ANLEC Milestone 3 report; project 7-1215-0261.

APPENDIX A – CHECK SHOT DATA

The Harvey 2 well

MD, m	TWTT (ms), Datum=15.4 m from MSL	TWTT (ms), Datum = MSL	TWTT (ms), matched to seismic Xline 5727	Vint (km/s)	Vmean (km/s)	Vlay (km/s)
45	63.5	44.9	89.2	1.649	1.418	1.921
60	81.1	62.5	81.1	1.782	1.480	1.921
75	96.9	78.3	96.9	1.859	1.548	1.921
90	112.0	93.4	112.0	1.915	1.607	1.921
105	128.7	110.1	128.7	1.953	1.631	1.921
120	143.5	124.9	143.5	2.028	1.672	1.921
135	157.9	139.3	157.9	2.096	1.710	1.921
150	171.4	152.8	171.4	2.123	1.751	1.921
165	186.3	167.7	186.3	2.082	1.771	1.921
180	200.0	181.4	200.0	2.115	1.800	1.921
195	215.7	197.1	215.7	2.167	1.808	1.921
210	227.6	209.0	227.6	2.204	1.845	2.300
225	241.8	223.2	241.8	2.227	1.861	2.300
240	255.0	236.4	255.0	2.230	1.882	2.300
255	269.3	250.7	269.3	2.279	1.893	2.300
270	281.1	262.5	281.1	2.332	1.921	2.300
285	294.5	275.9	294.5	2.396	1.935	2.300
300	306.7	288.1	306.7	2.402	1.956	2.300
315	319.1	300.5	319.1	2.456	1.974	2.300
330	331.3	312.7	331.3	2.459	1.992	2.538
345	343.4	324.8	343.4	2.461	2.010	2.538
360	355.6	337.0	355.6	2.487	2.025	2.538
375	367.9	349.3	367.9	2.508	2.039	2.538
390	379.3	360.7	379.3	2.525	2.056	2.538
405	391.3	372.7	391.3	2.491	2.070	2.538
420	403.3	384.7	403.3	2.528	2.083	2.538
435	416.1	397.5	416.1	2.596	2.091	2.538
450	426.3	407.7	426.3	2.640	2.111	2.538
465	437.6	419.0	437.6	2.670	2.125	2.538
480	449.4	430.8	449.4	2.582	2.136	2.538
495	460.7	442.1	460.7	2.523	2.149	2.656
510	472.8	454.2	472.8	2.613	2.157	2.656
525	485.3	466.7	485.3	2.637	2.163	2.656

540	494.5	475.9	494.5	2.671	2.184	2.656
555	506.8	488.2	506.8	2.711	2.190	2.656
570	518.3	499.7	518.3	2.670	2.200	2.656
585	528.8	510.2	528.8	2.666	2.213	2.656
600	539.7	521.1	539.7	2.617	2.224	2.656
615	552.3	533.7	552.3	2.717	2.227	2.656
630	563.8	545.2	563.8	2.857	2.235	3.027
645	571.9	553.3	571.9	3.049	2.256	3.027
660	582.4	563.8	582.4	3.069	2.267	3.027
675	592.2	573.6	592.2	2.979	2.279	3.027
690	602.5	583.9	602.5	3.022	2.290	3.027
705	612.2	593.6	612.2	3.023	2.303	3.027
720	622.0	603.4	622.0	3.099	2.315	3.027
735	632.1	613.5	632.1	3.119	2.326	3.027
750	641.0	622.4	641.0	3.026	2.340	3.027
765	650.8	632.2	650.8	2.949	2.351	3.027
780	662.3	643.7	662.3	2.899	2.356	3.027
795	672.3	653.7	672.3	2.939	2.365	3.027
810	682.0	663.4	682.0	3.084	2.376	3.027
825	692.0	673.4	692.0	3.117	2.384	3.027
840	701.0	682.4	701.0	3.177	2.396	3.027
855	710.9	692.3	710.9	3.211	2.405	3.325
870	719.7	701.1	719.7	3.205	2.418	3.325
885	729.4	710.8	729.4	3.275	2.427	3.325
900	738.6	720.0	738.6	3.356	2.437	3.325
915	747.2	728.6	747.2	3.380	2.449	3.325
930	755.5	736.9	755.5	3.380	2.462	3.325
945	765.3	746.7	765.3	3.277	2.470	3.325
960	773.9	755.3	773.9	3.115	2.481	3.139
975	783.8	765.2	783.8	3.102	2.488	3.139
990	794.4	775.8	794.4	3.077	2.492	3.139
1005	803.4	784.8	803.4	3.103	2.502	3.139
1020	812.9	794.3	812.9	3.244	2.510	3.139
1035	822.9	804.3	822.9	3.196	2.516	3.139
1050	830.9	812.3	830.9	3.414	2.527	3.139
1065	841.3	822.7	841.3	3.454	2.532	3.574
1080	847.6	829.0	847.6	3.377	2.548	3.574
1095	858.0	839.4	858.0	3.553	2.552	3.574
1110	867.0	848.4	867.0	3.729	2.561	3.574
1125	873.8	855.2	873.8	3.955	2.575	3.574
1140	879.9	861.3	879.9	3.835	2.591	3.574

1155	889.5	870.9	889.5	3.464	2.597	3.574
1170	898.3	879.7	898.3	3.386	2.605	3.574
1185	907.9	889.3	907.9	3.472	2.610	3.574
1200	914.9	896.3	914.9	3.497	2.623	3.574
1215	924.4	905.8	924.4	3.481	2.629	3.574
1230	933.0	914.4	933.0	3.465	2.637	3.574
1245	942.0	923.4	942.0	3.598	2.643	3.574
1260	949.4	930.8	949.4	3.677	2.654	3.574
1275	957.8	939.2	957.8	3.651	2.662	3.620
1290	965.9	947.3	965.9	3.573	2.671	3.620
1305	974.9	956.3	974.9	3.568	2.677	3.620
1320	982.9	964.3	982.9	3.629	2.686	3.620

The Harvey 3 well

MD, m	TWTT (ms), Datum=20.2 m from MSL	TWTT (ms), Datum = MSL	TWTT (ms), matched to seismic Inline 1112	Vint (km/s)	Vmean (km/s)	Vlay (km/s)
615	536.5	521.0	558.3	2.605	2.293	2.436
630	547.8	532.3	547.8	2.794	2.300	2.881
645	558.5	543.0	558.5	2.765	2.310	2.881
660	568.6	553.1	568.6	2.845	2.321	2.881
675	580.3	564.8	580.3	2.804	2.326	2.775
690	589.6	574.1	589.6	2.759	2.340	2.775
705	601.5	586.0	601.5	2.750	2.344	2.775
720	612.4	596.9	612.4	2.741	2.351	2.775
735	623.5	608.0	623.5	2.862	2.358	2.953
750	633.4	617.9	633.4	2.912	2.368	2.953
765	643.5	628.0	643.5	2.953	2.378	2.953
780	653.9	638.4	653.9	2.954	2.386	2.953
795	664.0	648.5	664.0	2.961	2.395	2.953
810	673.9	658.4	673.9	3.003	2.404	2.993
825	684.2	668.7	684.2	2.998	2.412	2.993
840	693.8	678.3	693.8	2.987	2.421	2.993
855	704.1	688.6	704.1	3.000	2.429	2.993
870	714.1	698.6	714.1	3.012	2.437	2.993
885	724.0	708.5	724.0	3.075	2.445	2.993
900	733.7	718.2	733.7	3.166	2.453	3.292
915	743.1	727.6	743.1	3.249	2.463	3.292
930	752.0	736.5	752.0	3.292	2.474	3.292
945	761.0	745.5	761.0	3.278	2.484	3.292

960	770.3	754.8	770.3	3.209	2.493	3.292
975	779.7	764.2	779.7	3.117	2.501	3.036
990	789.4	773.9	789.4	3.079	2.508	3.036
1005	799.6	784.1	799.6	3.036	2.514	3.036
1020	809.0	793.5	809.0	3.073	2.522	3.036
1035	819.3	803.8	819.3	3.151	2.527	3.036
1050	828.3	812.8	828.3	3.199	2.535	3.268
1065	837.6	822.1	837.6	3.276	2.543	3.268
1080	846.8	831.3	846.8	3.298	2.551	3.268
1095	855.8	840.3	855.8	3.269	2.559	3.268
1110	864.7	849.2	864.7	3.256	2.567	3.268
1125	874.5	859.0	874.5	3.207	2.573	3.268
1140	883.5	868.0	883.5	3.174	2.581	3.141
1155	893.2	877.7	893.2	3.174	2.586	3.141
1170	902.6	887.1	902.6	3.174	2.593	3.141
1185	912.2	896.7	912.2	3.135	2.598	3.141
1200	921.3	905.8	921.3	3.122	2.605	3.053
1215	931.7	916.2	931.7	3.103	2.608	3.053
1230	940.9	925.4	940.9	3.110	2.614	3.053
1245	950.7	935.2	950.7	3.203	2.619	3.287
1260	960.0	944.5	960.0	3.217	2.625	3.287
1275	969.0	953.5	969.0	3.266	2.632	3.287
1290	978.4	962.9	978.4	3.324	2.637	3.392
1305	987.4	971.9	987.4	3.347	2.643	3.392
1320	995.9	980.4	995.9	3.369	2.651	3.392
1335	1005.1	989.6	1005.1	3.288	2.656	3.392
1350	1014.1	998.6	1014.1	3.253	2.662	3.246
1365	1023.9	1008.4	1023.9	3.239	2.666	3.246
1380	1032.6	1017.1	1032.6	3.246	2.673	3.246
1395	1042.2	1026.7	1042.2	3.304	2.677	3.246
1410	1051.2	1035.7	1051.2	3.348	2.683	3.246
1425	1060.0	1044.5	1060.0	3.464	2.689	3.670
1440	1068.4	1052.9	1068.4	3.597	2.696	3.670
1455	1076.9	1061.4	1076.9	3.650	2.702	3.670
1470	1084.5	1069.0	1084.5	3.695	2.711	3.670

The Harvey 4 well

MD, m	TWTT (ms), Datum=19.89 m from MSL	TWTT (ms), Datum = MSL	TWTT (ms), matched to seismic Inline 1112	Vint (km/s)	Vmean (km/s)	Vlay (km/s)
470	457.2	443.7	479.3	2.932	2.038	2.897
485	464.5	451.0	464.5	2.808	2.070	2.897
500	479.9	466.4	479.9	2.798	2.067	2.897
515	490.2	476.6	490.2	2.712	2.085	2.897
530	498.0	484.5	498.0	2.821	2.112	2.897
545	510.8	497.2	510.8	2.809	2.118	2.970
560	522.8	509.2	522.8	2.899	2.127	2.970
575	531.2	517.6	531.2	2.970	2.150	2.970
590	539.6	526.0	539.6	2.933	2.172	2.970
605	552.9	539.3	552.9	2.739	2.174	2.970
620	563.1	549.5	563.1	2.756	2.188	2.837
635	574.2	560.6	574.2	2.857	2.198	2.837
650	583.4	569.8	583.4	2.881	2.214	2.837
665	595.3	581.7	595.3	2.980	2.221	2.837
680	604.6	591.0	604.6	2.852	2.236	2.582
695	613.9	600.4	613.9	2.648	2.251	2.582
710	626.6	613.1	626.6	2.582	2.253	2.582
725	640.9	627.3	640.9	2.601	2.250	2.582
740	649.2	635.6	649.2	2.847	2.267	2.582
755	660.3	646.7	660.3	3.037	2.274	3.227
770	669.6	656.0	669.6	3.008	2.288	3.227
785	680.1	666.5	680.1	2.980	2.296	2.815
800	689.2	675.6	689.2	2.857	2.310	2.815
815	700.9	687.3	700.9	2.799	2.314	2.815
830	711.7	698.2	711.7	2.774	2.321	2.815
845	722.4	708.8	722.4	3.008	2.328	3.195
860	732.5	718.9	732.5	3.083	2.337	3.195
875	740.4	726.8	740.4	3.195	2.353	3.195
890	751.4	737.8	751.4	3.110	2.358	3.195
905	759.9	746.3	759.9	3.035	2.371	3.195
920	770.9	757.4	770.9	3.006	2.376	2.739
935	780.0	766.4	780.0	2.779	2.387	2.739
950	791.3	777.7	791.3	2.795	2.391	2.739
965	803.7	790.1	803.7	2.898	2.391	2.739
980	812.8	799.2	812.8	3.147	2.401	3.161

995	821.0	807.4	821.0	3.235	2.414	3.161
1010	830.3	816.7	830.3	3.102	2.423	3.161
1025	841.3	827.7	841.3	2.900	2.427	3.161
1040	851.0	837.4	851.0	3.053	2.435	3.718
1055	862.4	848.8	862.4	3.383	2.437	3.718
1070	868.9	855.3	868.9	3.718	2.454	3.718
1085	876.7	863.1	876.7	3.692	2.466	3.718
1100	884.1	870.6	884.1	3.212	2.479	3.718
1115	895.4	881.8	895.4	3.247	2.481	3.425
1130	906.2	892.7	906.2	3.206	2.485	3.425
1145	911.9	898.3	911.9	3.441	2.502	3.425
1160	922.7	909.1	922.7	3.395	2.506	3.425
1175	930.7	917.2	930.7	3.107	2.516	3.087
1190	941.0	927.4	941.0	3.121	2.521	3.087
1205	951.0	937.4	951.0	3.064	2.526	3.087
1220	960.6	947.1	960.6	3.128	2.531	3.087
1235	969.9	956.3	969.9	3.168	2.538	3.087
1250	979.5	965.9	979.5	3.202	2.544	3.087
1265	988.9	975.4	988.9	3.222	2.550	3.344
1280	998.0	984.4	998.0	3.315	2.557	3.344
1295	1007.2	993.6	1007.2	3.337	2.563	3.344
1310	1015.6	1002.0	1015.6	3.316	2.572	3.344
1325	1025.0	1011.5	1025.0	3.360	2.577	3.344
1340	1034.3	1020.7	1034.3	3.376	2.583	3.344
1355	1042.5	1028.9	1042.5	3.486	2.592	3.344
1370	1051.3	1037.8	1051.3	3.569	2.598	3.590
1385	1059.6	1046.0	1059.6	3.544	2.607	3.590
1400	1067.8	1054.2	1067.8	3.639	2.615	3.590
1415	1076.6	1063.0	1076.6	3.639	2.621	3.590
1430	1084.0	1070.5	1084.0	3.613	2.631	3.590
1445	1092.7	1079.1	1092.7	3.562	2.637	3.590
1460	1101.3	1087.7	1101.3	3.504	2.644	3.590
1475	1110.1	1096.5	1110.1	3.496	2.650	3.590
1490	1118.1	1104.5	1118.1	3.488	2.658	3.326
1505	1127.1	1113.6	1127.1	3.386	2.663	3.326
1520	1135.8	1122.2	1135.8	3.371	2.669	3.326
1535	1145.6	1132.0	1145.6	3.371	2.673	3.326
1550	1153.4	1139.8	1153.4	3.297	2.681	3.326
1565	1162.8	1149.2	1162.8	3.387	2.685	3.326
1580	1172.6	1159.1	1172.6	3.290	2.688	3.326
1595	1180.3	1166.7	1180.3	3.418	2.696	3.449

1610	1190.3	1176.7	1190.3	3.497	2.698	3.449
1625	1197.9	1184.3	1197.9	3.481	2.706	3.449
1640	1206.7	1193.1	1206.7	3.651	2.711	3.449
1655	1215.1	1201.5	1215.1	3.599	2.717	3.729
1670	1222.7	1209.2	1222.7	3.633	2.725	3.729
1685	1231.6	1218.0	1231.6	3.715	2.730	3.729
1700	1239.8	1226.2	1239.8	3.678	2.736	3.729
1715	1247.0	1233.4	1247.0	3.799	2.744	3.729

APPENDIX B – ACRONYMS AND NOTATION

- AVO – amplitude versus offset
- GR – gamma-ray log
- NG – net-to-gross;
- PHIT – total porosity;
- PSTM – pre-stack time migration;
- PSDM – pre-stack depth migration;
- QC – quality control;
- QI – quantitative interpretation;
- RMO – residual moveout removal
- SNR – signal-to-noise ratio
- V_P – P-wave velocity;
- V_S – S-wave velocity;
- VSP – Vertical seismic profiling
- Z_P – acoustic impedance;
- ρ - bulk density;

APPENDIX C – THE LESUEUR, SW HUB: ADVANCED WELL LOG ANALYSIS, CONSTRAINTS FOR THE STRESS FIELD AND GEOMECHANICAL MODELLING OF CO2 INJECTION - MILESTONE 6 REPORT